University of Oxford

DPhil Thesis

Field-induced assembly of fibrous network structures in magneto-rheological fluids



David R. Robinson

St Edmund Hall

2012-2016

David R. Robinson, St Edmund Hall

A thesis submitted for the degree of Doctor of Philosophy of The University of Oxford

Abstract

Self-assembly is a process by which a disordered system becomes an organised, complex structure as a result of a given chemical or physical change. Many experiments have been able to show the effect of an applied field on the self-assembly of superparamagnetic, micrometre scale particles at a low surface coverage. As such, particle positions are able to be monitored in real time from which the chain aggregation process can be analysed in terms of coordination environments. Therefore mathematical and simulation models have become useful in order to describe the interaction between particles and act as a predictive tool for future experimental research. The majority of simulation work regarding electro- and magneto-rheology attaches a permanent, fixed dipole to the particles and measures the response to an applied field. This thesis employs and justifies a model where particles are fully (dipole) polarizable with dipoles induced both by an external field (the direction and magnitude of which may be controlled) and by the presence of other dipole moments (dipole-induced-dipole effects) and consequently the potential contains a many-body character. A 'real' particle system is necessarily represented by a dispersion of polarizabilities (magnetizations) which is the motivation for the choice of model. Two models are therefore employed to investigate the effects of the dipole-induced-dipole term in bulk systems containing monodisperse particles and bidisperse particles respectively. Justification of the model allows prediction of more complex systems, namely confined systems as discussed in the final chapter.

Acknowledgements

I dedicate this thesis to Amy Bridgford. This is as much your triumph as it is mine. I am forever in your debt.

I would also like to thank Mark Wilson, my supervisor for his direction and patience over the last 5 years. I have enjoyed the entire process immensely and his support has been invaluable. I am indeed a better version of myself as a result of his input in my work and I genuinely hope I haven't put him off taking any more DPhil students in the future!

Finally I would like to thank all of those who have supported me either financially, indirectly or out of necessity: The EPSRC for their research funding allowing this thesis to develop as it has. St Edmund Hall for putting up with me for the best part of 8 years. The Ogden Trust and Bolton School Boys' for their financial support throughout my early school and undergraduate life, without which I would not be in the position I am today. Dirk Aarts, Roel Dullens, Bill Sampson and Colin Reynolds for their collaboration with this work and many interesting discussions. The PTCL and Organic lab demonstration team and my unfortunate friends Kelvin and Pete (who kept me sane over the years). Last but by no means least, thank you Mum you have always been my greatest supporter.

Bring on the next challenge.

Contents

1 Introduction **1**

1.1 Colloidal Physics 7

1.2 Thesis Structure 12

2 Simulation Methods **15**

2.1 The Potential Energy 17

2.2 Molecular Dynamics Simulation 18

2.3 General Mathematical Formalism 19

2.3.1 Lagrangian Dynamics 20

2.3.2 Hamiltonian 21

2.3.3 Velocity Verlet Integration Algorithm 22

2.4 The Induced Dipole and Applied Field 23

2.4.1 Polarization Effects 25

2.4.2 Extending the Lagrangian to Include Polarization 27

2.4.3 Maintaining the Adiabatic Condition 32

2.5 Short-range Potential 33

2.6 Energy Minimisation 35

2.6.1 Nosé-Hoover Thermostat 36

2.7 Boundary Conditions 37

2.7.1 Minimum Image Convention 39
2.7.2 Ewald Summation Technique 40
2.8 Analytical Techniques 45
2.8.1 Radial Distribution Function 46
2.8.2 Partial Radial Distribution Functions 47
2.8.3 Structure Factor 48
2.8.4 Coordination Number Statistics 49
2.8.5 Local Coordination Parameter 49
2.8.6 Local Order Parameter 52
2.8.7 Mean Chain Length 52
2.8.8 Chain Length Distributions 53
2.8.9 Bond Angle Distribution Function 54
2.9 Chapter Summary 55

3 Chain Formation **57**
3.1 Two-Particle Simulations 59
3.2 Infinite Chains 64
3.2.1 Single Chain vs. 2-Particle Simulation 65
3.2.2 Interaction Between Chains 66
3.3 Chapter Summary 69

4 Monodisperse Systems **71**
4.1 Simulation Methodology 72
4.2 Dipole Distributions 74
4.3 Structure 81
4.3.1 Molecular Graphics 81
4.3.2 Coordination Environments 83

4.3.3 Radial Distribution Functions 83
4.3.4 Chain Alignment 86
4.4 Density Variation 87
4.4.1 Cell Elongation 93
4.4.2 System Size Variation 99
4.5 Chapter Summary 100

5 Using Experiment to Direct Simulation 101

5.1 Experimental Background 102
5.2 Experiment → Simulation 104
5.3 Energetics 107
5.4 Structure 111
5.5 Chain Growth Statistics 113
5.5.1 Chain Length and Coordination Number 114
5.6 Chapter Summary 120

6 Bidisperse Systems 121

6.1 Dipole Distributions 123
6.2 Structure 126
6.3 Coordination Environments 129
6.3.1 Coordination Number 130
6.3.2 Chain Lengths 137
6.3.3 Aggregation Over Time 143
6.4 Scaling 146
6.4.1 Scaling With Fixed $\langle\alpha\rangle$ 146
6.4.2 Scaling with $\Delta\alpha$ 150
6.5 Field Ramping and Hysteresis 154

6.5.1 Coordination Environments 155
6.6 Radial Distribution Function and $\boldsymbol{S}(\boldsymbol{k})$ 162
6.6.1 Partial RDF 172
6.7 Chain Alignment 179
6.8 Chapter Summary 181

7 Self-Assembly Under Confinement **183**
7.1 Confinement Using Discrete Particle Walls 184
7.2 No Inclusions 185
7.3 Symmetric Wall Inclusions 188
7.3.1 Elongated Cell 191
7.4 Offset Wall Inclusions 192
7.4.1 Varying $\{\alpha, \mathbf{E}_{ex}\}$ at Constant μ 193
7.4.2 Varying γ_{off} 198
7.4.3 Varying Field Direction 200
7.5 Chapter Summary 202

8 Conclusions **203**

Appendices **205**

A Multipole Interaction Tensors **205**
A.1 Tensor Expressions 205
A.1.1 Derivation of Interaction Tensors 206
A.2 Einstein Summation Convention 208

B Further Simulation Methods **209**
B.1 Energy Conservation 209
B.2 Velocity Verlet Integration Algorithm 209

B.3 Verlet Integration Algorithm 210
B.4 Steepest Descent Minimisation 211

C Analytical Techniques **213**
C.1 Chain Length Distribution Derivations 213
C.2 Continuous Analogue of Chain Length Distributions 215
C.3 Reduced Units 218

D Dipoles in Chains **219**
D.1 Two Dipoles 219
D.2 A Chain of Dipoles 220
D.3 The Distribution of Dipoles along a Chain 220
D.4 The Monodisperse Model 221

E Table of Bidisperse Runs **223**

Bibliography **223**

Chapter 1

Introduction

Self-assembly is a process by which a disordered system becomes an organised, complex structure as a result of a given chemical or physical change. Dipolar fluids are an example of one such system specifically due to characteristic aggregation properties with [1, 2] or without [3] the application of an external field. Complex structure formation has been widely observed for a number of years, specifically regarding dipolar fluids where there are a number of key review papers which aim to shed light on the current understanding of the system in order to control and predict the extent of self-assembly [1–7].

In 1985, Skjeltorp first identified the formation of chain-like structures formed in MR (magneto-rheological) fluids, a dipolar fluid with magnetic colloidal particles dispersed in a non-magnetic solvent (or non-magnetic colloidal particles dispersed in a magnetic fluid) [8]. After applying an external magnetic field, chain-like fibrous network structures may appear, which act to alter the viscosity of the system. Thus MR fluids have a wide range of applications in mechanical systems that require the control of vibrations or transmission of torque [6], such as in shock absorbers [9], brake fluids or prosthetic limbs [10]. Since then there have been a plethora of experiments in the field focusing primarily on string formation in dilute systems [11–14] or

crystallisation in dense systems [11, 15]. There is also a growing amount of simulation work that models a variety of MR fluids [16, 17] (see below).

Ferromagnetism in a solid (*e.g.* a crystal or polycrystalline material) is described as a long range ordering of the magnetic moments of individual atoms (*e.g.* in iron, nickel and cobalt) which, at temperatures below the curie temperature, separate into non-permanent domains and sub-domains in order to minimise the field energy [18, 19]. A domain is a region of the material in which all the magnetic moments of the particle components are in one direction. Each domain therefore can exhibit an overall magnetization (magnetic dipole moment per unit volume) pointing in different directions and the boundaries of such domains are called domain walls which act to reduce the overall magnetostatic energy of the system. Antiferromagnetism in contrast (*e.g.* found in MnO, FeO and NiO) exhibits no net moment over long range given alternate ordering of parallel and antiparallel magnetic moments on atoms in the solid. Interestingly ferrimagnetism contains atoms of unequal alternating moments such that the overall magnetic moment is lower than that in a ferromagnetic material. More importantly in reference to this work, a colloidal magnetic fluid consists of ferro- or ferrimagnetic, single-domain particles, with no long range ordering similar to that of paramagnetism but with larger magnetization in low fields, this is known as a superparamagnetic material (which has no net magnetization when the field is removed unlike a ferromagnetic solid with many domains). Many types of magnetic fluid exist with ferrohydrodynamic properties (mechanics of fluid motion influenced by strong forces of magnetic polarization [19]) one such interesting type is a colloidal ferrofluid. A colloid is a suspension of particles in a continuous medium. A ferromagnetic colloid therefore is a suspension of small, solid, magnetic, single-domain particles ($3 - 15nm$) coated with a molecular layer of dispersant (preventing particle sticking) and suspended in a liquid carrier. Brownian motion accounts for

this suspension given collisions of the particles with the liquid cause thermal agitation and a random-walk of translational movement.

After the application of an external magnetic field (or change in field) the ferrofluid must relax such that the magnetic dipoles and particle velocity adjust to the new equilibrium. There are two mechanisms that allow this change, Brownian and Néel. The Brownian mechanism or particle rotation mechanism describes a Brownian rotational diffusion time $\tau_B = 3V\eta_0/k_BT$ which depends on the volume of the particle V and the viscosity of the carrier liquid η_0 [20]. The second mechanism allows relaxation to occur by rotation of the magnetic vector in the particle. In the absence of an external magnetic field, if the thermal energy k_BT is larger than an activation energy KV which is the energy required to change the orientation of the magnetization from along one easy-axis to the other antiparallel axis, through a hard plane (K is the anisotropy constant) then the fluctuation time is $\tau_N = \tau_0 \exp \frac{KV}{k_BT}$. This was first introduced by Néel [21] which helps to describe a superparamagnetic colloid and $\tau_0 = \frac{1}{f_0}$ gives the attempt time which is unique to the fluid (proportional to the attempt frequency for the fluctuation). Therefore when $\tau_N \ll \tau_B$ the fluid has intrinsic superparamagnetism (Néel mechanism) and when $\tau_B \ll \tau_N$ the fluid has extrinsic superparamagnetism (Brownian mechanism). The fluid is ferromagnetic when both time constants are much larger than the experimental timescale. Both mechanisms lead to superparamagnetism in a colloidal ferrofluid and depend on particle volume V where $\tau_B \ll \tau_N$, as the particle size increases and the colloidal ferrofluid is dominated by the Brownian mechanism for superparamagnetism. The temperature at which magnetization time τ_m is equal to τ_N is the blocking temperature T_B which blocks the nanoparticle in the intitial magnetisation state where the magnetisation of the particle will not invert during the measurement. This also depends on the size of the particle, $T_B = \frac{KV}{k_B ln(\tau_m/\tau_0)}$. Further physical properties of magnetic colloidal fluids

are discussed in **Section 1.1** below.

The principal difference between the more popularized ferrofluids and MR fluids is simply the size of the magnetically susceptible particles. In ferrofluids these particles are on the nanometre scale whereas MR particles are several orders of magnitude larger, on the micrometre length scale, which not only settle in the carrier fluid (without suspension from Brownian motion as with the ferrofluid) but most importantly these system particles can be monitored using both optical- and electron-microscopes [22]. As a result, the evolution of these potentially complex structures can be directly observed and characterised [11, 22–35]. The structural information obtained from the MR particle aggregation experiments (with real time visual observation) provides extremely precise positional information, however the field of vision is typically limited to a few thousand particles with self-assembly 'events' often confined to a relatively small number of independent observations. As such, the alternative method of structure elucidation providing highly spatial and time-averaged information on the bulk system can be obtained using a number of diffraction and scattering experiments [34–44].

Consequently, mathematical and simulation models (which may relate the sample of experimentally observed structures to more general property distributions *e.g.* [45]) now become useful interpretative tools, particularly concerning the mechanism of network formation, allowing real time particle position information to reveal information about bulk system properties which have been previously unobtainable by scattering experiments alone. The simple dipolar fluid problem is particularly attractive theoretically and computationally as the inter-particle interaction energies may often be expressed in relatively simple (and hence computationally-tractable) terms and yet the strongly directional nature of the particle interactions may generate a vast richness of structure on a number of (often competing) length-scales [46, 47].

The key principle in the majority of the simulation work to date, is the assumption that the dipoles are of fixed magnitude, pinned to the centre of the simulation particles (*e.g.* modelled as rods of an infinitesimal length with opposing charges on either end) where the response to the presence of other dipole moments and/or to an applied field can be studied. This class of models is therefore useful as the interaction energy may be expressed in a pair-wise additive form, and hence are relatively computationally-tractable, linking easily to established liquid state theories [48, 49]. The simplest systems studied consist of a single species (with fixed dipole magnitude and particle size) [16, 50–62]. Complexity can be built into a simulation model with relative ease, for example introducing systems of mixed particle species as opposed to a homogenous particle set. Examples include the formation of complex structures in simple mixtures of hard-sphere and hard-sphere dipoles [63–68] or mixtures of Lennard-Jones particles and dipolar species [69–75]. Under certain conditions significant de-mixing (phase separation) behaviour is observed [63, 64, 67, 69, 72, 76]. It can be observed that for mixtures of dipolar and non-dipolar species, the origin of the de-mixing effect is relatively clear. Above a (temperature-dependent) dipole moment threshold the dipole-dipole interactions are sufficiently strong (compared to interactions involving the non-polar particles) to overcome the entropic mixing contribution to the free energy. Analogous behaviour applies to mixtures of particles with differing dipole magnitudes [67]. In recent years a number of experimental groups have focused on controlling aggregation phenomena on the micro- and nano-particle length scales [8, 11, 22–35]. In these cases dipole moments arise directly from the application of an external field (rather than as a direct consequence of the structure of the particle), that is, moments are induced rather than permanent. It must be stated that all simulations which have fixed point dipoles (the majority of phase separation calculations for strongly interacting dipolar particles as discussed above) are quantitatively

wrong due to the mean field approximation. However, the methodology used in this thesis includes the many-body effects of the dipole-dipole interactions, providing an alternative simulation approach.

The overall focus of this thesis is field-induced assembly using MR fluids as the framework, studying the response to a magnetic field. Similar behaviour occurs with an electric field and therefore the magnitude of the induced moments is controlled either by the magnetic susceptibility or the dipole polarizability of the particle. Aggregation phenomena for systems of this type can be modelled using fixed dipoles with the implicit assumption that the magnitude of the dipole used matches the first order induced moment, such that any potential many-body dipole-induced-dipole (DID) effects are neglected, or incorporated as a mean average. However, the effectiveness of this approach is unclear, in particular in the limit of a high susceptibility and low applied field where such many-body effects may become significant. The role of polarization in systems of this type has been investigated [4, 70, 71, 77, 78] again highlighting potential de-mixing scenarios [79, 80]. Furthermore, real particle ensembles would be expected to have a dispersion of properties, for example, in terms of both particle diameter and susceptibility. These systems are most commonly (though not exclusively) modelled as monodisperse (for which the appropriate properties represent a mean average) or by directly linking particle diameter and dipole [67, 81]. Significant simulation work has been performed on systems with a polydispersity in dipole strength and/or particle diameter, with the general conclusion that larger particles (higher dipole moments) tend to preferentially aggregate [81–87].

In this thesis therefore, the extent of complex structure formation is investigated under the influence of an applied electric field. The models employed are fully (dipole) polarizable with dipoles induced both by an external field (whose direction and magnitude may be controlled) and by the presence of other dipole moments (dipole-induced-

dipole effects) and, as a result, the potential contains a many-body character. Two basic models are employed; in the first monodisperse polarizabilities are used whilst, in the second, a bidisperse arrangement is selected where the difference in polarizabilities can be varied. Central aims are to establish the role of dipole-induced-dipole effects and the potential implications of the system having a dispersion of polarizabilities. To accomplish this, computer simulation models have been developed in order to improve the understanding of structural and dynamical processes involved in field-induced assembly of fibrous networks, specifically in magneto-rheological (MR) systems as mentioned. The factors that control the material properties of these systems such as density, particle size, particle susceptibility, confinement and flow, additionally the presence of a dispersion of properties, are considered. This provides an in-depth understanding of the mechanisms describing network formation in this way and will aid in the development of magnetic devices such as tunable nanofilters, optical gratings and conducting networks.

1.1 Colloidal Physics

As described above a magnetic ferrofluid comprises of a stable colloidal dispersion of sub-domain magnetic particles in a carrier fluid [19]. The colloidal particles require adsorbtion of long chain molecules to their surface (such as polystyrene) in order to prevent cluster aggregation of particles, this is known as the dispersant. As mentioned above, solid colloidal particles (usually on the nanometre to micrometre scale [88]) collide randomly with the liquid particles leading to Brownian Motion [89] which is diffusive by nature. The mean squared displacement that describes this motion (in 2D) is given as

$$msd = \left\langle |\mathbf{r}(t) - \mathbf{r}(0)|^2 \right\rangle = 4Dt = \frac{4k_B T t}{\gamma} \tag{1.1.1}$$

in the limit of infinite dilution [90], where **r** describes the positional coordinates of the atoms, D is the diffusion coefficient, k_B is the Boltzmann constant, t is the time and γ is the drag coefficient. The diffusion coefficient (D) is the amount of a particular substance that diffuses across a unit area in one second under the influence of a gradient of one unit [91]. $\gamma = 6\pi\eta r$ for a simple spherical particle, where η is the viscosity of the liquid and r is the particle radius. For the simulations described in this thesis the motion of the particles in the absence of an applied field is ballistic ($\langle x^2 \rangle \propto t^2$) at short range and diffusive over long range ($\langle x^2 \rangle \propto t$). Particle interactions in the simulation will be discussed in the following chapter. For real colloidal systems that undergo substantial Brownian motion, the Langevin equation is used to describe the particle motion, with noise and drag terms respectively. In 1D (for illustration, as this equation can easily be extended to 3D) the Langevin equation is described by

$$\frac{dv(t)}{dt} = \frac{-\gamma}{m} v(t) + \frac{1}{m}\xi(t) \tag{1.1.2}$$

where $\xi(t)$ is the force exerted on a particle in the colloid as a result of random density fluctuations in the liquid, γ is the drag coefficient as mentioned above and all other variables have their usual meaning. The average force on a particle is $-\gamma m v(t)$ therefore the average of the stochastic fluctuating force must be zero. $\xi(t)dt$ is determined by a Gaussian function with zero mean in order to provide meaningful solutions to **Equation 1.1.2**.

There are a number of interactions between colloidal particles which are of interest in ferrofluid systems. When the overall particle interactions are repulsive the colloid is known as stabilised or dispersed. When the overall particle interactions are attractive this leads to flocculation (also known as aggregation) to form a gel [92]. Electrostatic stabilisation is the mechanism by which these two forces are balanced to stabilise the colloid. The main attractive interaction in neutral particles is the van der Waals force

which arise due to the fluctuating electric dipole moments. Its interaction distance is on the order of $10nm$ between separated particles beyond which it is negligible and several k_BT in magnitude. Colloidal particles experience different contributions to the net repulsive interactions, each can be tuned to prevent gel aggregation from large van der Waals attractions. To assist in the description of colloidal particle repulsive interactions, electrical double layers (EDs) must be discussed as shown in **Figure 1.1** and are comprised of three components: The surface charge (*black* line), the Stern layer (dashed *green* line) [93] and the diffuse layer. A particle with negative surface charge (produced when negatively charged ions in the medium adsorb onto the particle surface) attracts counterions in the medium by Coulomb electrostatic force. The diffuse layer then is the layer of ions surrounding the particle of higher mean concentration than that in the medium [94]. The value of the electrical potential is largest at the surface, drops when increasing the distance from the surface to the Stern layer and drops more rapidly again at distances greater than the Stern layer until it reaches zero at the boundary of the diffuse layer which is known as the slipping plane with corresponding electrical potential equal to the ζ-potential. The Debye length (κ^{-1}) quantifies the distance at which the electric potential drops by $1/e$ and is a characteristic length scale in colloidal systems inversely proportional to the ionic strength of the medium.

$$\kappa^{-1} = \sqrt{\frac{\epsilon k_B T}{e^2 \sum_i C_i^0 z_i}} \tag{1.1.3}$$

where ϵ is the solution permittivity, e is the unit charge and $\sum_i C_i^0 z_i$ is the ionic strength: The sum of the concentration of species, C_i^0 multiplied by the squared charge z_i. The Debye length (typically $0.3nm \rightarrow 300nm$) is governed by the solvent, the solid colloidal particles and the interactions of the counterions on the solid particles [95]. Two colloidal particles experience a Coulomb repulsive interaction throughout the region of the electric double layer. This repulsion is known as charge

stabilisation and occurs due to the dissociation/association equilibrium present when the ionic species bound to the surface of the ferromagnetic particles interact with the solvent. When the surface molecules temporarily dissociate, forming counterions that interact with the solvent, a charged surface is exposed, which at short range repels other colloidal particles. Steric stabilization occurs when a small polymer is attached to the surface of a colloidal particle (with tunable length, set larger than the van der Waals interaction) such that when colloidal particles move closer to each another, the polymer interactions cause a repulsive steric force. A depletion interaction involves polymers added to the colloid which do not interact or adsorb to the solid particles but provide additional repulsive forces between polymer and solid preventing solid-solid interaction.

The DLVO (Derjaguin, Landau, Verwey and Overbeek) theory is also used to summarise the attractive and repulsive interactions of charge stabilised colloidal systems [96, 97]. Assumption of this theorem are (i) dispersion is dilute, (ii) there are only two contributions to the 'DLVO' potential ($U_{DVLO} = U_{vdw} + U_e$), the van der Waals potential, U_{vdw} and the electrostatic potential, U_e, (iii) the electric charge is uniformly distributed along the colloidal particle surface and (iv) the ions are distributed as determined by the electrostatic force and Brownian motion.

$$U_{vdw} = \frac{-Aa}{12r}, \tag{1.1.4}$$

where A is the Hamaker constant, a is the particle radius and r is the distance between surfaces and

$$U_e = z^2 k_B T \lambda_B \left(\frac{\exp \kappa a}{1+\kappa a}\right)^2 \frac{\exp -r\kappa}{r} \tag{1.1.5}$$

where z is the particle charge, κ^{-1} is the Debye length and λ_B is the length at which the electrostatic interactions equal $k_B T$, known as the Bjerrum length [98].

The ferrofluid particles each have a number of types of energy which govern their interaction in the fluid, these are: (i) a thermal energy term $k_B T$. (ii) a magnetic

energy term $\mu_0 MHV$ where $M = \rho_s/\mu_0$ is the intensity of magnetization of the ferromagnetic particle (assuming uniform) and ρ_s is the surface density of the magnetic poles, H is the magnetizing field, μ_0 is the permeability of free space and V is the volume of the particle. (iii) a gravitational potential energy term $\Delta\rho VgL$, where $\Delta\rho = \rho_{solid} - \rho_{liquid}$ is the density difference between solid particles and the fluid, g is the acceleration by gravity and L is the gravitational height. L can be expressed as the ratio of thermal energy to the gravitational energy

$$L = \frac{k_B T}{\Delta\rho V g L} \tag{1.1.6}$$

or the height the thermal energy can raise a particle. This property is referred to a gravitational buoyancy as both energies are in competition with one another, affecting the stability of the particle. Therefore there exists a density gradient in the fluid. If $\Delta\rho$ is large then L is small and the particles settle in the cell, if $\Delta\rho$ is small enough then L is larger than the height of the container and the particles are buoyant in the liquid of the colloid, therefore the density is constant throughout. This is referred to as density matching, similarly smaller solid particles will also increase L. Refractive index matching can also be undertaken in order to successfully visualise and track colloidal particles using image software [99]. This is particularly important for magnetorheological fluids where solid particles are on the micrometre length scale. An opaque solution would prevent easy viewing of solid particles in the medium of different refractive index under a microscope, thus index matching is a mechanism which avoids this problem.

In this work inertial molecular dynamics calculations are used to study nanoparticles which are moved along their respective lines of force using Newtonian mechanics (linking back to atomistic simulations) with the aim of establishing how the formation mechanisms, determined in this manner, may differ (or not) to those observed in experiment where alternative (e.g. Brownian) dynamics schemes may dominate (as

in colloidal nanoparticles discussed above).

Unit System in this Thesis

It is important to note the rationale for the use of real units and when it is appropriate to introduce reduced units (**Appendix C.3**) throughout this thesis. The latter clearly has more relevance to the dipolar model field whereas, the use of the former where the majority of units are reported in atomic units (of length *etc.*), fit in with the field of basic electrostatic simulations. The reason for reporting the simulation work in 'real' units is to allow contact to be made with previous computation work in which dipole-dipole interactions have been significant. Whenever relevant reduced units are used to compare to the analogous colloidal system.

1.2 Thesis Structure

The structure of this thesis is as follows:

Chapter 2: A review of simulation model techniques with an in-depth description of each component used for computation as presented in this work. In particular, this includes the functional form of the potential energy governing inter-particle interactions; the induced-dipole effect and the mathematical formalism of multipoles; energy minimisation techniques, boundary conditions and the host of analytical techniques used to quantify chain-aggregation in the particle systems.

Chapter 3: A bridging chapter to highlight the development of the model from low N systems to infinite idealised chains, presenting a justification for the choice of pair-potential specifically in the production of simulation models displaying single chain aggregation properties.

Chapter 4: The simulation of bulk MR fluids using particles with a fixed polarizability such that the effect of the dipole-induced-dipole on the extent of chain formation is taken into consideration. Phase and parameter space is explored and the relationship between chain formation and density, cell-size and system size is covered.

Chapter 5: This chapter relates the simulation models to parallel experimental work, providing a relationship between the coordination number, particle aggregation time and mean chain length properties.

Chapter 6: The simulation of bulk MR fluids using a bidisperse system, such that there are equal number of particles with either a high or low set polarizability. The role of the DID term controls the extent of chain formation even at low field and the construction of the chains in terms of a mixed chain (high and low polarizabilty particles) or a de-mixed chain (high or low polarizability particles only). The particle polarizability difference is investigated and in addition to the potential scaling properties that exist in the system.

Chapter 7: A speculative chapter which introduces confinement into the particle cell. A pseudo-continuous wall with an attractive potential is placed in the system and chain formation is tuned based on the construction of the wall.

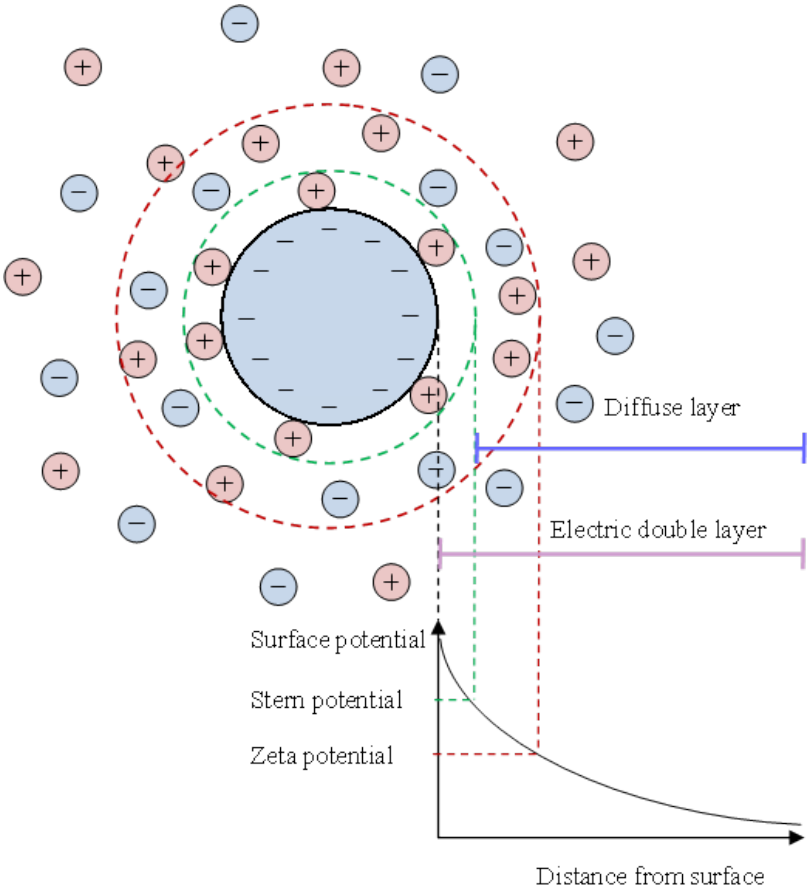


Figure 1.1: A figure to depict the electrical double layer with a corresponding potential curve for illustration. The electrical potential is largest at the particle surface (central colloidal particle is depicted negatively charged at the surface). The Stern layer is between the colloidal particle surface and the dashed *green* line. The dashed *red* line is the slipping place with in which the colloidal particle acts a single entity with corresponding electric potential equal to the ζ-potential.

Chapter 2

Simulation Methods

There are a variety of computational techniques employed to simulate the dynamics of a system in a condensed phase. In a molecular dynamics simulation each particle moves along a line of force, determined as a function of their positions. As a result, for a given particle configuration, the accelerations, velocities and positions can readily be evaluated allowing key properties, such as the temperature and pressure of the system, to be calculated with ease [100]. Simulations may be greatly simplified by employing relatively uncomplicated functions to describe the inter-particle interactions. The simplicity of such a simulation allows for both accessible computational length- and time-scales, without compromising the reliability of the output [100].

Models of this type do not explicitly account for changes in the electron density, as in pure electronic structure calculations. However this classical method allows the modelling of a multi-component system with a relatively large number of particles [101] and thus it is the most logical approach to this area of research. In addition, relatively simple potential model-based methods allow full control over the inter-particle interactions. Key parameters (controlling, for example, complex self-assembly behaviour) may be identified and modelled in a systematic manner. As a result, significant insight may be gained which is more difficult to achieve with (more

computationally demanding) electronic structure methods.

Electronic structure calculations are simply solutions to the Schrödinger equation for a given atomic configuration. The calculations are made from first-principles, such that they contain only a few key parameters in order to provide a basic description of the system and therefore can be made without the direction provided from experimental work. The issues in this method lie with the fact that exact solutions to the Schrödinger equation are only available for a single electron system. Adding complexity, by increasing the number of particles in the system, will naturally lead to the use of more elaborate approximation methods within the model. Consequently, this defeats the purpose of selecting this approach over a system governed by effective pair-potentials, given that there is there is no more of an advantage to the accuracy or speed at which the calculations are made. As such, the inclusion of rigorous electron-electron interactions adds unnecessary complexity in the form of a wildly increased system size (runtime scales exponentially with N). For the bulk systems investigated in this thesis, a large number of particles described by effective pair-potentials simplify the calculation of average properties in a more efficient manner.

As mentioned, electronic effects are expensive to compute explicitly and would naturally involve minimisation of the global energy state of the system at each time step over the run. By using effective pair-potentials to model particle interactions, such that molecular dynamics simulations are the method of particle advancement over time, local energy minima can be probed, providing information on realistic configurations of the bulk systems in question. Polarization effects, specifically the dipole-induced-dipole effects characteristic of MR/ER fluids, are also included within the model. Methods developed by Car and Parrinello [102] are applied (originally designed for density functional theory) to Lagrangian dynamics [100, 103, 104], as discussed in the next several sections, in order to facilitate calculation of these effects

in relation to an applied field. The work of M. Sprik [105], M. Wilson and P. A. Madden detail the development of this model extensively in a number of key publications as listed above [106].

The following chapter will provide the technical simulation details required in order to construct and utilise the model developed in this project. The chapter covers the underlying theory of the molecular dynamics (MD) technique in the context of the model used as well as the functional form of the potential energy, methods of energy minimisation and the surfeit of individual analytical techniques required in order to evaluate the results. The chapter also outlines the underlying theory required to model the interactions resulting from the dipoles induced by an external field.

2.1 The Potential Energy

The potential energy $U(\mathbf{r})$, is a function of the set of $\{\mathbf{r}\}$ particle coordinates. Therefore provided that the function is relatively simple to calculate and can accurately depict the physical system of interest, then the bulk properties of a system can easily be determined. In general the energy of N interacting particles in a system can be written as a cluster expansion,

$$U(\mathbf{r}) = \sum_i V_1(\mathbf{r}^i) + \sum_{i<j} V_2(\mathbf{r}^i, \mathbf{r}^j) + \sum_{i<j<k} V_3(\mathbf{r}^i, \mathbf{r}^j, \mathbf{r}^k) + \dots \qquad (2.1.1)$$

where $\mathbf{r}^n$ is the position of the n^{th} particle and V_m describes an m body potential [107]. The first expansion term in **Equation 2.1.1** refers to any external potential (one-body interaction) and is often neglected (although it will be considered throughout this thesis). The second term describes the true pair-potential for a dimer which can be parametrised by using a number of gas-phase molecular spectroscopic techniques. The third term describes the exact three-body energy of interaction of an isolated trimer. A common approximation is to introduce an effective pair-potential (V^{eff})

which incorporates the true pair-potential and also averages the higher order terms. Lennard-Jones '6-12' and Born-Mayer potentials are examples of simple, effective pairwise potential models that incorporate higher order terms into a pairwise additive form [108]. These effective pair-potentials portray the interaction between particles in a closed-shell, close-packed system with relatively high accuracy as the 'correction terms' (V_3 and higher order) are relatively small.

Effective pair-potentials are, however, often unsuitable when describing systems where directional forces may be significant (*i.e.* $V_3 \sim V_2$ in **Equation 2.1.1**) and which, for example, may control a variety of differing polytypes (*e.g.* carbon). For covalent systems, for example [101], the third term in the energy expansion (**Equation 2.1.1**) must be included explicitly in order to account for the angular dependence of the interaction energy between particle triplets. Erkoc states that three-body potential models can be organised into two classes, ($\phi_{2,3}$) and ($\phi_2 + \phi_3$) [109]. The two- and three-body terms may be combined into a single potential function:

$$\phi_{2,3} = \sum_{i<j:k} U_{ij:k}, \tag{2.1.2}$$

e.g. the Tersoff II potential for covalent materials [107, 110], or they may be treated separately as a sum of the two- and three-body interactions:

$$\phi_2 + \phi_3 = \sum_{i<j} U_{ij} + \sum_{i<j<k} W_{ijk} \tag{2.1.3}$$

as in the Stillinger-Weber [111] potential model. The explicit form of the total potential energy is justified and written out in **Sections 2.4** and **2.5**.

2.2 Molecular Dynamics Simulation

Molecular dynamics simulation is a technique for computing the equilibrium and transport properties of a classical many-body system [112]. The motion of each

particle in the system is controlled by applying Newton's laws of classical mechanics, thus by solving Newton's second law of motion, using methods of integration, a prediction of a valid trajectory for each particle can then be determined [113]. A simple molecular dynamics scheme would contain the following steps [112, 114]:

1. Initialisation of the system by selecting N particle positions and velocities at time, $t = 0$.

2. Calculation of the forces on all particles determined from a potential model, the complexity of which depends entirely on the nature of the system of interest.

3. Movement of the particles along their respective line of force via integration of Newton's second law of motion.

4. Steps 2-3 are then repeated. Properties of interest can then be determined by averaging over the configurations generated.

Such a scheme is a simplistic view of the MD process contained in the work of this thesis, however it is useful to state the underlying principles which will be expanded in the following **Section 2.3**.

2.3 General Mathematical Formalism

Allen and Tildesley [114], along with many other publications [112], provide a formalism to outline the generalised mathematical approach used to describe a simplistic MD simulation. This involves solving the classical equations of motion of a particle system as set out by Goldstein [115]; for an ensemble containing N particles interacting via a potential, $\mathscr{U}$.

2.3.1 Lagrangian Dynamics

The microscopic state of a system containing N particles can be specified in terms of their generalized coordinates ($\mathbf{r}$) and momenta ($\mathbf{p}$);

$$\mathbf{r} = (\mathbf{r}^{(1)}, \mathbf{r}^{(2)}, \mathbf{r}^{(3)}, \ldots, \mathbf{r}^{(N)}) \qquad \mathbf{p} = (\mathbf{p}^{(1)}, \mathbf{p}^{(2)}, \mathbf{p}^{(3)}, \ldots, \mathbf{p}^{(N)}) \tag{2.3.1}$$

where the i^{th} particle has a position, $\mathbf{r}^{(i)}$ and momentum, $\mathbf{p}^{(i)}$. Note the label i is **not** indicative of a power series and is written in this way, as will become clear in **Section 2.4.1**, in order to include the Cartesian components of the polarization effects clearly and precisely. The fundamental Lagrangian equation of motion [115] for a conservative system is

$$\frac{d}{dt}\left(\frac{\partial \mathscr{L}}{\partial \dot{\mathbf{r}}^i}\right) - \left(\frac{\partial \mathscr{L}}{\partial \mathbf{r}^i}\right) = 0 \qquad (i = 1, 2, 3, \ldots, N) \tag{2.3.2}$$

which contains the Lagrangian function ($\mathscr{L}$), defined as the difference between the net kinetic energy ($\mathscr{K}$) and the net potential energy ($\mathscr{U}$);

$$\mathscr{L}(\mathbf{r}, \dot{\mathbf{r}}) = \mathscr{K}(\dot{\mathbf{r}}) - \mathscr{U}(\mathbf{r}). \tag{2.3.3}$$

It is important to note that $\mathscr{L}$ is a function of $\mathbf{r}$ <u>*and*</u> $\dot{\mathbf{r}}$ (the time derivative of $\mathbf{r}$, equivalent to the velocity vector of the motion). Indeed both $\mathbf{r}$ and $\dot{\mathbf{r}}$ are a function of time for any arbitrary particle in motion, however only by using the chain rule and thus total derivatives of the Lagrangian, can the time evolution of each property of motion be derived (**Equation 2.3.2** which is equivalent to Newton's second law of motion). For a classical system, the kinetic energy term in **Equation 2.3.3** is

$$\mathscr{K}(\dot{\mathbf{r}}) = \frac{1}{2}\sum_{i=1}^{N} m^i (\dot{\mathbf{r}}^i)^2 \tag{2.3.4}$$

and $\mathscr{U}(\mathbf{r})$ is the potential energy which is determined by the potential model employed (as discussed for the general case in **Section 2.1**). The force on the i^{th} particle is

$$\mathbf{f}^i = \nabla_{\mathbf{r}^i}\mathscr{L} = -\nabla_{\mathbf{r}^i}\mathscr{U} \tag{2.3.5}$$

in terms of Cartesian coordinates, $\mathbf{r}^i$.

As a result,

$$m^i(\ddot{\mathbf{r}}^i) = \mathbf{f}^i \tag{2.3.6}$$

is Newton's second law where m^i is simply the mass of the i^{th} particle/molecule. Therefore by solving this second-order differential equation (**2.3.6**) in Euclidean space, the trajectories of each particle can be followed as a function of time [101, 114, 115]. In addition it is also worth noting that in Newtonian/Lagrangian Dynamics the equations of motion are reversible in time [114], as reversing the sign of each velocity will reverse the path of the trajectory.

2.3.2 Hamiltonian

The Hamiltonian of a system can be expressed solely as a function of the nuclear variables, as the rapid electron motion can be averaged out as a result of utilising the well-known Born-Oppenheimer approximation [116]. Classically, the Hamiltonian ($\mathscr{H}$) describing the total energy of a system can be expressed as a sum of the kinetic and potential energy functions

$$\mathscr{H}(\mathbf{r}, \mathbf{p}) = \mathscr{K}(\mathbf{p}) + \mathscr{U}(\mathbf{r}) \tag{2.3.7}$$

providing that the potential function is independent of velocity and time [114]. $\mathscr{H}$ is the conserved property in the simulation and in terms of the Lagrangian, can be strictly defined as

$$\mathscr{H}(\mathbf{r}, \mathbf{p}) = \sum_{i=1}^{N} \mathbf{p}^i \dot{\mathbf{r}}^i - \mathscr{L}(\mathbf{r}, \dot{\mathbf{r}}) \tag{2.3.8}$$

with the Hamiltonian equations of motion,

$$\dot{\mathbf{r}}^i = \frac{\partial \mathscr{H}}{\partial \mathbf{p}^i} \qquad\qquad \dot{\mathbf{p}}^i = -\frac{\partial \mathscr{H}}{\partial \mathbf{r}^i}. \tag{2.3.9}$$

Thus in Cartesian coordinates the equations of motion become

$$\dot{\mathbf{r}}^i = \frac{\mathbf{p}^i}{m^i} \tag{2.3.10}$$

and

$$\dot{\mathbf{p}}^i = -\nabla_{\mathbf{r}^i}\mathscr{U} = \mathbf{f}^i. \tag{2.3.11}$$

Therefore, by solving $6N$ first-order differential equations (**2.3.10**) and (**2.3.11**), or $3N$ second-order differential equations (**2.3.2**) the trajectories of the particles can then be obtained. As described above, the total system energy (sum of the potential and kinetic energies) is the conserved variable (see **Appendix B.1**). This is termed the micro-canonical ensemble (NVE).

2.3.3 Velocity Verlet Integration Algorithm

There are many algorithms available that can be used to integrate the equations of motion, directly solving **Equation 2.3.6**. The most widely used (and that used in this work) is the velocity-Verlet scheme [117, 118]. This method stores position, velocity and acceleration information explicitly at time t, in order to calculate the corresponding values at time $t + \delta t$. This algorithm is more computationally flexible than the more awkward Verlet scheme, it is self-starting whilst still minimising the loss of numerical precision given by rounding error. Derivation of this integration scheme can be accomplished using the finite difference method, which is shown in **Appendix B.2**. This method makes use of a Taylor expansion about time (t) in order to estimate the positions and velocities of the particles in a system, at a progressed time ($t + \delta t$), assuming that the classical trajectories are continuous. As such

$$\mathbf{r}^i(t + \delta t) = \mathbf{r}^i(t) + \dot{\mathbf{r}}^i(t)\delta t + \frac{1}{2}\ddot{\mathbf{r}}^i(t)\delta t^2 + \mathcal{O}(\delta t^3). \tag{2.3.12}$$

Substitution of $\mathbf{v}^i(t) = \dot{\mathbf{r}}^i(t)$ and $\mathbf{f}^i(t)/m^i = \ddot{\mathbf{r}}^i(t)$ into **Equation 2.3.12** with further alegbraic manipulation as in **Appendix B.2** gives

$$\mathbf{r}^i(t+\delta t) = \mathbf{r}^i(t) + \mathbf{v}^i(t)\delta t + \frac{\mathbf{f}^i(t)}{2m^i}\delta t^2 + \mathcal{O}(\delta t^3), \tag{2.3.13}$$

and

$$\mathbf{v}^i(t+\delta t) = \mathbf{v}^i(t) + \frac{1}{2m^i}[\mathbf{f}^i(t) + \mathbf{f}^i(t+\delta t)]\delta t + \mathcal{O}(\delta t^3), \tag{2.3.14}$$

which is the velocity Verlet algorithm used. The Taylor expansion is usually truncated after the $\mathcal{O}(\delta t^2)$ term in order to minimise the computational expense of the MD steps while upholding the accuracy of the calculation. The time step, δt [101, 114] must be long enough to give a significant amount of simulation time in a reasonable number of integration steps, yet as short as possible to preserve the accuracy of the simulation reducing deviations from the correct classical trajectories. For an additional reference **Appendix B.3** contains information on the Verlet scheme and leapfrog algorithm as a contrast to the velocity Verlet scheme.

2.4 The Induced Dipole and Applied Field

In order to complete a description of the individual particles used for MD simulations (as described in this thesis) there must be an adequate description of polarization effects arising from a change in dipole moment resulting from exposure to an applied field. Dipoles are *induced* by an external field; $\boldsymbol{\mu} = \alpha\mathbf{E}$ for an electric field or $\boldsymbol{\mu} = \chi\boldsymbol{B}$ for a magnetic field, where $\mathbf{E}$ and $\boldsymbol{B}$ are electric and magnetic field vectors and α and χ are the respective particle polarizability and magnetic susceptibility. In the case of the electric field the induced dipole can be written as,

$$\boldsymbol{\mu}^i = \alpha(\mathbf{E}_{ex} + \mathbf{E}^i_{int}), \tag{2.4.1}$$

where the dipole on site i arises from both an applied external field, $\mathbf{E}_{ex}$ and an internal field, $\mathbf{E}_{int}$ generated by the dipoles induced on all other sites. This external

field may vary in both magnitude and direction in the simulation model and therefore give rise to an additional term in the total potential energy. The entire potential energy of the system can be written as

$$U^{all} = \sum_{i=1}^{N-1} \sum_{j=i+1}^{N} \left\{ U^{sr}(\mathbf{r}^{ij}) - T^{ij}_{\alpha\beta}\mu^{i}_{\alpha}\mu^{j}_{\beta} \right\} + k_1 \sum_{i=1}^{N} (\boldsymbol{\mu}^{i})^2 - \sum_{i=1}^{N} \boldsymbol{\mu}^{i} \cdot \mathbf{E}_{ex} \tag{2.4.2}$$

such that the first term, U^{sr}, describes the short range inter-particle potential. The second term gives the dipole-dipole interaction energy between particles i and j, using the tensor $T^{ij}_{\alpha\beta}$ as derived in **Equation A.1.5**. The final two terms detail the energy required to polarize particle i, with $k_1 = \dfrac{1}{2\alpha}$ and then the interaction of the induced dipoles with the external field. Tensors, $\mathbf{T}$, are (see for example, [119])

$$T^{ij}_{\alpha\beta\gamma\delta\ldots} = \nabla_{\alpha}\nabla_{\beta}\nabla_{\gamma}\nabla_{\delta}\ldots\left(\frac{1}{\mathbf{r}^{ij}}\right) \tag{2.4.3}$$

which are written out in full in **Appendix A.1**, and act to describe the interactions between the induced moments. Further to this, the Einstein summation convention relevant to tensor notation is detailed in **Appendix A.2**. Thus for a single i, j pair, the dipole-dipole interaction energy may be expressed as:

$$U^{dd} = -T^{ij}_{\alpha\beta}\mu^{i}_{\alpha}\mu^{j}_{\beta} = -\frac{\mu^{i}_{\alpha}\mu^{j}_{\beta}}{(\mathbf{r}^{ij})^5}\left(3r^{ij}_{\alpha}r^{ij}_{\beta} - \delta_{\alpha\beta}(\mathbf{r}^{ij})^2\right) \tag{2.4.4}$$

and under an applied unidirectional electric field (for example the y-direction in **Figure 2.1**), the energies of the induced dipoles can then be calculated. This is due to the fact that $\alpha = \beta = y$ (both dipoles are pointing in the same direction) and the product, $r^{ij}_{\alpha}r^{ij}_{\beta}$ is equal to $\mathbf{r}^{ij\,2}\cos^2\theta^{ij}$. The functional form of a two dimensional, pairwise, dipole interaction therefore becomes:

$$U^{dd} = \frac{\boldsymbol{\mu}^{i}\boldsymbol{\mu}^{j}}{(\mathbf{r}^{ij})^3}\left(1 - 3\cos^2\theta^{ij}\right), \tag{2.4.5}$$

the angular dependence of which is shown in **Table 2.1**. This table illustrates that the head-to-tail orientations of the dipole pairs gives the most energetically stable

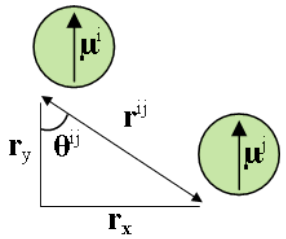


Figure 2.1: Dipole-dipole interaction between particles i and j at a distance $\mathbf{r}^{ij}$ apart.

configurations, *i.e.* at an angle of 0, π. This holds when the dipoles are pointing in the same direction, under an external applied electric field. However by introducing an additional angular component to **Equation 2.4.5**, to describe the rotation of the dipoles in relation to one another, the equation becomes:

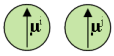
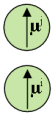
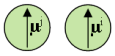
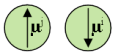
$$U^{dd} = \frac{\boldsymbol{\mu}^i \boldsymbol{\mu}^j}{(\mathbf{r}^{ij})^3} \cos\phi \left(1 - 3\cos^2\theta^{ij}\right), \tag{2.4.6}$$

where $\phi = \pi$ if the dipoles are tail-to-tail and $\phi = 0$ if the dipoles are head-to-tail. Thus the least energetically stable orientation then becomes tail-to-tail dipoles aligned along the direction of the electric field. Polarization effects are further explored in **Section 2.4.1** by extending the system further, including both dipolar and quadrupolar terms. This is to highlight the scalability of this technique for the generalised multipole.

2.4.1 Polarization Effects

In early versions of the simulation model, polarization effects were included by representing the induced dipoles as a pair of dynamically variable charges fixed onto either end of a short rod where orientation may vary. Thus by extending the Lagrangian to include these point charges, an induced dipole can be represented [103, 120]. This concept was developed from that proposed by Sprik & Klein [105, 121], in which dipoles on H_2O were represented by a tetrahedron of charges fixed with reference to the (static) H_2O molecular orientation.

Table 2.1: Induced-dipole interaction energy.

θ^{ij}	ϕ	U^{dd}	Orientation
0	0	$-2\dfrac{\mu_\alpha^i \mu_\beta^j}{(\mathbf{r}^{ij})^3}$	
$\dfrac{\pi}{2}$	0	$\dfrac{\mu_\alpha^i \mu_\beta^j}{(\mathbf{r}^{ij})^3}$	
π	0	$-2\dfrac{\mu_\alpha^i \mu_\beta^j}{(\mathbf{r}^{ij})^3}$	
$\dfrac{3\pi}{2}$	0	$\dfrac{\mu_\alpha^i \mu_\beta^j}{(\mathbf{r}^{ij})^3}$	
0	π	$2\dfrac{\mu_\alpha^i \mu_\beta^j}{(\mathbf{r}^{ij})^3}$	
$\dfrac{\pi}{2}$	π	$-\dfrac{\mu_\alpha^i \mu_\beta^j}{(\mathbf{r}^{ij})^3}$	
π	π	$2\dfrac{\mu_\alpha^i \mu_\beta^j}{(\mathbf{r}^{ij})^3}$	
$\dfrac{3\pi}{2}$	π	$-\dfrac{\mu_\alpha^i \mu_\beta^j}{(\mathbf{r}^{ij})^3}$	

To account for higher order moments, for example induced quadrupoles, more complex polyhedra (of charges) are required, which is found to be problematic. As a result, the system of charges was replaced with the point moments themselves [122]. There are a number of other models used to approximate the complex nature of polarization in these particle systems. The popularised shell model is one such example [123] whereby a particle core is joined to a shell with a harmonic spring, the polarizability of which is detailed by the magnitude of the shell and core partial charge, and the stiffness of the adjoining spring. However the shell model provides a less reliable representation of induced dipoles (notably when describing the interaction between anions in systems with a relatively large fraction of anions, for example in metal dihalides, MX_2 compounds [103]), with respect to the models used in this work.

2.4.2 Extending the Lagrangian to Include Polarization

Buckingham describes the coupling between the induced dipoles and the induced quadrupoles in an environment supportive of electric fields and electric field gradients [119]. As in the case of Buckingham, in relation to the work of Wilson [122], the mathematical formalism that describes the system investigated in this thesis is written within the context of an applied electric field rather than the magnetic analogue. Electricity and magnetism are indeed closely related but they are not entirely analogous, there are subtle differences however, as justified below with respect to polarization effects, they can be treated in the same manner.

The source of an electric field, such as that in an electrically polarised rod, is the excess of positive charge at one end of the rod and an excess of an opposing negative charge at the other. A magnetic field outside that of a magnetized rod behaves very similarly but as in the electric field case, there are no formal magnetic charges (magnetic monopoles, though theoretically possible, have not yet been shown to exist

in nature). This concept of magnetic 'charge' as a source for a magnetic field may or may not be true, however what is known is that the only sources of a magnetic field are electric currents and $\nabla \cdot B = 0$ everywhere. The magnetic field (with a small current loop) and electric field are similar when describing two separated charges, which is the approximation given in this work. The component of the magnetic field along the direction of the field is described as

$$B_x = \frac{\mu_0}{4\pi} \frac{m(3\cos^2\theta - 1)}{r^3} \tag{2.4.7}$$

which is the same expression as for the electric dipole (q) with $m \to q$ and $\mu_0 \to \frac{1}{\epsilon_0}$. m is the magnetic dipole moment, μ_0 is the vacuum permeability and ϵ_0 is the vacuum permittivity. The magnetic field close to the current loop therefore is different to the electric field, in that it is pointing in the opposite direction as the current loops around. This close magnetic field can be neglected given the presence of particle bodies which the dipoles are induced. This is entirely consistent with the properties of the simulation as field-specification is completely arbitrary given their scalable behaviour. The electric field strength is reported throughout in atomic units in order to retain consistency (and ease) of handling of the electrostatic interactions. The key terms throughout are the induced dipole moments (which may be readily expressed in any number of unit systems or in reduced units as and when required) and, since we are attempting comparison between magnetically- and electrically-induced dipole-driven self assembly, we avoid discussing the electric field magnitudes in anything other than atomic units.

In order to highlight the flexibility of this method, quadrupole effects are considered in addition to dipole polarization effects, which add minimal complexity to the equations of motion when extending the Lagrangian. The kinetic energy $\mathscr{K}(\dot{\mathbf{r}})$ and total potential energy $U(\mathbf{r})$ as detailed in **Equation 2.3.4** and in **Section 2.1** respectively can be extended to include the additional degrees of freedom for dipolar

and quadrupolar interactions. Therefore the K.E. becomes:

$$\mathscr{K}(\dot{\mathbf{r}}) = \frac{1}{2}\sum_{i=1}^{N} m^i (\dot{r}^i)_\alpha{}^2 + \frac{1}{2}\sum_{i=1}^{N} m^i_\mu (\dot{\mu}^i)_\alpha{}^2 + \frac{1}{2}\sum_{i=1}^{N} m^i_\theta (\dot{\theta}^i)_{\alpha\beta}{}^2 \tag{2.4.8}$$

where induced moments are represented by including the set of dynamical variables for the three components of the dipole moment $\{\mu^i\}_{\alpha=\{x,y,z\}}$ and six for the quadrupole $\{\theta^i\}_{\alpha\beta=\{xx,yy,zz,xy,xz,yz\}}$ (reduced to five components to account for symmetry considerations - as discussed below). The m^i_μ and m^i_θ are the 'fake masses' for the additional degrees of freedom, used to give a 'fake K.E.' for each variable.

The general functional form of the induced dipole, for a spherical particle, under the quadrupole approximation, has the basic relationship [120, 122],

$$(\mu^i)_\alpha = \alpha_{\alpha\beta} E_\beta(\mathbf{r}^i) + \frac{1}{3} B_{\alpha\beta,\gamma\delta} E_\beta(\mathbf{r}^i) E_{\gamma\delta}(\mathbf{r}^i) \tag{2.4.9}$$

and that for the quadrupole,

$$(\theta^i)_{\alpha\beta} = \frac{1}{2} B_{\alpha\beta,\gamma\delta} E_\gamma(\mathbf{r}^i) E_\delta(\mathbf{r}^i) + C_{\alpha\beta\gamma\delta} E_{\gamma\delta}(\mathbf{r}^i). \tag{2.4.10}$$

The tensors α and C are the dipole and quadrupole polarizabilities respectively, whereas B is the dipole-dipole-quadrupole hyperpolarizability in relation to a field E_α, with field gradient $E_{\alpha\beta}$. In order to complete the Lagrangian (**Equation 2.3.3**) we require an expression for the total potential energy. The total potential energy $U^{tot}(\mathbf{r})$ can be written as the sum of the pair-potentials (which act over short range, $U^{sr}(r^{ij})$) over N particles, along with the terms representing the interactions of the respective induced moments. We neglect the formal charge interactions as the particles are chargeless in the present work. Note: U^{tot} is equal to U^{all} as first specified in **Equation 2.4.2**, without the energy of interaction with the applied field ($-\boldsymbol{\mu}\cdot\mathbf{E}_{ex}$) term. The total P.E. under the dipole and quadrupole approximation can be written

as:

$$U^{tot}(\mathbf{r}) = \sum_{i=1}^{N-1}\sum_{j=i+1}^{N}\left\{ U^{sr}(\mathbf{r}^{ij}) - T^{ij}_{\alpha\beta}\mu^i_\alpha\mu^j_\beta + \frac{1}{3}T^{ij}_{\alpha\beta\gamma}(\mu^i_\alpha\theta^j_{\beta\gamma} - \mu^j_\alpha\theta^i_{\beta\gamma}) + \frac{1}{9}T^{ij}_{\alpha\beta\gamma\delta}(\theta^i_{\alpha\beta}\theta^j_{\gamma\beta})\right\}$$
$$+ k_1\sum_{i=1}^{N}(\boldsymbol{\mu}^i)^2 + k_2\sum_{i=1}^{N}\mu^i_\alpha\theta^i_{\alpha\beta}\mu^i_\beta + k_3\sum_{i=1}^{N}\theta^i_{\alpha\beta}\theta^i_{\alpha\beta} + k_4\sum_{i=1}^{N}(\boldsymbol{\mu}^i)^4, \quad (2.4.11)$$

where the tensors, $\mathbf{T}$, again describe the interactions between the induced moments (**Equation 2.4.3**). The additional terms in **Equation 2.4.11** refer to the polarization energies (also termed self-potentials) such that k_{1-4} give the harmonic and anharmonic force constants proportional to the dipolar and quadrupolar polarizabilities. These terms are described as:

$$k_1 = \frac{1}{2\alpha} \qquad k_2 = \frac{-B}{6\alpha^2 C} \qquad k_3 = \frac{1}{6C} \qquad k_4 = \frac{-B^2}{36\alpha^4 C} \qquad (2.4.12)$$

and generate the correct representative expression for induced potential when the adiabatic energy is calculated. As the particles in the system are spherical and highly symmetric, the only relevant self-potential terms are the scalar products up to fourth order that describe charge displacement.

Equations of motion can be generated for the additional degrees of freedom brought about by the inclusion of dipole and quadrupole moments. These additional variables (describing the dipole and quadrupole moments) are also solved using the Verlet integration algorithm (**Section 2.3.3**), in conjunction with the positions and velocities. For the dipole,

$$\frac{d}{dt}\left(\frac{\partial\mathscr{L}}{\partial\dot{\mu}^i_\alpha}\right) - \left(\frac{\partial\mathscr{L}}{\partial\mu^i_\alpha}\right) = 0 \qquad (2.4.13)$$

which leads to

$$m^i_\mu\ddot{\mu}^i_\alpha = \sum_{j\neq i}^{N}\left\{T^{ij}_{\alpha\beta}\mu^j_\beta - \frac{1}{3}T^{ij}_{\alpha\beta\gamma}\theta^j_{\beta\gamma}\right\} - 2k_1\mu^i_\alpha - 2k_2\mu^i_\beta\theta^i_{\alpha\beta} - 4k_4\mu^i_\alpha(\boldsymbol{\mu}^i)^2, \qquad (2.4.14)$$

and for the quadrupole,

$$\frac{d}{dt}\left(\frac{\partial \mathscr{L}}{\partial \dot{\theta}^i_{\alpha\beta}}\right) - \left(\frac{\partial \mathscr{L}}{\partial \theta^i_{\alpha\beta}}\right) = 0, \tag{2.4.15}$$

leading to

$$m^i_\theta \ddot{\theta}^i_{\alpha\beta} = \sum_{j\neq i}^{N}\left\{\frac{1}{3}T^{ij}_{\alpha\beta\gamma}\mu^j_\gamma - \frac{1}{9}T^{ij}_{\alpha\beta\gamma\delta}\theta^j_{\gamma\delta}\right\} - k_2\left(\mu^i_\alpha\mu^i_\beta - \frac{\delta_{\alpha\beta}(\boldsymbol{\mu}^i)^2}{3}\right) - 2k_3\theta^i_{\alpha\beta}. \tag{2.4.16}$$

It is required that the induced quadrupole is traceless hence the additional k_2 term in **Equation 2.4.16** which accounts for the reduction, from six to five components of the quadrupole (as $\theta_{\alpha\alpha} = 0$) [124]. The adiabatic condition holds when $\left\{\ddot{\mu}^i_\alpha, \ddot{\theta}^i_{\alpha\beta}\right\} = 0$, thus the energy is minimised corresponding to no 'force' acting on the induced moments. **Equation 2.4.14** then becomes:

$$0 = \underbrace{\sum_{j\neq i}^{N}\left\{T^{ij}_{\alpha\beta}\mu^j_\beta - \frac{1}{3}T^{ij}_{\alpha\beta\gamma}\theta^j_{\beta\gamma}\right\}}_{\bar{E}_\alpha(\mathbf{r}^i)} - 2k_1\mu^i_\alpha - 2k_2\mu^i_\beta\theta^i_{\alpha\beta} - 4k_4\mu^i_\alpha(\boldsymbol{\mu}^i)^2 \tag{2.4.17}$$

and **Equation 2.4.16** becomes:

$$0 = \underbrace{\sum_{j\neq i}^{N}\left\{\frac{1}{3}T^{ij}_{\alpha\beta\gamma}\mu^j_\gamma - \frac{1}{9}T^{ij}_{\alpha\beta\gamma\delta}\theta^j_{\gamma\delta}\right\}}_{\frac{1}{3}\bar{E}_{\alpha\beta}(\mathbf{r}^i)} - k_2\left(\mu^i_\alpha\mu^i_\beta - \frac{\delta_{\alpha\beta}(\boldsymbol{\mu}^i)^2}{3}\right) - 2k_3\theta^i_{\alpha\beta}, \tag{2.4.18}$$

where the sum of T^{ij} terms becomes $\bar{E}_\alpha(\mathbf{r}^i)$, the α component of the adiabatic electric field at site i, in **Equation 2.4.17** and $\frac{1}{3}\bar{E}_{\alpha\beta}(\mathbf{r}^i)$, a third of the adiabatic field gradient of this field at site i, in **Equation 2.4.18** [119].

From this point we can confirm the correct coefficients, k_{1-4} in the **Equations of 2.4.12** by substituting the basic functional form of the dipole (**2.4.9**) and quadrupole (**2.4.10**) with adiabatic fields and field gradients, into **Equations 2.4.17** and **2.4.18**. Furthermore by substituting the above equations back into the total potential then the adiabatic polarization energy (as denoted by the bar above the fields) can be derived as:

$$U^i_{ind} = -\frac{1}{2}\alpha(\bar{E}^i_\alpha)^2 - \frac{1}{6}B\bar{E}^i_\alpha\bar{E}^i_\beta\bar{E}^i_{\alpha\beta} - \frac{1}{6}C(\bar{E}^i_{\alpha\beta})^2. \tag{2.4.19}$$

The full self-consistent equation of motion for the movement of a particle within the quadrupole approximation under the adiabatic condition can therefore be written as:

$$m^i \ddot{r}^i_\alpha = -\sum_{j\neq i}^{N} \left(\nabla_{r^i_\alpha} U^{sr}(\mathbf{r}^{ij}) - \mu^j_\beta \bar{E}^i_{\alpha\beta} - \frac{1}{9}\theta^i_{\beta\gamma}\bar{E}^i_{\alpha\beta\gamma} \right). \tag{2.4.20}$$

Thus in summary, dipole and quadrupole moments are calculated self-consistently *i.e.* are induced by the electric (Coulomb) fields, their field gradients and the short range/overlap effects as described by the aforementioned potential model.

2.4.3 Maintaining the Adiabatic Condition

The adiabatic condition must be maintained during the molecular dynamics [103]. In order to achieve this, the equations of motion governing the additional degrees of freedom (those which describe the multipoles) are integrated simultaneously, with the same, small timestep from a starting configuration that upholds the adiabatic condition. As the coordinates of the particles in the system evolve in time, the additional variables are then updated to a corrected version on the adiabatic surface. These techniques are a variation on Car-Parrinello MD [102] as suggested by Sprik and Klein [121]. As time progresses the instantaneous dipoles may lose adiabaticity owing to energy transfer between the dipolar subsystem (which is kept cold) and the particles (which are hotter) [125]. The overlap between the actual and fictitious densities of states (which controls the rate of energy transfer between systems) can be monitored by appropriate selection of the fake masses (m_μ, m_θ). Suitable values allow for maintenance of the adiabatic condition over a relatively long time period. Deviation from adiabaticity can be monitored via the fictitious kinetic energy (or alternatively but equivalently, a fake temperature). An increase in this temperature is indicative of an increase in the amplitude of the oscillations of the extended degrees of freedom about the adiabatic values. Even with well chosen fake masses (which

well separate the actual and fictitious density of states) there is still enough energy transfer over typical MD time-scales (heading towards equilibrating the hot particle modes with the cold fictitious motion) [103]. As a result we employ Nosé-Hoover thermostats, as discussed more generally in **Section 2.6.1**. Therefore by including further additional components to the equations of motion, akin to coupling the system to a heat bath, the equilibration of hot and cold real and fictitious modes lasts over longer time-scales. As an example, the equation of motion that describes the evolution of a dipole over time is given as:

$$m_{\mu}^{i}\ddot{\mu}_{\alpha}^{i} = \sum_{j\neq i}^{N} T_{\alpha\beta}^{ij}\mu_{\beta}^{j} - 2k_{1}\mu_{\alpha}^{i} - \zeta_{\mu}m_{\mu}\dot{\mu}_{\alpha}^{i} \tag{2.4.21}$$

where $\dot{\zeta_{\mu}} = \left(T_{kin,\mu}/T_{\mu}^{target} - 1\right)/\tau_{\mu}^{2}$ is a function from which controls the heat transfer between the heat bath and the density of states to which it is coupled. $T_{kin,\mu}$ describes the kinetic temperature relevant to the system at hand (dipolar temperature in this example), T_{μ}^{target} is the necessarily, non-zero target temperature and τ_{μ} is the thermostat relaxation time. Target temperatures are selected in a manner similar to that used by Fois *et al.* [126] as function of the mass and target temperature that governs the particle adiabatic surface. Analogous thermostats are employed for all other additional variables.

2.5 Short-range Potential

The short-range potential, $U^{sr}(\mathbf{r})$, may take any number of forms, for example, a hard-sphere potential [127–129] combined with a point electric dipole moment produces a dipolar hard-sphere (DHS) model useful in analytical calculations. The *black* dashed line in **Figure 2.2** as quantified by **Equation 2.5.1** gives the functional form of the

hard-sphere potential;

$$U^{HS} = \begin{cases} 0 & \text{if} \quad \mathbf{r}^{ij} \geq \sigma \\ \infty & \text{if} \quad \mathbf{r}^{ij} < \sigma. \end{cases} \tag{2.5.1}$$

A hard-sphere pairwise potential is therefore defined to be infinitely repulsive at a distance $\mathbf{r}^{ij} < \sigma$, (where σ is the particle diameter or other basic length scale parameter) and zero otherwise [16]. A Lennard-Jones potential [130, 131] combined with a point dipole is known as a Stockmayer fluid (SMF) [132]. The full expression for the '6-12' Lennard-Jones pair-potential is written out in **Equation 2.5.2** and displayed as the *green* curve in **Figure 2.2**:

$$U^{LJ} = 4\epsilon \left[\left(\frac{\sigma}{\mathbf{r}^{ij}} \right)^{12} - \left(\frac{\sigma}{\mathbf{r}^{ij}} \right)^{6} \right]. \tag{2.5.2}$$

Removal of the attractive dispersion force expression (the 'r^{-6}' term), results in a soft repulsive, short-range potential as shown in **Figure 2.2** (*red* curve) and **Equation 2.5.3**:

$$U^{SS} = 4\epsilon \left(\frac{\sigma}{\mathbf{r}^{ij}} \right)^{12}. \tag{2.5.3}$$

This potential when combined with an electric point dipole is described as a dipolar soft-sphere (DSS) model [3]. Both SMF and DSS models require a parametrised particle diameter, σ and potential well depth (minimum point in potential curve) ϵ, as shown on the same figure. Therefore the minimum of the LJ potential occurs at a particle displacement of $\mathbf{r}^{ij}/\sigma = 2^{\frac{1}{6}} \simeq 1.12$. In the present work the particles in the system are considered as closed-shell argon atoms giving $\sigma = 6.43$ a.u. and $\epsilon/k_B = 118K$.

In this body of work, both the LJ and SS models have been investigated in order to establish the relative significance of each term in the potential model. It is important to note, as discussed in **Section 2.4**, that the dipole is induced by an applied field rather than by utilising a fixed permanent dipole as with SMF/DSS models. The majority of the simulations henceforth are SS (with an induced dipole

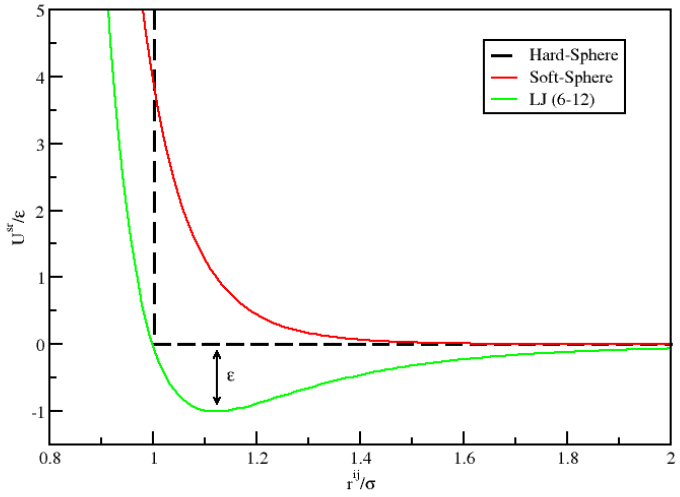


Figure 2.2: An illustrative graph displaying possible two-particle, short-range potential models (scaled for well depth ϵ) as a function of particle-particle distance (scaled by the particle diameter σ): Hard-Sphere (*black* line), Soft-Sphere (*red* curve) otherwise known as an 'r^{-12}' repulsive potential and the '6-12' Lennard-Jones potential (*green* curve).

component) and as will become apparent in the following chapters, compares well with experimental observation.

2.6 Energy Minimisation

A central requirement of the current research, as briefly mentioned above in **Section 2.4.3** is to locate the local energy minima of a number of specific particle configurations. Global energy minimisation is not the aim, which provides the lowest possible energy configuration of the system (therefore a crystal structure). This is useful information but not the aim of the work presented in this thesis. By probing the varied local energy landscape, amorphous configurations can be generated and the

average properties of which can be calculated. Energy minimisation is controlled by a Nosé-Hoover thermostat in the system (see below) but an alternative method is by using steepest descent (SD) minimisation (**Appendix B.4**).

2.6.1 Nosé-Hoover Thermostat

The equations of motion discussed in **Section 2.3** probe the micro-canonical ensemble (constant NVE). The canonical ensemble (constant NVT) can be investigated in a similar manner by employing Nosé-Hoover thermostats. We note that pressure can be controlled (NPT ensemble) in a similar manner, using a barostat (*e.g.* Parrinello-Rahman barostat [133]). For constant temperature dynamics the system of interest is coupled to a theoretical heat-bath and the instantaneous temperature (or kinetic energy) fluctuates around an average temperature determined by the function describing the thermostat. Hoover [134] improved the approach taken by Nosé [135, 136] whereby the thermostat can be combined with the Hamiltonian function used to derive the equations of motion. Therefore, the modified Hamiltonian $\mathscr{H}'$ (in terms of a generalised coordinate system) is

$$\mathscr{H}'(\mathbf{p}, \mathbf{q}, \xi, \mathbf{p}_\xi) = \mathscr{V}(\mathbf{q}) + \sum_{i=1}^{N} \frac{(\mathbf{p}^i)^2}{2m^i} + \frac{\mathbf{p}_\xi^2}{2Q} + \chi k_B T \xi \tag{2.6.1}$$

where T is the temperature of the system, χ is the number of degrees of freedom in the system and ξ is the friction coefficient. Additionally $Q = \chi k_B T \tau^2$, which is the thermal inertia parameter outlining the extent of coupling of the system to the thermostat. Q therefore depends strongly on the value of the relaxation time τ, where a large value of Q gives weak coupling of the system to the heat-bath and the thermostat is only effective at long time scales. Conversely, a low value of Q forces the thermostat to dominate the equations of motion which become 'stiff' as a result producing instabilities in the system. The corresponding equations of motion are

therefore:

$$\dot{\mathbf{q}} = \frac{\mathbf{p}}{m} \qquad \dot{\mathbf{p}} = \mathbf{f} - \mathbf{p}\frac{\mathbf{p}_\xi}{Q} \tag{2.6.2}$$

$$\dot{\mathbf{p}}_\xi = \sum i = 1^N \left[\frac{(\mathbf{p}^i)^2}{m^i} - \chi k_B T\right] \qquad \xi = \frac{\mathbf{p}_\xi}{Q}. \tag{2.6.3}$$

A Nosé-Hoover thermostat is employed primarily to control the rate of quenching of configurations, from high to low temperature, the use of which will be discussed in the following chapters. The rate of this quenching is controlled primarily by the thermostat relaxation time, τ.

2.7 Boundary Conditions

There are a number of common but easily circumventable simulation problems when attempting to model a bulk liquid material. Firstly, the time taken to calculate the forces (or potential energy) in an N particle system is proportional to N^2. Thus, as this calculation determines the overall speed of the MD program, low N models are computationally less expensive and are therefore greatly preferred. In the present work, for example, there is a need to control the relaxation times (simulation time-scales) and also be able to perform high throughput calculations (maximising the number of rheological configurations generated at each point in phase space). As a result, each model created for this work comprises of a small number of particles in the order of 10^2. In addition, the MD simulation models the bulk material, confined to a cubic container (square in 2D) with a fixed set of boundary conditions. Thus particles in the bulk will experience different forces compared to the particles at the surface. These unwanted surface effects can be overcome by replicating the simulation cell throughout infinite space in order to form a repeating, periodic lattice [114]. Therefore all systems are modelled with a set of periodic boundary conditions where the number density in the central cell (and system) is strictly conserved. When a

given particle moves in any direction in one cell, the corresponding particle in the other repeating cells, all move in the same direction. Additionally, if a particle leaves the central cell, its image then enters through the opposite face from the relevant contiguous cell (as shown in **Figure 2.3**). As such the system can be described to be the topological equivalent of a torus. By focusing on the interactions contained in a single cell the effect of particle-surface interactions are removed and the simulation is thus more reliable (the errors in the energy calculation are proportional to $1/N$). Furthermore the periodicity is also important for the calculation of long range particle-particle interaction properties.

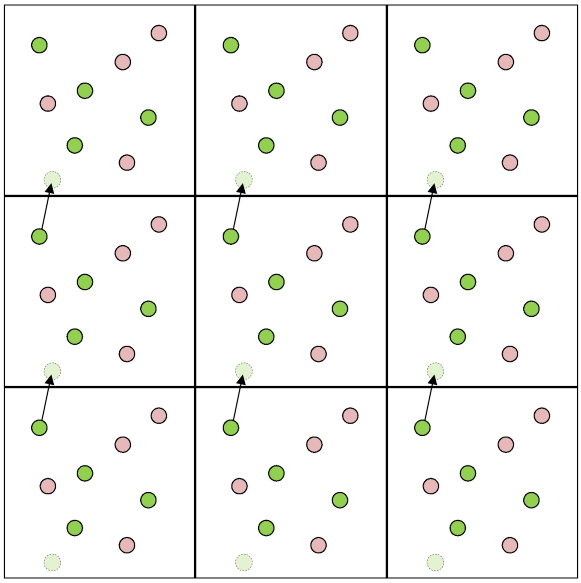


Figure 2.3: The central cell is surrounded by an infinite number of identical cells each with identical particle images. If the particle moves out of the cell from one face, its image enters from the opposite face.

2.7.1 Minimum Image Convention

There are an infinite number of interactions between a given particle i and $[(N-1)+\lambda N]$ surrounding particles that contribute to the potential energy/force on that particle. λ is the number of repeating images that surround the central simulation cell and tends to infinity for a strict MD simulation. As a result there are an infinite number of terms in the potential energy summation used to calculate the force on particle i, which is of course computationally unreasonable. However, the calculation becomes viable when employing a minimum image convention, whereby only the particle interactions of the closest $N-1$ particles (or equivalent mirror images) are used, as shown in **Figure 2.4** (left). The simulation cell is then re-centred for every particle and only particles within a distance of $\frac{L}{2}$ (in x,y,z), are considered to have non-negligible interactions. This approximation is further improved by considering the nearest neighbours and applying a spherical truncation to the minimum image with a cut-off of $< \frac{L}{2}$, as shown in **Figure 2.4** (right).

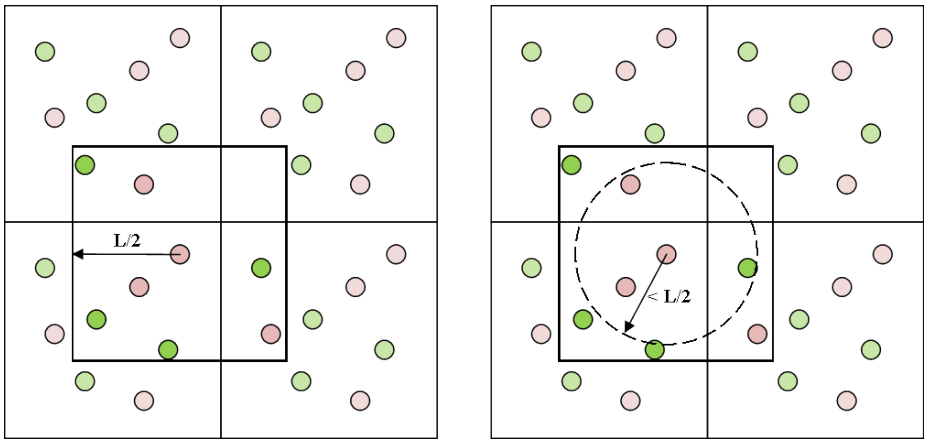


Figure 2.4: An illustration of the minimum image convention for potential truncation at a short range. The diagram on the left shows particle interaction with $N-1$ nearest neighbours and the diagram on the right highlights the spherical truncation cut-off of the potential.

In addition to periodic boundary conditions an Ewald Summation is also used in order to improve the model for long range force interactions. This is particularly relevant in ionic systems and conveniently used in the simulation of dipolar particles susceptible to an applied field. Thus useful in the context of the simulations, specifically for runs characterised in this thesis.

2.7.2 Ewald Summation Technique

In 1921 P. P. Ewald determined the electrostatic energies of ionic crystals using a technique described as the Ewald summation method [137]. This method allows efficient summation of interactions between an ion its periodic images over longer range than can be observed using the minimum image approximation [114]. Key concepts taken from this seminal work allowed improvement on simulations of MR and ER fluids (*e.g.* in [138–140]) as long range multipole interactions can be modelled in much the same way. Wang and Holm [141] also detailed Ewald summation error calculations in the context of dipole-dipole interactions and concluded that there is a vast improvement in accuracy of simulations when including this technique.

Long range interactions, as defined by Allen and Tildesley [114], are those in which the spatial interaction is less than a function of r^{-d} where d is the dimensionality of the system. Examples being, charge-charge interactions (r^{-1}) and dipole-dipole interactions (r^{-2} or r^{-3}, dependent on whether it is a two- or three-dimensional system) between particles. The range of these forces are of an order greater than $\frac{L}{2}$ thus a contributing factor to additional computational retardation. These effects can be reduced by increasing the simulation cell size however the simulation time is proportional to N^2 and thus an obvious limit to this strategy presents itself.

An Ewald summation can reduce computation time from N^2 to an order of $N \log N$ by splitting the problem into two independent rapidly decaying parts al-

lowing for system truncation without great loss of accuracy [142, 143]. Any criticism that arises of the Ewald method, due to loss of accuracy and difficulty in the calculation (mainly in the reciprocal space part) of the summation, can be mitigated sensibly by the gain in speed. Careful selection of splitting parameter (see below) and with use of FFT (fast Fourier transform) techniques, these apparent 'failures' can be negated.

Derivation of Charge-Charge Ewald Sum

The Ewald method was first derived in the context of charge-charge interactions (q_i describes the charge on particle i), therefore a Coulombic pair-potential outlining the interaction between charged particles may be written as:

$$U^{qq} = \frac{1}{2} \sum_{n}{}' \left(\sum_{ij}^{N} \frac{q_i q_j}{|\mathbf{r}_{ij} + n|} \right) \tag{2.7.1}$$

where $n = (n_x L, n_y L, n_z L)$ with n_x, n_y, n_z being integers, giving cubic lattice points over Cartesian space. The sum over n is primed ($'$) in order to denote that we ignore the term for $i = j$, such that all particles interact with other particles and other images of itself but not itself. Furthermore, factors of $4\pi\epsilon_0$ are omitted for convenience in this derivation. i and j return to the more natural notation of subscripts rather than superscripts with the move away from tensor notation in order to reduce confusion.

The sum in **Equation 2.7.1** is conditionally convergent where a summation of the cells directly surrounding the central cell gives the most logical calculation. Approximate spherical layers are then constructed as observed in **Figure 2.5**. This potential can differ depending on the medium at the boundary of the 'sphere', constructed from the cell stacking. The relationship is

$$U^{qq}(\epsilon_s = \infty) = U^{qq}(\epsilon_s = 1) - \frac{2\pi}{3L^3} \left| \sum_i q_i \mathbf{r}_i \right|^2, \tag{2.7.2}$$

where ϵ_s is the relative permittivity or dielectric constant. For example, $\epsilon_s = \infty$ when the 'spheres' border excellent conducting materials such as metals and $\epsilon_s = 1$ when the sphere is surrounded by a vacuum [144]. According to Leach [142] the key

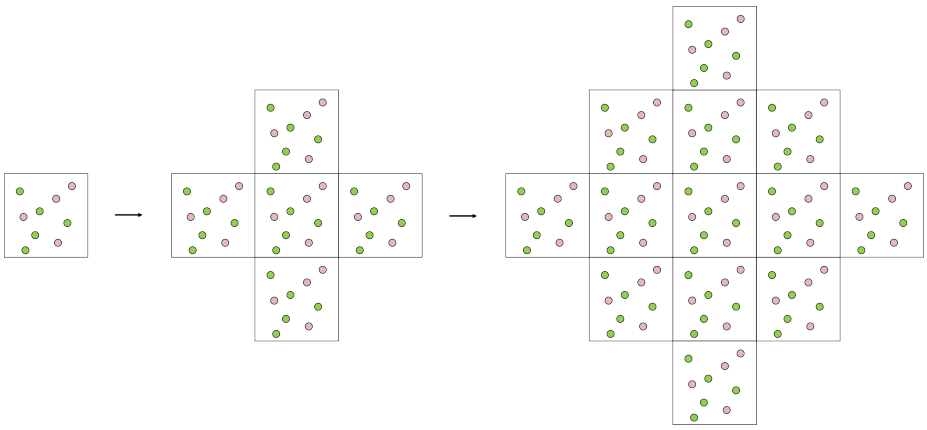


Figure 2.5: Periodic sum in two-dimensions which may be continued indefinitely but more realistically until the system is truncated.

ideas of the Ewald sum are to transform the slowly converging **Equation 2.7.1** into rapidly converging, real space and reciprocal space components. A Fourier transform on the reciprocal space term then provides more accurate results by extending the calculation over even larger space. Point charges on particles/ions can be described to experience a neutralising radial charge distribution (equal magnitude, opposite sign) in the form of a Gaussian function as shown below;

$$\rho_i^q(r) = q_i \kappa^3 \frac{\exp(-\kappa^2 r^2)}{\pi^{3/2}}. \tag{2.7.3}$$

Here κ can be varied to determine the width of the Gaussian distribution and r gives the position of the distributions relative to the point charge positions. Therefore the overall real space contribution to the Ewald sum can be given by **Equation 2.7.1** with additional neutralising Gaussian function:

$$U_{real}^{qq} = \frac{1}{2} \sum_n {}' \left(\sum_{ij}^{N} q_i q_j \frac{\mathrm{erfc}(\alpha |\mathbf{r}_{ij} + n|)}{|\mathbf{r}_{ij} + n|} \right) \tag{2.7.4}$$

where the complimentary error function is;

$$\mathrm{erfc}(x) = \frac{2}{\sqrt{\pi}} \int_x^\infty \exp(-t^2).dt \tag{2.7.5}$$

that tends to zero with increasing x. **Figure 2.6** illustrates this system of screened charges. A further system as shown in **Figure 2.7** is added in order to reduce the overall potential back to the original charge magnitude as set[1]. This method of screening charge inclusion allows for the sum to converge much more rapidly than in a system where the screening and cancelling charges are not used.

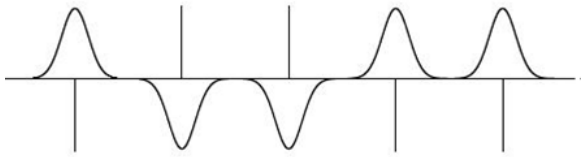


Figure 2.6: Point charges (line) and Gaussian screening distribution.

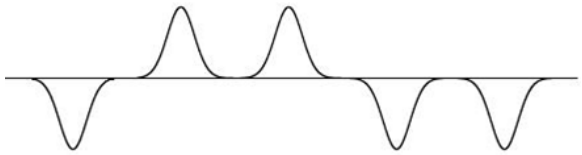


Figure 2.7: Cancelling distribution opposite in sign to screening distribution.

As the cancelling distribution is summed in reciprocal space, before then further transformation back into real space, as is characteristic of FT manipulation; the contribution to the long range potential by completing a Fourier transformation of the Gaussian function can be derived (**Equation 2.7.3**) [112]. Therefore the reciprocal contribution can be approximated as:

$$U^{qq}_{recip} = \frac{2\pi}{L^3} \sum_{\mathbf{k}\neq 0} \sum_{ij}^{N} \frac{q_i q_j}{k^2} \exp\left(\frac{-k^2}{4\kappa^2}\right) \cos(\mathbf{k} \cdot \mathbf{r}_{ij}). \tag{2.7.6}$$

[1] Images reproduced from 'Computer Simulation of Liquids' - Allen and Tildesley [114].

The reciprocal wave vectors are $\mathbf{k} = 2\pi\mathbf{n}/L$ and around 100-200 vectors are used, which in conjunction with a sensible choice of parameter $\kappa = 5/L$ such that the Gaussian is not too wide, the optimal accuracy is achieved [114]. Self-interaction terms are also required to be subtracted as are included coincidentally in **Equation 2.7.4**.

$$U_{self}^{qq} = -\frac{\kappa}{\sqrt{\pi}} \sum_{i=1}^{N} q_i^2 \tag{2.7.7}$$

Finally the correction as detailed in **Equation 2.7.2** is used for $\epsilon_s = 1$. Therefore the overall Ewald potential sum for long range force contributions regarding charge-charge systems can be described as:

$$U^{qq}(\epsilon_s = 1) = U_{real}^{qq} + U_{recip}^{qq} + U_{self}^{qq} + \frac{2\pi}{3L^3} \left| \sum_i q_i \mathbf{r}_i \right|^2 \tag{2.7.8}$$

Extension to Dipolar Systems

The Ewald summation method can be extended to account for long range dipole-dipole interactions by replacing q_i with $\boldsymbol{\mu}_i \cdot \boldsymbol{\nabla}_{\mathbf{r}_i}$ and deriving as above [144]. By constructing a summation of simulation boxes in the same manner as in **Figure 2.5** the total Ewald potential for dipole-dipole interactions can be described as:

$$\begin{aligned} U^{dd}(\epsilon_s = 1) \;&=\; U_{real}^{dd} + U_{recip}^{dd} + U_{self}^{dd} + \frac{2\pi}{3L^3} \left| \sum_{ij} \boldsymbol{\mu}_i \cdot \boldsymbol{\mu}_j \right| \\ &= \sum_{ij}^{N} \left[\frac{1}{2} \sum_{\boldsymbol{n}}{}' \left[(\boldsymbol{\mu}_i \cdot \boldsymbol{\mu}_j) B(|\boldsymbol{r}_{ij} + \boldsymbol{n}|) - (\boldsymbol{\mu}_i \cdot (\boldsymbol{r}_{ij} + \boldsymbol{n}))(\boldsymbol{\mu}_j \cdot (\boldsymbol{r}_{ij} + \boldsymbol{n})) C(|\boldsymbol{r}_{ij} + \boldsymbol{n}|) \right] \right] \\ &+ \frac{2\pi}{L^3} \sum_{\mathbf{k} \neq 0} \sum_{ij}^{N} \frac{(\boldsymbol{\mu}_i \cdot \mathbf{k})(\boldsymbol{\mu}_j \cdot \mathbf{k})}{k^2} \exp\left(\frac{-k^2}{4\kappa^2} \right) \cos(\mathbf{k} \cdot \mathbf{r}_{ij}) \\ &- \sum_{i}^{N} \frac{2\kappa^3 \mu_i^2}{3\sqrt{\pi}} + \frac{2\pi}{3L^3} \left| \sum_{ij} \boldsymbol{\mu}_i \cdot \boldsymbol{\mu}_j \right|, \end{aligned} \tag{2.7.9}$$

with

$$B(r) = \frac{1}{r^3}\left[\mathrm{erfc}(\kappa r) + \left(\frac{2\kappa r}{\sqrt{\pi}}\right)\exp(-\kappa^2 r^2)\right] \tag{2.7.10}$$

$$C(r) = \frac{1}{r^5}\left[3\mathrm{erfc}(\kappa r) + \left(\frac{2\kappa r}{\sqrt{\pi}}\right)(3 + 2\kappa^2 r^2)\exp(-\kappa^2 r^2)\right]. \tag{2.7.11}$$

The dipole-dipole interactions in this work are handled with a standard three dimensional Ewald summation as outlined above, in which the system is treated as quasi-two-dimensional by repeating the basic unit cell perpendicular to the confining plane with a relatively long repeat length ($L_z = 100$ a.u.). A truly two-dimensional simulation cell (utilising a two-dimensional form of the Ewald summation) is not used as one of the longer-term aims of this work is to make contact with the analogous experimental systems. In experiment, whilst the systems are essentially two-dimensional (as a result of the confinement between plates) the systems are not strictly two-dimensional in the sense that particles may show a small deviation from the confinement plane (that is, the confining length is greater than the particle diameter). 2D Ewald summations are discussed in Gingrich & Wilson [145] which corrects the 2D Ewald sum of Gaussian charges as presented by Reed *et al.* [146, 147] where the energy terms do not reflect that the change in size of the Gaussian distribtion which does affect the interaction between neighbouring sites. The fact that a 3D Ewald sum calculation is used for this work will affect the calculated dipolar energies however explicitly accurate energy values are not the focus of this work.

2.8 Analytical Techniques

A host of analytical techniques are applied in order to maximise the understanding of the nature of the bulk system in the liquid and crystalline phases. The principal focus is to characterise the extent of chain formation in the simulation cell based on the composition of the fluid. This section therefore aims to summarise, in the general

sense, techniques which are used in all subsequent chapters and to define interesting nuances in the methods.

2.8.1 Radial Distribution Function

The radial distribution function (RDF or pair correlation function), $g(r)$ describes how the density of particles in the surrounding environment varies as a function of the distance from the particle origin. In 3D, the RDF is essentially a measurement of the probability that a particle will be found within a spherical shell of thickness dr at a distance r from the particle origin (a circular shell analogue for 2D) [148]. Thus as every particle position is known explicitly at each time step in the MD simulation, the particle-particle separations can be calculated for each particle in the cell boundary, using the minimum image convention. Each separation is then used to build up a histogram of the values by sorting them into bands determined by r. Finally after a normalisation for the area/volume of the shell, the RDF depicts local deviations from the bulk density as a function of r. **Figure 2.8** gives a schematic depiction of the RDF calculation algorithm which in 2D can be described by the equation,

$$2\pi\rho r g(r) = \left\langle \frac{1}{N} \sum_{i=1}^{N} \sum_{j \neq i}^{N} \delta(\mathbf{r} - |\mathbf{r}_j - \mathbf{r}_i|) \right\rangle \tag{2.8.1}$$

where N is the number of particles in the simulation cell, ρ is the average number density of particles and the sum over $\delta(\mathbf{r} - |\mathbf{r}_j - \mathbf{r}_i|)$ is the particle count centred on i (*blue* particle in **Figure 2.8**). The explicit form of the ideal probability is defined as, $g_{ideal}.dr = 2\pi\rho r.dr$, which is the normalisation factor with respect to a circular 2D ideal gas [149].

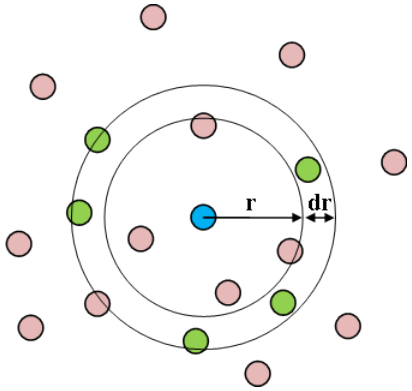


Figure 2.8: For each particle (reference *blue*), the number of particles falling within the bounds of the shell dr, are summed over the range r (*green*).

2.8.2 Partial Radial Distribution Functions

$g(r)$ can be further separated into parts in order to highlight certain dependencies on specific structural properties or local density differences in the simulation box [150]. For example, in a bidisperse environment containing two species, α and β, the total RDF (in 2D), $g_{\alpha\beta}(r)$ is defined as

$$2\pi\rho r g_{\alpha\beta}(r) = \left\langle \frac{1}{N} \sum_{i=1}^{N_\alpha} \sum_{j \neq i}^{N_\beta} \delta(\mathbf{r} - |\mathbf{r}_j - \mathbf{r}_i|) \right\rangle \tag{2.8.2}$$

where the particle summation is similar to that observed in **Equation 2.8.1** centred this time around particles, α or β. Additionally partial RDFs can be calculated for a variety of properties. For example, in order to explore the shell composition of the environments surrounding individual particles in the composition. Consider

$$g(r) = \sum_{i=1}^{N} g_i(r) \tag{2.8.3}$$

such that $g_1(r)$ describes the probability of finding the closest particle to a given particle over a distance r and therefore $g_i(r)$ gives the probability of finding the i^{th} particle *etc.* This method of RDF splitting is particularly useful for chain structure determination. Furthermore $g^{\parallel}(r)$ and $g^{\perp}(r)$ can be calculated which are the parallel

(along the x-axis) and perpendicular (along the y-axis) RDFs where

$$\rho g^{\gamma}(r) = \left\langle \frac{1}{N} \sum_{i=1}^{N} \sum_{j \neq i}^{N} \delta(\mathbf{r}^{\gamma} - |\mathbf{r}_j^{\gamma} - \mathbf{r}_i^{\gamma}|) \right\rangle \tag{2.8.4}$$

such that $\gamma = \parallel$ or $\perp$ refers to the sampling direction parallel or perpendicular to the direction of the applied field and $\mathbf{r}_{ij}^{\gamma} = \hat{\mathbf{r}}^{\gamma} \cdot \mathbf{r}_{ij}$ gives the relevant vector component.

2.8.3 Structure Factor

The structure factor, $S(k)$ is related to the Fourier transform of the pair distribution function. However, in a simulation model knowledge of the particle coordinates allows these functions to be determined directly *via*

$$S(k) = \langle A^*(k) \cdot A(k) \rangle \tag{2.8.5}$$

where

$$A(k) = \frac{1}{\sqrt{N}} \sum_{i=1}^{N} \exp(i\mathbf{k} \cdot \mathbf{r}_i) \tag{2.8.6}$$

are the Fourier components of the particle density, N gives the number of particles and $\mathbf{k}$ is the wave vector [151, 152]. Partial structure factors can also be generated by splitting $S(k)$ into components, for example for species α and β,

$$S_{\alpha\beta}(k) = \frac{1}{\sqrt{N_\alpha N_\beta}} \left\langle \sum_{i=1}^{N_\alpha} \exp(-i\mathbf{k} \cdot \mathbf{r}_i) \cdot \sum_{j=1}^{N_\beta} \exp(i\mathbf{k} \cdot \mathbf{r}_j) \right\rangle. \tag{2.8.7}$$

The noise in the value of $S(k)$ increases with k as a result of employing a Debye-Scherrer method to generate the functions as outlined above. In this method a 'k_{max}' is specified which restricts the calculation of k along either direction in k-space. The noise in $S(k)$ only decreases in k if all possible contributions to each k-point are generated (if $k_{max} = \infty$). For example, the largest k-vector sampled will be (k_{max},k_{max}) but this will be the only contribution to this k-value. The other possibilities, for example ($\sqrt{2}k_{max}$,0), are not generated as $\sqrt{2}k_{max} > k_{max}$.

2.8.4 Coordination Number Statistics

The total coordination number about a given particle is calculated by counting the number of particles within a specified cut-off radius, usually taken as the location of the first minimum in the RDF. The mean coordination number, $\langle n \rangle$ can be determined simply by averaging the coordination number for each simulation cell over all particles such that

$$\langle n \rangle = \frac{\sum_i i n_i}{\sum_i n_i}, \tag{2.8.8}$$

where n_i is the number of particles of coordination number i. Coordination number statistics can be produced as a function of time whereby one can observe the evolution of each average coordination number over the course of a given simulation. This is an effective window into simple chain growth as the number of two coordinate particles in the system will increase over time as the number of zero and one-coordinate environments decreases.

2.8.5 Local Coordination Parameter

An indirect way of characterising ordering in a bulk system is to analyse the average local coordination of the particles in a given simulation cell coloured in terms of the magnitude of the induced dipoles. When a chain is formed it may be energetically favourable for a particle to be surrounded by adjacent particles with relatively large 'induced' dipoles. For purposes of this metric, particles are separated into two types, A and B, dependent on the absolute magnitudes of the dipoles ($\boldsymbol{\mu}^i$). As described in **Section 2.4**, dipoles on site i are $\boldsymbol{\mu}^i = \alpha(\mathbf{E}_{ex} + \mathbf{E}^i_{int})$, arising from the dipole induced by the applied external field, in addition to an internal contribution from the induced dipoles on adjacent sites. As $\mathbf{E}^i_{int}$ depends heavily on the particle environment, a distribution of dipoles is produced. Therefore in terms of characterisation, for a monodisperse system, particles in the top 25% of $|\boldsymbol{\mu}|$ labelled A with the remaining

particles labelled B. **Figure 2.9** highlights this selection criteria for monodisperse particle simulations. As a note, for a bidisperse system, particles are by default initially separated into species 'A' and 'B', with distinct and different dipole moment distributions, therefore the method of characterisation detailed in **Figure 2.9** is not required.

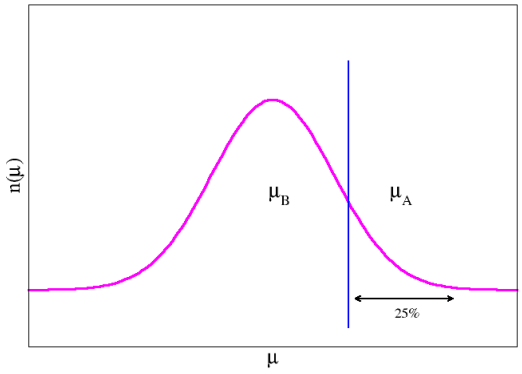


Figure 2.9: An illustrative diagram detailing a dipole moment distribution and an example of the selection criteria used to characterise species 'A' and 'B', for a monodisperse system, in which there is no initial particle species diversity. μ_A is calculated as an average over all available configurations for the run.

For an n-coordinate 'A' particle a difference function, $\Delta p_A(k)$, can be defined in order to quantify the ratio of neighbouring particle species, relative to a random distribution of particles in the system:

$$\Delta p_A(k) = p_A^{sim}(k) - p_A^{rnd}(k). \tag{2.8.9}$$

$p_A^{sim}(k)$ is the fraction of particles 'A' with k 'A' neighbours and $(n-k)$'B' neighbours. $p_A^{rnd}(k)$ is the expected fraction of 'A' particles assuming a random distribution of 'A' and 'B' particles [153] such that

$$p_A^{rnd}(k) = \frac{n!}{k!(n-k)!} p^k (1-p)^{n-k}. \tag{2.8.10}$$

Here, the coordination number is set as $(n = 2)$, which allows consideration of the closest two neighbours about all 'A' particles, *i.e.* a search over all triplets in the simulation cell, AAA $(k = 2)$, AAB or BAA $(k = 1)$ and BAB $(k = 0)$, corresponding to neighbour pairs as seen in **Table 2.2**. p is a ratio related to the composition, defined as the fraction of 'A' particles in the system, $p = n_A/N = \frac{1}{4}$ based on the imposed upper 25% rule.

Table 2.2: Values of $p_A^{rnd}(k)$ for k neighbour pairs.

k	$p_A^{rnd}(k)$	Neighbouring Particles
2	$\frac{1}{16}$	AAA
1	$\frac{6}{16}$	AAB/BAA
0	$\frac{9}{16}$	BAB

In order to illustrate this metric, for the coordination environment about all 'A' particles, let $k = 2$ which would correspond to the probability of encountering two adjacent 'A' neighbouring particles around the central 'A' particle. Then if $p_A^{sim}(2) > p_A^{rnd}(2)$, the number of AAA triplets in the simulation cell exceeds that expected for a given random distribution of 'A' and 'B' particles, therefore $\Delta p_A(2) > 0$ and we expect chain formation environments. Conversely if $\Delta p_A(2) < 0$ then the number of BAB coordination triplets in the simulation cell is high and chain formation is less likely to have occurred. This metric therefore is useful in quantifying the relative chain formation within simulation cells.

2.8.6 Local Order Parameter

The local bond orientation order parameter $\psi_n(r_{ij})$ can quantify the extent of the average columnar structure over a given number of cell configurations. It is essentially a parameter to quantify how 'straight' particle chains are. It is defined as

$$\psi_n(r_{ij}) = \frac{1}{N}\sum_{i,j=1}^{N} \exp[ni\theta(\mathbf{r}_{ij})] \tag{2.8.11}$$

where $\theta(\mathbf{r}_{ij})$ is the angle between the bond vector connecting i and j with a fixed reference axis (along the x-axis unless specified otherwise). N is the the total number of particles in the simulation cell and n specifies the reference lattice. For example averaging over all particles i yields $\langle|\psi_n|\rangle$ which is 1 for a perfect 2D hexagonal crystal ($n = 6$) and 1 for a perfect 2D square lattice ($n = 4$). Nearest neighbours are located within a centre-centre distance of $r = 1.35\sigma$, as outlined in Klokkenburg *et al.* [13] which corresponds to a value slightly higher than the minimum in the RDF.

2.8.7 Mean Chain Length

The mean chain length, $\langle c\rangle$, of a series of simulations may be generated in a variety of ways each with various ambiguities based on the treatment of boundary conditions or the presence of 'defect' coordination environments. A simple method of mean chain length approximation is to relate $\langle c\rangle$ to the mean coordination number. Therefore if we assume all particles are either 0-, 1- or 2-coordinate then **Equation 2.8.8** for the mean coordination number simplifies to

$$\langle n\rangle = \frac{2n_2 + n_1}{n_2 + n_1 + n_0}. \tag{2.8.12}$$

Ideal chains can be modelled as 2-coordinate particles 'book-ended' by single-coordinate particles such that

$$\langle c \rangle = \underbrace{\frac{\left(\frac{n_1}{2}\right)\left(\frac{n_1+n_2}{n_1/2}\right)+n_0}{(n_1/2)+n_0}}_{\mathbf{A}} = \frac{n_0+n_1+n_2}{(n_1/2)+n_0}, \tag{2.8.13}$$

where the denominator, $(n_1/2)+n_0$, gives the total number of chains and the left hand equation (**A**) represents the average of the $(n_1/2)$ chains plus the 0-coordinate $(c=1)$ chains. Combining equations 2.8.12 and 2.8.13 to eliminate n_2 gives

$$\langle c \rangle = 1 + \frac{N\langle n \rangle}{2n_0+n_1}, \tag{2.8.14}$$

where $N = n_0+n_1+n_2$. Additionally, the fraction of $n-$coordinate sites is $f_n = n_n/N$ and so

$$\langle c \rangle = 1 + \frac{\langle n \rangle}{2f_0+f_1}. \tag{2.8.15}$$

Therefore, mean chain length calculations can supplement the previous metrics in order to characterise the extent of chain formation in a given simulation cell.

2.8.8 Chain Length Distributions

Chain lengths can be calculated in a more direct manner by defining how a chain is constructed and counting the particles within that chain between predefined termini or 'nodes'. This problem is analogous to ring size determination in inorganic compounds (examples of definitions include: Gutmann [154], King [155], Primitive rings [156] and Strong rings [157]). As such, a 'shortest chain approximation' is used which counts all non-two-coordinate units as chain termini.

If, as discussed in the previous section (**2.8.7**), chains are only constructed from zero-, one- and two-coordinate particles then both mean chain length calculation methods outlined will give exactly identical results. Here zero- and one-coordinate

particles are classified as chain termini and two-coordinate particles form the 'body' of a chain. Problems arise if the chains become infinitely long as a result of periodic boundary conditions, but these effects can be accounted for. In the simulations with greater network structuring, where sites exist with coordination numbers greater than two, the algorithm then treats higher coordinate sites as chain termini. For example, the network cluster shown in **Figure 2.10** will be broken down into two chains comprising four-particles each (*green* and *pink* routes) and one chain comprising of three particles (*yellow* route). The advantage of this algorithm over other potential routes is that only the particles with a coordination number greater than two appear in more than one chain, and even then only as the terminus.

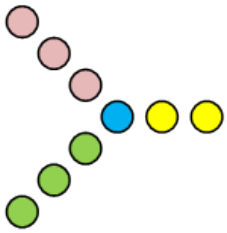


Figure 2.10: An example cluster, which when applying the chain length counting algorithm, gives 3 chains, two of length four (*green* and *pink* route) and one of length three (*yellow* route). The chain termini are at the ends of the chain, with coordination number one in addition to the central node (*blue* particle), with coordination number three.

2.8.9 Bond Angle Distribution Function

For each triplet of particles (i, j and k) in a bulk structure the bond angle is defined as θ_{ijk}, see **Figure 2.11**. Valid triplets are identified if the magnitudes of both vectors $\mathbf{r}_{ij}$ and $\mathbf{r}_{jk}$ are less than a given cut-off (again usually taken as the location in the first minimum in the RDF). As a result, a histogram containing the frequency information

of each bond angle is constructed which provides the distribution statistics of each triplet angle.

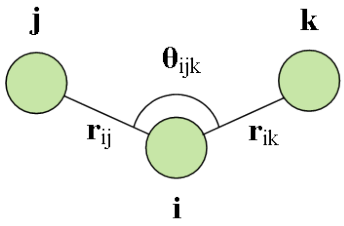


Figure 2.11: A simple representation of a triplet of particles (i,j and k), taken from a bulk crystal structure where θ_{ijk} is the value of the bond angle and $\mathbf{r}_{ij}/\mathbf{r}_{jk}$ are vectors between the particles ij and ik respectively.

2.9 Chapter Summary

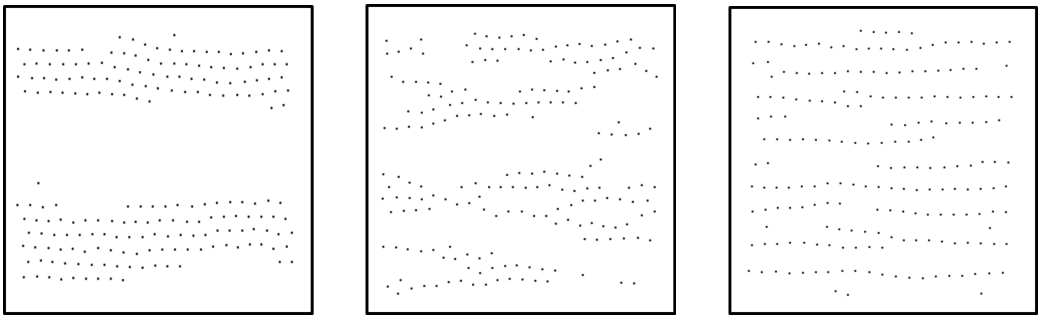
The techniques discussed in this chapter outline the core foundations used in the following work. When a model is created and run in an MD simulation all the approximations above act to reduce the computational expense of the program, whilst maintaining the accuracy of the simulation required. The following chapters will focus on simple chain formation in MR/ER fluids, building from single stranded low-dimensionality chains to monodisperse and bidisperse systems, particularly in the case of bidispersity in the liquid phase. This thesis will also touch on more speculative simulations involving system confinement and variability in flow properties.

Chapter 3

Chain Formation

Rheology is a term that refers to the change in bulk flow properties of an MR/ER fluid (as discussed in the **Introduction**) on application of a magnetic or electric field [158]. The viscosity of the colloid increases, indicated by the increasing stiffness of the fluid as the particles line along the field lines causing chain growth as a result of this particle aggregation. The 'stiffness' can be tuned, depending on the conditions under which the fluid is exposed. Therefore by varying the simulation conditions over parameter space, using the methods in **Chapter 2**, the model can produce a wide range of rheology within the system. However in this thesis, flow properties and rheology is not explicitly studied in this work. The extent of chain formation of the solid MR/ER particles suspended within a carrier fluid are of initial interest.

Examples of networks produced from three independent electro-rheological simulations, at constant density, temperature and runtime can be seen in **Figure 3.1**. Here the simulation parameters alone differ in terms of varying the dispersive (attractive) term in the short range potential. The clear result is that the extent and nature of chain formation can be altered by relatively subtle changes in the potential model. In order to understand specific simulation details of bulk MR or ER fluids therefore, the functional form of the short-range inter-particle potential must be investigated



(a) LJ + the dipole-dipole term.

(b) LJ (halved attractive/dispersive term) + the dipole-dipole term.

(c) Function of r^{-12} (LJ with no attractive/dispersive term) + the dipole-dipole term.

Figure 3.1: Final configurations after a fixed number of MD steps, $\rho^* = 0.4$, $T_{final} = 50K$, particle polarizabilities are set at $\alpha = 10$ a.u. and external field strength $\mathbf{E}_{ex} = 0.05$ a.u., using differing inter-particle potentials. **(a)** Stockmayer fluid with dipole-induced-dipole term rather than a point dipole. **(b)** as in **(a)** with a reduced (halved) attraction term. **(c)** Dipolar soft-sphere with dipole-induced-dipole term rather than a point dipole, *i.e.* totally repulsive inter-particle pair-potential. This diagram is for illustration and parameter choice will be explained in the following sections.

briefly. Consequently this chapter begins by discussing the effect of varying the dispersive and attractive terms in the '6-12' Lennard-Jones potential. **Figure 3.1** shows that the LJ potential leads to an energetically favourable, hexagonally close-packed structure. This is in contrast to the mainly single-stranded chains observed in simulations omitting the dispersive term of the Lennard-Jones potential. The effect of the r^{-12} repulsive potential term alone is less obvious and the omission of the dispersive term allows for dipole-dipole interactions to be effectively isolated in the model. It is also worth noting that the attractive terms can be added into the potential model at a later date once the effect of the most basic 'r^{-12}' potential is investigated. Simulation techniques have the advantage (specifically with the use of effective pair-potentials

and MD, as detailed in **Chapter 2**) of easy modification, therefore allowing a large variety of short-range potentials to be trialled; see **Figure 2.2** for commonly used effective pair-potentials. Point energy calculations for ideal chains (from two-particle chains to infinitely long single/double stranded chains) can be used in order to survey the effect of each potential model on the structural configurations produced from simulation.

3.1 Two-Particle Simulations

Point energy calculations are performed for a two-particle system over a range of separations, r. The entire potential energy of the two-particle system, U^{all} is calculated from **Equation 3.1.1** (for particles $i = 1$ and $j = 2$) such that it is given as the sum of: the short-range potential (*e.g.* U^{LJ} or $U^{r^{-12}}$), the dipole-dipole interaction term (**Equation 2.4.6**), the energy required to polarize the particles U^{pol} and the energy of interaction with an applied field;

$$U^{all} = U^{tot} - \sum_{i=1}^{2} \boldsymbol{\mu}\cdot\mathbf{E}_{ex} = \underbrace{U_{ij}^{sr}(\mathbf{r}^{ij}) + \frac{\boldsymbol{\mu}^i\boldsymbol{\mu}^j}{(\mathbf{r}^{ij})^3}\cos\phi\left(1 - 3\cos^2\theta^{ij}\right)}_{U^{sr}+U^{dd}} + \underbrace{\frac{1}{2\alpha}\sum_{i=1}^{2}(\boldsymbol{\mu}^i)^2}_{U^{pol}} - \sum_{i=1}^{2}\boldsymbol{\mu}^i\cdot\mathbf{E}_{ex}. \tag{3.1.1}$$

Again as introduced in **Equation 2.4.2**, U^{tot} is equal to U^{all} without the energy of interaction with the applied field, $-\boldsymbol{\mu}\cdot\mathbf{E}_{ex}$ term. **Figure 3.2** shows a plot of $U^{sr} + U^{dd}$ as a function of particle separation, constructed from point energy calculations of a two-particle system. U^{dd} (**Equation 2.4.6**) is calculated with a polarizability, $\alpha =$ 10 a.u. and external field strength $\mathbf{E}_{ex} = 0.05$ a.u. as characterised by a unidirectional field along which the particles are aligned ($\phi = 0$ and $\theta^{ij} = 0$), such that $\boldsymbol{\mu}_{ex} = 0.5$ a.u. and $U^{dd} = -2/(\mathbf{r}^{ij})^3$ (*black* line). Various combinations of U^{sr} and U^{dd} are also shown. By applying an external field, a dipole is induced on each particle which when head-to-tail, is attractive in nature. For example, the minimum in the potential

energy curve for $U^{dd}(\alpha = 10 \text{ a.u.}, \mathbf{E}_{ex} = 0.05 \text{ a.u.}) + U^{LJ}$ (*green* line) is at a lower energy than with U^{LJ} alone (*blue* line). Increasing the magnitude of $\mathbf{E}_{ex}$ will increase the size of the induced dipoles and change the potential energy curve. For example increasing $\mathbf{E}_{ex}$ to 0.065 a.u., labelled as $U^{dd+}(\alpha = 10 \text{ a.u.}, \mathbf{E}_{ex} = 0.065 \text{ a.u.})$ in **Figure 3.2**, then $U^{dd+} + U^{r^{-12}}$ (*brown* line) gives a similar functional form to $U^{dd} + U^{LJ}$ (*green* line), with the same minimum energy. This highlights the tunability of the simulations and justifies the selection of a less complicated pair-potential ($U^{r^{-12}}$ rather than U^{LJ}) as used throughout this thesis.

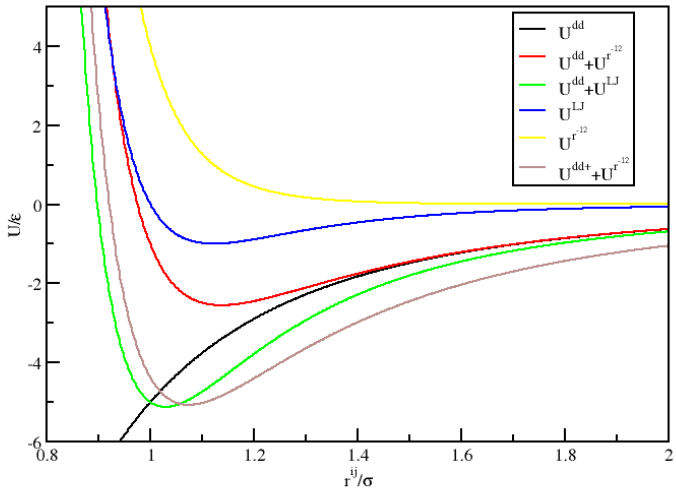


Figure 3.2: Various terms contributing to U^{tot} for a two-particle system *i.e.* combinations of $U^{sr}(= U^{LJ}$ (*blue* curve) and $U^{r^{-12}}$ (*yellow* curve)) + $U^{dd}(\alpha = 10 \text{ a.u.}, \mathbf{E}_{ex} = 0.05 \text{ a.u.})$ (*black* curve). Therefore $U^{dd} + U^{LJ}$ is the Stockmayer fluid potential (*green* line) and $U^{dd} + U^{r^{-12}}$ is the dipolar soft-sphere potential (*red* line). $U^{dd+}(\alpha = 10 \text{ a.u.}, \mathbf{E}_{ex} = 0.065 \text{ a.u.}) + U^{r^{-12}}$ (*brown* curve) is equal to the *red* curve at higher external field strength.

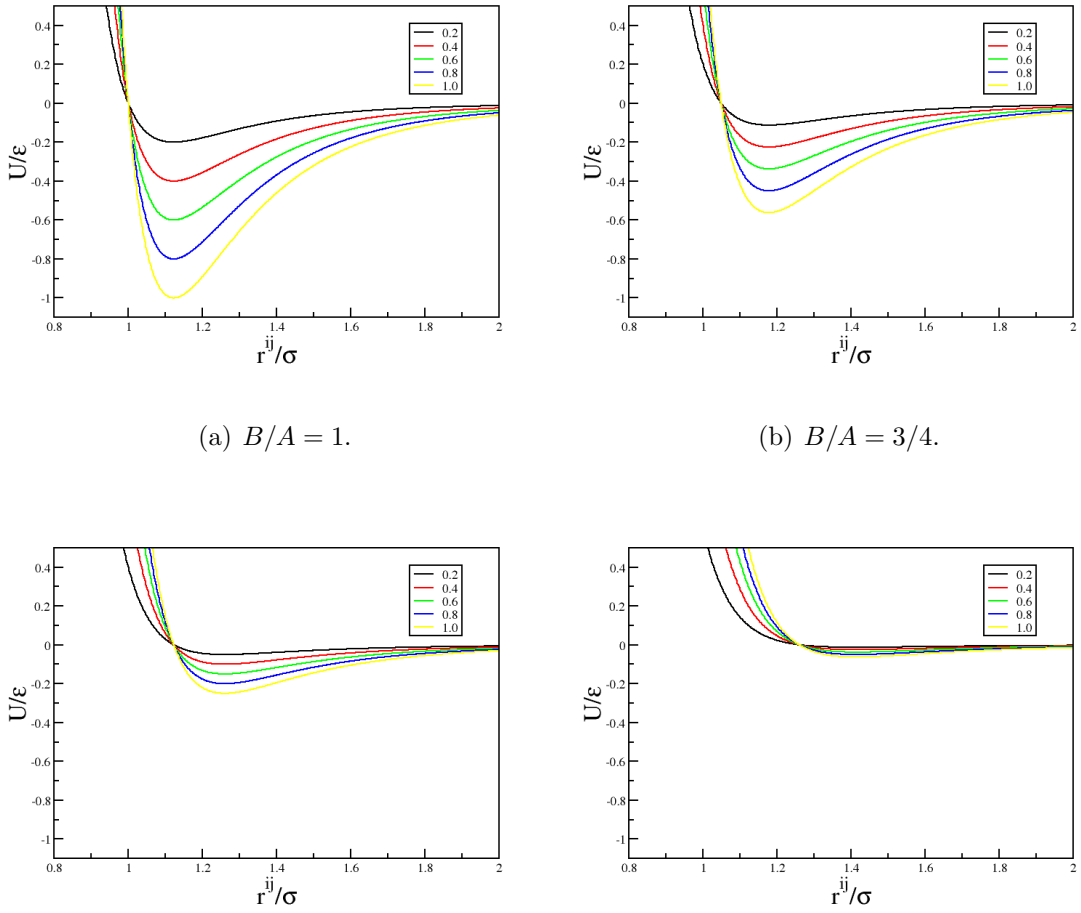
The functional form of the Lennard-Jones short-range potential, as discussed in **Section 2.5**, can be modified based on the values of constants AC and B/A in

Equation 3.1.2,

$$U_{AB}^{LJ} = 4\epsilon AC\left[\left(\frac{\sigma}{\mathbf{r}^{ij}}\right)^{12} - \frac{B}{A}\left(\frac{\sigma}{\mathbf{r}^{ij}}\right)^{6}\right]. \tag{3.1.2}$$

A, B and C are simply scaling parameters and are not independent. ϵAC is the effective energy parameter where $\epsilon/k_B = 118K$ as stated before. When $A = B = C = 1$ then $U_{AB}^{LJ} = U^{LJ}$, the standard Lennard-Jones potential, conversely, when $A = 1$, $B = 0$ and $C = 1$ then U_{AB}^{LJ} becomes a factor of r^{-12} only and is purely repulsive. These parameters are selected as shown purely to highlight the changing well depth of the LJ potential form. As shown in **Figure 3.3**, it can be seen that by altering the factor C and the ratio B/A, then the extent of repulsion/attraction between the particles can be modulated. The four sub-figures are separated by fixed ratios of A and B such that $B/A = 1,\ 3/4,\ 1/2,\ 1/4$ respectively. At the limit, in figure **(a)** $B/A = 1$ therefore an increase in the factor C from $0.1 \rightarrow 1$ increases the size of ϵ, the well depth. From **(b)** to **(d)** the weight of B decreases therefore reducing the size of the attractive interaction and the repulsive wall is greater at higher r, separation. This analysis highlights, along with the simple two-atom potentials above, that there are infinite possible routes when selecting an adequate short-range inter-particle potential for the work in this thesis. The 'r^{-12}' potential has therefore been used to reduce complexity in calculation.

$U^{sr} + U^{dd}$ combinations have been investigated in detail (see above). The additional terms contributing to the total energy of a two-particle system, with a short-range 'r^{-12}' potential, are illustrated in **Figure 3.4**. Various $\{\alpha, \mathbf{E}_{ex}\}$ pairs are trialled with fixed $\boldsymbol{\mu}_{ex} = \alpha\mathbf{E}_{ex}$ (see **Table 3.1**) for a number of two-particle point energy calculations, again as a function of particle separation r. The solid curves at higher energy describe U^{tot} whilst the lower energy curves (delineated with crosses), gives $U^{all} = U^{tot} - \boldsymbol{\mu}\cdot\mathbf{E}_{ex}$ (the total P.E. minus the interaction energy with the applied field). Therefore, the $U^{tot} - \boldsymbol{\mu}\cdot\mathbf{E}_{ex}$ potential energy curves tend to the polarization



(a) $B/A = 1$.

(b) $B/A = 3/4$.

(c) $B/A = 1/2$.

(d) $B/A = 1/4$.

Figure 3.3: A set of four figures showing the effect on the functional form of the short-range potential when varying fixed ratios of (A:B) in **Equation 3.1.2**: **(a)** Ratio (1:1); **(b)** Ratio (1:0.75); **(c)** Ratio (1:0.5); and **(d)** Ratio (1:0.25). The factor C is also varied within each sub-figure, the values of which, are displayed in the legend.

energy limit, $-\frac{1}{2}\alpha\mathbf{E}_{ex}^2$ at high $\mathbf{r}^{ij}$. This metric reveals the effect of the external field on the magnitude of the polarization energy of the particles in the system as highlighted when the values of the polarizability and external field strength are varied. As expected and shown in **Figure 3.4**, a lower polarizability, α, coupled with a high external field strength, $\mathbf{E}_{ex}$, gives a high (negative, stabilising) polarization energy

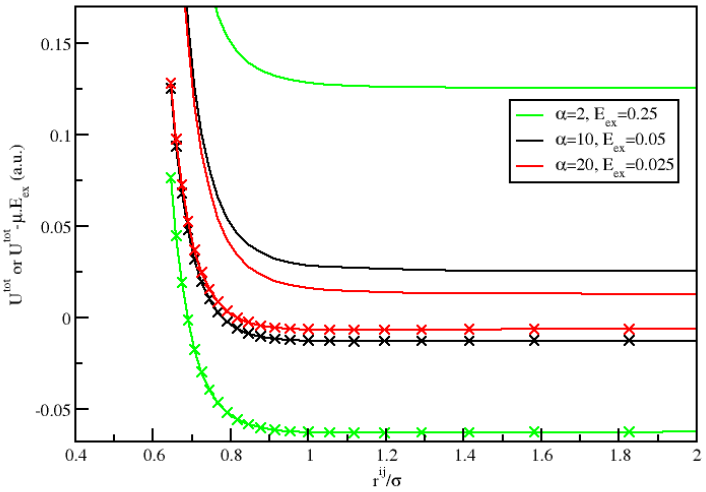


Figure 3.4: Three $\{\alpha, \mathbf{E}_{ex}\}$ combinations which give $\boldsymbol{\mu}_{ex} = 0.5$ a.u.. Therefore by varying the polarizability and external field strength, the energy profile of the simulation is modulated. The solid curves correspond to U^{tot} for the two-particle system. If $\boldsymbol{\mu} \cdot \mathbf{E}_{ex}$ is subtracted (crosses) then the limits tend to the polarization energy for the two-particle system, as confirmed in **Table 3.1**.

Table 3.1: $\{\alpha, \mathbf{E}_{ex}\}$ combinations with terms contributing to the total potential energy (per particle), U^{all}.

α (a.u.)	$\mathbf{E}_{ex}$ (a.u.)	$-\frac{1}{2}\alpha\mathbf{E}_{ex}^2$ (a.u.)	$\boldsymbol{\mu} \cdot \mathbf{E}_{ex}$ (a.u.)
2	0.25	-0.0625	0.125
10	0.05	-0.0125	0.025
20	0.025	-0.00625	0.0125

(U^{pol}), the dominant term at high $\mathbf{r}^{ij}$. Therefore it is observed that the *green* curve for the $\{\alpha, \mathbf{E}_{ex}\} = \{2, 0.25\}$ a.u. system has a greater total energy and $U^{tot} - \boldsymbol{\mu}.\mathbf{E}_{ex}$ is more negative implying a greater polarization energy contribution than the other pairs. $\{\alpha, \mathbf{E}_{ex}\} = \{20, 0.025\}$ a.u. has the lowest polarization energy contribution for example, given the dominance of the external energy, $\mathbf{E}_{ex}$ in the term. However at lower inter-particle distance ($\mathbf{r}^{ij}$), the repulsive wall is present and the first two terms,

$U^{sr} + U^{dd}$, become large at the limit hence the rapid increase in $U^{tot} - \boldsymbol{\mu} \cdot \mathbf{E}_{ex}$. Here the combination of these terms is at a similar order of magnitude to the polarization term, competing therefore to destabilise/stabilise the particles respectively. As shown in **Equation 2.4.1** a large polarizability magnifies the dipole-induced-dipole contribution to $\boldsymbol{\mu}^i$ (internal field term) but given that there are only two-particles in this system the effect of this term is washed out. However for an infinite chain this competing effect can be more easily demonstrated at this low $\mathbf{r}^{ij}$ limit (see below).

3.2 Infinite Chains

The above analysis for the two-particle system can be extended for an infinite chain. The infinite chain is constructed by making use of the periodic boundary conditions of the simulation cell (see schematic in **Figure 3.5**). A system with entirely infinite chains would highlight the limits of chain formation in that system and investigation of the effects of two-infinite chain systems would improve the understanding of network formation.

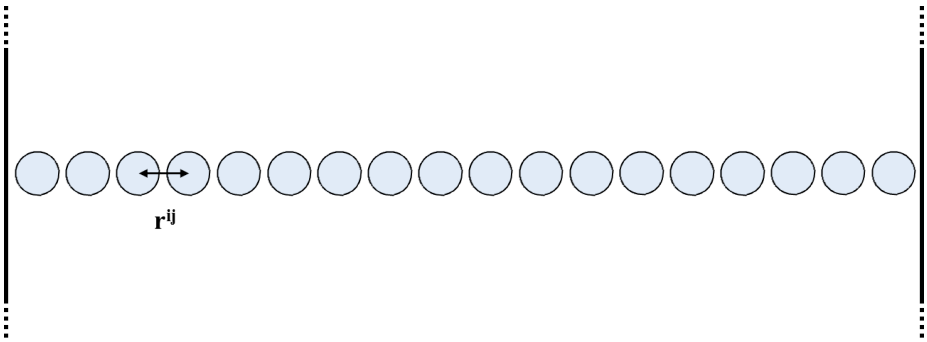


Figure 3.5: Twenty particles are placed along a single axis in a regular square box such that the distance between the last particle and the border of the box (thick *black* line) is $r/2$. The value of r is varied for the analysis below. The size of the box, thus the volume of the cell changes based on the size of r.

3.2.1 Single Chain vs. 2-Particle Simulation

Figure 3.6 extends the argument of **Figure 3.4** showing the values of $U^{tot} - \boldsymbol{\mu} \cdot \mathbf{E}_{ex}$ per particle, for particles in an infinite chain and two-particle chain respectively. At the large $\mathbf{r}^{ij}$ limit the energies again tend to that of the two-particle polarization energies for the same $\{\alpha, \mathbf{E}_{ex}\}$ pairs. The dominant term is the polarization term given the external field dependence. However at low $\mathbf{r}^{ij}$, in the case of the infinite chain, there exists a steeper repulsive wall at higher inter-particle distance than the two-particle analogue. Particles in an infinite chain now have a repulsive force from two-particles (one on either side) as $\mathbf{r}^{ij}$ is reduced, hence the increase in potential at an earlier stage than the two-particle case. However the stability of each chain at different $\{\alpha, \mathbf{E}_{ex}\}$ pairs depends on the value of α more so at low $\mathbf{E}_{ex}$. Additional stability in the U^{dd} term of the potential arises from the dipole-induced-dipole effect at high α, stabilising the chain (*e.g. red* curve), therefore the effect of the repulsive wall arises at a lower $\mathbf{r}^{ij}$ than for the low α high $\mathbf{E}_{ex}$ pairs (*e.g. light-green* curve).

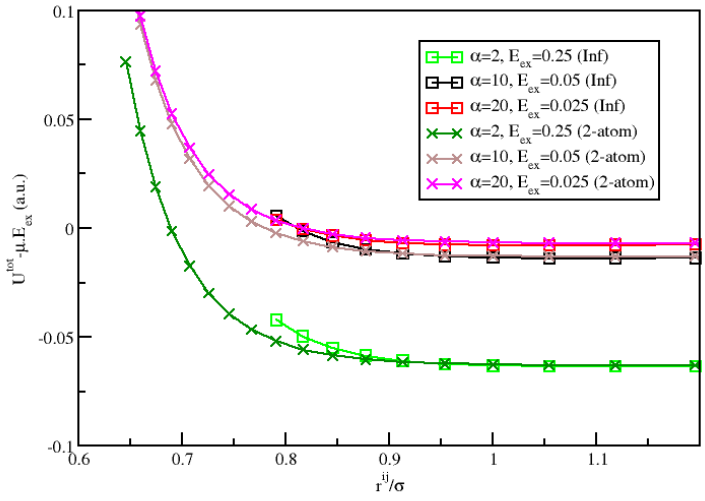


Figure 3.6: A comparison showing $U^{tot} - \boldsymbol{\mu} \cdot \mathbf{E}_{ex}$ against $\mathbf{r}^{ij}$ for the infinite chain and two-particle case for several $\{\alpha, \mathbf{E}_{ex}\}$ pairs.

3.2.2 Interaction Between Chains

By looking at two-infinite chains, in registry and out of registry a better picture of the behaviour of these systems can be found. **Figures 3.7** and **3.8** give schematics for an 'infinite' chain system (when including boundary conditions) for these ideal chain systems.

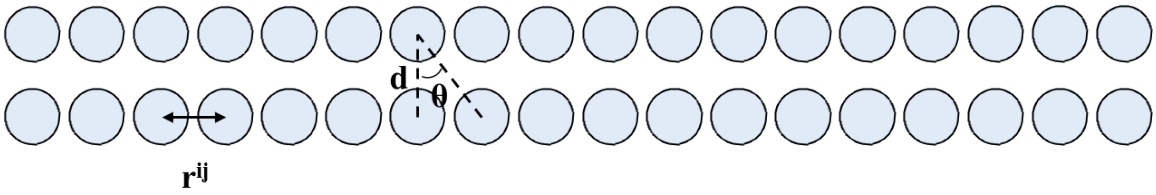


Figure 3.7: Infinite chain system, in registry. The chain-chain separation is labelled d. Adjacent particles, in the same chain are separated by $\mathbf{r}^{ij}$ at an angle of $\theta = \pi/2$ to one another. In opposing chains, particles are separated by an angle, $\tan\theta = (n\mathbf{r}^{ij}/d)$.

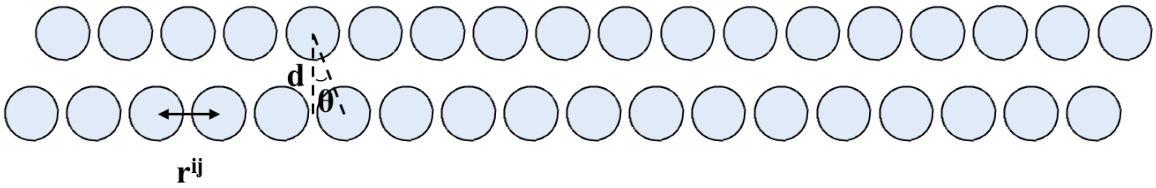


Figure 3.8: Infinite chain system, out of registry. The chain-chain separation is labelled d. Adjacent particles, in the same chain are separated by $\mathbf{r}^{ij}$ at an angle of $\theta = \pi/2$ to one another. In opposing chains, particles are separated by an angle, $\tan\theta = (n\mathbf{r}^{ij}/2d)$.

Figure 3.9 makes use of an order parameter, ψ_n (the method of calculation is detailed in **Section 2.8.6**), to quantify the ordering within the system in relation to a square lattice ($\psi_4 = 1$) or hexagonal lattice ($\psi_6 = 1$). The inter-chain distance is fixed at $d = 7$ a.u. whilst the particle-particle distance, $\mathbf{r}^{ij}$ is varied.

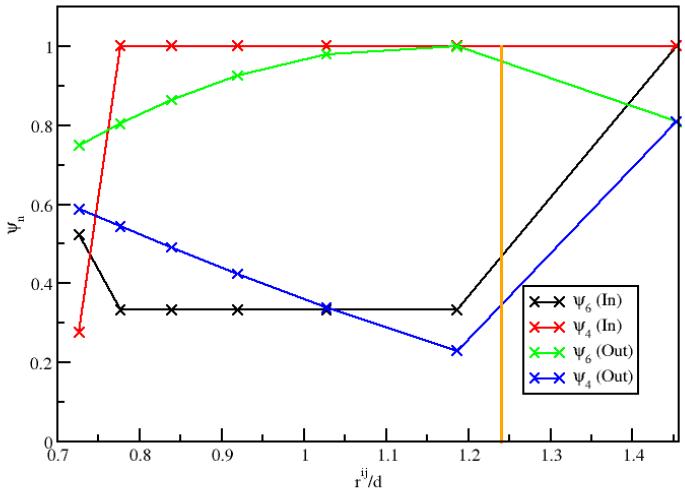
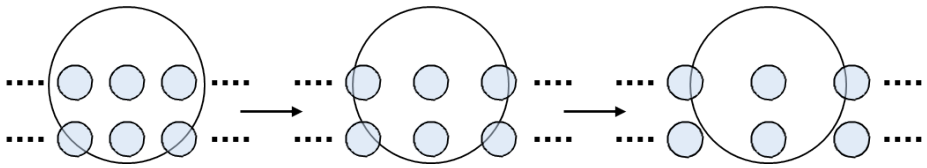


Figure 3.9: ψ_n as inter-particle distance is varied with two infinite chains at a fixed inter-chain distance. Chains are either in registry or out of registry and $n = 4, 6$. The thick *orange* line denotes the position of 1.35σ, the capture/cut-off distance for the algorithm.

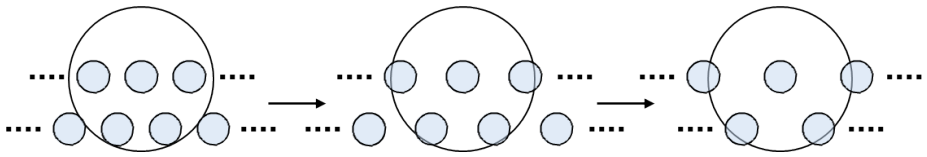
For single chains it is evident that $\psi_4 = \psi_6 = 1$, aside from when $\mathbf{r}^{ij} > 1.35\sigma$ (the capture/cut-off distance), then therefore $\psi_4 = \psi_6 = 0$. Thus for two-chains with separation $d > 1.35\sigma$, the local order parameter algorithm views each chain as single stranded and again $\psi_4 = \psi_6 = 1$. However when the chains are $d \leq 1.35\sigma$ apart ψ_n modulates as detailed in **Figure 3.9**. To illustrate this calculation **Figure 3.10** has been created whereby $\mathbf{r}^{ij}$ is increased from left to right, in registry (**Figure 3.10(a)**) and out of registry (**Figure 3.10(b)**) with one another.

At small $\mathbf{r}^{ij}$, in registry particles (*black* and *red* lines) are calculated with five nearest neighbours (far left diagram in **Figure 3.10**) therefore the values of ψ_4 and ψ_6 begin relatively low (dependent on distance), with ψ_4 slightly larger due to the square-lattice formation along the chains. As the inter-particle distance is increased, the central configuration in **Figure 3.10**, $\psi_4 = 1$ and $\psi_6 = \frac{1}{3}$ which persists over a long range until $\mathbf{r}^{ij} > 1.35\sigma$ where we reach the final configuration in **Figure 3.10** (far right). Then $\psi_4 = \psi_6 = 1$ denoting relatively few lattice points. The out of reg-

istry analogue (*green* and *blue* lines for ψ_6 and ψ_4 respectively) can be characterised over this range as follows. For short inter-particle distance, left diagram in **Figure 3.10(b)**, $0.7 \leq \psi_6 \leq 1$ which increases towards the limit of 1 as $\mathbf{r}^{ij}$ increases. Similarly ψ_4 mirrors this and decreases over this range due to the positioning of particles at lattice points. After the cut-off radius (*orange* line) both ψ_6 and $\psi_4 = 0.8$ indicative of the far right diagram in **Figure 3.10(b)** which is a triangular configuration of particles within the capture distance. The entire point of this is to provide a justification of ψ_n at different inter-particle distances for reference to the chain formation behaviour in later work.



(a) In registry.



(b) Out of registry.

Figure 3.10: A sampling schematic giving a visual explanation of the method of ψ_n measurement. The large circle indicates the capture radius (1.35σ) for the algorithm.

By varying the distance between the chains (d), at a fixed inter-particle distance the effect on the total potential energy of the chain structures can be investigated. **Figure 3.11** shows the $U^{tot} - \boldsymbol{\mu} \cdot \mathbf{E}_{ex}$ profile against $d/\mathbf{r}^{ij}$ for the in registry (upper) and out of registry (lower) configurations of the infinite chains. At low d as at low $\mathbf{r}^{ij}$ the inter-particle repulsive wall reduces the stability of the particle configuration and the

energy becomes more positive at higher $d/\mathbf{r}^{ij}$ ratios (*black* line in both configurations). For a fixed $\mathbf{r}^{ij}$, upon reducing the distance between chains, d the repulsive pair-potential term increases for the in registry case when the ratio $d/\mathbf{r}^{ij} < 1$ as expected. However for the out of registry case, this only occurs at low $\mathbf{r}^{ij}$, where conversely at low $d/\mathbf{r}^{ij}$ and high $\mathbf{r}^{ij}$ the potential flattens. This is expected, beyond the repulsive pair-potential range when out of registry, which is marginally lower in energy (more stable) than the in registry configuration.

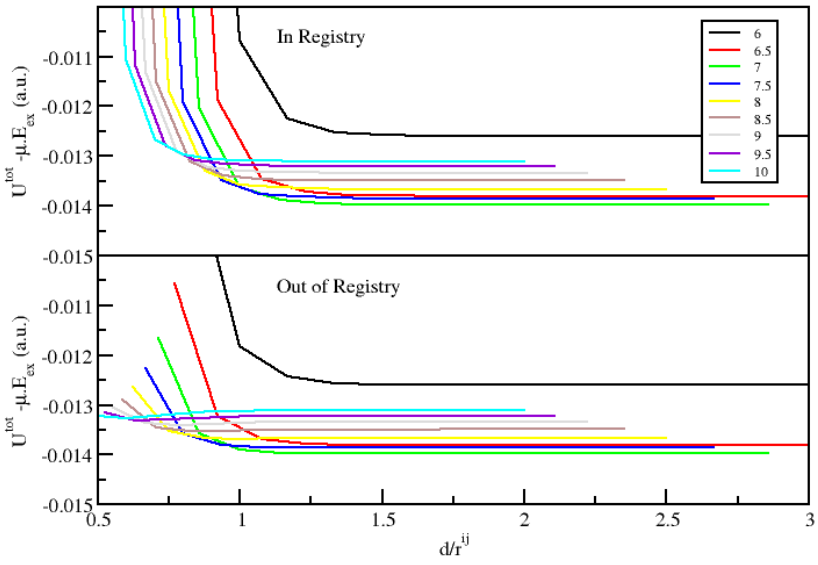


Figure 3.11: $U^{tot} - \boldsymbol{\mu} \cdot \mathbf{E}_{ex}$ as a function of $d/\mathbf{r}^{ij}$ for two parallel chains, in and out of registry. The legend gives varying values of $\mathbf{r}^{ij}$.

3.3 Chapter Summary

By reviewing a number of short-range potential models, this short chapter justified our use of the simple 'r^{-12}' potential for all subsequent work rather than a more

complicated LJ potential with dispersion interactions. As found in the 2-particle system by varying the values of $\{\alpha, \mathbf{E}_{ex}\}$ various contributions to the total potential energy of the system can be modulated. This is a first hint at the important role of the dipole-induced-dipole term, which is explored in the next chapter. A brief look at infinite chains and pairs of infinite chains acts to bridge the gap between the two-particle system and bulk system with large amounts of chain formation.

Chapter 4

Monodisperse Systems

This chapter aims to explore bulk monodisperse simulations, building on the work in **Chapter 3** by investigating two-dimensional systems with large N (≥ 200), the number of particles in the simulation cell. The term *monodisperse* in this context refers to a simulation in which particles are identical, not only in terms of σ and ϵ as defined by the effective pair-potential but where the particle polarizabilities are uniform (*i.e.* $\alpha_i = \alpha$). Simulations have been conducted in order to find the ranges of reduced density (ρ^*) over which fibrous network structures appear when applying an external electric field to our bulk two-dimensional monodisperse systems. Reduced units are used and discussed in **Appendix C.3**. For each simulation, the number of particles and cell shape are fixed, along with the magnitude and direction of the applied electric field, as are the key system variables; the polarizability α, the particle diameter, σ and the effective pair-potential, governing the extent of inter-particle repulsion (set as the 'r^{-12}' potential unless otherwise stated).

After outlining this method of parameter searching, resulting structures are analysed in their final configurations based on a number of metrics as detailed in **Section 2.8**. Principally this chapter gives a brief investigation of field strength modulation (by extension, varying the particle polarizability), cell-size (density, ρ^*), cell-shape

(elongation of a single axis) along with particle number ($N = 200 \rightarrow 1000$). The extent of chain formation and particle aggregation can be determined by the extent of the dipole-induced-dipole effect. A distribution of dipoles is produced to describe the differing internal fields of each particle brought about by the environment surrounding each particle. The width and mean value of these distributions can be controlled depending on the initial particle polarizability and magnitude of the external field set. Therefore an in-depth investigation of this effect must be conducted.

4.1 Simulation Methodology

Starting configurations are generated by performing molecular dynamics simulations on the fluid phase. Each simulation was initially run for 250000 MD steps ($\approx 0.151ns$) at a temperature high above the system melting point ($T = 10000K$), creating an isotropic fluid configuration represented by the *black* line in **Figure 4.1**. 50 independent configurations are then extracted from the equilibrium fluids at time separations (τ) significantly greater than the characteristic system relaxation time (as determined from the intermediate scattering functions [159]). The result is that successive configurations can be considered as effectively independent.

The self-intermediate scattering function can be described by the equation

$$\phi_s(\mathbf{k}, t) = \left\langle \exp\left\{ i\mathbf{k} \cdot \left[\mathbf{r}^i(t) - \mathbf{r}^i(0) \right] \right\} \right\rangle, \tag{4.1.1}$$

where $\mathbf{r}^i$ describes the position of particle i and $\mathbf{k}$ gives the scattering vector for an incoherent neutron scattering experiment. Thus as highlighted in **Figure 4.2**, when the value of τ equals 5000 steps ($\approx 0.00302ns$) then the difference of particle positions between this configuration and the starting configuration ($\tau = 0$) is significant such that the new configuration is sufficiently randomly distributed and contains no saved coordinate information from the previous configuration. The inset to **Figure**

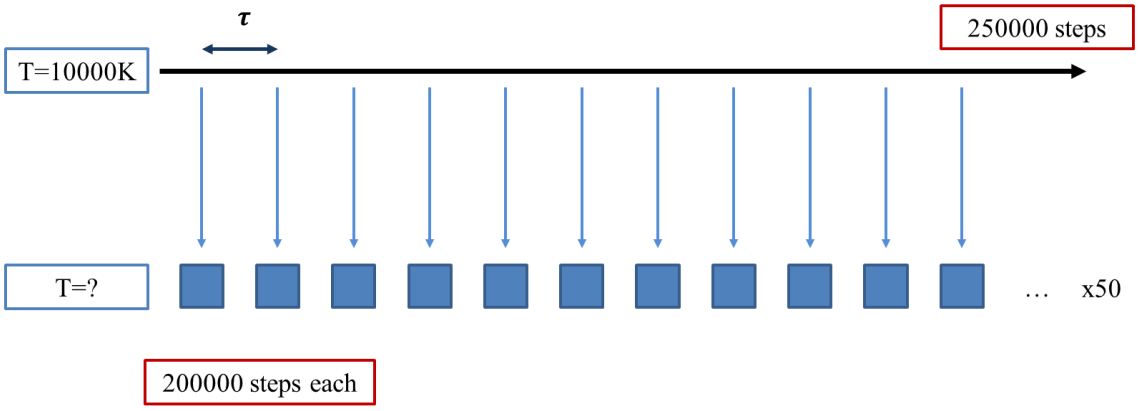


Figure 4.1: Method: The initial run (at high T and 250000 steps) is depicted by the bold *black* line. The configurations generated by this run were divided into 50 isotropic fluid structures separated by time, τ and quenched to a given low T, for 200000 steps.

4.2 shows the structure factor, $S(k)$ for the isotropic fluid configurations. This corresponds to the self-intermediate scattering function at $t = 0$. The characteristic liquid form is highlighted by the sharp initial peak around $k = 1$ a.u.$^{-1}$ followed by subsequent, more diffuse peaks at higher k.

Finally, each unique configuration is quenched to $T_{final} \sim 50K$ making use of Nosé-Hoover thermostats, akin to coupling the system to a heat bath, as outlined in **Section 2.6.1**. These are the starting configurations used for each run, the quenching removes the residual kinetic energy present. Parameter searches can then be conducted (varying properties such as the reduced density, at fixed external field) by advancing particle positions over a fixed number of steps, starting from coordinates on the *black* line in **Figure 4.1**. The subsequent quenched final coordinates from these runs (*blue* squares in **Figure 4.1**), including dipole magnitudes and directions, were taken for analysis as an average over the ensemble. By fixing the time over which the production run is simulated (*blue* line in **Figure 4.1**) and by only analysing the fixed final quenched configurations of these sets we aim to produce results as an

experimental analogue would. Of course metrics are used to monitor the evolution over time for each simulation, in this case more than the final quenched configurations are analysed. The following sections outline the results of various monodisperse simulations.

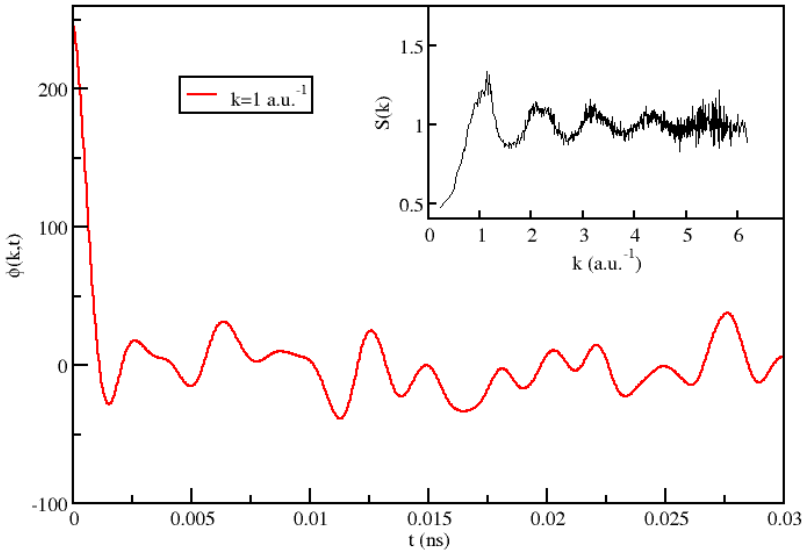


Figure 4.2: Self-intermediate scattering function for a run $\rho^* = 0.4$, $N = 200$, using the method detailed in **Figure 4.1**. An interval $\tau = 5000$ ($\approx 0.00302ns$) is selected in order to ensure each subsequent initial starting configuration is sufficiently randomly distributed. $\phi(k,t)$ decays to zero over the time-scale of the simulation. The inset shows $S(k)$ for the isotropic liquid configurations at $t = 0$, from high temperature before quenching occurs.

4.2 Dipole Distributions

The dipole distribution of a monodisperse electrorheological fluid reveals interesting information about the extent of chain formation under an applied electric field. As

discussed in **Section 2.4**, dipoles are *induced* by the external field

$$\boldsymbol{\mu}^i = \alpha(\mathbf{E}_{ex} + \mathbf{E}^i_{int}) = \boldsymbol{\mu}_{ex} + \alpha^i \mathbf{E}^i_{int} = \boldsymbol{\mu}_{ex} + \boldsymbol{\mu}^i_{int}, \tag{4.2.1}$$

where the dipole on site i arises from both an external field vector, $\mathbf{E}_{ex}$ and an internal field vector, $\mathbf{E}_{int}$ generated by all other dipoles in the system. Additionally α^i defines the fixed particle polarizability which, for monodisperse particles, is constant ($\equiv \alpha$). The division of the dipole moments into external and internal contributions ensures that the choice of α and $\mathbf{E}_{ex}$ effectively controls the relative magnitude of those contributions. The magnitude of the internal contribution can have a significant effect on chain formation. By using polarizable species, a distribution of dipole moments can be produced. The width and mean of these distributions can be controlled therefore, by varying the external field strength and polarizability (**Equation 4.2.1**) as discussed above. **Figure 4.3** shows the effect of varying the pair of values $\{\alpha, \mathbf{E}_{ex}\}$ on the distribution of dipoles obtained from the final quenched configurations such that the fixed dipole contribution from the applied field is $\boldsymbol{\mu} = \alpha \cdot \mathbf{E}_{ex} = 0.5$ a.u.. The use of different $\{\alpha, \mathbf{E}_{ex}\}$ pairs varies the significance of the two contributions to $\boldsymbol{\mu}$ in **Equation 4.2.1**. At low α (high $\mathbf{E}_{ex}$) the total dipole is dominated by the external field and the mean dipole is close to $\boldsymbol{\mu} = 0.5$ a.u.. At high α (low $\mathbf{E}_{ex}$) the internal fields (dipole-induced-dipoles) are relatively strong and the dipole distribution is shifted to high $\boldsymbol{\mu}$. The inset to figure **Figure 4.3** shows the mean dipole moment, $\langle\mu\rangle$, as a function of the applied field. For a two-particle cluster the first-order dipole-induced-dipole is given by

$$\mu^{(1)}_{DID} = \frac{2\alpha\boldsymbol{\mu}_{ex}}{r^3} \equiv \frac{2\alpha^2\mathbf{E}_{ex}}{r^3}. \tag{4.2.2}$$

Since both particles in the pair are polarizable then iterative equations must be solved in order to determine the self-consistent dipole, $\mu^{(\infty)}_{DID}$ (*i.e.* if there are two identical particles i and j, then if particle i induces a dipole on particle j, particle j therefore

induces a larger dipole on particle i, which again induces a larger dipole on j and so on). More detail on this derivation is covered in **Appendix D**. Now for a chain of dipoles the field on a given particle due to the dipoles resident on the particles in the chain, can be given by the equation

$$\begin{aligned}\mathbf{E}_{chain} &= \frac{4\alpha\mathbf{E}_{ex}}{r^3} + \frac{4\alpha\mathbf{E}_{ex}}{(2r)^3} + ... \\ &= \frac{4\alpha\mathbf{E}_{ex}}{r^3}\left\{1 + \frac{1}{8} + \frac{1}{27} + ...\right\}, \\ &= \frac{4\alpha\mathbf{E}_{ex}}{r^3}\sum_{n=1}^{\infty} n^{-3} = \frac{4\alpha\mathbf{E}_{ex}}{r^3}\zeta(3), \end{aligned} \tag{4.2.3}$$

where the '4' arises from the chains of dipoles percolating away in two directions from a given site and $\zeta(3)$ is a Riemann zeta function (also known as Apéry's constant) having a value of $\zeta(3) \simeq 1.2021$. As a result, the first-order DID dipole term is given by

$$\mu_{DID}^{(1)} = \frac{4\alpha^2\mathbf{E}_{ex}\zeta(3)}{r^3}, \tag{4.2.4}$$

and $\mu_{DID}^{(\infty)}$ can be generated by subsequent iterations. Since $\boldsymbol{\mu}_{ex}$ is fixed ($= \alpha \cdot \mathbf{E}_{ex}$) we can write the above equation as

$$\mu_{DID}^{(1)} = \frac{4\boldsymbol{\mu}_{ex}{}^2\zeta(3)}{r^3}\frac{1}{\mathbf{E}_{ex}}, \tag{4.2.5}$$

which shows that the DID term should scale inversely to the applied field if significant chain structures are formed. Therefore, the inset to **Figure 4.3** shows the first-order corrected and self consistent dipoles predicted for a pair of particles and for an infinite chain. The separation r is taken as the first peak position in the pair distribution function. At low $\mathbf{E}_{ex}$ (high α) the observed mean dipole 'shifts' from sitting on the two-particle curve to sitting on the infinite chain curve, indicative of the formation of significant chains at low $\mathbf{E}_{ex}$. There is evidently a limit on the magnitude of the polarizability which can be applied. Once $\mu_{DID}^{(1)} \geq \boldsymbol{\mu}_{ex}$ then the DID terms are too large for convergence to a self consistent value (a 'polarization catastrophe'). As a

result, we can evaluate the 'critical' polarizability, α^*, by substituting the conditional $\mu_{DID}^{(1)} = \boldsymbol{\mu}_{ex}$ into **Equation 4.2.5** to obtain

$$\frac{4\alpha^* \mathbf{E}_{ex}}{r^3}\zeta(3) = \mathbf{E}_{ex}, \tag{4.2.6}$$

and therefore,

$$\alpha^* = \frac{r^3}{4\zeta(3)}. \tag{4.2.7}$$

Interestingly, the critical polarizability is independent of $\mathbf{E}_{ex}$.

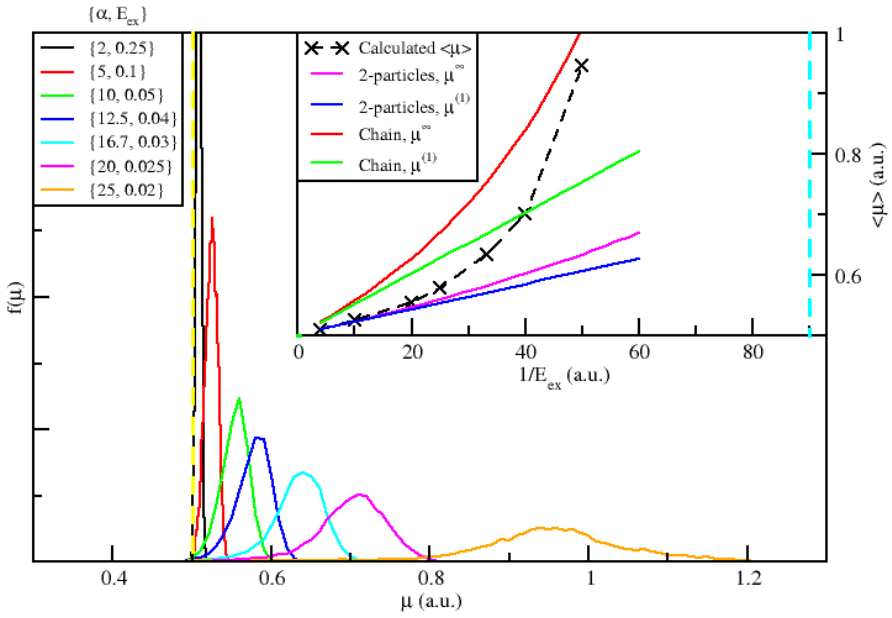


Figure 4.3: Monodisperse dipole distributions, averaged over 50 configurations, at seven different external fields and particle polarizabilities ($\{\alpha, \mathbf{E}_{ex}\}$ in legend). Each $\{\alpha, \mathbf{E}_{ex}\}$ pair has a fixed product at $\mu = 0.5$ a.u.. y-axis scaling labels are removed for clarity. The inset shows the mean dipole of the distributions as a function of the applied field, $\mathbf{E}_{ex}$, along with the total dipoles predicted for a pair of particles ('2-Particles') and for an infinite chain ('Chain') for a first-order corrected DID term, μ_1, and the full self-consistent term, μ_∞.

Distribution Fitting

The dipole distributions in **Figure 4.3** can be fitted analytically to a distribution model, potentially highlighting properties associated with the particle aggregation process. It is pertinent to note that the distributions, especially at the high α region, are minimum-extreme distributions resulting from the few 0-coordinate particles present in the final configurations with low relative induced-dipoles.

In the previous section, dipole distributions are calculated as an average over 50 final configurations, from simulations at varying $\{\alpha, \mathbf{E}_{ex}\}$ pairs ($\{20, 0.025\}$, $\{10, 0.05\}$, $\{5, 0.1\}$, $\{2, 0.25\}$ a.u.). Instead of fixing the bin width, as in **Figure 4.3** for each distribution, the number of bins between a maximum and minimum value (of μ) are now fixed. This is to observe the finer detail of the distributions at the low α end of the pairings. From this set of distribution data, a cumulative distribution function (cdf) can be calculated for each pairing, in preparation for a non-linear 'least-squares' fitting. Wolfram Mathematica [160] was used to fit a non-linear function to the data based on trial forms of well-known cdfs (Normal, Gumbel-type). The cumulative distribution function represents the probability that the variable takes a value less than or equal to x. For a discrete distribution the cdf is calculated as such:

$$\mathrm{cdf}(x) = \sum_{i=0}^{x} f(i), \tag{4.2.8}$$

where $f(i)$ represents the points on a scaled discrete dipole distribution function in this case. For a continuous function this would represent the probability distribution function (pdf), where the cdf is equal to the integral of the pdf from $-\infty \to x$.

The two trial functions are the Normal distribution and the Gumbel distribution. First of all, the pdf of the Normal distribution about the mean ($\langle\mu\rangle$), scaled by the

standard deviation (σ) is given as

$$\mathrm{P}^{Norm}(\mu) = \frac{1}{\sigma\sqrt{2\pi}}\exp\left\{-\left[\mu - \langle\mu\rangle\right]^2/(2\sigma^2)\right\}. \tag{4.2.9}$$

The cdf is the integral of the pdf (from $-\infty \rightarrow x$) and can be shown to be of the form

$$\mathrm{cdf}^{Norm}(\mu) = \frac{1}{2}\mathrm{erfc}\left(\frac{-\mu + \langle\mu\rangle}{\sqrt{2}\sigma}\right). \tag{4.2.10}$$

The 'Gumbel' distribution is the name used to refer to a type I Fisher-Tippett distribution, (a minimum extreme value distribution) which contains a location parameter $\langle\mu\rangle$ (the mean) and a scaling parameter β.

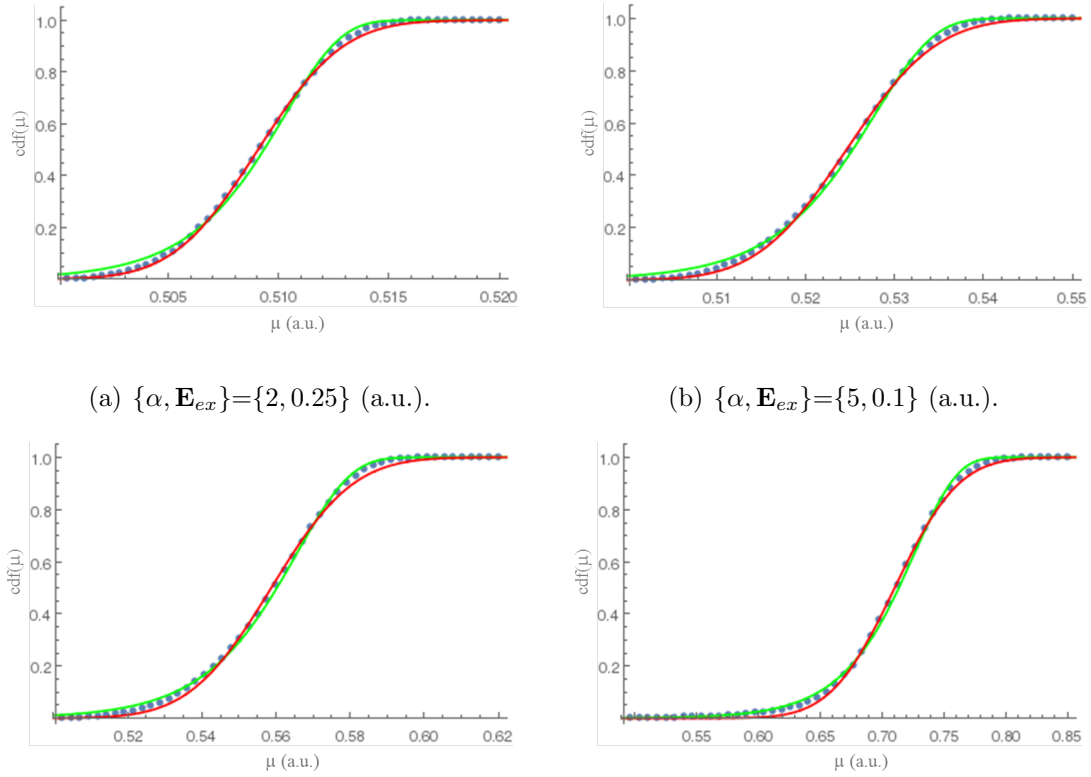
$$\mathrm{P}^{Gum}(\mu) = \frac{1}{\beta}\exp\left\{\left[(\mu - \langle\mu\rangle)/\beta\right] - \exp\left[(\mu - \langle\mu\rangle)/\beta\right]\right\}. \tag{4.2.11}$$

Again the cdf is the integral of this pdf, (from $-\infty \rightarrow x$) and is of the form

$$\mathrm{cdf}^{Gum}(\mu) = 1 - \exp\left\{-\exp(\mu - \langle\mu\rangle\right\}/\beta). \tag{4.2.12}$$

Figure 4.4 gives the cdf data for four $\{\alpha, \mathbf{E}_{ex}\}$ pairs (*blue* points) calculated from the data in **Figure 4.3**. Each cdf is fitted to a Normal distribution using **Equation 4.2.10** and to a 'Gumbel' minimum-extreme distribution using **Equation 4.2.12**, from which fitting parameters be calculated. **Table 4.1** shows these parameters along with the corresponding R^2 value for each. It is interesting to note that at low field, high α pairing, the cdf most resembles the Gumbel, minimum extreme model, evident particularly at high μ. Whereas, at high field and low α, the cdf resembles the Normal distribution (reflected loosely in the R^2 values). As the polarizability increases (for a fixed $\boldsymbol{\mu} = 0.05$ a.u.) the DID effect is larger resulting in a greater disparity between particles with high and low dipole moment. Given that particles of high dipole moment inhabit space in close proximity to other particles of high dipole moment and that conversely some particles do not interact at all (zero-coordinate particles) then it is obvious to see that the distribution is more minimum extreme. In the case

of high field and low α the DID effect is much lower, therefore the particles have similar dipole magnitudes, with similar environments, implying that the distribution of dipoles are more Normally distributed.



(a) $\{\alpha, \mathbf{E}_{ex}\}$=$\{2, 0.25\}$ (a.u.).

(b) $\{\alpha, \mathbf{E}_{ex}\}$=$\{5, 0.1\}$ (a.u.).

(c) $\{\alpha, \mathbf{E}_{ex}\}$=$\{10, 0.05\}$ (a.u.).

(d) $\{\alpha, \mathbf{E}_{ex}\}$=$\{20, 0.025\}$ (a.u.).

Figure 4.4: cdf(μ) as a function of the dipole magnitude for four $\{\alpha, \mathbf{E}_{ex}\}$ pairs. The *blue* points are cdf data for each sample, calculated from **Figure 4.3**. The *green* curve is the analogous cdf fitting for a Gumbel distribution and the *red* curve is the Normal distribution.

Table 4.1: Parameter table for distribution fitting.

$\{\alpha, \mathbf{E}_{ex}\}$ (a.u.)	Gumbel-fit: β and $\langle\mu\rangle$ (a.u.)	Normal-fit: σ and $\langle\mu\rangle$ (a.u.)	Gumbel R^2	Normal R^2
$\{2, 0.25\}$	$\langle\mu\rangle = 0.510$, $\beta = 0.00256$	$\langle\mu\rangle = 0.509$, $\sigma = 0.00303$	0.999232	0.999987
$\{5, 0.1\}$	$\langle\mu\rangle = 0.528$, $\beta = 0.00669$	$\langle\mu\rangle = 0.525$, $\sigma = 0.00791$	0.999391	0.999705
$\{10, 0.05\}$	$\langle\mu\rangle = 0.566$, $\beta = 0.0147$	$\langle\mu\rangle = 0.559$, $\sigma = 0.0173$	0.999657	0.999609
$\{20, 0.025\}$	$\langle\mu\rangle = 0.727$, $\beta = 0.0346$	$\langle\mu\rangle = 0.712$, $\sigma = 0.0406$	0.999556	0.99966

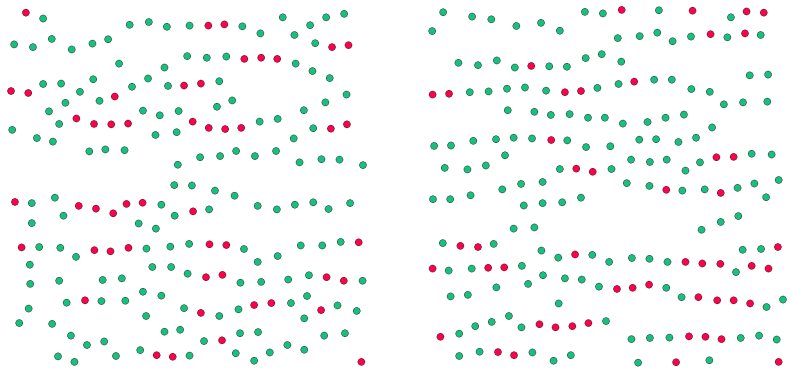
4.3 Structure

The main focus of the next section is to understand how the presence of the DID effect quantifies the degree of ordering in the formation of chain structures, using the molecular graphics 'snapshots' as a visual aid. This qualitative analysis complements the quantitative work in the following sections by providing a simple yet effective method to confirm any conclusions on the behaviour of the structures formed as a result of field induced chain formation.

4.3.1 Molecular Graphics

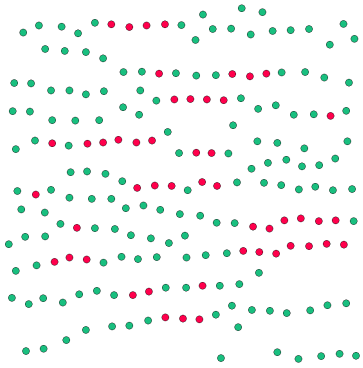
Figure 4.5 shows molecular graphics ('snapshots') of the final configurations of monodisperse runs with varying $\{\alpha, \mathbf{E}_{ex}\}$ pairs ($\{2, 0.25\}$, $\{5, 0.1\}$, $\{10, 0.05\}$, $\{20, 0.025\}$ a.u.). In all cases clear chain-like structures form in which the major component of each dipole lines up with the applied field (along the x-axis). The chain structures arise from the presence of dominant (attractive and highly anisotropic) dipole-dipole interactions and appear (by eye) to be more ordered in the low field (high α) case, reflecting the larger dipoles present as a result of the larger DID interactions. Particles

are divided into A (upper 25% of dipole distribution, *red* colour) and B (lower 75% of dipole distribution, *green* colour) as discussed in **Section 2.8.5**. The snapshots confirm that preferentially,‘ A’ particles form chains adjacent to other ‘A’ particles, especially at the low field (high α) where the DID effect is greatest. The following sections aim to quantify this ordering in more detail than can be obtained by simply viewing the graphics.

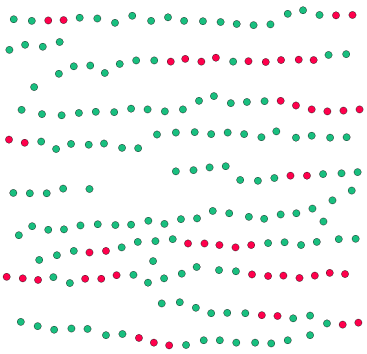


(a) $\{\alpha, \mathbf{E}_{ex}\}$=$\{2, 0.25\}$ (a.u.).

(b) $\{\alpha, \mathbf{E}_{ex}\}$=$\{5, 0.1\}$ (a.u.).



(c) $\{\alpha, \mathbf{E}_{ex}\}$=$\{10, 0.05\}$ (a.u.).



(d) $\{\alpha, \mathbf{E}_{ex}\}$=$\{20, 0.025\}$ (a.u.).

Figure 4.5: Molecular graphic snapshots of the final configuration, after a fixed number of steps, for a variety of $\{\alpha, \mathbf{E}_{ex}\}$ pairs, with fixed $\boldsymbol{\mu} = 0.05$ a.u.. Particles are divided into A (upper 25% of dipole distribution, *red* colour) and B (lower 75% of dipole distribution, *green* colour).

4.3.2 Coordination Environments

Section 2.8.5 first introduces the local coordination parameter ($\Delta p_A(k)$) as a metric to quantify the extent of chain formation. By assigning the upper 25% of the dipole moments, from the distributions in **Figure 4.3**, 'A' (*red* colour in **Figure 4.5**) and the remaining 75% 'B' (*green* colour in **Figure 4.5**) then further ordering that occurs within the chains can be probed. It is important to note that k refers to the number of particles with coordination k surrounding the central particle in question. Such that $\Delta p_A(k) = p_A^{sim}(k) - p_A^{rnd}(k)$ gives the difference between $p_A^{sim}(k)$ (ratio of particles A with coordination numbers, k) and $p_A^{rnd}(k)$ (those expected for a random distribution). For the chain structures $n = 2$, *i.e.* for a central particle coloured A, the options are AAA ($k = 2$), AAB or BAA ($k = 1$) and BAB ($k = 0$) with random probabilities as given in **Table 2.2**. For example, if $p_A^{sim}(2) > p_A^{rnd}(2)$ or $\Delta p_A(2) > 0$ there are more AAA triplets in the configuration than expected purely by random chance. Thus here exists a metric to quantify the extent of chain formation in a given cell. **Figure 4.6** shows $\Delta p_A(k)$ as a function of the external field, $\mathbf{E}_{ex}$ again with fixed $\boldsymbol{\mu} = 0.05$ a.u. about central 'A' particles. It follows that large dipoles are significantly more likely to be found adjacent to other large dipoles, for example, $\Delta p_A(2)$ is positive, corresponding to the presence of AAA units and $\Delta p_A(0)$ is negative, corresponding to a relative reduction of BAB units. This preference becomes more prominent at the low field (high polarizability) end of the scale.

4.3.3 Radial Distribution Functions

Figure 4.7 shows the partial RDFs averaged over 50 configurations for the $\{\alpha, \mathbf{E}_{ex}\}$ pairs, where again $\boldsymbol{\mu} = \alpha \cdot \mathbf{E}_{ex} = 0.5$ a.u.. As described in the metric for the local coordination parameter (**Section 2.8.5**), particles are assigned a label A or B depending on the final dipole magnitude (A being the upper 25% of the distribution).

The field direction is fixed along the x-axis (along vector $\{x, y, z\}$=$\{100\}$). Thus partial RDFs have been calculated considering only 'A' particles (g_A), only 'B' particles (g_B) and both 'A' and 'B' particles (g_{tot}).

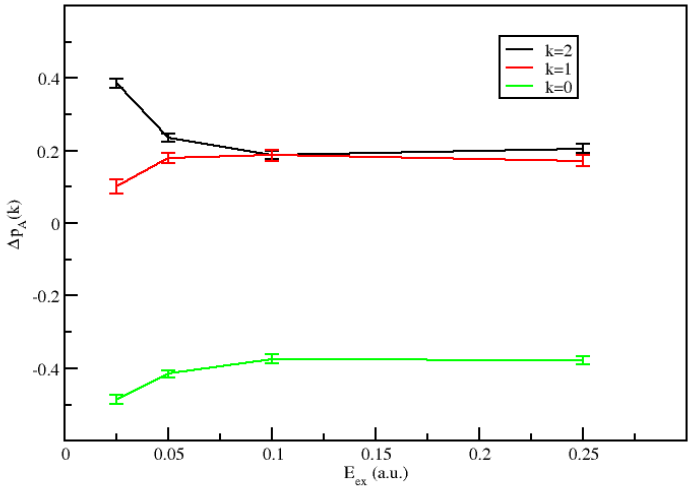


Figure 4.6: Coordination difference functions, $\Delta p_A(k)$, about central particle species A vs. the external field, $\mathbf{E_{ex}}$ at fixed μ. $\Delta p_A(2)$ increases as the external field falls (larger α) corresponding to greater AAA triplet formation as a result of larger DID effects. The error bars are true standard deviations about the sample mean calculated over the set of configurations.

The partial RDF taken parallel to this field vector ($g^{\parallel}$, lower set in **Figure 4.7**) gives regular peaks, separated by the diameter of the particle, denoting the linear alignment of particles in chain-like formation. The regularity of the peaks increases at low $\mathbf{E}_{ex}$ (*black* line). This mirrors the observations in the cell snapshots (**Figure 4.5**) given that the corresponding polarizability is therefore large, the DID effect becomes dominant as the internal field dominates the weaker effects of the external field, the particles are therefore more strongly attracted to one another, able to form longer, more well-defined, chains. For the partial RDF perpendicular to the

field vector along the x-axis ($g^{\perp}$, upper set in **Figure 4.7**) it can also be observed that there is increased inter-chain structure (multiple chains aligned) at the low field and high polarizability pairing, again highlighting the increased network and chain formation at this $\{\alpha, \mathbf{E}_{ex}\}$ set.

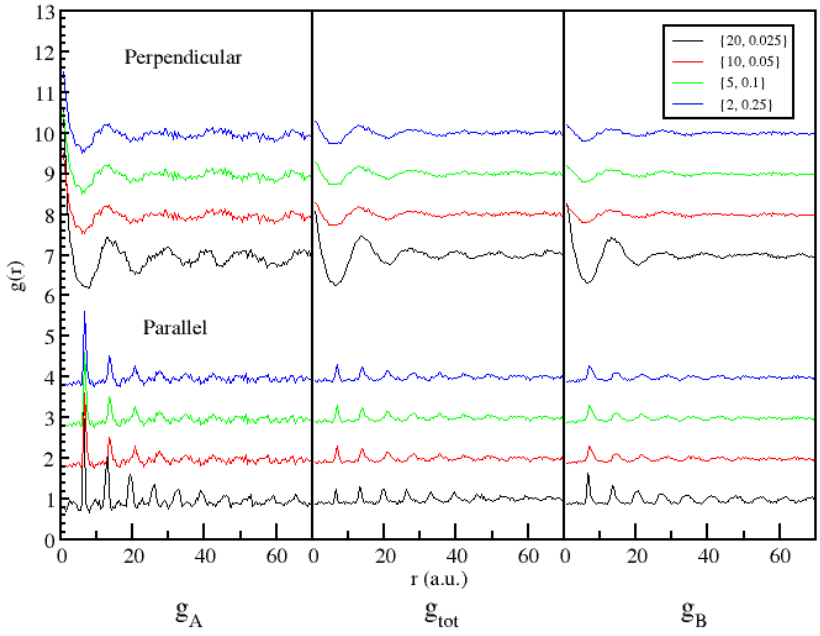


Figure 4.7: $g^{\parallel}$ (lower) and $g^{\perp}$ (upper) for A-A pairs, B-B pairs and total (all particle pairs) over a range of $\{\alpha, \mathbf{E}_{ex}\}$ sets as shown in the legend (in a.u.). RDFs are shifted along the y-axis for illustration purposes.

It is interesting to note that $g_A^{\parallel}$ (A-A pairs only, where 'A' particles have a greater dipole) is much more pronounced with a larger magnitude at low r. This confirms the understanding that upon chain formation, 'A' particles are surrounded by other 'A' particles preferentially. $g_B^{\parallel}$ (B-B pairs only) and $g_{tot}^{\parallel}$ (A-A, B-B and A-B pairs) are almost identical as are $g_B^{\perp}$ and $g_{tot}^{\perp}$. If 'A' particles are more likely to be surrounded by other 'A' particles then it follows that 'B' particles are more likely to be in close

proximity to other 'B' particles, in addition to the fact that B-B pairs are statistically likely given the composition ratio of A:B is 25:75. g_{tot} is similar for each $\{\alpha, \mathbf{E}_{ex}\}$ pair to reflect this.

4.3.4 Chain Alignment

The dot product, $\mathbf{r}^{ij} \cdot \mathbf{E}_{ex}$, where $\mathbf{r}^{ij}$ is the vector joining the positions of i and j particles, is a metric to highlight the extent of particle pair alignment with the field direction (x-axis).

$$\mathbf{r}^{ij} \cdot \mathbf{E}_{ex} = |\mathbf{r}^{ij}||\mathbf{E}_{ex}| \cos\theta \tag{4.3.1}$$

where θ is the angle between the x-axis ($\mathbf{E}_{ex}$) about particle i relative to particle j. Thus θ tends to zero or π for a system with idealized chain formation. As is shown in **Figure 4.8**, confirming the results in the sections above, for low $\mathbf{E}_{ex}$ (high α) the dot product $\mathbf{r}^{ij} \cdot \mathbf{E}_{ex}$ (averaged over all pairs and normalised by $|\mathbf{r}^{ij}||\mathbf{E}_{ex}|$) tends to give higher values compared with the high $\mathbf{E}_{ex}$ (low α) set. Again this is a function of the relative DID effect with the larger polarizability particles able to interact more strongly with the internal field contribution allowing for reduced θ and well aligned chains. $\mathbf{r}^{ij} \cdot \mathbf{E}_{ex}$ calculated for A-A pairs only is much larger than observed for B-B pairs only, highlighting the preferential formation of chains comprised of A particles in the configurations, as a result of the larger dipole-induced-dipole effect leading to enhanced alignment with the external field. The *black* and *green* curves are the calculations for all pairs of particles (labelled tot) and for only A-B pairs respectively. As such they are similar in magnitude.

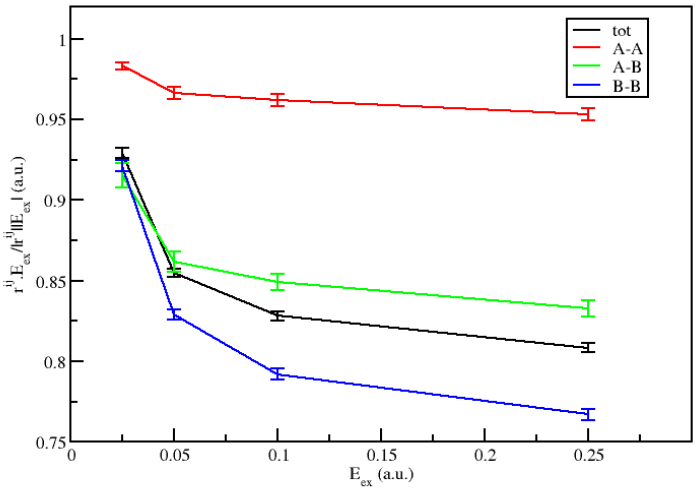


Figure 4.8: The normalised dot product metric $\mathbf{r}^{ij} \cdot \mathbf{E}_{ex}$ (averaged over pairs: A-A, A-B or B-B), or all pairs (tot) as a function of $\mathbf{E}_{ex}$ with fixed $\boldsymbol{\mu}_{ex} = \alpha \cdot \mathbf{E}_{ex} = 0.05$ a.u.. The error bars are true standard deviations about the sample mean calculated over the set of configurations.

4.4 Density Variation

Simulations were conducted over a range of densities with a fixed number of particles ($N = 200$), a fixed $\{\alpha = 10 \text{ a.u.}, \mathbf{E}_{ex} = 0.05 \text{ a.u.}\}$ pairing, using the same methodology discussed previously, for 50 isotropic configurations. The increase in density in the simulation is achieved by contracting the cell dimensions maintaining the regular square shape of the cell. The ensemble average is taken, with true standard deviation error bars about the sample mean as shown, depicting the variation in the configurations. **Figure 4.9** shows the increase in mean average dipole, $\langle \mu \rangle$ as the density of the cell increases, for the final configuration. At low density ($\rho^* \sim 0 \rightarrow 0.3$) the particles are initially very sparse and aggregation is less favourable, therefore giving a wider variation in particle network configurations (as quantified by the larger standard deviation) with a lower $\langle \mu \rangle$ indicating fewer chain

structures. At high density ($\rho^* \sim 0.6 \rightarrow 0.8$) the particles are initially more confined and aggregate more favourably over the given time-scale, forming pseudo-close-packed structures. The dipole-induced-dipole effect is thus larger and the variation in configurations becomes smaller. This is mirrored in the coordination number distributions (and mean coordination number) shown in **Figure 4.10**. As the density is increased the mean coordination number of the final configuration migrates from $\langle n \rangle = 2$ to $\langle n \rangle = 6$. In confinement, a pseudo-close-packed 6-coordinate structure is preferred. For subsequent calculations, the density is set at $\rho^* = 0.4$, which lies within the range of 2-coordinate chain structure formation, whilst allowing for relatively rapid chain formation on the simulation time-scale. **Figure 4.11** shows molecular graphics 'snapshots' for a series of monodisperse runs with a square cell and r^{-12} potential at varying reduced density ($\rho^* = 0.2,\ 0.4,\ 0.6,\ 0.8$). The direction of the applied field is along the x-axis and each set of images describes the progression of time, from left to right in $\sim 0ns$, $0.00756ns$, $0.0151ns$, $0.0303ns$, $0.0605ns$, $0.121ns$ steps. $\{\alpha, \mathbf{E}_{ex}\} = \{10, 0.05\}$ and all other variables are fixed. These runs illustrate the trends as discussed above in **Figures 4.9** and **4.10** where increasing ρ^* gives an increased $\langle n \rangle$ and $\langle \mu \rangle$ leading to close packing despite lack of attractive interaction in the pair potential. At low ρ^* close packing is less favourable and single stranded chain aggregation occurs. **Figure 4.12** gives the difference functions, $\Delta p_A(k)$ (upper) and $\Delta p_B(k)$ (lower) respectively for the same final configuration structures, over an identical range of densities, as above. At low density, $\Delta p_A(2) > \Delta p_A(1) > \Delta p_A(0)$, where $\Delta p_A(0)$ is in fact less than zero. For $k = 2$ the difference function is largest given that again as stated in previous sections, 'A' particles preferentially form into chains with other 'A' particles. For $k = 0$ the difference function is negative which implies that BAB particle triplets are less likely to form. This confirms the chain forming behaviour of the simulation fluid on application of an external field.

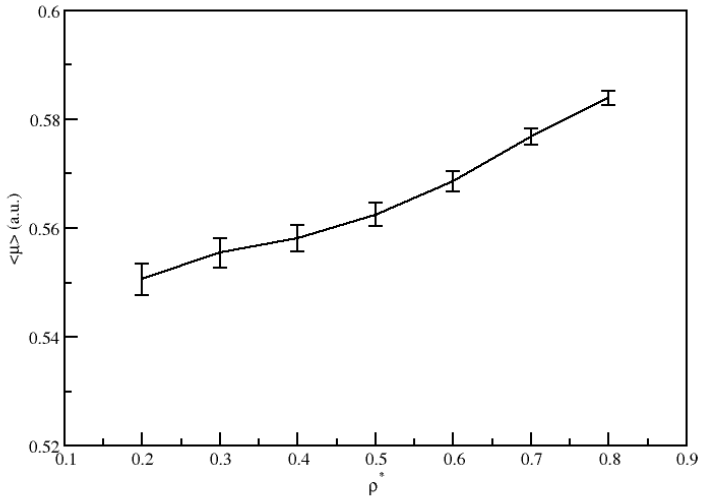


Figure 4.9: $\langle\mu\rangle$ as a function of ρ^*, for a fixed number of MD steps. $\langle\mu\rangle$ increases as ρ^* increases over the range. The error bars are true standard deviations about the sample mean.

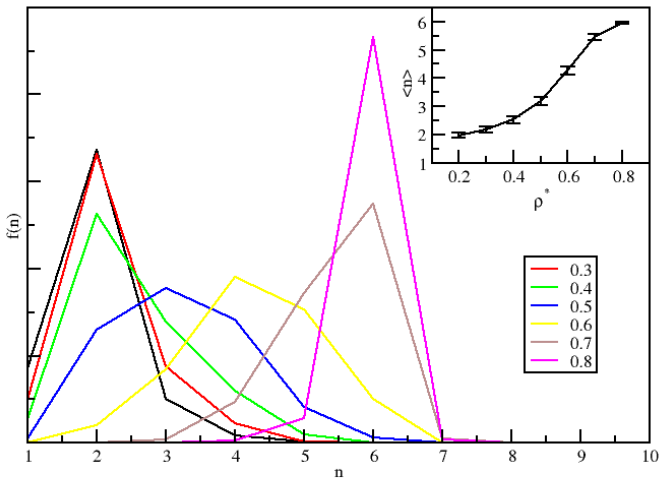
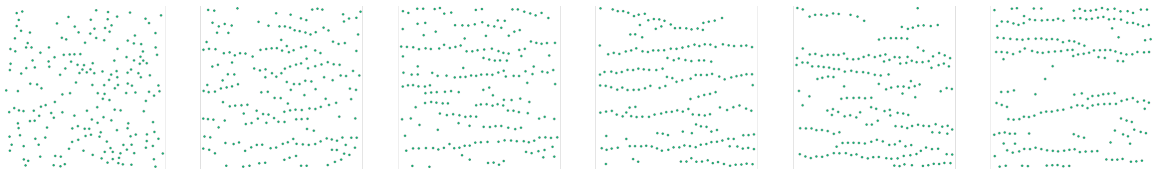
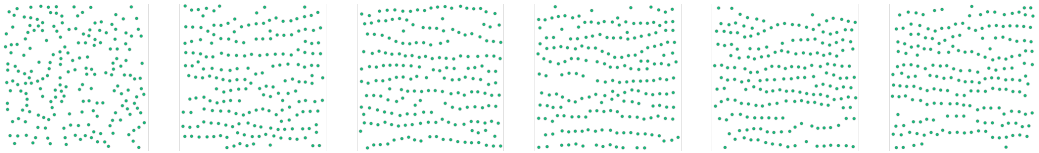


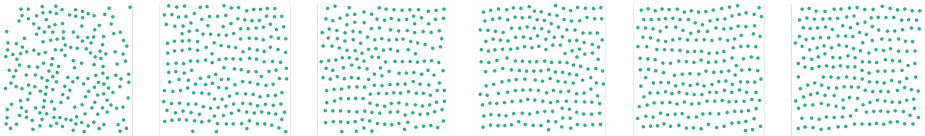
Figure 4.10: The main window depicts the coordination number distribution variation as a function of ρ^* (values are given in the legend) after a fixed number of MD steps. $\boldsymbol{\mu}_{ex} = 0.5$ a.u., $\alpha = 10$ a.u. and $\mathbf{E}_{ex} = 0.05$ a.u.. y-axis scaling labels are removed for clarity. The inset shows the mean average coordination number $\langle n\rangle$ over the same reduced density range. The error bars are true standard deviations about the sample mean.



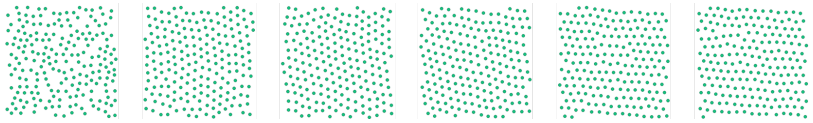
(a) Monodisperse run, square cell, r^{-12} potential, $\rho^* = 0.2$.



(b) Monodisperse run, square cell, r^{-12} potential, $\rho^* = 0.4$.



(c) Monodisperse run, square cell, r^{-12} potential, $\rho^* = 0.6$.



(d) Monodisperse run, square cell, r^{-12} potential, $\rho^* = 0.8$.

Figure 4.11: Molecular graphics 'snapshots' of cell runs at a different reduced density. The direction of the applied field is along the x-axis and each set of images describes the progression of time, from left to right in $\sim 0ns$, $0.00756ns$, $0.0151ns$, $0.0303ns$, $0.0605ns$, $0.121ns$ steps. $\{\alpha, \mathbf{E}_{ex}\}$= $\{10, 0.05\}$ and all other variables are fixed.

Conversely the behaviour of $\Delta p_B(k)$ mirrors the above argument, therefore $\Delta p_B(0) > \Delta p_B(1) > \Delta p_B(2)$ such that BBB formation is indeed more likely than ABA formation. As density increases the initial coordinates are essentially frozen and there is a shift to a pseudo-close packed configuration, as confirmed in **Figure 4.10** and the snapshots in **Figure 4.11**. Therefore the difference functions all tend to zero.

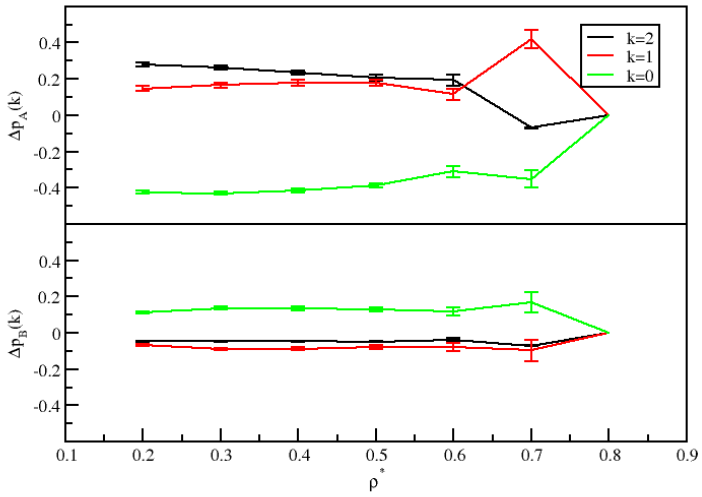


Figure 4.12: $\Delta p(k)$ difference functions vs. reduced density about central particle A (upper) and central particle B (lower). The error bars are true standard deviations about the sample mean.

Similarly **Figure 4.13(c)** shows the order parameter, ψ_n for $n = 4, 6$ (as mentioned in **Section 2.8.6**) which decreases and increases respectively, as the density increases. This further confirms the switch from two-coordinate species to 6 coordinate pseudo-closed packed arrangements. The distributions of order parameters over the 50 configurations are displayed in **Figures 4.13(a)** and **4.13(b)**.

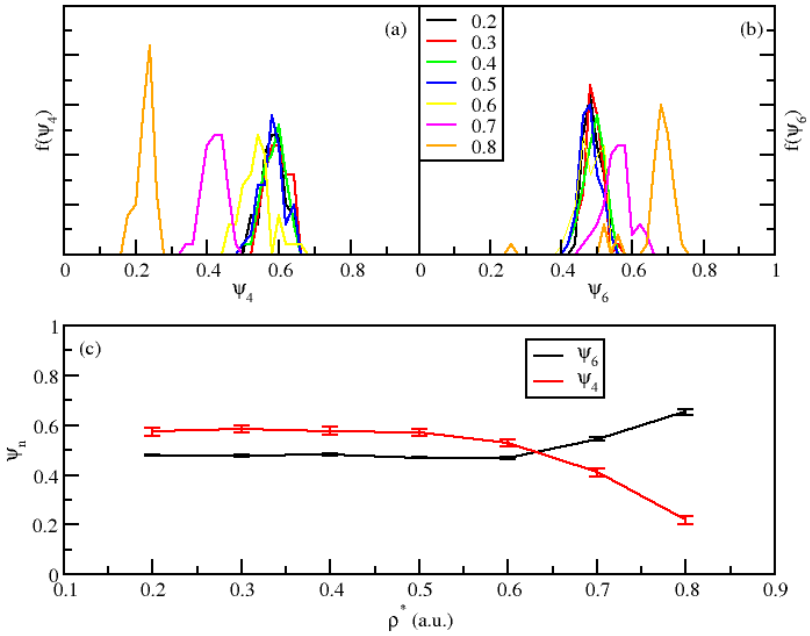


Figure 4.13: **(a)** and **(b)** show the distribution of order parameters ψ_n for $n = 4, 6$ as a function of reduced density (value in the legend). y-axis scaling labels are removed for clarity. **(c)** gives the mean average of these distributions ψ_4 and ψ_6 as a function of density. The error bars are true standard deviations about the sample mean.

At low density ($\rho^* = 0.2 \rightarrow 0.6$) both ψ_n sets of distributions lie on top of each other and for ψ_6 the mean (**4.13(c)**) is ~ 0.5, highlighting that the configurations are not pseudo-close packed (the value of ideal close packing would be $\psi_6 = 1$). As density is increased from $\rho^* = 0.6 \rightarrow 0.8$, ψ_4 decreases highlighting the lack of chain structures and similarly ψ_6 increases tending towards one for an ideal close-packed configuration. Finally, the RDF, g_{tot} of the final configurations at varying densities (**Figure 4.14**) shows increased ordering at high density, the peaks of which denote particle separations in a.u.. In conclusion therefore, the reduced density shall be fixed at $\rho^* = 0.4$, which is a mid-range value such that a close packed structure is not observed and particle chaining can occur.

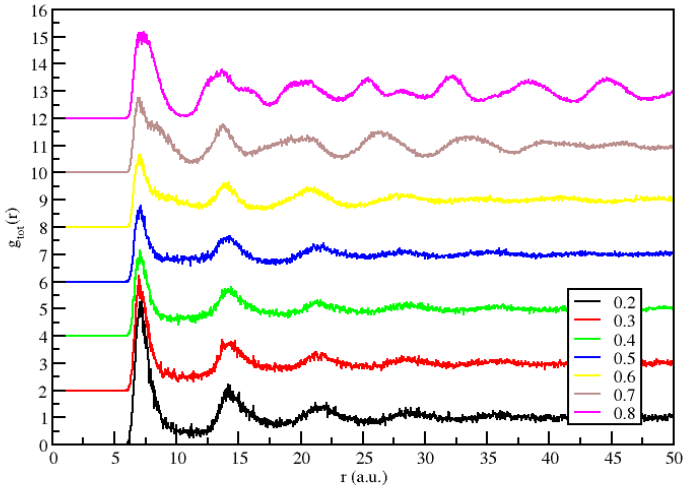


Figure 4.14: g_{tot} as a function of reduced density, ρ^* the values of which are given in the legend. RDFs are shifted along the y-axis for illustration purposes.

4.4.1 Cell Elongation

Properties of chain formation are now investigated as the aspect ratio of the cell is increased for a given density. The size of the cell is increased from high density ($\rho^* = 0.8$) to low density ($\rho^* = 0.2$) by elongating the cell in the x-direction (L_x) and fixing L_y. Therefore the aspect ratio (L_x/L_y) is increased as the density is decreased. The aspect ratios for each density are given in **Table 4.2** and **Figure 4.15** gives a schematic for this elongation method. The aim of this section is to find out whether the chain formation process is affected, not only by the density of the cell (as shown in **Section 4.4**) but by the aspect ratio of the cell over a given range of densities, irrespective of periodic boundary conditions. However, as highlighted in **Figures 4.16(a)** and **4.16(b)**, elongation of the box does not significantly affect the chain formation properties for this range of particle densities and number of particles. **Figure 4.16(a)** shows the mean average dipole for the final structures over a fixed number of runs with $\{\alpha, \mathbf{E}_{ex}\}= \{10, 0.05\}$ a.u. and pair potential r^{-12}-type fixed.

The curves are almost identical, well within acceptable standard deviation error.

Table 4.2: A table giving the aspect ratio of the cell as a function of density for the elongated cell runs.

ρ^*	L_x (a.u.)	L_y (a.u.)	L_x/L_y
0.8	103.508	100.000	1.035
0.7	118.294	100.000	1.183
0.6	138.010	100.000	1.380
0.5	165.612	100.000	1.656
0.4	207.015	100.000	2.070
0.3	276.020	100.000	2.760
0.2	414.030	100.000	4.140

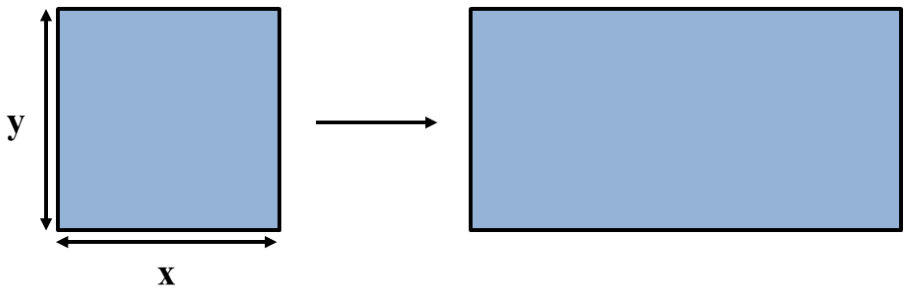
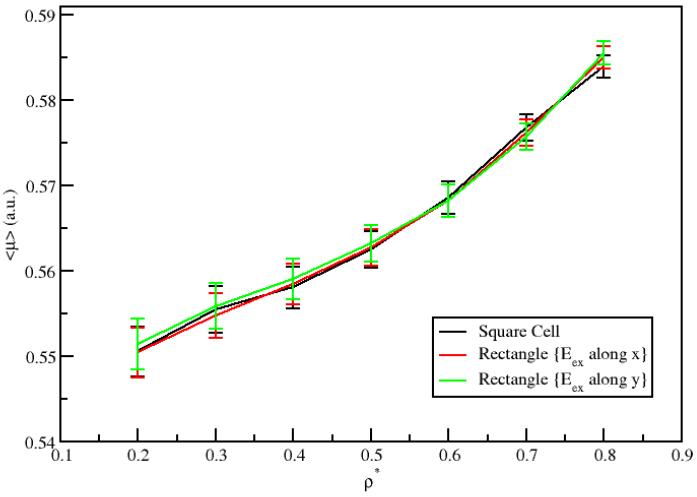


Figure 4.15: The method of cell elongation where L_x is increased and L_y is fixed.

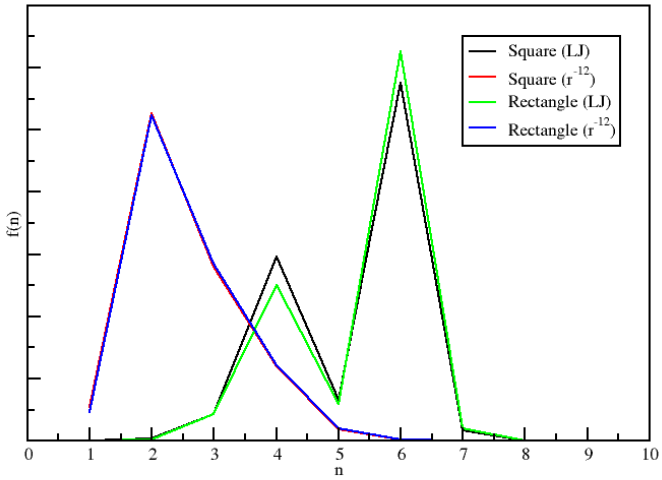
The *black* curve is identical to **Figure 4.9** and included for comparison. The *red* and *green* curves are the analogous curves for the elongated cells at each density, with the applied field along the x- and y-axes (or long and short side of the rectangular cell) respectively. This is to highlight the lack of change in chain structures when varying the aspect ratio of the cell. **Figure 4.16(b)** shows the coordination number distributions for a fixed density case $\rho^* = 0.4$ (aspect ratio is 2.07), for the square-cell and elongated cells using different pair-potential models, labelled 'r^{-12}' and LJ

(Lennard-Jones) for final configuration structures, examples of which are provided in **Figure 4.17**. Coordination number distributions are the same for both cell types in the 'r^{-12}' case and similar in the LJ case, where the lengthening of one cell direction with simultaneous contraction of the other allows for slightly more six-coordinate particles to exist. Throughout the remainder of the thesis, only the 'r^{-12}' potential model is considered given that the LJ case with the additional attractive dispersion forces does not form single particle width chains as is the main focus of this work.

Figure 4.17 shows the molecular graphics 'snapshots' of four simulations over time (from left to right) with the applied field direction along the x-axis for two cell-shapes and two inter-particle pair-potentials. $\rho^* = 0.4$ (for the rectangular cells the aspect ratio is 2.07) and all other variables are fixed including starting configuration for each cell type. As can be observed, there is little difference in the single stranded chain structures formed in **(a)** and **(c)** with the former a square cell and the latter a rectangular cell; the presence of longer chains in the latter type due to larger cell-dimensions is the only discernible difference. **(a)** and **(b)** along with **(c)** and **(d)** are comparative runs with different pair-potentials. It is also evident as discussed above that by introducing a dispersive attractive force in the Lennard-Jones potential then the particles aggregate to higher coordination number forming multi-stranded chains initially and then pseudo-close packed structures. **Figure 4.18** shows the final configurations of the elongated, rectangular cell using the 'r^{-12}' pair-potential model, at an applied field ($\mathbf{E}_{ex}$) along **(a)** the x-axis (greater cell dimension) and **(b)** the y-axis (shorter cell dimension). As can be empirically observed chain formation is similar in each case. Those particles with the largest 25% of dipole magnitudes are shown *red*, all others are *green*. This confirms that particles with the greatest $\boldsymbol{\mu}$ (resulting from DID enhancement) inhabit the central positions of chains (not the termini) where the DID effect is largest.

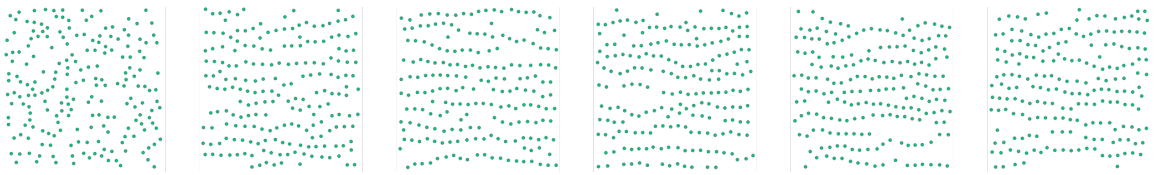


(a) $\langle\mu\rangle$ vs. ρ^* varying cell shape and applied field direction. The pair-potential is fixed as 'r^{-12}'.

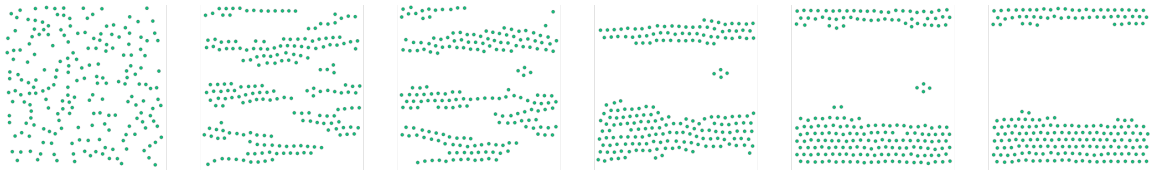


(b) Coordination number distributions at a fixed $\rho^* = 0.4$ (aspect ratio is 2.07), varying cell shape and pair-potential. y-axis scaling labels are removed for clarity.

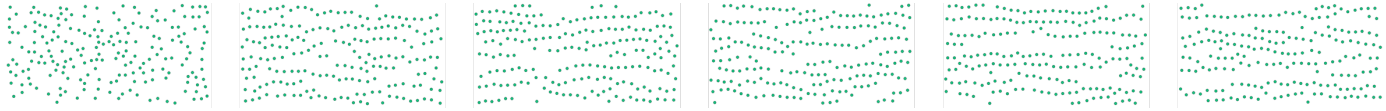
Figure 4.16: A set of graphs to highlight the similarity of the network formation properties when varying the cell shape, direction of the applied field and pair-potential. $\{\alpha, \mathbf{E}_{ex}\}= \{10, 0.05\}$ a.u. for each run. The error bars shown in **(a)** are true standard deviations about the sample mean.



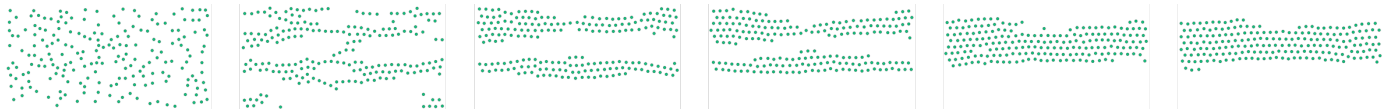
(a) Monodisperse run, square cell, r^{-12} potential



(b) Monodisperse run, square cell, Lennard-Jones potential

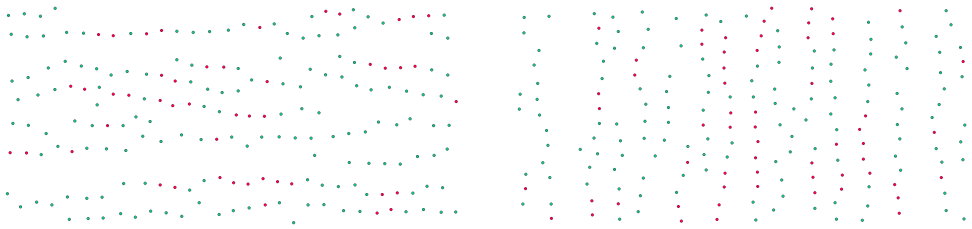


(c) Monodisperse run, rectangular cell, r^{-12} potential



(d) Monodisperse run, rectangular cell, Lennard-Jones potential

Figure 4.17: Molecular graphics 'snapshots' of cell runs at a fixed reduced density, $\rho^* = 0.4$ (for the rectangular cells the aspect ratio is 2.07) and $\{\alpha, \mathbf{E}_{ex}\} = \{10, 0.05\}$ a.u.. The direction of the applied field is along the x-axis and each set of images describes the progression of time, from left to right in $\sim 0ns$, $0.00756ns$, $0.0151ns$, $0.0303ns$, $0.0605ns$, $0.121ns$ steps. Two cell sizes are investigated along with two different pair-potential models.



(a) Field direction along the x-axis. (b) Field direction along the y-axis.

Figure 4.18: Final configurations of monodisperse runs with a rectangular cell, 'r^{-12}' potential and different field directions, **(a)** x-axis, **(b)** y-axis. Particles are divided into A (upper 25% of dipole distribution, *red* colour) and B (lower 75% of dipole distribution, *green* colour).

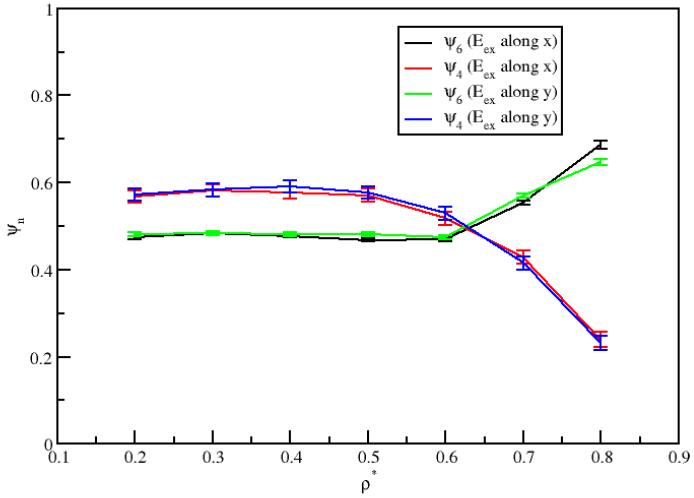


Figure 4.19: Order parameters, ψ_n for $n = 4, 6$ about x- and y-axes in an elongated cell, as a function of ρ^*. ψ_n is calculated along the direction of the applied field $\mathbf{E}_{ex}$. The error bars shown are true standard deviations about the sample mean.

Figure 4.19 shows the order parameters and quantitatively backs up the molecular graphics snapshots in **Figure 4.18**. By looking at the order parameters (ψ_n) for each n, there is minimal difference in each case when comparing the calculation

along the E_x^{ex} or E_y^{ex} field direction, well within acceptable error. In conclusion there is no change in the statistics to describe the chain formation process over a given time period, therefore the use of a square cell can be exclusively justified.

4.4.2 System Size Variation

The final question as to the validity of the simulation is whether or not the system size affects chain formation for an electro/magneto-rheological fluid. Simulations were conducted at the same reduced density ($\rho^* = 0.4$), for 1000 particles in each simulation cell.

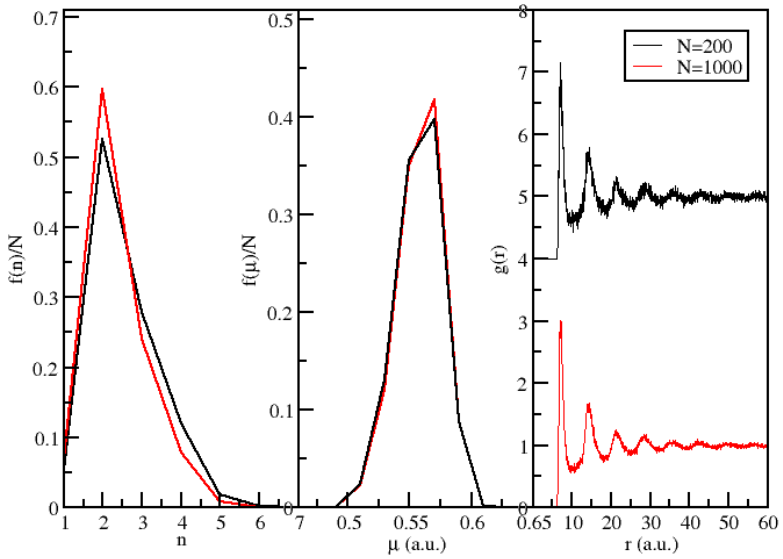


Figure 4.20: Left window: Scaled coordination number distributions. Central window: Scaled dipole distributions. Right window: RDF. The *black* curve denotes $N = 200$ particles and the *red* curve $N = 1000$. RDFs are shifted along the y-axis for illustration purposes.

Figure 4.20 provides the coordination number distributions, dipole distributions and RDFs for different system sizes ($N = 200$ and $N = 1000$), as a comparison. The coordination number and dipole distribution frequencies are scaled as a function of $N = 200$ or $N = 1000$ depending on the simulation run. For the $N = 1000$ simulation there are marginally more two-coordinate species than in the $N = 200$ case, with fewer higher-coordinate particles, though given that the dipole distributions for the $N = 200$ and $N = 1000$ cases are almost identical it is evident that this is a function of the natural fluctuation in starting configurations. The RDFs (right window of **Figure 4.20**) show identical peak positions in both cases.

4.5 Chapter Summary

Overall, the system appears to 'self assemble' as a function of the distribution of the low and high dipole moments. The effect is more pronounced at high α (low $\mathbf{E}_{ex}$) compared to the low α (high $\mathbf{E}_{ex}$) case, a direct result of the strength of the DID term (larger $\boldsymbol{\mu}^{(i)}$ term in **Equation 4.2.1**, due to the large internal field contribution $\boldsymbol{\mu}^{i}_{int} = \alpha^{i}\mathbf{E}^{i}_{int}$). Various nuances of this monodisperse set of particles are discussed in detail and it is shown that the nature of the coordination environment can act as a quantitative measure for the extent of chain formation, a factor which is explored in the following chapter. Furthermore, the pair-potential selection ('r^{-12}'), cell-shape (2D, square) and particle number ($N = 200$) are justified along with cell density ($\rho^* = 0.4$), which falls within the range of single-stranded chain formation, rather than more network-forming, high coordination chains. Finally this model, though simple, expresses the chain-formation properties of the fluid with ease and low computational expense. As such, an extension of this model can be made in which the particles are bidisperse with respect to their polarizability and this is explored in **Chapter 6**.

Chapter 5

Using Experiment to Direct Simulation

Much of the motivation for the simulation work exhibited in this thesis originated from parallel experimental investigations [161] that focused on the extent of chain formation on application of an external magnetic field to a colloidal suspension of superparamagnetic spheres suspended in water (see experimental details in the section below). Hess and Parker, Jr. [162] first reported steric stabilization of ferromagnetic cobalt colloids using polymers and noted the chain formation in the absence of a magnetic field. This prompted the investigation into magnetic colloids by Skjeltorp in 1985 and Helgesen *et al.* in 1988 [8, 23]. In addition, De Gennes' theoretical work on the magnetic properties of simple spherical ferromagnetic grains at thermal equilibrium in a passive carrier fluid initiated simulation and computation studies into a range of ferrmomagnetic fluids [46]. The key difference between ferromagetic and superparamagnetic fluids is that (as discussed in the introduction) the former displays permanent magnetic moments (*e.g.* in [8, 23, 46]) whereas the superparamagnetic particles may carry induced magnetic moments [24]. Skjeltorp was a key contributor to the development of studies into chain formation of super-

paramagnetic/ferromagnetic particles in a magnetic field, specifically with magneto-rheological fluids containing particles on the micrometre length scale. Investigations ranged from a ferromagnetic carrier fluid with non-magnetic polystyrene spheres (acting as effective holes) [8] to ferromagnetic spheres, suspended in a non-magnetic solvent (along with Helgesen *et al.* [23]) which crucially can be observed in real time under a microscope. The latter is the system of interest in the experimental work coupled to this thesis.

There are a number of more directly relevant recent experiments using magneto-rheological fluids as generated in a similar manner to Skjeltorp, at low particle density, which produce similar chain-like structures to the monodisperse simulation examples shown in **Chapter 4**. Chain formation results from the application of an external magnetic field to a suspension of micrometre scale, monodisperse superparamagnetic particle spheres [11, 163, 164]. The motivation for the work exhibited in this thesis originated from these experimental papers, the aim being to select a useful yet uncomplicated theoretical model in order to describe the directional nature of the self-assembly process of this simple material under a variety of complex conditions.

5.1 Experimental Background

The experimental suspensions are prepared by Reynolds [161] using a purchased bulk solution of superparamagnetic polystyrene spheres with a diameter of 2.8μm and mass density of $\rho_{bead} = 1.6\text{g cm}^{-3}$ (carboxylic acid functionalised Dynabeads®, M-270, Invitrogen, Life Technologies) which are diluted further with distilled water (at room temperature, $\rho_{water} = 0.997\text{g cm}^{-3}$) as required. This stock solution has $\sim 2 \times 10^9$ beads/ml. The experimental solution prepared for the comparative work in this thesis is 7.5ml of the Dynabeads® stock solution in 1000ml of pure water, therefore the experimental solution has $\sim 1.5 \times 10^7$ beads/ml. The carboxylic acid

functional groups stabilises the colloidal particles, providing a net negative charge on each particle and hence an electric double layer which prevents particle aggregation in the absence of a field (as discussed in the introduction). These solutions are dilute to exhibit the behaviour of systems with low packing fractions (equivalent to a reduced density, $\rho^* < 0.05$). A pseudo-two-dimensional system is created as the particles are gravitationally confined to a monolayer at the bottom of a quartz glass sample cell ($A = 9 \times 20$mm and depth = 200μm, Hellma Analytics), a product of the high mass density of the particles. The gravitational height is calculated at 0.06μm. After settling, the solution equilibrates after a few minutes with particle Brownian relaxation times approximately $50s$.

Two 470 turn solenoids, placed symmetrically at either side of the sample, generate a locally uniform external magnetic field (at fixed voltage= $5V$) whose strength, B, equals 3.14mT (measured using a Gaussmeter - Hirst Magnetic Instruments Ltd. GM07 Gaussmeter, PT002 Hall Probe) [161]. The power supply is controlled by LabJack U3-LV and has sub-milisecond response times allowing easy field modulation and control. When applying the external magnetic field, a magnetic moment is therefore induced in the superparamagnetic particles which may result in particle aggregation (unidirectional chain formation) with the chains increasing in length over time [164]. The aforementioned conditions are well within the range of reversible magnetisation. Potentially more complex network formation (as observed in [11]) is effectively suppressed at low density. The aggregation process is captured using optical video-microscopy which have a resolution of 2048×2048px and at $40\times$ magnification where 1px = 0.5555μm (details of microscope and camera used are outlined in Reynolds [161]). **Figures 5.1** show examples of chain formation under the above conditions (using the experimental coordinates and visualised using XBS image software) at a density of $\rho^* \sim 0.0227$. For each camera viewing window (1038×1038px)

there are $\sim$ 4000 beads in that area corresponding to the densities observed. For completeness the packing fraction is $\phi = \frac{\pi}{4}\rho^* = 0.0178$. Image analysis techniques allow the time-resolved experimental coordinates to be captured.

5.2 Experiment $\rightarrow$ Simulation

The availability of direct sets of experimental coordinates is relatively unusual. Spatial relationships between particles are more commonly extracted from diffraction experiments. However, experiments of this sort are perhaps best suited to the study of systems in equilibrium which benefit from the high level of information averaging over both time and space (although rapid data acquisition techniques are being developed).

The ability to extract the particle coordinates directly from experiment, therefore, affords a unique opportunity. In 'traditional' MD simulation (*e.g.* most of the simulations described in this thesis) the particle coordinates are generated purely computationally. Here the experimental coordinates themselves may be used as a direct input, in two different ways. In the first (procedure I), the initial ($t = 0$, isotropic - **Figure 5.1(a)**) particle positions are used as a starting configuration to initiate a 'normal' MD relaxation. In the second (procedure II), the experimental coordinates are extracted at each experimental timestep and the total energy of that configuration is determined (as described in detail below) without any further relaxation. In both cases, using the experimental coordinates presents certain challenges. Firstly, the systems are aperiodic. Secondly, and more significantly here, the configuration may contain 'close' particle pairs, that is, pairs of particles separated by less than an approximate diameter. The origin of these pairs lies either in problems with the image analysis (*i.e.* how the system selects the particle coordinates) or in the system not acting in a truly two-dimensional manner, meaning that particles which overlap

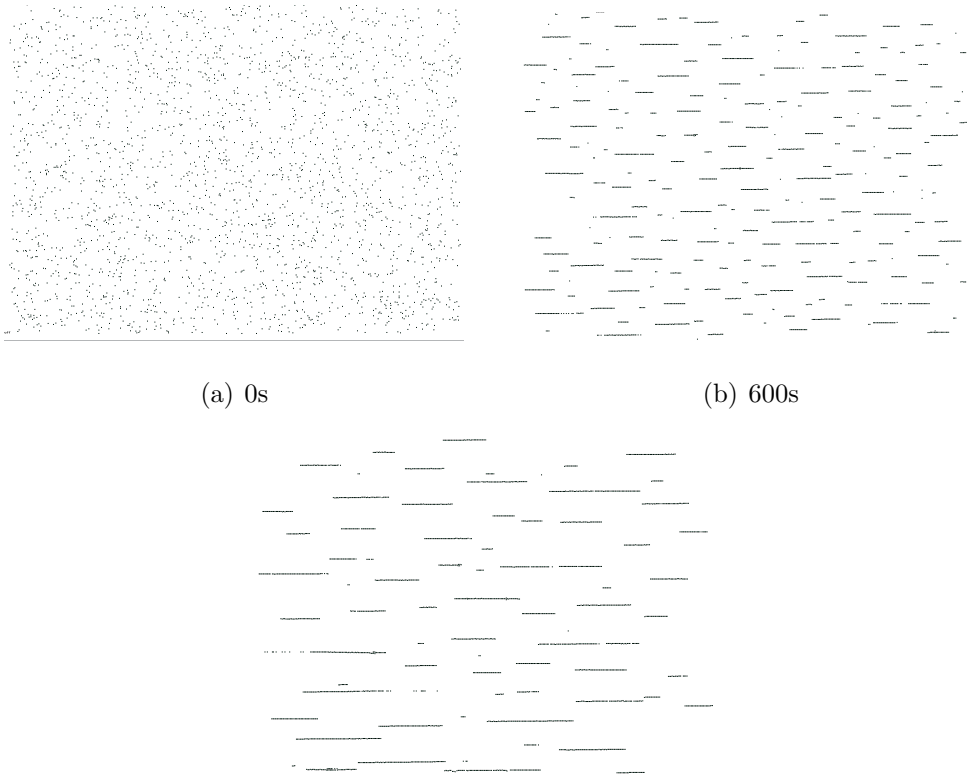
with each other out of the confining plane appear closer than when assumed to sit in a plane. Using the directly obtained experimental coordinates therefore, allows these 'close' pairs to be extracted and accounted for. The choice of the model, based on a pairwise repulsive interaction and induced dipoles (as discussed in **Chapters 3** and **4**) is therefore clearly physically motivated. If significant interactions had been omitted, or inappropriately parametrised, then the energetics would not evolve in analogous fashion to the 'normal' MD simulations (*e.g.* the results from procedures I and II would look different).

The process of coordinate system conversion is as follows.

- The experimental coordinates are based on superparamagnetic particles of diameter $\sigma_{\text{ex}} = 2.8\mu$m. However, since we expect the interactions to scale with length we can use the experimental coordinates scaled onto simulation coordinates. Relative experimental (x, y) coordinates are taken and converted from pixels to a.u. by using the conversion factor $(x, y) \cdot \dfrac{\sigma_{sim}}{\sigma_{\text{ex}}}$, thereby scaling the experiment to the same coordinate system used in the simulations.

- The coordinates are then placed in a large cell, relative to the coordinate window, in order to isolate the cluster after which point energy calculations can be performed on the system.

- It is important to note that N, the number of species in each cell frame, is not fixed given the viewing window only captures a fixed area and the boundaries are naturally aperiodic. For a more accurate calculation of the point energy, a plane could be tiled with many sets of experimental particle coordinate windows, however the particle count is sufficiently large in a single window that the boundary conditions will not affect the mean shape of the curve, which is the principal interest.



(a) 0s

(b) 600s

(c) 2500s

Figure 5.1: Experimental particle coordinates over a 2500s run depicting the chain forming process at low density and high field strength. Each frame contains the extracted and scaled coordinates taken from the image analysis of the real particle positions.

For procedure I, the reduced density is $\rho^* = 0.0227$, where starting configurations are generated by taking a 200 particle sample from the experimental starting configuration, at the same density. Again as in the monodisperse simulation runs, 50 independent isotropic configurations are generated by increasing the temperature to $10000K$ to sufficiently randomise the particles before quenching and running for 1×10^6 steps. This is to produce a further 49/50 coordinate sets for a bulk average to be taken. The first set is of course directly taken from the experimental coordi-

nates and evolves much in the same manner as the randomised sets. To accelerate the aggregation process the field strength is set at $\mathbf{E}_{ex} = 0.1$ a.u.. For procedure II it is important to note that the field strength is set at $\mathbf{E}_{ex} = 0.05$ a.u. which only influences the energy and dipole calculations not the positions of the particles given they are fixed at each timestep according to the image analysis. The following section aims to expand on the energetic evolution of each run, using the experimental coordinates as discussed above.

5.3 Energetics

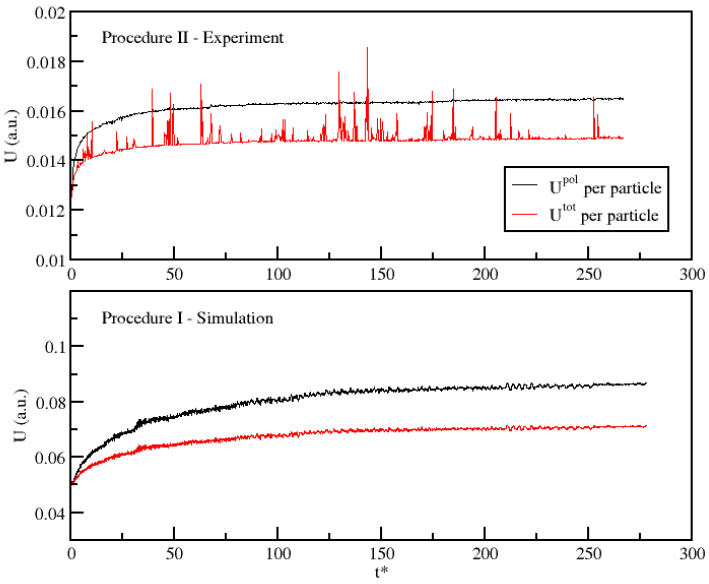
Figure 5.2 shows the energy (given per particle) progression (U^{tot}, U^{pol} in **Figure 5.2(a)** and $U^{all} = U^{tot} - \boldsymbol{\mu} \cdot \mathbf{E}_{ex}$ in **Figure 5.2(b)**) as a function of time for the first procedure (lower windows, using only the starting configuration from scaled experimental coordinates) and second procedure (upper windows, energies determined at each timestep without further relaxation) as described in the section above. U^{all} is the entire potential energy of the system calculated as the sum of the short-range potential, the dipole-dipole interaction term, the energy required to polarize the particles (U^{pol}) and the energy of interaction with an applied field ($-\boldsymbol{\mu} \cdot \mathbf{E}_{ex}$).

$$U^{all} = U^{sr} + \underbrace{\sum_{i,j=1}^{N} \frac{\boldsymbol{\mu}^i \boldsymbol{\mu}^j}{(\mathbf{r}^{ij})^3} \cos\phi \left(1 - 3\cos^2\theta^{ij}\right)}_{U^{dd}} + \underbrace{\frac{1}{2\alpha} \sum_{i=1}^{N} (\boldsymbol{\mu}^i)^2}_{U^{pol}} - \sum_{i=1}^{N} \boldsymbol{\mu}^i \cdot \mathbf{E}_{ex}. \quad (5.3.1)$$

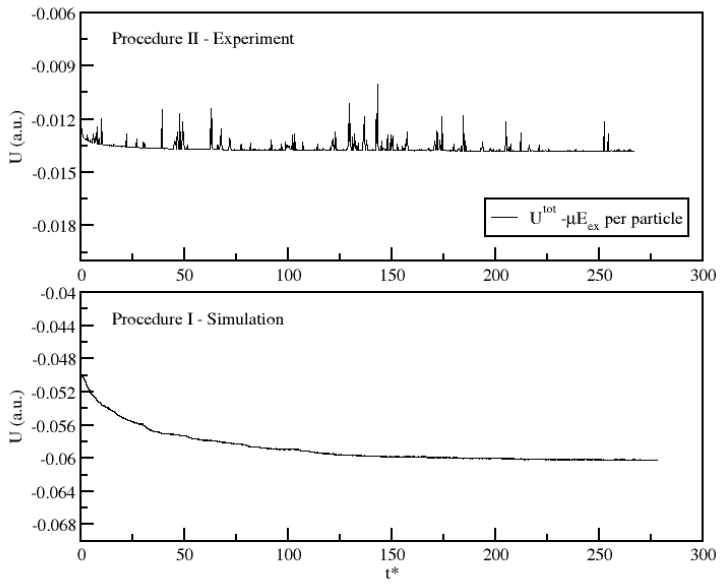
$U^{all} = U^{tot} - \boldsymbol{\mu} \cdot \mathbf{E}_{ex}$ is shown therefore to highlight the energy of the particles with the addition of the energy from the interaction of the dipole with the external field. The simulation and experimental time is scaled to reduced time, t^* as detailed in **Appendix C.3** in order to allow an effective comparison. The important result therefore, is that the behaviour of the energy profiles are similar, independent of the procedure used. This indicates strongly that the simple model used in simulation,

with short-range repulsive effective pair-potentials coupled with a dipole-induced-dipole component, mirrors the experimental behaviour well. For procedure II, the total and polarization energies start at $t^* = 0$ with $U^{pol}(r) = \frac{1}{2}\alpha \mathbf{E}_{ex}{}^2 = 0.0125$ a.u. (where $\alpha = 10$ a.u. and $\mathbf{E}_{ex} = 0.05$ a.u.). For procedure I however the field strength is doubled to give results in a more acceptable time frame. Scaling to reduced time by using Equation C.3.4 requires the selection of appropriate constants in the case of Procedure II. As such, $\sigma = 2.8\mu$m, $m = 8 \times 10^{-10}$g (realistic approximate particle weight) and crucially the well-depth ϵ can take a range of values from $\sim 6.3 \times 10^{-23} \rightarrow 4 \times 10^{-21}$J whereby the latter value maps the simulation curves to the beginning of the experimental curve. As such the model is validated and can be used as a predictive tool for other more speculative simulation runs.

Due to the aforementioned 'close' particle pairs, striking energy spikes can be observed in U^{tot} (and are present in the U^{pol} curves at a much lower intensity) at some timesteps in procedure II. Full justification of these particles is highlighted in **Figure 5.3** where **(a)** shows a schematic of a 'close' particle pair, which when viewed from the z-axis direction the particles appear to violate rules of proximity as visualised in two-dimensions. As a result an unrealistically small separation is included in the energy calculation, generating a large (short-range) overlap interaction and hence leading to a 'spike' in the energy. **Figure 5.3(b)** shows, using a radial distribution function of a single configuration containing an energy spike with and without 'close' pairs. The *blue* arrow highlights the distribution at a much less than physically acceptable particle diameter (~ 1 a.u.). The total energy per particle, calculated at this timestep ($t^* = 252.52$) is 0.01566 a.u. with the 'close' particle pair and 0.01495 a.u. with the problem particle removed. This shows that the energy spike disappears on removal of 'close' particle pairs returning the energy curve to the expected level.

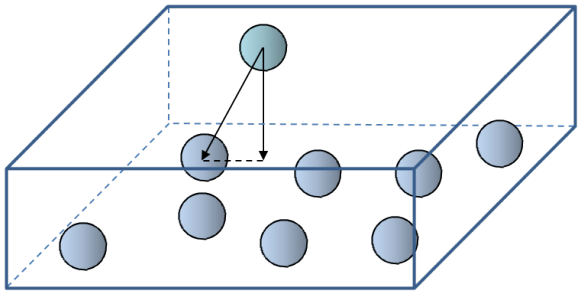


(a) U^{pol} and U^{tot} per particle.

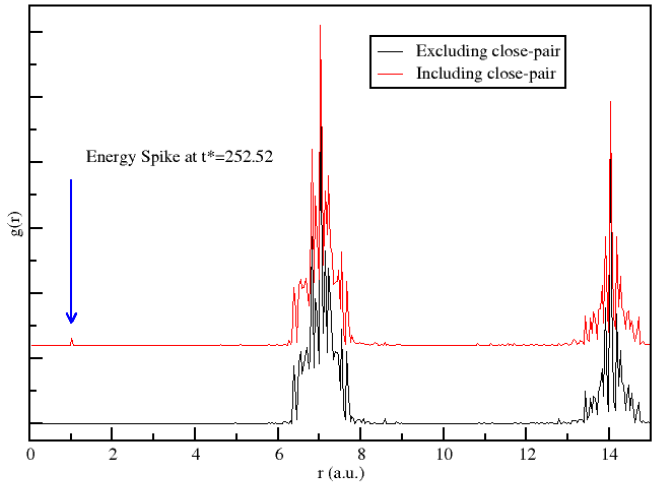


(b) $U^{tot} - \mu \cdot \mathbf{E}_{ex}$ per particle.

Figure 5.2: Energy profiles as a function of reduced time, t^* for both procedure I (lower) and II (upper), depicting U^{pol} and U^{tot} **(a)**, and $U^{tot} - \boldsymbol{\mu} \cdot \mathbf{E}_{ex}$ **(b)**.



(a) Schematic: 'close' particle pairs.



(b) RDF at $t^* = 252.52$.

Figure 5.3: **Figure (a)** shows a simple schematic in order to demonstrate the existence of 'close' pairs in the experimental particle configurations. **Figure (b)** quantitatively proves, by using a radial distribution function obtained from a single configuration, that the energy spikes existing in **Figure 5.2** are due to the 'close' pairs.

5.4 Structure

By expanding on the results of procedure II, using the experimental coordinates at each timestep, more information can be obtained about the nature of particle aggregation in real systems. **Figure 5.4** shows the mean coordination number increase as a function of reduced time obtained directly from the experimental image analysis (*red* curve). Here it is evident that chain formation occurs as the mean coordination tends to a value of 2. The simulation analogue is also included (*green* curve) which shows comparative behaviour, tending to $\langle n \rangle = 2$ again at high t^* where results are averaged over 50 configurations.

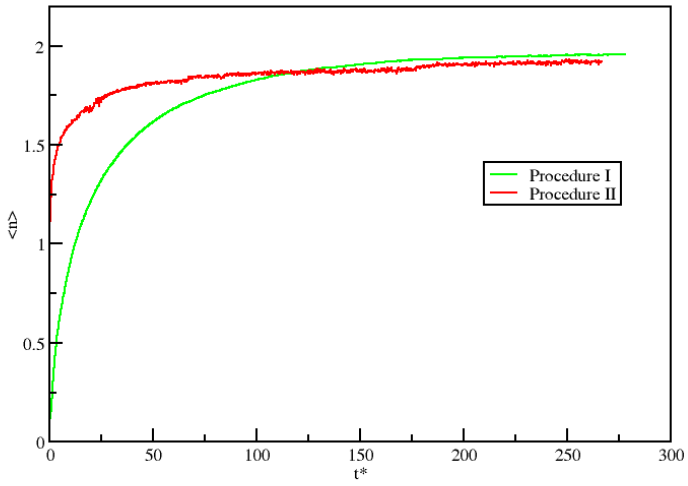


Figure 5.4: Particle aggregation in the real system, comparing procedure I and procedure II. The mean coordination number tends towards a value of $\langle n \rangle = 2$ over the reduced time-scale.

Figure 5.5 shows the evolution in the dipole distributions as a function of reduced time. The initial configuration (*black* distribution) indicates an isotropic liquid at $t = 0$. When the field is applied and the particles aggregate to form chains a bimodal

distribution is observed which diminishes in intensity at the lower dipole value, with time. This indicates the presence of zero-coordinate, 'lone' particles and small chains along with a mix of larger chains with particles experiencing a high DID effect. At high t^* the bimodal distribution disappears and a single peak emerges indicating that the majority of particles are sitting in long chains.

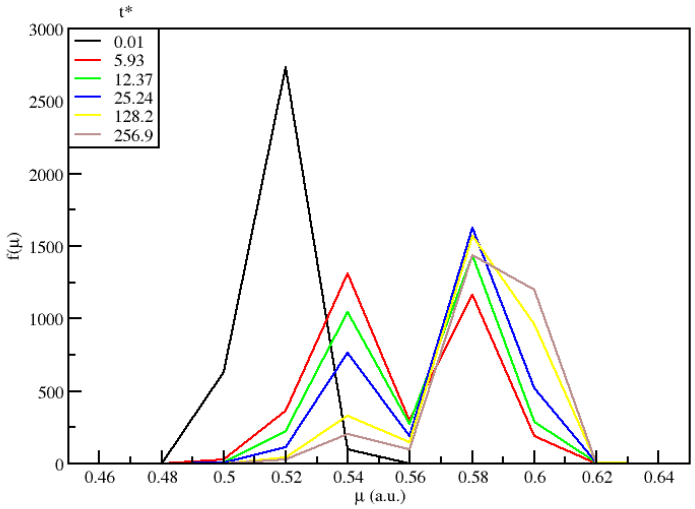


Figure 5.5: Dipole distribution evolution over reduced time, using procedure II where experimental particle coordinates are used coupled with an effective pair-potential in addition to a DID component. The legend states the reduced time, t^* for the run.

As is shown above, this method of utilising the experimental coordinates either by starting configuration only, with further MD relaxation (procedure I) or by analysis of each real timestep (procedure II), the simple simulation model presented in earlier chapters appears to reproduce the required underlying interactions. This will act as a predictive tool for more expansive and complicated systems.

5.5 Chain Growth Statistics

Coordination number statistics are considered key metrics in particle aggregation and cluster growth experiments [165–171]. In many molecular systems, the local environment, geometry and nature of directional interactions between particles determines the structure of the system under a variety of conditions [172]. Furthermore, as highlighted in this thesis, the magneto-rheological systems discussed are subject to directional interactions, control of which can be measured by monitoring the coordination number evolution. This is a strategy employed by many experimental groups [173–180] but the statistics of coordination number environments have seldom been focused on, until recently [45].

Simple statistical considerations are used to provide a prediction of the distribution of coordination numbers for individual particles in a generalised chain forming system. The theoretical model is compared to the experiment (superparamagnetic polystyrene spheres under an applied external field) in addition to the analogous simulation runs (as described in this thesis). These systems, shown in **Section 5.3**, are comparable and provide an excellent model system to establish the relation between cluster formation and coordination number statistics. The chain length distribution (described conceptually in **Section 2.8.8**) provides the means of characterising chain growth and, as will be justified below for a monodisperse system, is well described by a shifted geometric distribution consistent with interpreting the chain formation as a compound Poisson process from an initial configuration of randomly distributed particles. The coordination number distribution also fully characterises the chain length distribution, independent of run time. Therefore in principle, the probabilistic approach can be applied to more complex self-assembling systems, providing a general perspective on self-assembly based on local geometry as characterised by the coordination number.

5.5.1 Chain Length and Coordination Number

For growth processes using the simulation methods described in **Section 2.8.8**, *i.e.* chain formation by repeated addition of particle components, the chain length distributions follow a compound Poisson process. This can be justified in the following manner: If there exists a sparse monolayer of spherical superparamagnetic particles, each with initial coordination number $n = 0$, then on application of a magnetic field at $t^* = 0$, particles will associate instantaneously, in order to form short chains of lengths c, characterised by a Poisson distribution ($\{c|c \in \mathbb{Z}^+\}$) with mean, $\langle c \rangle$ (as encountered in **Section 2.8.7**). At $t^* > 0$, these short chains grow via a compound process consisting of N chains of length c. It is important to note that N exhibits a Poisson distribution again with mean $\langle N \rangle$ which increases as aggregation proceeds. Accordingly, the chain length distribution for the overall chain length ($s = N\,c$) arises from a classical compound Poisson process as outlined in Papoulois and Pillai [181] where again $\{s|s \in \mathbb{Z}^+\}$. Lengths s and c are in essence equivalent but by splitting the aggregation up in this manner highlights the compound growth nature of the process. The simplest chain length distribution for such a process is a shifted-geometric distribution which is fully characterised by its mean, $\mu_s = \langle N \rangle \langle c \rangle$, and has a probability function given by

$$P(s) = \frac{1}{\mu_s}\left(1 - \frac{1}{\mu_s}\right)^{s-1} \tag{5.5.1}$$

such that $P(s)$ gives the probability of finding a chain of length s when randomly selecting a cluster such that $\sum_{s=1}^{\infty} P(s) = 1$. The mean of the distribution therefore, can simply be calculated as $\mu_s = \sum_{s=1}^{\infty} sP(s)$. Similarly, for all other growth processes the functional form of $P(s)$ can be replaced with a more appropriate distribution. The geometric distribution in this example however, is the discrete analogue of the exponential distribution, which arises as the continuous distribution of interval lengths between independent events (see **Appendix C.2**). Here we may interpret

such events as being the termini of chains, *i.e.* those particles with a coordination number of one.

It should be noted that **Equation 5.5.1** and subsequent equations that follow, can also be derived using the Smoluchowski rate equation with a single rate constant k (as diffusion coefficient, D is directly proportional to the size of the chains) [182]. Cluster growth is described by the rate of change in clusters containing s particles,

$$\frac{dc_s}{dt} = \frac{1}{2}k \sum_{i+j=s} c_i c_j - kc_s \sum_i c_i \tag{5.5.2}$$

where c_s is the concentration of chains of length s. The first term describes the formation of clusters, of size s, by aggregation of two smaller clusters whereas the second term describes the loss of s clusters by further aggregation [24]. Solving this equation for c_s yields

$$c_s = \frac{\rho(k\rho)^{s-1}}{(1+k\rho t)^{s+1}} \tag{5.5.3}$$

where ρ is the density of the s clusters and t is the time scale. Additionally $\mu_s = \langle s \rangle = 1 + k\rho t$ which is the mean cluster size. The probability therefore, that a particle is in a chain of length s, is

$$P(s) = \frac{\mu_s c_s}{\rho} = \frac{(k\rho t)^{s-1}}{(1+k\rho t)^s} = \frac{1}{\mu_s}\left(1 - \frac{1}{\mu_s}\right)^{s-1}. \tag{5.5.4}$$

This equation is the same as **Equation 5.5.1** and therefore shows how Smoluchowski kinetics can be used for equivalent derivations of the chain length probability.

The probability that a particle, i has a coordination number n is conditional on s, the size of the chain containing particle i. More formally this is written as $P(n|i;s)$. Additionally, the probability that a particle i, chosen at random, is in a chain of length s, is written as $P(i;s)$. Therefore the product of which, $P(n \cap i;s) = P(n|i;s)P(i;s)$, is the probability of randomly selecting a particle that is in a cluster of size s and has a coordination number n. Subsequently it follows that the probability of a particle

selected at random, that has coordination n is given by the sum over all cluster sizes of this probability [183]:

$$P_n = \sum_{s=1}^{\infty} P(n \cap i; s) = \sum_{s=1}^{\infty} P(n|i; s)P(i; s). \tag{5.5.5}$$

$P(i; s)$ is simply an expanded definition of $P(s)$ where

$$P(i; s) = \frac{s\,P(s)}{\sum_{s=1}^{\infty} s\,P(s)} = \frac{s}{\mu_s^2}\left(1 - \frac{1}{\mu_s}\right)^{s-1} \tag{5.5.6}$$

and again normalised as $\sum_{s=1}^{\infty} P(i; s) = 1$. In the case of linear chains, only zero-coordinate, one-coordinate and two-coordinate particles exist. *I.e.* in isolation ($n = 0$), one of the two termini of a chain ($n = 1$) or one of the remaining interior particles of a chain ($n = 2$) respectively. $P(n|i; s)$ is therefore described in terms of the cluster sizes: $P(n = 0|i; s) = \delta_{s,1}$ for $s = 1$ only as this species must be a monomer. When $s \geq 2$ however, $P(n = 1|i; s) = 2/s$ and $P(n = 2|i; s) = (s - 2)/s$. Note that this model describes simple chains only and neglects the possibility of cruciform defects [184] and laterally aggregated chains. The probability that a particle has a coordination number n, P_n, is now easily found by combining **Equations 5.5.5** and **5.5.6** where it follows that the fraction of zero coordinate particles is given as

$$P_0 = P(i; s = 1) = \frac{1}{\mu_s^2}\ . \tag{5.5.7}$$

Similarly the fractions of particles with coordination number one and two, as outlined in **Appendix C.1** can be described as

$$P_1 = \sum_{s=2}^{\infty} \frac{2\,P(i; s)}{s} = \frac{2(\mu_s - 1)}{\mu_s^2}, \tag{5.5.8}$$

$$P_2 = \sum_{s=2}^{\infty} \frac{(s-2)\,P(i; s)}{s} = \frac{(\mu_s - 1)^2}{\mu_s^2}, \tag{5.5.9}$$

such that $\sum_{c=0}^{2} P_c = 1$. From **Equations 5.5.7**, **5.5.8** and **5.5.9** we obtain the mean

and variance of the coordination number

$$\langle n \rangle = \frac{2\left(\mu_s - 1\right)}{\mu_s}, \tag{5.5.10}$$

$$\sigma_n^2 = \frac{\langle n \rangle}{\mu_s}, \tag{5.5.11}$$

respectively. Note that $\lim_{\mu_s \to 1} \langle n \rangle = 0$, $\lim_{\mu_s \to 1} \sigma^2 = 0$, $\lim_{\mu_s \to \infty} \langle n \rangle = 2$ and $\lim_{\mu_s \to \infty} \sigma^2 = 0$, as required. **Equation 5.5.10** highlights the one-to-one relationship between the mean coordination number and the mean chain length such that knowledge of either allows the full statistics of the coordination number distribution to be calculated. Furthermore, as shown in **Equation 5.5.4**, the mean chain length also depends linearly on time, t.

Figure 5.6 shows the fraction of particles with coordination number $n = 0$, 1 and 2 in *black*, *red* and *green* respectively, calculated using the MD simulation procedure I at the same low density as used in the experiments, as a function of the mean chain length, μ_s. The theoretical model is also compared (*blue*, *orange* and *purple* curves) using **Equations 5.5.7**, **5.5.8** and **5.5.9**. Experimental data have also been added, courtesy of Reynolds *et al.* [161] with triangular points, again in *black*, *red* and *green*. Excellent agreement is observed between the theory, simulation and experiment across the entire range of mean chain lengths. At high μ_s differences between experiment and theory emerge due to the presence of a small number of species with coordination number greater than two. As shown by Reynolds *et al.* [45] discounting these particles ($n > 2$) improves agreement between theory and experiment. For example, a plot of the variance of the coordination number (σ_n^2) against its mean ($\langle n \rangle$) shows ideal agreement with the theoretical model (**Equations 5.5.10** and **5.5.11**) where $n > 2$ are omitted. The presented statistical model for cluster formation holds for both the colloidal (experimental) and particle (simulation) systems, despite the overdamped dynamics exhibited by the experimental system. This is the result of resistance created by the carrier fluid which subsequently leads to a different growth process for

these experimental systems potentially forming higher coordinate clusters and leading to deviations at high chain length. Even so the simulation model is further validated and able to describe this system at the low μ_s range. This model is not an exact description of the experimental run, given the large separation in time of the initial and subsequent aggregation events, however the compound Poisson interpretation improves the understanding of the system in a more generalised sense. The length of a chain therefore, is derived from a random number of aggregation events of clusters of random length, depending on the initial spatial arrangement of particles. On cooling, the system would be expected to fall out of equilibrium (effectively when the temperature reaches the simulation glass transition temperature). This very much mimics the experimental procedure. In order to average over the glassy states a number of configurations are generated by quenching from different liquid state configurations (from the same state point).

With knowledge of the chain length distributions, it follows that the coordination number statistics can be recovered in order to complete the description of the system. **Figure 5.7** shows the calculated coordination number probability for $n = 0$, 1, 2, 3 coordinate particles in the particle simulation as a function of reduced time, using procedure I. It is important to note that this is calculated independently of the mean chain length distribution statistics shown for the same system in **Figure 5.6**. At $t^* = 0$ the initial configuration contains mainly 0-coordinate particles sparsely distributed, with few 1-coordinate particles as a result of the random distribution, and extremely low numbers of $\geq$ 2-coordinate particles. Over time, as the particles aggregate due to the presence of an external field, the DID effect increases the energetic stability of particles within chains therefore the number of 2-coordinate particles increases with simultaneous decrease in 0-coordinate particles. 1-coordinate particle species increase upon initial aggregation only to decrease upon significant chain lengthening.

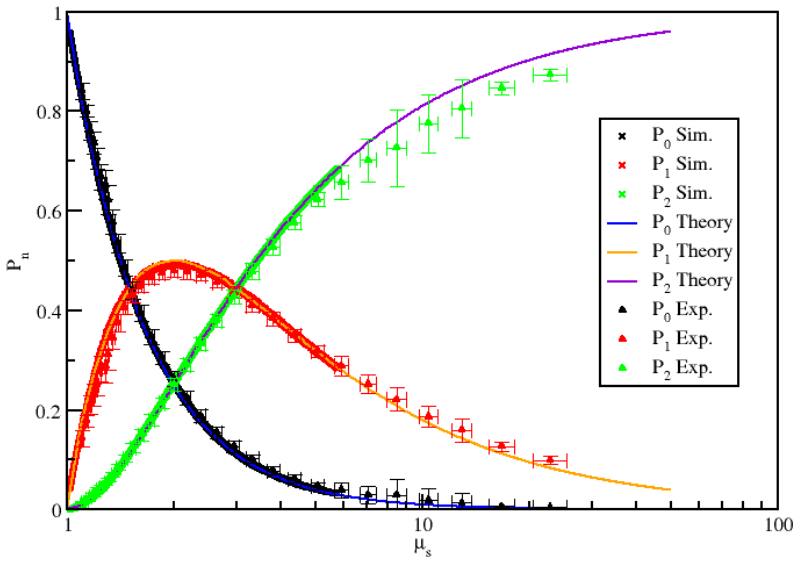


Figure 5.6: Mean chain length distributions as a function of cluster size using simulation procedure I, the ideal theoretical prediction and experimental work attributed to Reynolds *et al.* of the real system.

This simulation result is significant as it mirrors the experimental results in **Figure 4** of Reynolds *et al.* [45]. The time domain is the more natural 'reaction coordinate' when concerned with chain growth processes and is related to mean chain length by a simple function

$$\mu_s = a + b(t^*)^z. \tag{5.5.12}$$

For values of $a = 1.03694$, $b = 0.079016$ and $z = 1.00169$ as fitted to the coordination probability curves, an accurate description of the mean chain length distributions are provided recovering the curves in **Figure 5.6** using **Equations 5.5.7**, **5.5.8** and **5.5.9**. As described above the values of a and z are effectively 1 which is in close agreement with the model derived using Smoluchowski kinetics. The coordination number distribution therefore, fully characterises the chain length distribution and vice versa. Self-assembly in this system is explored fully using a probabilistic approach and provides an interesting perspective on chain aggregation in this system.

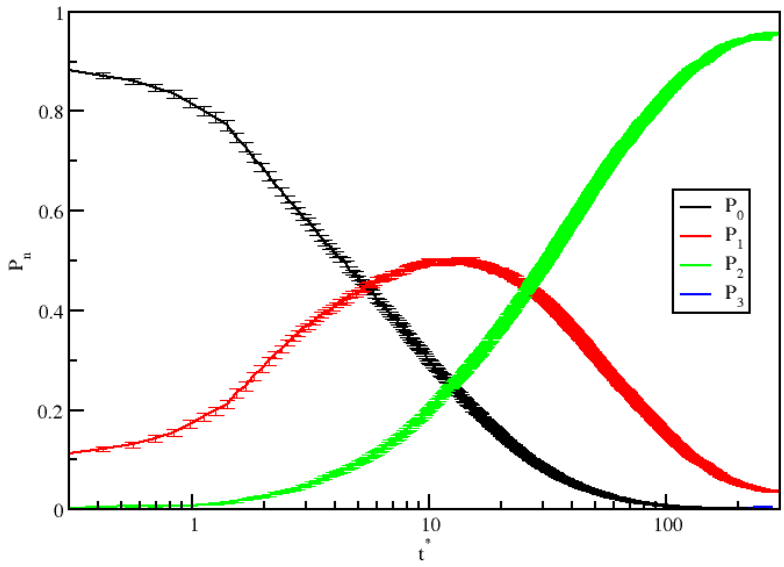


Figure 5.7: Coordination number probabilities as a function of reduced time using procedure I. The error bars are true standard deviations about the sample mean calculated over the set of configurations.

5.6 Chapter Summary

The simple simulation model used throughout this thesis has been fully justified in describing the growth aggregation process of monodisperse, superparamagnetic particles at low density. As a result of this, the aim of the following chapters is to act in a predictive sense, where more complicated systems are introduced and explored. The main themes investigated are the effect of particles with bidisperse polarizabilities on the extent of chain formation and the role of confinement in these systems.

Chapter 6

Bidisperse Systems

A central aim of this work is to investigate the role of the dipole-induced-dipole (DID) effect, which for monodisperse systems, as discussed in **Chapter 4**, can be characterised based on the form of the dipole distributions. These systems 'self-assemble', the extent of which is governed by the distribution of the low and high dipole moments. The effect, termed 'de-mixing', is more pronounced at high α due to the increase in mean dipole moments as a direct result of the strength of the DID term.

For a real system the value of α is not uniform and there may be a dispersion of properties, *e.g.* in terms of both particle diameter and susceptibility. Indeed, particle diameters and dipole moments are often linked, mimicking experimental observables [67, 81]. Simulation work has been performed on systems with a polydispersity in dipole strength and/or particle diameter, with the general conclusion being, that larger particles (higher dipole moments) tend to preferentially aggregate [81–87]. This is evident from the work in **Chapter 4**. As a result, a distribution of polarizabilities (α_i) would in some ways better represent a real system more accurately. Here we simplify the problem as much as possible by investigating a bidisperse system whereby half of the particles are assigned one polarizability, α_1 and the remaining half

another, α_2. To further probe any potential de-mixing we study a range of systems in which equal numbers of particles have different polarizabilities, $\{\alpha_1, \alpha_2\}$, with the mean polarizability, $\langle\alpha\rangle = \frac{1}{2}(\alpha_1 + \alpha_2)$ and polarizability difference, $\Delta\alpha = \alpha_2 - \alpha_1$. The majority of calculations performed are at a fixed field strength and mean polarizability, keeping the product, $\langle\alpha\rangle \cdot \mathbf{E}_{ex}$ fixed at 0.5 a.u.. The effective pair-potential is fixed using the 'r^{-12}' model described previously and with equal particle diameter, σ. As a result, the polarizability of a particle and its size are effectively decoupled. **Table E.1** (in the **Appendix**) lists all the parameter sets for which simulations are performed, allowing a number of different potential trends to be explored. For example,

- $\Delta\alpha$ is fixed, an example set being $\{\Delta\alpha = 2$ a.u., $\langle\alpha\rangle = 10$ a.u.$\}$ observed in rows: 33, 47, 53, 61, 67, 75, 84, 90, 98, 110, 128, 143, 154.
- $\langle\alpha\rangle$ is fixed, an example set being $\langle\alpha\rangle = 10$ a.u. observed in rows: 31-33, 44-47, 50-53, 58-61, 64-67, 72-75, 80-84, 87-90, 95-98, 107-110, 125-128, 140-143, 151-154.
- $\frac{\Delta\alpha}{\langle\alpha\rangle}$ is fixed.

The shape and form of bidisperse dipole distributions are first investigated and compared with the monodisperse analogue. This chapter then explores the network formation properties of bidisperse systems, principally through particle coordination environments, the effect of varying the polarizability difference with scaling functions and ramping the electric field rather than using the method of quenching (described in **Chapter 4**) including the effect of gradual field reversal (hysteresis).

6.1 Dipole Distributions

Figure 6.1 shows the distribution of dipoles for the final configurations of three bidisperse systems, at fixed applied external field, $\mathbf{E}_{ex} = 0.05$ a.u. (under the same conditions as the monodisperse analogue), with different pairs of particle polarizabilities $\{\alpha_1, \alpha_2\}$ such that the product $\langle\alpha\rangle \cdot \mathbf{E}_{ex} = \langle\boldsymbol{\mu}_{ex}\rangle$ is fixed at 0.5 a.u.. The distributions of dipoles are evidently bimodal for starting configurations in these bidisperse systems, due to the selection of polarizability pairs $\{\alpha_1, \alpha_2\}$ (vertical dashed lines show the initial values of $\boldsymbol{\mu}_{ex}$ for each species). As the run progresses there is a DID enhancement, where the more polarizable species ($\alpha_2 = 13$ and 15 a.u. in **Figure 6.1**) show the largest increase in mean dipole. The high α species produce a distinct 'three-peak' structure (*e.g. red* and *black* distributions at high $\boldsymbol{\mu}$ in the main graph window) which will correlate to the differing coordination environments surrounding the particles. For example, for $\alpha_2 = 15$ a.u. the distribution shows peaks at $\langle\mu\rangle = 0.77,\ 0.90$ and 1.08 a.u. respectively which correspond to 0-, 1- and 2-coordinate particles as rationalised below.

The inset to **Figure 6.1** shows the mean 'excess' dipole predicted ($\langle\mu_{DID}\rangle = \langle\mu\rangle - \boldsymbol{\mu}_{ex} = \langle\mu\rangle - \alpha \cdot \mathbf{E}_{ex}$) *i.e.* the dipole present as a result of the DID effect only without the dipole present from the initial applied field which is reported as a function of polarizability, calculated from the distributions shown in the main window. If for example, $\alpha_2 = 15$ a.u., the largest 'three-peak' mean value is used ($\langle\mu\rangle = 1.08$ a.u.) such that $\langle\mu_{DID}\rangle = 0.33$ a.u.. The inset also includes for comparison, the two-particle pair and infinite chain values of μ_{DID} (calculated as in **Chapter 4** with **Equations 4.2.2** and **4.2.4** respectively) for both the first order correction, $\mu_{DID}^{(1)}$, and the self-consistent correction, $\mu_{DID}^{(\infty)}$. The calculated values of $\langle\mu_{DID}\rangle$ show a clear 'upturn' at high α, moving away from the '2-Particle' predicted values indicative of significant chain formation approaching the limit of an ideal infinite chain.

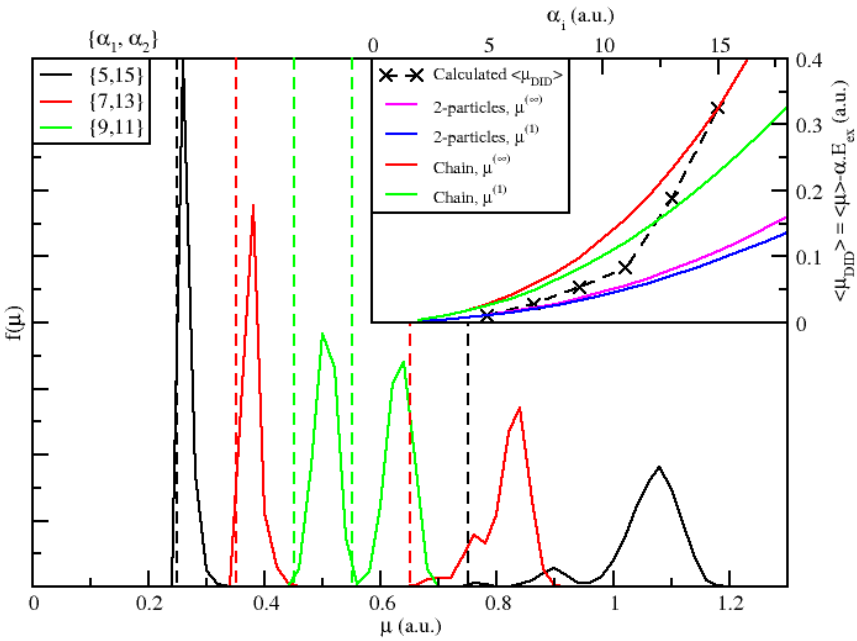


Figure 6.1: A distribution of dipole moments for three sets of bidisperse systems with a fixed applied field of $\mathbf{E}_{ex} = 0.05$ a.u. and $\langle\alpha\rangle = 10$ a.u.. Polarizability pairs, $\{\alpha_1, \alpha_2\}$ are shown in the legend of the main window and the vertical dashed lines indicate the value of $\alpha_1 \cdot \mathbf{E}_{ex}$ or $\alpha_2 \cdot \mathbf{E}_{ex}$. The inset shows the mean μ_{DID} as a function of the polarizability for each species present. y-axis scaling labels are removed for clarity.

At the highest polarizability ($\alpha_2 = 15$ a.u.), the observed dipoles agree with those predicted from **Equation 4.2.4** demonstrating that the chains formed are, firstly, relatively long and, secondly, dominated by a single (high polarizability) species. At low α the dipoles become smaller than these limiting values indicating that the chains formed in the bidisperse simulations contain a mixed number of higher and lower polarizability species. Therefore to summarise there is a distinct 'de-mixing' effect when the difference in polarizability for the two species in the bidisperse mixture, $\Delta\alpha$ increases. If chains were indeed composed of an equal mixture of the two species, rather than shown to preferentially aggregate, then the value of $\langle\mu_{DID}\rangle$ would be much smaller at high α than shown in the inset, without the dramatic upturn in $\langle\mu_{DID}\rangle$

observed. The origin of the three peak structure in the dipole moment distribution can now be fully rationalised. For chains comprised of the more polarizable species, $\left\langle \mu_{DID}^{(1)} \right\rangle$ is equal to zero, $2\alpha^2 \mathbf{E}_{ex}\zeta(3)/r^3$ and $4\alpha^2 \mathbf{E}_{ex}\zeta(3)/r^3$ for the 0-, 1- and 2-coordinate particles respectively, where both the 1- and 2-coordinate sites form a part of the long chains. The peak positions in $f(\mu)$ for, for example $\alpha = 15$ a.u., correspond to these predicted values with the greatest number of particles in 2-coordinate sites (the largest of the 'three-peaks'). The extent and form of this 'de-mixing' effect is discussed subsequently in the sections to follow.

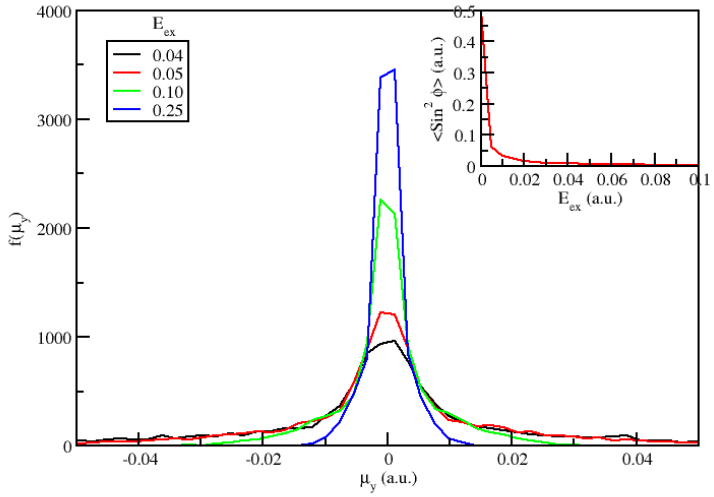


Figure 6.2: Dipole distributions for the bidisperse system calculated for the y-axis contribution only. All future calculations may now only consider the x-axis contributions for efficiency. The $\rho^* = 0.8$ system is used as a rudimentary example varying $\mathbf{E}_{ex}$ as shown in the graph legend. The inset shows the variance in the dipole orientations for a single fixed dipole, which decreases with $\mathbf{E}_{ex}$.

Interestingly, the dipole distributions in **Figure 6.1** are calculated using only x-axis contributions (in the direction of the applied field). The y-axis contribution as highlighted by **Figure 6.2** can be neglected as the distributions are symmetric,

averaging around zero given over a range of arbitrarily calculated field strengths. As a point of interest, the variance of the distribution decreases as the field strength increases, for a fixed $\frac{\Delta\alpha}{\langle\alpha\rangle}$ ratio and a fixed $\langle\alpha\rangle$. This indicates that there is a lower alignment of particles out of the direction of the applied field at high field (note: the runs are two-dimensional and fixed in the 2D-plane as before) therefore the greater the applied field strength the larger the affinity for longer chains.

The inset to **Figure 6.2** shows that the variance in the dipole orientations (for a single fixed dipole) decreases as the magnitude of $\mathbf{E}_{ex}$ increases. With the applied field in the x-direction, the variance is calculated using the equation

$$\left\langle \mu_y^2 + \mu_z^2 \right\rangle = \left\langle \sin^2\phi \right\rangle = 1 - \frac{\int_0^\pi \cos^2\phi \ \exp(\beta\cos\phi).d\phi}{\int_0^\pi \exp(\beta\cos\phi).d\phi} \tag{6.1.1}$$

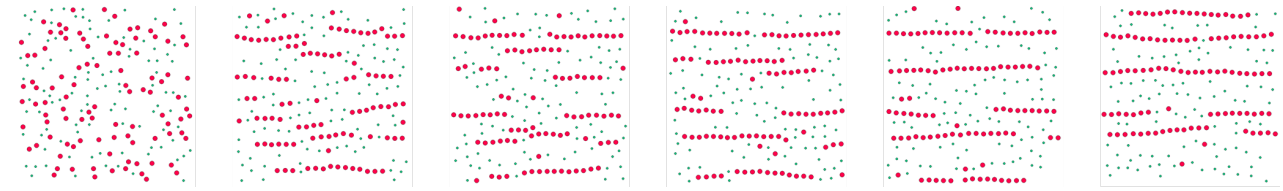
where $\beta = \mu\mathbf{E}_{ex}/k_BT$ (the Langevin parameter), $\mu = 0.5$ a.u. and k_BT is also reported in a.u. corresponding to a fixed $T = 50K$. This result is expected given that alignment along an applied field is much greater with increasing field strength.

6.2 Structure

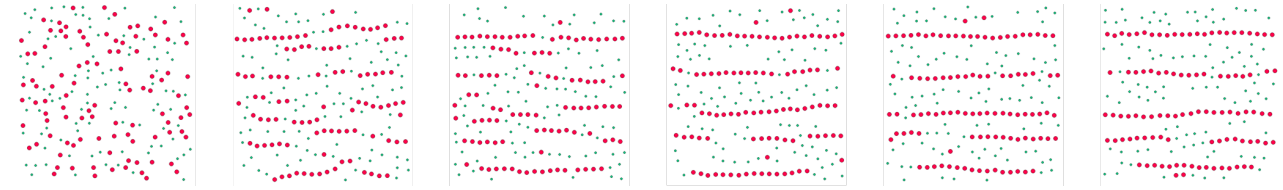
In order to highlight the extent of chain-formation in a bidisperse system, molecular graphics 'snapshots' can be produced in a similar manner to the monodisperse **Section 4.3.1**. **Figure 6.3** shows a set of configurations at fixed external field, $\mathbf{E}_{ex} = 0.05$ a.u. and fixed mean polarizability, $\langle\alpha\rangle = 10$ a.u.. **Figures 6.3(a)**, **6.3(b)**, **6.3(c)**, **6.3(d)**, **6.3(e)** give pairs of polarizabilities $\{\alpha_1, \alpha_2\}$ = $\{5, 15\}$, $\{6, 14\}$, $\{7, 13\}$, $\{8, 12\}$ and $\{9, 11\}$ a.u. respectively. From left to right the simulation evolves over time, for a fixed number of steps as described in the figure caption. The final configurations (cells to the far right in **Figure 6.3**) all show a clear chain structure. The particles are coloured according to their respective polarizabilites: the higher polarizability particles, labelled 'A' (α_2) are in *red* and the

lower labelled 'B' (α_1) are in *green* with relative size scaling based on the magnitude of α_i. As a result, it is clear from the figure that for $\{\alpha_1, \alpha_2\} = \{5, 15\}$ a.u. (high $\Delta\alpha$), the more polarizable of the two species ($\alpha_2 = 15$ a.u.) form well-defined chains whilst the less polarizable species ($\alpha_1 = 5$ a.u.) form more liquid-like, less well-defined structures. In contrast, for the $\{\alpha_1, \alpha_2\} = \{9, 11\}$ a.u. (low $\Delta\alpha$) configuration the chain structure is more apparent in both sublattices, containing a mixture of species, as a result the chains appear less well aligned with the applied field, $\mathbf{E}_{ex}$ compared to the more polarizable particles in the high $\Delta\alpha$ configuration. It is this de-mixing effect that will become the principal point of interest in this chapter. What is increasingly evident however is the improved ability to tune the properties of the bidisperse fluid, based on the particle species present. This has far reaching implications for the development of model systems for electro-rheological fluids.

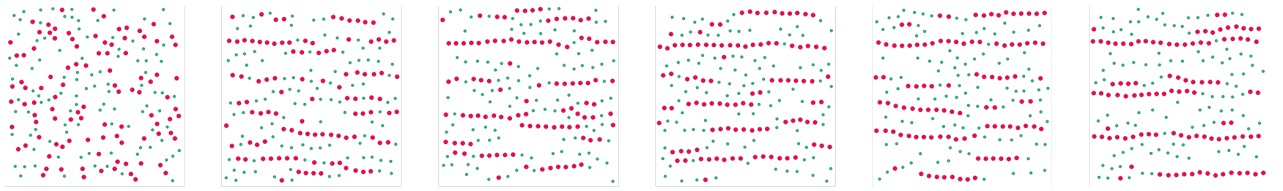
In order to demonstrate the statistical significance of the number of configurations used in the simulation, compared to the monodisperse case (50 independent configurations for the average) the value of $\Delta p_A(k)$ is calculated for two different sets (each of 50 configurations) with completely independent starting positions along with the combination of both of these sets. The particle types 'A' and 'B' are defined again here purely in terms of their polarizability (rather than the magnitude of the dipole moment in the context of the distribution of moments). $\Delta p_A(k)$ for the bidisperse system will be covered in detail in further sections, however, it has been used as a metric in this case for illustration only. **Figure 6.4** shows the almost negligible difference in average and standard deviation of $\Delta p_A(k)$ calculated for each set. Thus it is shown that the initial sample number of 50 configurations gives an acceptable statistical average for each value of $k = 2$, 1 or 0; the largest difference in $\Delta p_A(k)$ (for the $k = 2$ case) is of the order of 0.001 with respect to a scale from $0 \rightarrow 1$.



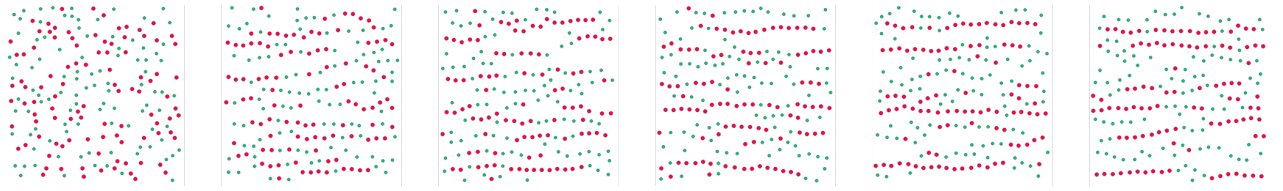
(a) {5,15}



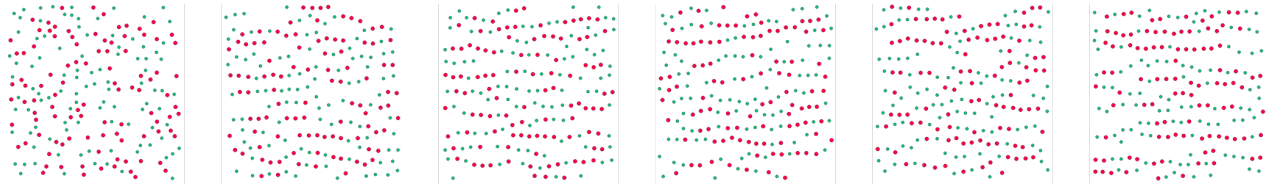
(b) {6,14}



(c) {7,13}



(d) {8,12}



(e) {9,11}

Figure 6.3: Molecular graphics 'snapshots' for a set of six configurations at $\mathbf{E}_{ex} = 0.05$ a.u. and $\langle\alpha\rangle = 10$ a.u.. The direction of the applied field is along the x-axis and each set of images describes the progression of time, from left to right in $\sim 0ns$, $0.00756ns$, $0.0151ns$, $0.0303ns$, $0.0605ns$, $0.121ns$ steps. Each image has a set of polarizabilities $\{\alpha_1, \alpha_2\}$, the low polarizability species is coloured *green* and the high polarizability species is coloured *red* with relative size scaling based on the magnitude of α_i included.

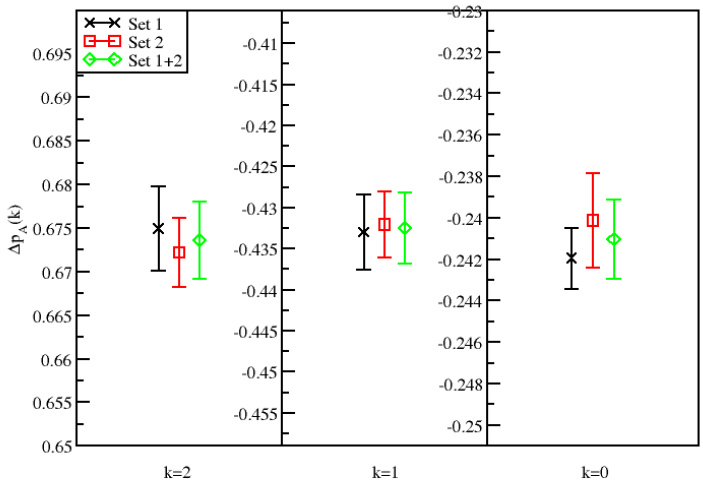


Figure 6.4: $\Delta p_A(k)$ for a bidisperse system with $\mathbf{E}_{ex} = 0.05$ a.u. and $\{\alpha_1, \alpha_2\} = \{5, 15\}$ a.u. for two different sets of 50 configurations along with the sum of both sets; the error bars are true standard deviations about the sample mean.

6.3 Coordination Environments

The coordination environments surrounding particle species were also explored by fixing $\Delta\alpha$ and also by investigating the evolution of $f(n)$ (the number of particles with coordination, n) at varying field strengths. Using these observations, quantitative characterisation of the behaviour of particles in a two-species system can be completed. It is important to first clarify the labelling system used throughout this section. For a bidisperse system with polarizabilities $\{\alpha_1, \alpha_2\}$, half of the particles are labelled 'A' (high polarizability or α_2) and half 'B' (low polarizability or α_1). The particle species are analysed in the following manner, a system which will become obvious as the chapter progresses:

Total (A+B): both species of particles in the system considered are in the analysis. *I.e.* all particles surrounding particles 'A' and all particles surrounding particles 'B'.

Total (About A): all particles surrounding species 'A' only, are considered in the analysis. *I.e.* the interaction of particles 'A' and 'B' about all 'A' species.

Total (About B): all particles surrounding species 'B' only, are considered in the analysis. *I.e.* the interaction of particles 'A' and 'B' about all 'B' species.

Partial (About A): only 'A' particles exclusively surrounding other 'A' particles, are considered in the analysis.

Partial (About B): only 'B' particles exclusively surrounding other 'B' particles, are considered in the analysis.

6.3.1 Coordination Number

Figure 6.5(a) shows the Total (A+B) coordination number distributions for the final configurations for a range of polarizability differences $\{\alpha_1, \alpha_2\} = \{6, 14\}$, $\{7, 13\}$, $\{8, 12\}$, $\{9, 11\}$ a.u., for a fixed $\langle\alpha\rangle = 10$ a.u. at varying field strengths, $\mathbf{E}_{ex}$. **Figure 6.5(b)** shows an additional perspective on the same calculations for the cumulative number of particles, $f(n)$, at each field strength. It is evident that as the field strength increases, the number of two coordinate sites are shown to increase ($f(2)$ in **Figure 6.5(b)**), highlighted by the increase in the sharpness of the peaks at $n = 2$ for each $\Delta\alpha$ in **Figure 6.5(a)**. When $\Delta\alpha$ is lower (*e.g.* for $\{9, 11\}$ compared with the $\{6, 14\}$ case) the particle distribution is significantly narrower with greater numbers of two-coordinate species. Given that a chain comprises of mainly two-coordinate particle sites (terminated by single coordinate species), this metric therefore indicates crudely, that the length of chains and/or number of chains in the configuration increases (see **Section 6.3.2** on chain length analysis). At low field, ($\mathbf{E}_{ex} \rightarrow 0.04$ a.u.), the populations of particles at each discrete coordination number are similar over the

range of $\Delta\alpha$. In this range of $\mathbf{E}_{ex}$, species 'A' and 'B' have a low induced-dipole and do not form significant numbers of chains. At high field however ($\mathbf{E}_{ex} > 0.04$ a.u.), as is evident in the molecular 'snapshots' (final configurations in **Figure 6.3**), there is a de-mixing effect, the extent of which depends on the values of α_2 and α_1. For low $\Delta\alpha$ (far right of **Figure 6.5(a)**) species 'A' and 'B' have closer values of α than for high $\Delta\alpha$, therefore the difference in the dipole induced by the field for each species is less significant. As such, both 'A' and 'B' species participate in the make-up of the chains at lower $\mathbf{E}_{ex}$ (mixing) and hence the number of two coordinate species ($f(2)$), as observed in the *green* curves of **Figure 6.5(b)**, shows a sharper initial increase compared to the high $\Delta\alpha$ species.

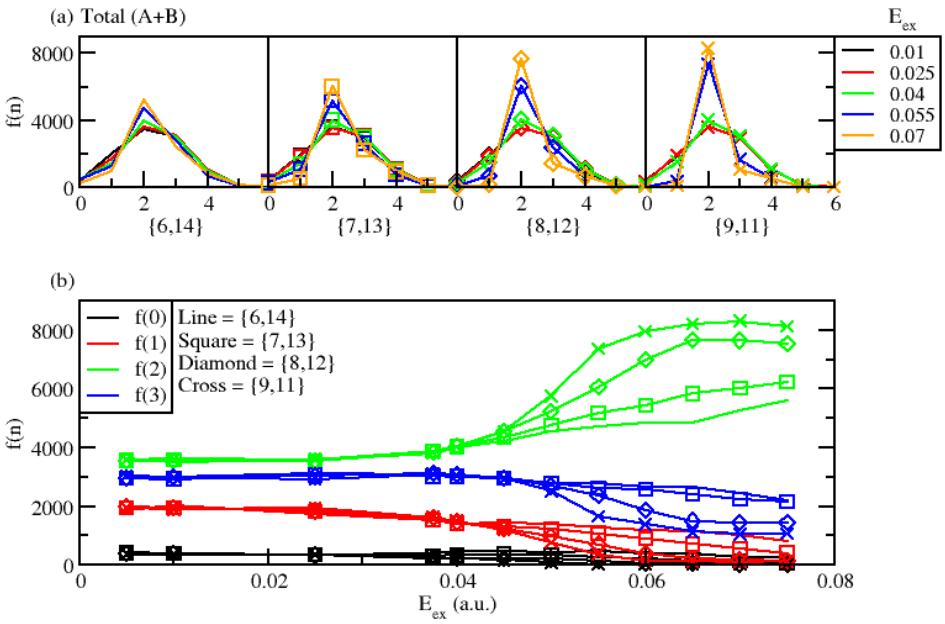


Figure 6.5: Total (A+B) coordination number distributions **(a)** upper, and frequency curves **(b)** lower, for a range of polarizability differences $\{\alpha_1, \alpha_2\}$ for a fixed $\langle\alpha\rangle = 10$ a.u. at varying field strengths $\mathbf{E}_{ex}$.

At high $\Delta\alpha$, species 'A' has a much larger polarizability and the dipole-induced-dipole effect is therefore also much larger (as shown in **Figure 6.1**) and conversely 'B' species have such a low α that the DID effect is negligible unless at extremely high field. As a result, species 'A' de-mixes and forms chain structures alone, whilst species 'B' (lower polarizability) becomes trapped between walls of 'A' species and remains liquid-like. **Figure 6.5(b)** emphasises this point displaying the total number of 0-, 1-, 2- and 3-coordinate species at varying $\mathbf{E}_{ex}$ as before, for the range of $\Delta\alpha$. As discussed above, there are increasing numbers of $n = 2$ species at higher field and decreasing 0-, 1- and 3-coordinate species. For small $\Delta\alpha$ (*e.g.* $\{9, 11\}$ - *crosses* in figure) the total number of all $n \neq 2$ species falls more dramatically at larger field, along with a much larger increase in the number of $n = 2$ species, compared with the analogue at large $\Delta\alpha$. At extremely high fields, for small $\Delta\alpha$, there is a turning point and slight decrease in total numbers of 2-coordinate species. This can be explained in this figure by the mirrored slight increase in 3-coordinate species as the chains become more compacted and closer together.

Figures 6.6 and **6.7** expand on this analysis showing a table of all distribution graphs for each polarizability difference, $\{\alpha_1, \alpha_2\}$ and a set of complementary cumulative frequency graphs for each coordination number respectively. Firstly **Figure 6.6(a)** (top set of figure) has a similar form to **Figure 6.5(a)** (albeit at lower particle frequency) as it describes the total A and B contribution about species 'A', *i.e.* sampling the coordination environment around all 'A' particles. The argument above justifies these higher polarizability particles that form chains easily. Secondly **Figure 6.6(b)** (second row) shows a departure at high $\Delta\alpha$ (for example $\{6, 14\}$), with significantly reduced $n = 2$ sites, when increasing the field strength compared to the analogue in **Figure 6.6(a)**. This confirms that the 'B' species remain liquid-like, trapped between walls of the high polarisability species in the de-mixing process.

By observing the partial coordination number distributions, *e.g.* considering only the interaction of 'A' species with other 'A' species only, or 'B' species with other 'B' species only, then the argument is even further strengthened. **Figure 6.6(c)** (third row) shows that as the field strength increases, the number of two coordinate particle sites increases (as expected and confirmed with the *green* curves in **Figure 6.7(a)**), to a peak around $\mathbf{E}_{ex} = 0.055$ a.u. before decreasing at larger field magnitudes. This inflection point effect is more pronounced at a middle value of $\Delta\alpha$ ($\{8, 12\}$ in **Figure 6.7(a)**) and the factors that affect this are discussed below with respect to the regions of the mean coordination number graphs.

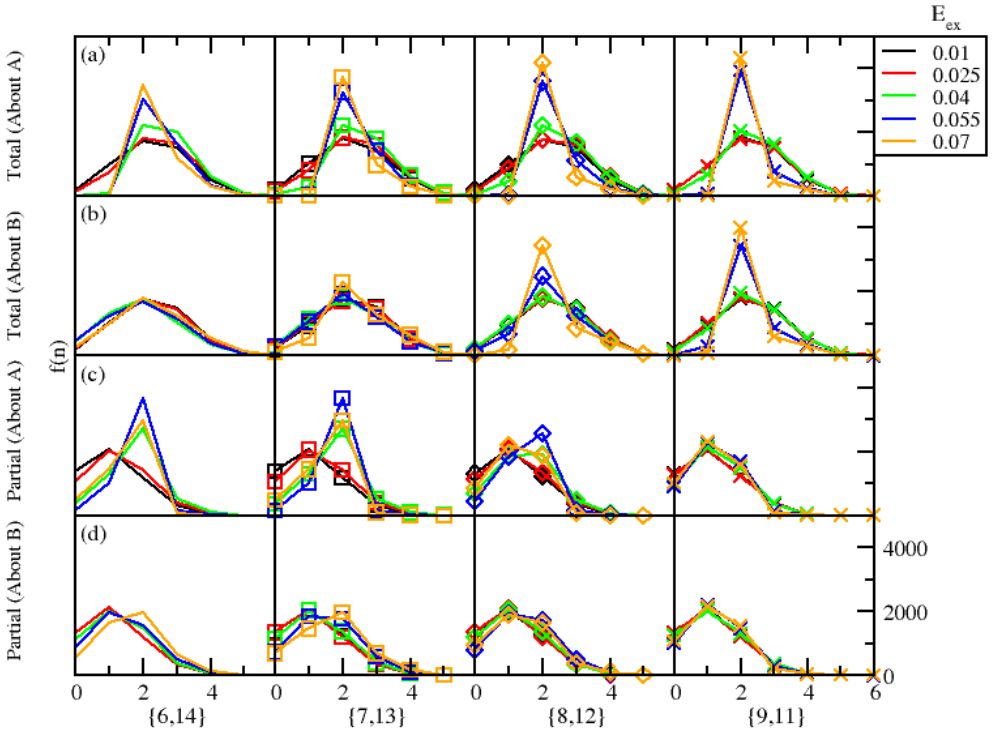


Figure 6.6: Coordination number distributions for a range of polarizability differences $\{\alpha_1, \alpha_2\}$ for a fixed $\langle\alpha\rangle = 10$ a.u. at varying field strengths $\mathbf{E}_{ex}$. Rows **(a)-(d)** denote the different calculation methods. Each graph has a uniform x- and y-scaling as shown by the last cell in row **(d)**.

Figures 6.6(d) and **6.7(b)** finally show that as the field strength increases the number of two-coordinate, 'B' sites increases steadily, and more slowly, than the two coordinate 'A' sites. However at high $\Delta\alpha$, by increasing the external field, where the 'A' and 'B' species are initially more de-mixed, there is a small increase in 'B' chain formation indicated by the distribution shift in **Figure 6.6(d)**. This implies that there are conditions to be explored to affect a reversible mixing $\longleftrightarrow$ de-mixing process.

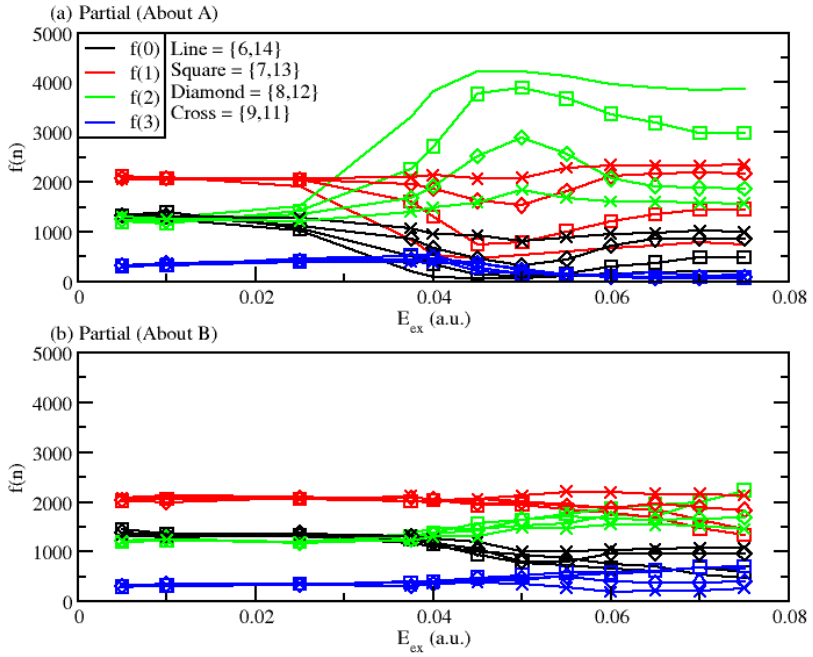
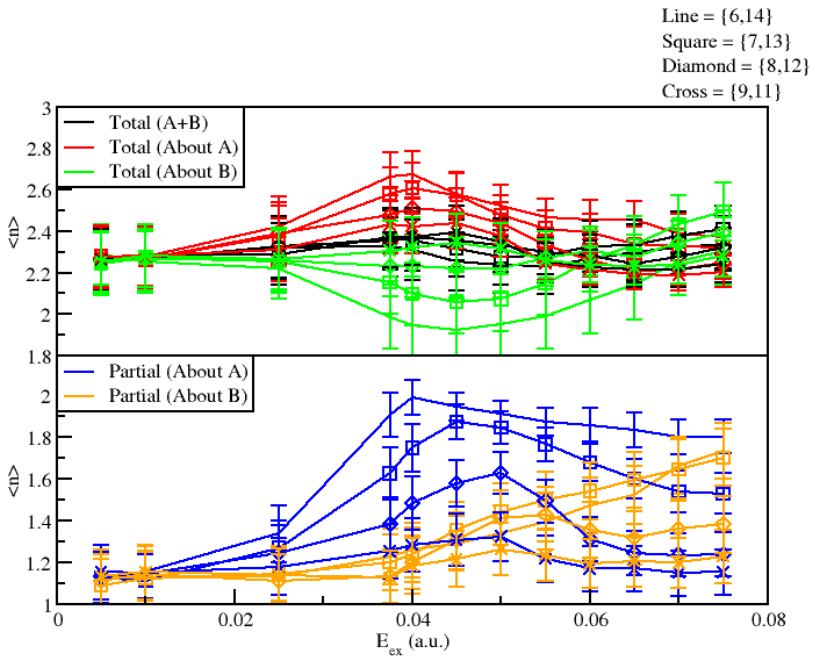
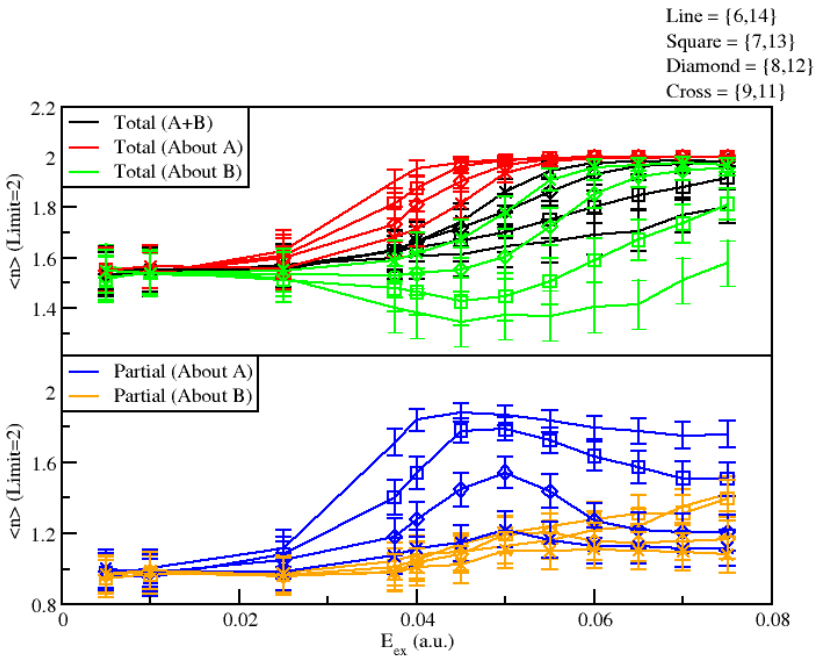


Figure 6.7: Cumulative $f(n)$ for a range of polarizability differences $\{\alpha_1, \alpha_2\}$ for a fixed $\langle\alpha\rangle = 10$ a.u. at varying field strengths $\mathbf{E}_{ex}$.

Figures 6.8(a) and **6.8(b)** give the mean coordination number vs. $\mathbf{E}_{ex}$, for all permutations of analysis as above. Calculations in **Figure 6.8(a)** are over all coordination numbers including higher order values (greater than $n = 2$). Whereas **Figure 6.8(b)** restricts calculations to $n = 0,\ 1\ \&\ 2$ only thereby reducing the noise generated from skewing the mean as a result of including the higher coordination. As the external field strength is increased three regimes may be identified.



(a) $\langle n \rangle_{max}$ = All.



(b) $\langle n \rangle_{max} = 2$.

Figure 6.8: Mean coordination number as a function of $\mathbf{E}_{ex}$, for the system above where $\langle \alpha \rangle = 10$ a.u. as before. **(a)** is over all coordination numbers whereas **(b)** is over only $n = 0,\ 1,\ 2$ possible coordination numbers, highlighting chain formation. The error bars are the true standard deviations about the sample mean.

1. **Low-field** ($\mathbf{E}_{ex} = 0 \rightarrow 0.04$ a.u.): Minimal chain formation occurs at lower field as a result of the lower magnitude of the induced dipole such that, irrespective of particle polarizability difference, the mean coordination numbers and by extension the final configurations, are all similar. As the applied field is increased and chain formation begins to occur, it can be seen that there is preferential 'A' (high particle polarizability) chain formation, increasingly so at higher $\Delta\alpha$. This is highlighted by the large increase in mean coordination for the *blue* curves (Partial A - considering the environments of all 'A' particles surrounding other 'A' particles) and relative slow increase in the *orange* curves (Partial B - considering the environments of all 'B' particles surrounding other 'B' particles) over the same range. Note again here that the presence of chains comprising entirely of 'A' particles, rather than a mixture of particle species 'A' and 'B', is due to the greater DID effect present on the higher polarizability, 'A' particles. In **Figure 6.8(b)** the total (A) curve (*red*) increases, levelling at $\langle n \rangle = 2$ with the higher $\Delta\alpha$ case arriving at this maximum value at lower $\mathbf{E}_{ex}$. Consequently the total (B) coordination number values drop mirroring this effect. Thus highlighting preferential 'A' chain formation in this region.

2. **Mid-field** ($\mathbf{E}_{ex} = 0.04 \rightarrow 0.06$ a.u.): For the mid-field region there are two competing factors contributing to the nuanced behaviour of the coordination curves. At a critical $\mathbf{E}_{ex}$ the DID on the 'B' particles finally becomes significant (as observed by the gradual increase in the number of chains exclusively made of 'B' particles, the *orange* curves in both graphs). As a result there is a turning point observed in the partial (A) graphs (*blue* curve) for which the number of 'A' particles surrounded by other 'A' particles decreases, implying 'B' particle inclusions and a mixture of species, both 'A' and 'B', in the chains formed. This is further highlighted by the simultaneous rise and fall of the total (A) graph

coupled with the fall and rise of the total (B) graph about the total (A+B) curve in **Figure 6.8(a)**.

3. **High-field** ($\mathbf{E}_{ex} = 0.06 \rightarrow 0.08$ a.u.): **Figure 6.8(b)** shows the slower, steadier rise in total coordination number over larger applied field for high $\Delta\alpha$ due to the increasingly delayed introduction of 'B' particles into the chains based entirely on the low DID contribution for the low α species. At very high applied field the mean coordination number plateaus at a constant value. This implies that all species, 'A' and 'B' are present in the chains. **Figure 6.8(b)** (*black* line for total coordination number about all species) highlights this result given the eventual levelling at $\langle n \rangle = 2$.

Therefore it is powerfully evident that there is a critical field for each pair of polarizabilities and the properties of the configurations can be tuned depending on the choice of species, field strength and polarizability difference. For $\mathbf{E}_{ex} = 0.05$ a.u. this corresponds to the maximum in the coordination peak of these species.

6.3.2 Chain Lengths

Mean chain lengths have also been calculated, as described in **Section 2.8.7** by using **Equation 2.8.13**, for the final configurations, at varying external field strengths. The same total and partial 'A' and 'B' particle metrics were also calculated as before. An infinite chain is observed as the limiting $\langle c \rangle$ which describes the case where only 2-coordinate particles exist in the system, allowed in the simulation due to the presence of periodic boundary conditions. As such, **Figure 6.9** highlights the formation of these infinite chains showing varying critical chain length formation fields which, depend on the polarizability difference. Firstly, it is shown from the upper window, that effective chain length increases as the applied field is increased. The *black* curves

give the total mean chain length considering both species 'A' (higher α) and 'B' (lower α) which increases with $\mathbf{E}_{ex}$ however, as also described in **Section 6.3.1**, the lower $\Delta\alpha$ systems reach a saturation of infinite chains at a lower field than the higher $\Delta\alpha$ species. This result can be explained by observing the *red* (total mean chain length concerning chains containing 'A' particles, with any 'B' only chains discounted) and *green* curves (total mean chain length concerning chains containing 'B' particles, with any 'A' only chains discounted).

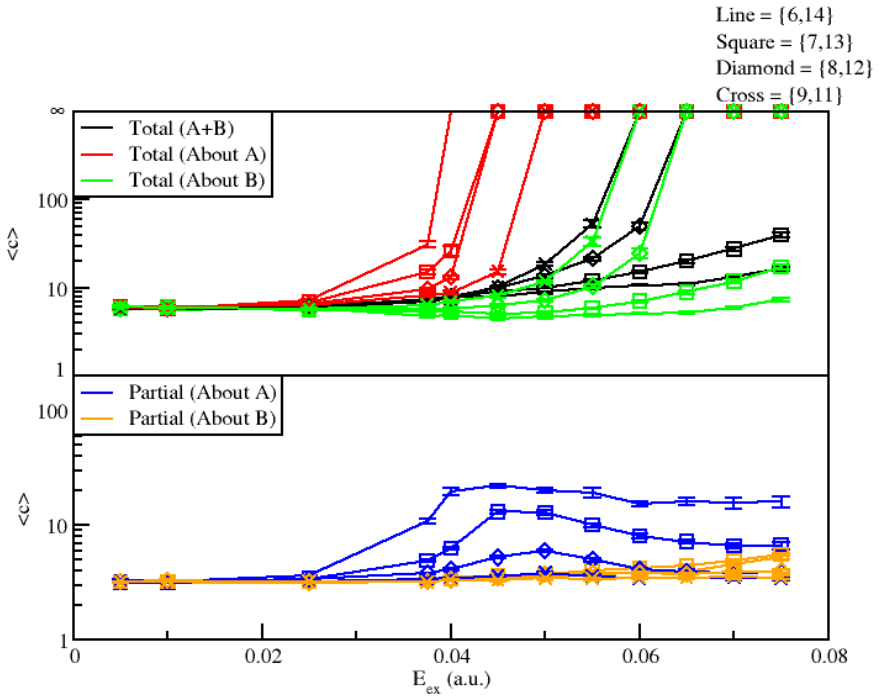


Figure 6.9: Mean chain length as a function of $\mathbf{E}_{ex}$ for the range of $\Delta\alpha$ as before ($\langle\alpha\rangle$ = 10 a.u.). Values at high $\langle c\rangle$ are indicative of infinite chains. The error bars are the true standard deviations about the sample mean.

Given that particles of a high polarizability have a greater DID effect at lower field, the 'A' (α_2 = 14 a.u.) reaches the infinite chain limit well before the 'B' (α_2 = 6 a.u.) does. This is due to the preferential formation of chains comprising of AAA species only at low field and the subsequent inclusion of 'B' species when the field

strength is increased further. This effect is again highlighted by the rise and fall in the partial mean chain length calculations (*blue* curve) at mid-range external field. Here the calculation measures the length of AAA species in chains only, which rises on formation as described but falls due to the increasing DID effect on 'B' species which allows the inclusion of 'B' species within chains. This effect is a de-mixing of bidisperse species followed by a mixing which leads to increased tunability of the liquids. For completeness, at low $\Delta\alpha$ such as the $\{\alpha_1, \alpha_2\} = \{9, 11\}$ pair, the species are relatively similar in polarizability, even though the 'A' species form preferential 'A' chains, this is at a higher relative field strength such that the 'B' inclusions are increasingly present in the chain formation process early on. The total (about B) curve (*green*) shows this with infinite chain saturation for highest $\alpha_1 = 9$ a.u. species at lower field than the other cases (*e.g.* $\alpha_1 = 6$ a.u.).

Section 5.5.1 previously described the utility of a chain length distribution calculation specifically with a comparison to analogous experimental work for a pseudo-monodisperse system. In that case, it is shown that for a system of aggregating particles, the coordination behaviour (measured through the mean coordination number) and the mean chain length distributions are intrinsically linked, such that knowledge of the statistics of one can lead to the recovery of the other. The probabilities (P_n) therefore (as defined in **Equation 5.5.5**) that a given particle with coordination number, n, is present in a configuration of this system as a member of a chain with mean length μ_s, can be shown graphically as in **Figure 5.6**. The process of chain formation in the monodisperse system closely follows the coordination profile of a shifted-geometric distribution for a compound Poisson chain aggregation process.

Therefore, given the utility of this calculation, a bidisperse analogue can be produced using the same calculation method as above, extended slightly given the mixing of two distinct species (A and B with high and low polarizability respectively). A

bidisperse system is selected where $\{\alpha_1, \alpha_2\} = \{7, 13\}$ a.u., $\mathbf{E}_{ex} = 0.05$ a.u. and the reduced density is fixed at $\rho^* = 0.4$. The lower window in **Figure 6.10** gives the probability distributions for this system, P_n for n = 0,1,2 as calculated for the monodisperse case, labelled 'tot' as it includes all species ('A' and 'B') in the calculation. The upper window in **Figure 6.10** shows the probability distribution functions where each species is taken to be independent of one another (*e.g.* 'A-A' denotes length of chains made up exclusively of 'A' chains and 'B-B' denotes length of chains made up exclusively of 'B' chains). Therefore the upper window mirrors the distribution behaviour of particles in the monodisperse system (given the selective calculation of each species) highlighting that the same type of aggregation process occurs (given the adherence to the ideal probability curves). Additionally the 'B-B' exclusive chains form at much lower mean chain lengths than the 'A-A' chains. For example, the P_2 distribution for 'A-A' chains (*green* circle points) is over the range $0.5 \leq \mu_s \leq 8$ a.u. whilst the 'B-B' chains (*purple* square points) are only present in the $0 \leq \mu_s \leq 0.5$ a.u. range. The larger range of the 'A-A' curves highlights earlier arguments for preferential 'A' chain formation hence longer chains obtained before 'B' chain formation in the system.

The shape of the curves in the upper window again agree closely with the model for particle-chain formation in which 0-coordination particles first aggregate to form singly-coordinated chains (P_0 decreases whilst P_1 increases), 2-coordinate particles form as these small chains join together or join to isolated particles (P_0 further decreases, there is a turning point for P_1 which now decreases and P_2 increases to a maximum). The lower window **Figure 6.10** does not display this behaviour. There is a small range of μ_s (between $\mu_s = 2$ a.u. and $\mu_s = 3$ a.u.) whereby there are effectively two probabilities for a given particle to exist in a chain. This refers again to the initial formation of 'A'-only chains (increased μ_s), over time the DID becomes large enough

on ‘B’ particles such that they are able to form chain inclusions (alternating particle species) and consequently μ_s decreases.

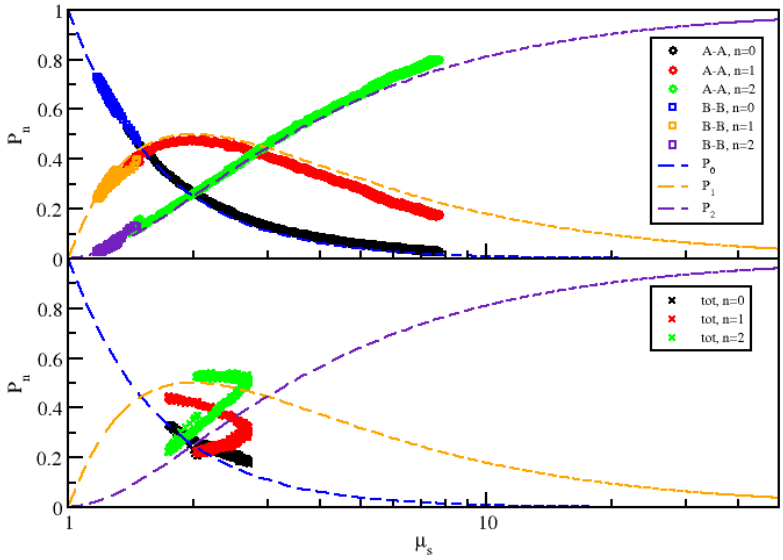


Figure 6.10: Mean chain length distributions for the bidisperse, $\{7, 13\}$ system where $\mathbf{E}_{ex} = 0.05$ a.u.. The lower window is the calculation including all species (‘tot’) and the upper window shows the same calculation for each species (‘A-A’ or ‘B-B’ only).

Figure 6.10 shows a single example, $\{\alpha_1, \alpha_2\} = \{7, 13\}$ a.u., of the chain length distributions for a bisdisperse system. When $\Delta\alpha$ is varied then **Figure 6.11** is produced highlighting the migration from the monodisperse set (lowest window, labelled $\{10, 10\}$ a.u.) to the high $\Delta\alpha = 10$, bidisperse analogue (highest window, labelled $\{5, 15\}$ a.u.), with all other conditions remaining constant. Note: the monodisperse case is calculated with half of the particles randomly selected as ‘A’ and half randomly selected as ‘B’ in order to compare the change from mono- to bidisperse systems. When moving from low to high $\Delta\alpha$ there are a number of interesting changes

to the system. First, and most strikingly the 'A-A' chains are shown to grow to a much longer mean length (*black*, *red* and *green* curves), shown to exceed an average length of $\mu_s = 10$ for the $\Delta\alpha = 10$ case. Again this can be explained by preferential 'A' particle aggregation of the (higher α species) given the large DID effect forming more energetically favourable chains than for a mixed species analogue. At low $\Delta\alpha$ the species are indistinguishable therefore the maximum 'A-A' or 'B-B' chain length is lower in addition to the lower maximum polarizability species present which stunts the formation of more favourable, longer chains (lower 'tot' chain length).

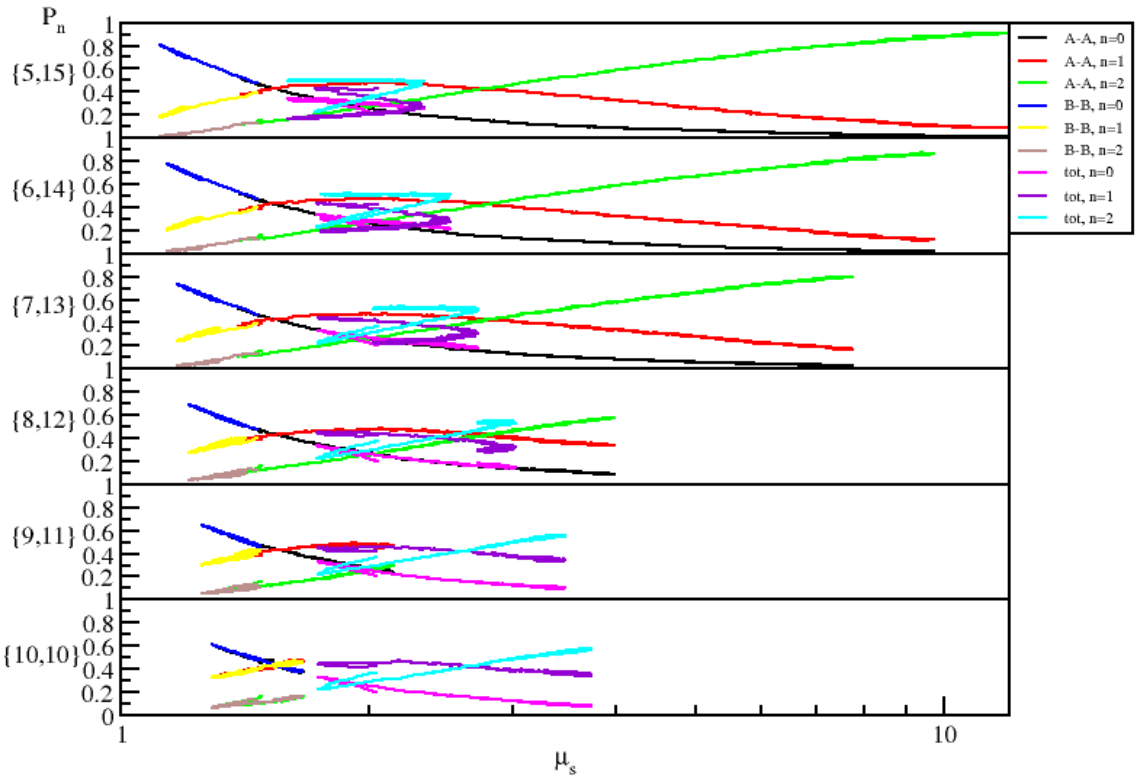


Figure 6.11: Mean chain length distribution for the bidisperse system over the range of $\Delta\alpha$ such that $\langle\alpha\rangle = 10$ a.u. and $\mathbf{E}_{ex} = 0.05$ a.u..

Consequently as $\Delta\alpha$ increases the 'B-B' chain length shifts to lower μ_s (*blue*, *yellow*

and *brown* curves) approaching a value of 1 which implies that the low α species do not form chains in this system, remaining liquid-like whilst the 'A' species form long single stranded chains. Finally as is most evident with the *cyan* ($n = 2$) and *purple* ($n = 1$) curves for the calculation over all particles (total), as $\Delta\alpha$ increases these lines morph from a description of a single species to that of two species (either part of a chain or not able to form one). Given at high $\Delta\alpha$ the polarizability difference is much larger and that the 'A' particles are in chains whilst the 'B' particles are trapped between these chains, then there is a dichotomy represented here by the possibility of two P_n probabilities at each mean chain length.

6.3.3 Aggregation Over Time

Over the course of the quenching run the particles aggregate until chain formation becomes saturated. The time domain is the natural 'reaction coordinate' when considering chain formation as a growth process, therefore this section briefly investigates key coordination parameters as a function of time in the bidisperse system. Here the external field is fixed, therefore there is a limit to the magnitude of the induced dipole on each particle and hence the speed at which chains are produced (along with the length of the chains) depends on the value of this external field. **Figure 6.12** shows the evolution in the frequency of particles, $f(n)$ with coordination number, n over time for the $\Delta\alpha = 6$, $\{\alpha_1, \alpha_2\} = \{7, 13\}$ a.u. system with fixed $\mathbf{E}_{ex} = 0.05$ a.u.. **(a)** shows the calculation with respect to all particle species. **(b)** and **(c)** give the total coordination evolution about each 'A' or 'B' particle species whereas **(d)** and **(e)** give the coordination number evolution of only 'A' species and only 'B' species respectively. As highlighted in the total (A+B) window, **(a)**, the number of 2-coordinate species tend to increase over time implying chain formation over the course of the run.

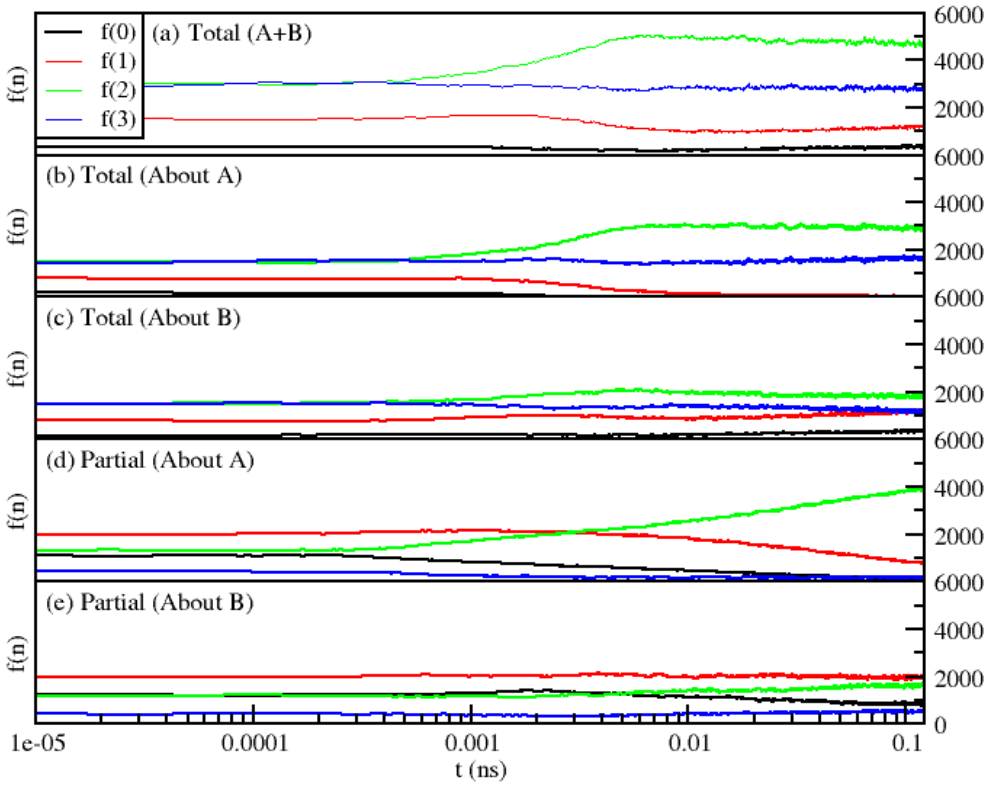


Figure 6.12: A set of coordination number frequency (f_n) curves as a function of time for the bidisperse, $\Delta\alpha = 6$, $\{\alpha_1, \alpha_2\} = \{7, 13\}$ a.u. system with fixed $\mathbf{E}_{ex} = 0.05$ a.u.. **(a)** shows the calculation with respect to all particle species. **(b)** and **(c)** give the total coordination evolution about each 'A' or 'B' particle species whereas **(d)** and **(e)** give the coordination number evolution of only 'A' species and only 'B' species respectively.

The number of two-coordinate species in the 'Partial A' system, **(d)** increases as $f(1)$, $f(0)$ and $f(3)$ decreases such that $\langle n \rangle \to 2$ commencing early in the run complemented by a slower rise and plateau for $f(2)$ in the 'Partial B' system, **(e)**. This confirms much of what is known to happen over time, *i.e.* preferential aggregation of the larger polarizability species (A) with the lower polarizability species (B) which is more liquid-like and trapped between chains of 'A' particles. The $\{7, 13\}$ a.u., $\mathbf{E}_{ex} = 0.05$ a.u. case corresponds to the point of inflection in **Figure 6.5** as discussed

previously. **(b)** and **(c)** are included to highlight the differences in environment around 'A' particles (members of chains highlighted by the increase in $f(2)$ and rapid decrease in $f(1)$) and 'B' particles (similar environments for $f(1)$, $f(2)$ and $f(3)$).

Section 4.3.2 first provides an indication to the usefulness of the metric $\Delta p(k)$. It describes the coordination environment of particles in a monodisperse system with respect to an entirely random configuration. To properly analyse any significant structural differences in a bidisperse system therefore, $\Delta p_A(k)$ is again calculated with the particle type 'A' and 'B' defined purely in terms of their polarizability (rather than the magnitude of the dipole moment in the context of the distribution of moments). This does retain the possibility that, when considering two particles of different polarizabilities, the particle with the higher polarizability may house the lower moment, depending upon the detail of the surrounding environment. **Figure 6.13** describes the evolution in $\Delta p_A(k)$ and $\Delta p_B(k)$ over time for the same set as in the coordination number analysis above.

As observed, $\Delta p_A(2)$ increases steadily over the course of the run implying increased formation of AAA triplets and hence chains made entirely of 'A' particles ($k = 1$ and $k = 0$ sets mirror this effect by decreasing in tandem). The y-axis ($\Delta p_A(k)$) is also scaled by $|\Delta p_A(k)_{lim}|$, the limit of total chain formation for A particles, the values of which are given below:

- $k = 2$ (AAA), $|\Delta p(2)| = |1 - \frac{1}{4}| = \frac{3}{4}$.
- $k = 0$ (BAB), $|\Delta p(0)| = |0 - \frac{1}{4}| = \frac{1}{4}$.
- $k = 1$ (BAA or AAB), $|\Delta p(1)| = |0 - \frac{1}{2}| = \frac{1}{2}$.

The more erratic nature of the curve in $\Delta p_B(0)$ (BBB formation) implies that the 'B' particles are less stable and trapped between walls of AAA chains.

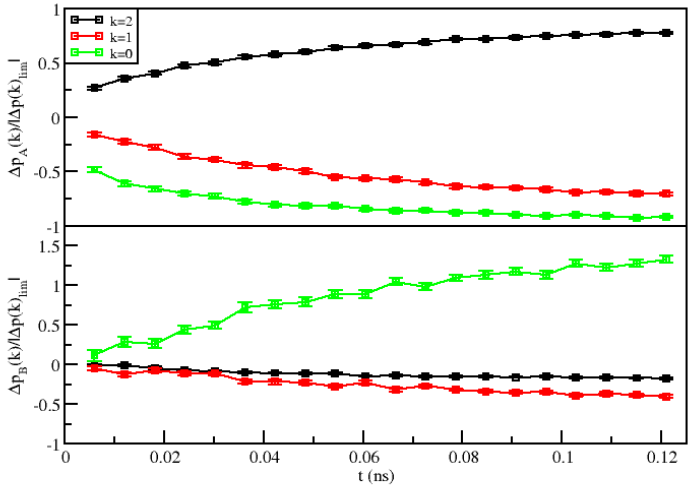


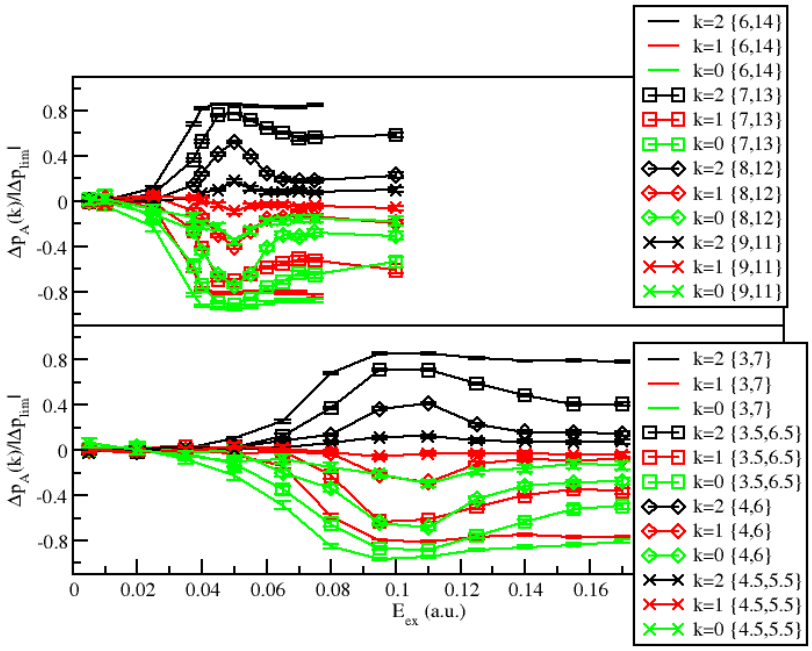
Figure 6.13: The evolution of $\Delta p_A(k)$ (upper) and $\Delta p_B(k)$ (lower) over time for the $\Delta\alpha = 6$, $\{\alpha_1, \alpha_2\} = \{7, 13\}$ a.u. case at $\mathbf{E}_{ex} = 0.05$ a.u.. The error bars are the true standard deviations about the sample mean.

6.4 Scaling

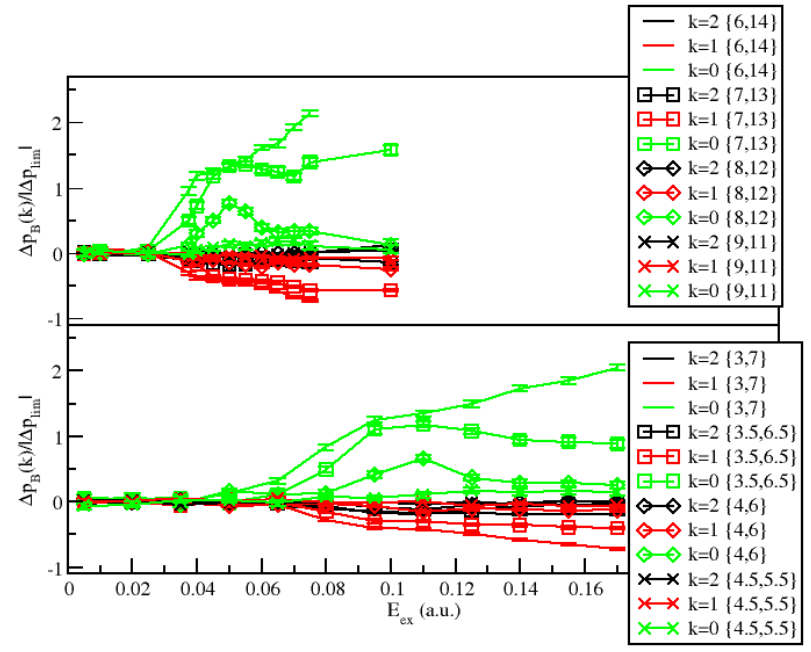
The following section will show, principally by using the metric $\Delta p_A(k)$, that the bidisperse systems can be scaled based on the choice of variables ($\Delta\alpha$, $\langle\alpha\rangle$ and the ratio $\frac{\Delta\alpha}{\langle\alpha\rangle}$) which indicates that a general classifiable behaviour exists within this model.

6.4.1 Scaling With Fixed $\langle\alpha\rangle$

Figure 6.14(a) shows $\Delta p_A(k)$ (for $k = 0, 1, 2$) as a function of the applied field, for a range of $\{\alpha_1, \alpha_2\}$ pairs with fixed $\langle\alpha\rangle = 10$ a.u. (top window) and $\langle\alpha\rangle = 5$ a.u. (bottom window). The y-axis is scaled by $|\Delta p_A(k)_{lim}|$, the limit of total chain formation for A particles (values of which are given in **Section 6.3.3**). At low fields, $\Delta p_A(k) \sim 0$ reflecting the lack of chain formation. As the field increases $\Delta p_A(2)$ becomes positive (and $\Delta p_A(0)$ becomes negative) indicating a preferred formation of AAA chains (chains comprising the more polarizable species only).



(a) $\Delta p_A(k)/|\Delta p(k)_{lim}|$.



(b) $\Delta p_B(k)/|\Delta p(k)_{lim}|$.

Figure 6.14: Scaled coordination number difference functions as a function of $\mathbf{E}_{ex}$. The top window in each set has a fixed $\langle\alpha\rangle = 10$ a.u. whilst the bottom window has a fixed $\langle\alpha\rangle = 5$ a.u.. The error bars are $\sigma/\sqrt{50}$.

The $\Delta p_A(0)$ and $\Delta p_A(1)$ functions effectively mirror $\Delta p_A(2)$ since the preferential formation of AAA chains (when $\Delta p_A(2) > 0$) must be associated with the relative lack of the AAB or BAB units. For large $\Delta\alpha$, $\Delta p_A(2)$ increases and reaches a plateau at the high field limit indicating the AAA-dominated chains to be stable to high field. For small $\Delta\alpha$, all of the $\Delta p_A(k)$ functions tend to zero (as expected for the limit that $\Delta\alpha \longrightarrow 0$ as the two species become equivalent).

Potentially the most interesting behaviour is displayed at intermediate values of $\Delta\alpha$. For each window, $\Delta p_A(2)$ shows a maximum at $\mathbf{E}_{ex} \sim 0.05$ a.u. (for $\langle\alpha\rangle =$ 10 a.u., upper panel) and $\mathbf{E}_{ex} \sim 0.1$ a.u. (for $\langle\alpha\rangle = 5$ a.u., lower panel) indicating that there is a range of applied fields for which there is greater preference for AAA-chain formation compared to that at the high field limit. This effect is observed in the coordination number statistics, as shown previously (**Section 6.3.1**). It is interesting to note that the same basic features are exhibited for both mean polarizabilities, however the applied field required to induce preferential AAA-chain formation is greater for $\langle\alpha\rangle = 5$ a.u. than for $\langle\alpha\rangle = 10$ a.u. though the curves can be shown to collapse onto each other after introducing the scaling functions (see below).

Figure 6.14(b) shows the analogous functions about B species, $\Delta p_B(k)$, for $\langle\alpha\rangle = 10$ and 5 a.u. (top and bottom figure respectively). Here the $k = 0$ (corresponding to BBB chains) have large positive values indicating the formation of BBB triplets. It is most apparent at large field and large $\Delta\alpha$, where the extreme values of $\Delta p_B(0)$ occur showing that BBB triplets exist in the system given exclusively as a by-product of the already established AAA chains, formed at lower fields preferentially. This graph is included for completeness and as is evident from the analysis above, the value of $\Delta p_A(2)$ alone is sufficient to describe the nuances of this bidisperse system. **Figure 6.15** (left panel) shows the same data as in **Figure 6.14(a)** for $\Delta p_A(2)$ only, with the field scaled to the size of the mean average dipole ($\langle\mu\rangle = \langle\alpha\rangle \cdot \mathbf{E}_{ex}$) therefore

$\Delta p_A(k)$ is shown to have predictable behaviour over this range. Chain formation is expected to be dominated by the attractive dipole-dipole interactions, therefore it can be expected that the $\Delta p_A(k)$ functions determined at different $\langle\alpha\rangle$, scale onto each other given that $\langle\mu\rangle = \langle\alpha\rangle \cdot \mathbf{E}_{ex}$ in the absence of DID effects. As a result, the data sets for $\langle\alpha\rangle = 5$ a.u. and $\langle\alpha\rangle = 10$ a.u. scale onto each other reasonably well (left in **Figure 6.15**), however there is a systematic shift to lower $\langle\alpha\rangle \cdot \mathbf{E}_{ex}$ as $\langle\alpha\rangle$ increases which may be rationalised as the DID effect.

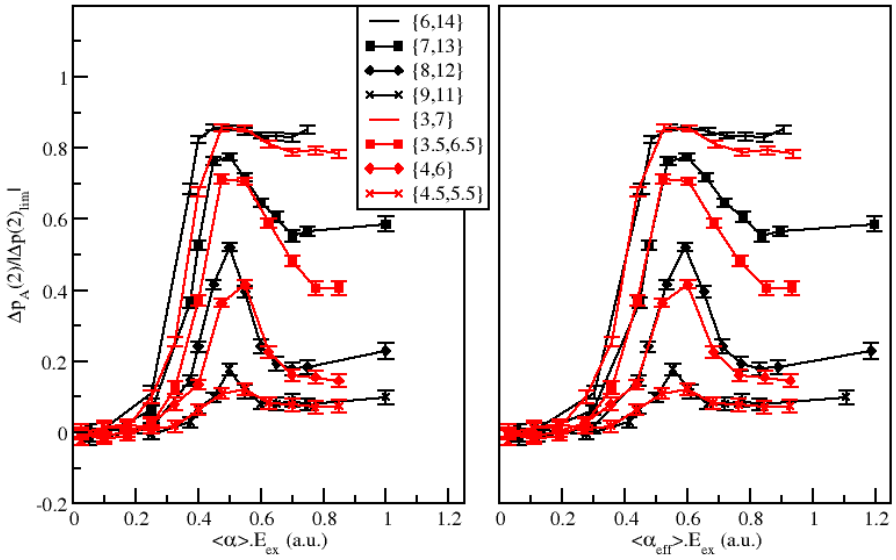


Figure 6.15: Left: Scaled $\Delta p_A(2)$ as a function of $\langle\alpha\rangle \cdot \mathbf{E}_{ex}$ for two sets of bidisperse runs, $\langle\alpha\rangle = 10$ a.u. and $\langle\alpha\rangle = 5$ a.u.. Right: the same calculations as a function of $\langle\alpha_{eff}\rangle \cdot \mathbf{E}_{ex}$ which shows greater scaling agreement in, peak position, initial gradient increase and levelling value. The error bars are the true standard deviations about the sample mean.

The right panel in **Figure 6.15** shows the same functions scaled by a mean 'effective' polarizability, $\langle\alpha_{eff}\rangle$, that is, the polarizability required to reproduce the

total dipole moments (including the first order DID correction) such that

$$\mu^{(1)} = \boldsymbol{\mu}_{ex} + \mu^{(1)}_{DID} = \boldsymbol{\mu}_{ex} + \frac{4\alpha_i^2 \mathbf{E}_{ex}\zeta(3)}{r^3} = \alpha_{eff} \cdot \mathbf{E}_{ex}. \tag{6.4.1}$$

As a result,

$$\frac{\alpha_{eff}}{\alpha_i} = \left(1 + \frac{4\alpha_i\zeta(3)}{r^3}\right) \tag{6.4.2}$$

where α_i is the species polarizability ($i = 1$ or 2 for the bidisperse system), r is the inter-particle distance take from the value at the first peak in the pair distribution function and $\zeta(3) = 1.2021$. The mean effective polarizability is calculated as $\langle\alpha_{eff}\rangle = \frac{1}{2}(\alpha_{2,eff} + \alpha_{1,eff})$ and the correction is made for each species present. Thus, the ratio of the effective polarizability to the actual polarizability scales linearly with increasing α for the first order DID correction. Consequently both the initial increase in $\Delta p_A(k)$ at low field and the location of the curve peaks, now map onto each other very well.

6.4.2 Scaling with $\Delta\alpha$

Figures 6.16(a) and **6.16(b)** (left panels) show $\Delta p_A(k)$ and $\Delta p_B(k)$ as a function of the polarizability difference, $\Delta\alpha$, at different combinations of $\langle\alpha\rangle$ and $\mathbf{E}_{ex}$ (such that $\langle\alpha\rangle \cdot \mathbf{E}_{ex}$ is again held fixed at 0.5 a.u.). The fraction of AAA chains increases as $\Delta\alpha$ increases, shown by the increase in $\Delta p_A(2)$ (with $\Delta p_A(1)$ and $\Delta p_A(0)$ simultaneously decreasing). $\Delta p_B(0)$ increases much in the same way as $\Delta p_A(2)$ (though less steeply) highlighting the formation of BBB chains after the formation of established AAA chains. This de-mixing is more apparent at low field given that in this case, $\Delta p_B(0)$ is lower at high $\Delta\alpha$. For the high field case, $\Delta p_B(0)$ increases from high to low $\Delta\alpha$, with a more similar gradient to the analogous $\Delta p_A(2)$. This shows the mixing effect with the 'A' and 'B' species (being of similar polarizability) forming mixed chains more immediately. As a side-note for large field ($\mathbf{E}_{ex} = 0.25$ a.u.) at high $\Delta\alpha$

(= 2 a.u.) there is a slight dip in $\Delta p_B(0)$ (mirrored by an slight increase in $\Delta p_B(1)$ and $\Delta p_B(2)$) which is only present on this graph as a result of the fixed time-scale. With a large relative $\Delta\alpha$ the formation of BBB chains is delayed and it is expected that at lengthier simulation times the values will plateau as shown in the other field cases. As a result, the degree of de-mixing in the 'A' and 'B' sublattices, therefore, is dependent upon the contrast in induced dipole moments. **Figures 6.16(a)** and **6.16(b)** (right panels) show the corresponding functions scaled by the mean polarizability. A two-state model can be used to justify how the curves generated at different combinations of $\langle\alpha\rangle$ and $\mathbf{E}_{ex}$ can fall onto an approximately universal curve. In a two state model [185, 186] an equilibrium is established between two species:

$$A \Leftrightarrow B \tag{6.4.3}$$

The free energy of mixing is given by

$$\Delta G = RT[x_A \ln(x_A) + (1 - x_A)\ln(1 - x_A)] + W x_A(1 - x_A), \tag{6.4.4}$$

where x_A is the mole fraction of species A and W is a non-ideal mixing parameter which is traditionally written as a difference in the interaction energies of the like-like and like-unlike terms. In this case the major interactions are the dipole-dipole terms and so,

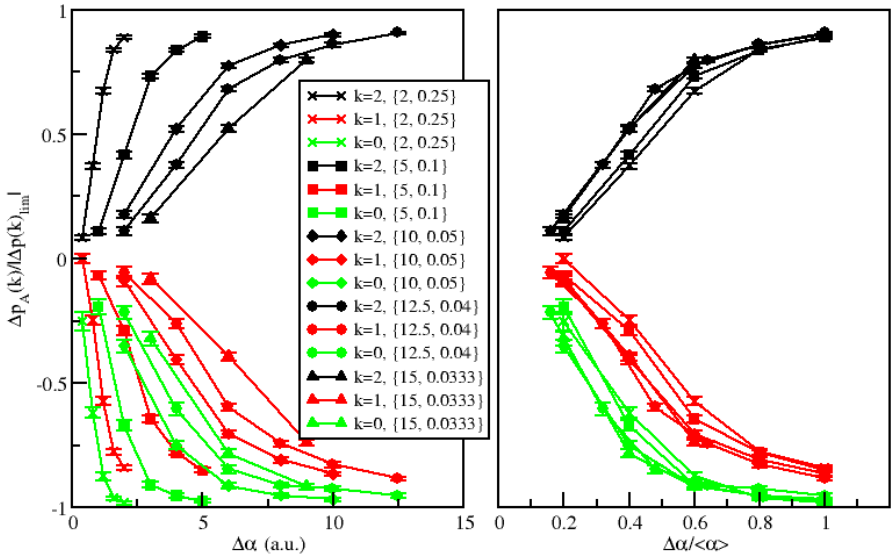
$$W = \beta(\boldsymbol{\mu}_1^2 + \boldsymbol{\mu}_1^2 - 2\boldsymbol{\mu}_1\boldsymbol{\mu}_2)r^{-3}. \tag{6.4.5}$$

Now, $\boldsymbol{\mu}_i = \alpha_i \cdot \mathbf{E}_{ex}$ and so

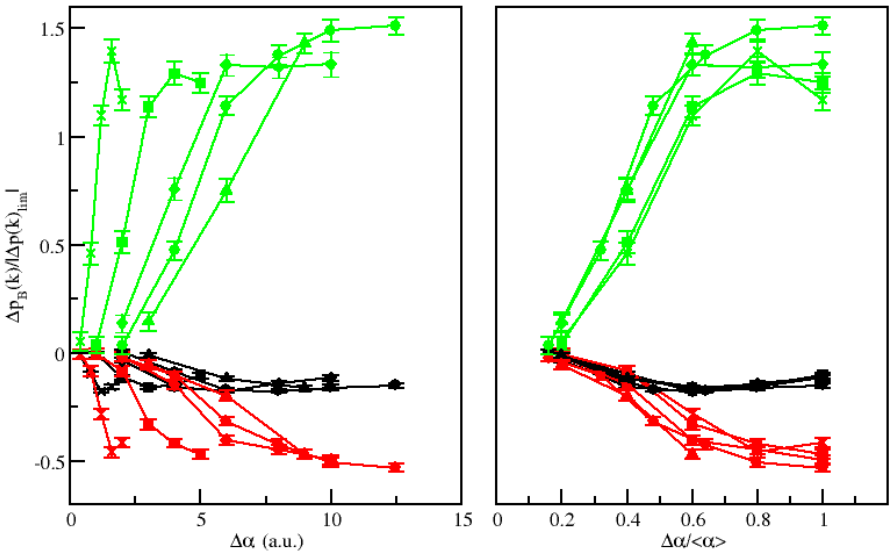
$$\begin{aligned} W &= \beta\mathbf{E}_{ex}^2(\alpha_1^2 + \alpha_2^2 - 2\alpha_1\alpha_2)r^{-3} \\ &= \beta\mathbf{E}_{ex}^2\Delta\alpha^2 r^{-3}. \end{aligned} \tag{6.4.6}$$

Now, $\langle\mu\rangle = \langle\alpha\rangle \cdot \mathbf{E}_{ex}$ and so

$$W = \beta\langle\mu\rangle^2 \left\{\frac{\Delta\alpha}{\langle\alpha\rangle}\right\}^2 r^{-3}. \tag{6.4.7}$$



(a) $\Delta p_A(k)/|\Delta p(k)_{lim}|$.



(b) $\Delta p_B(k)/|\Delta p(k)_{lim}|$.

Figure 6.16: Coordination number difference functions, $\Delta p(k)$ $(k = 0, 1, 2)$ as a function of $\Delta\alpha$ (left) and the ratio $\dfrac{\Delta\alpha}{\langle\alpha\rangle}$ (right) for a selection of $\{\langle\alpha\rangle, \mathbf{E}_{ex}\}$ pairs (as shown in the legend in a.u.). **(a)** shows $\Delta p_A(k)/|\Delta p(k)_{lim}|$ and **(b)** shows $\Delta p_B(k)/|\Delta p(k)_{lim}|$. The error bars are the true standard deviations about the sample mean.

$\beta\langle\mu\rangle^2 r^{-3}$ has units of energy and is effectively a polarization energy. As a result, $\beta = \frac{1}{2}\langle\alpha\rangle$. Therefore as is shown in the right panels, this method of scaling, by ratio, $\frac{\Delta\alpha}{\langle\alpha\rangle}$ can be justified.

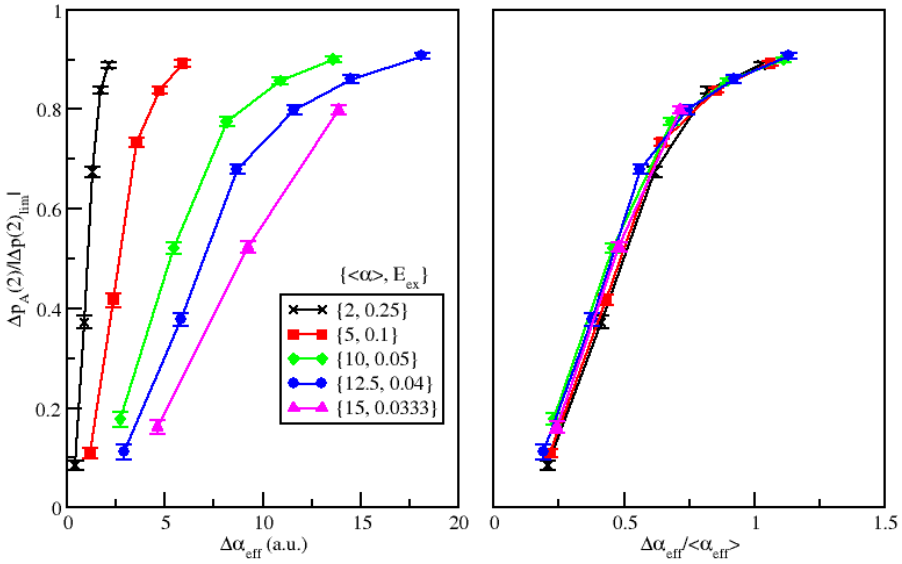


Figure 6.17: Coordination number difference functions, $\Delta p_A(2)/|\Delta p(2)_{lim}|$ as a function of $\Delta\alpha_{eff}$ (left) and the ratio $\dfrac{\Delta\alpha_{eff}}{\langle\alpha_{eff}\rangle}$ (right) for a selection of initial set $\{\langle\alpha\rangle, \mathbf{E}_{ex}\}$ pairs (as shown in the legend in a.u.). This scaling shows excellent agreement and as such the system is shown to have predictable behaviour. The error bars are the true standard deviations about the sample mean.

A further improvement can be made by scaling the polarizability difference, using the effective polarizability as described in the previous section (**6.4.2**), to a function of

$$\frac{\Delta\alpha_{eff}}{\langle\alpha_{eff}\rangle} \tag{6.4.8}$$

where

$$\Delta\alpha_{eff} = \alpha_{2,eff} - \alpha_{1,eff} \tag{6.4.9}$$

and again

$$\langle \alpha_{eff} \rangle = \frac{1}{2} \left(\alpha_{2,eff} + \alpha_{1,eff} \right). \tag{6.4.10}$$

Figure 6.17 shows this scaling showing $\Delta p_A(2)/|\Delta p(2)_{lim}|$ only as a function of $\Delta\alpha_{eff}$ (left) and the ratio $\frac{\Delta\alpha_{eff}}{\langle \alpha_{eff} \rangle}$ (right) for a selection of initial set $\{\langle \alpha \rangle, \mathbf{E}_{ex}\}$ pairs (as shown in the legend in a.u.). As is observed the scaling regime shows excellent agreement and each curve collapses onto a general, predictable value.

6.5 Field Ramping and Hysteresis

The quenching method, as first described in **Section 4.1**, gives rise to the characteristic chain-formation in the bidisperse systems as shown in the previous section. For the quenches, a field of a given strength is applied at the start of the simulation and the system structure is allowed to evolve. There are, however, potential alternatives to this strategy. In this section for example, the effect of gradually increasing ('ramping') the field is investigated, following the simulation as it progresses. The method of field ramping used is as follows: the starting configurations are taken at $T = 10000K$ as before and the system is cooled to $50K$ at zero field. The field is then ramped from $\mathbf{E}_{ex} = 0.005 \rightarrow 0.1$ a.u. in steps of $\Delta\mathbf{E}_{ex} = 0.005$ a.u. (every 10000 steps $\sim 0.00605ns$). **Figure 6.18** shows the total potential energy (including the interaction energy with the applied field per particle, $U^{tot} - \boldsymbol{\mu}.\mathbf{E}_{ex}$), for an example case ($\{\alpha_1, \alpha_2\} = \{7, 13\}$ a.u.) as a function of time. At each increase in the external field, the total energy changes (as expected). The initial perturbation of the system on changing field is clear in the response of the energy. However, the initial 'jump' in energy is quenched out relatively rapidly. The inset highlights an example of this step change at large t.

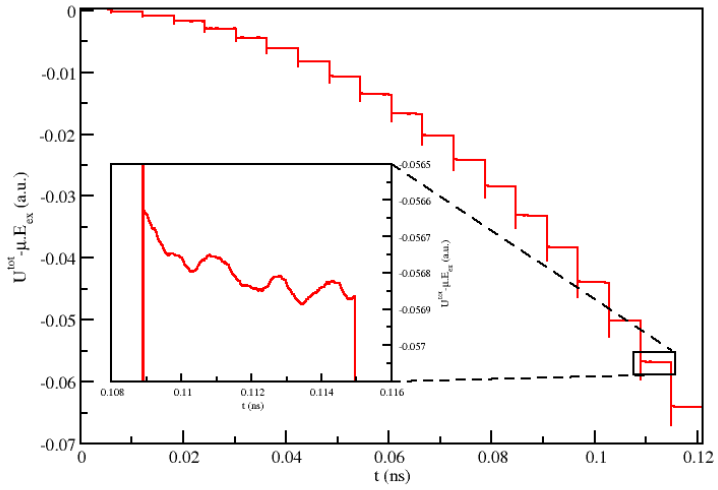


Figure 6.18: The evolution of total energy (including the interaction energy with the applied field, per particle) as a function of time, as the field is ramped sequentially for the bidisperse $\{\alpha_1, \alpha_2\} = \{7, 13\}$ a.u. set.

6.5.1 Coordination Environments

This section describes the effect on particle coordination environments when ramping the field using the fixed conditions: $\{\alpha_1, \alpha_2\} = \{7, 13\}$ a.u. and $\rho^* = 0.4$. A comparison can then be made to the quenching runs under analogous conditions. **Figure 6.19** below shows the evolution of mean coordination number as a function of time, **(a)** for the original quenching method at a fixed $\{\alpha_1, \alpha_2\} = \{7, 13\}$ a.u., $\mathbf{E}_{ex} = 0.05$ a.u. and **(b)** with the field ramped over time (again $\{\alpha_1, \alpha_2\} = \{7, 13\}$ a.u.). The form of the ramping curve closely resembles the quenching analogue (see **Figure 6.8(a)** as a function of field), with a couple of key feature differences. Firstly the total (A+B), total (about A) and total (about B) curves are extremely similar over the range of fields, however the partial (about A) and partial (about B) curves behave differently. This implies that the chains are less de-mixed than in the quenching runs (*i.e.* are made up of a mixture of 'A' and 'B' species). Furthermore the *blue* partial (about A) curve flattens at $\langle n \rangle \sim 1.5$ in **Figure 6.19(b)** and does not form the characteristic inflection point, as in the quench run at $\mathbf{E_{ex}} \sim 0.05$ a.u. and $\langle n \rangle \sim 1.9$ (lower window

in **Figure 6.8(a)**). This is understandable, given that as the field increases gradually over time, both 'B' particles (low α) and 'A' particles (high α) have limited scope for movement before the field is ramped up again. Eventually the field increases to a certain value such that the DID effect is similar for both species, then the 'B' particles in closer proximity given reduced movement to 'A' particles, form chains.

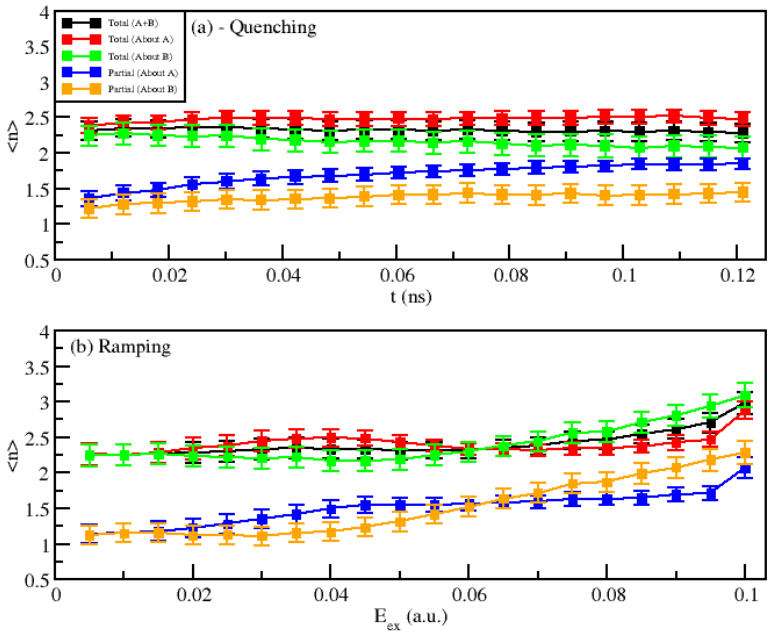


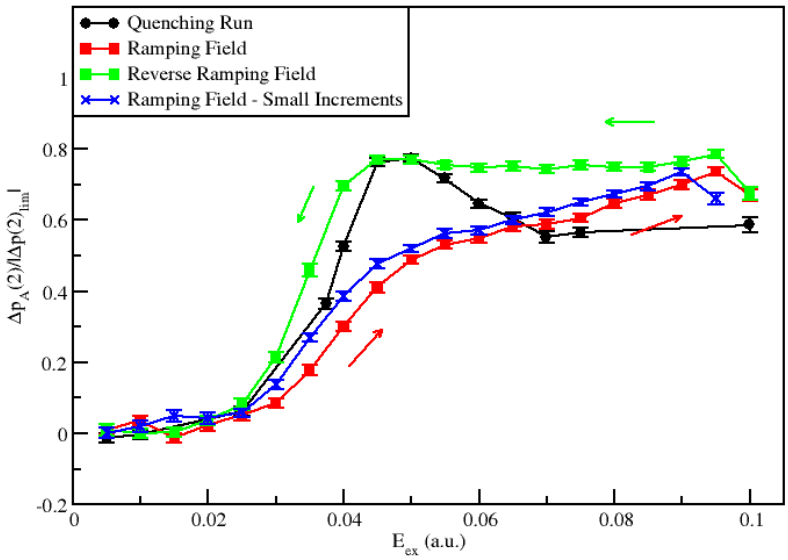
Figure 6.19: Upper: $\langle n \rangle$ as a function of time for the $\{\alpha_1, \alpha_2\} = \{7, 13\}$ a.u., $\mathbf{E}_{ex} = 0.05$ a.u. standard quenching run (as used in the majority of this work). Lower: $\langle n \rangle$ as a function of $\mathbf{E_{ex}}$ for the $\{7, 13\}$ a.u. case when sequentially ramping the field. The error bars are $\sigma/\sqrt{50}$.

This is further highlighted by the plateau of the partial (about A) curve (*blue*) which persists over a long field range until the extreme field limit, whilst the partial (about B) curve shows a steady increase (albeit a slower increase than in **Figure 6.19(b)**). The 'total' (over 'A' and 'B') curves remain similar in both schemes as the extent of chain formation remains the same irrespective of 'A' and 'B' composition.

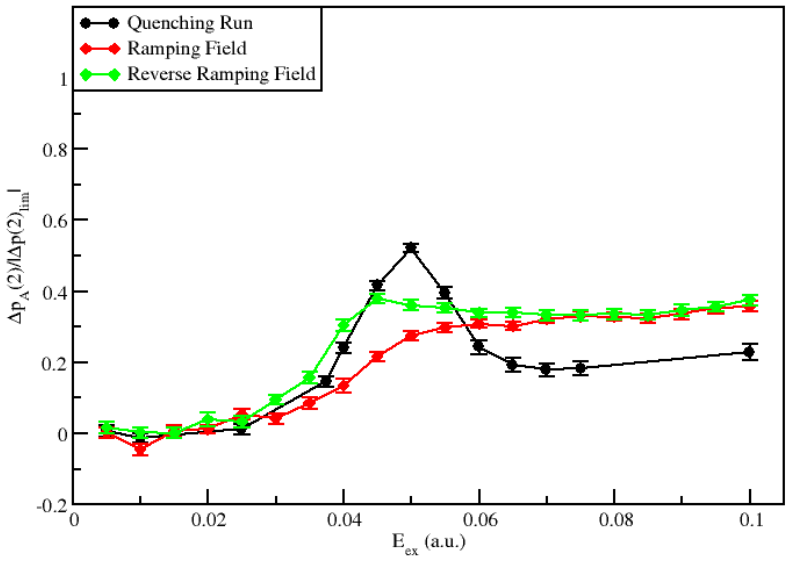
Figure 6.20 shows $\Delta p_A(2)$ calculated during the ramping simulations and compared to that observed from the quenches for two polarizability pairs; (**(a)** - $\{7, 13\}$ *a.u.* and **(b)** - $\{8, 12\}$ *a.u.*). Once the high field limit has been reached, the field may be ramped downwards (reducing the field) at the same intervals as the increasing field (*green* curves). Ramping the field results in a gradual increase in $\Delta p_A(2)$ (the metric showing AAA chain 'excess'). **Figure 6.20(a)** highlights the polarizability pair of particles, $\{7, 13\}$ a.u. and includes the *blue* curve which gives a finer increment of field changing (after each step rather than after every 10000 steps). There are three basic regimes which can describe the behaviour exhibited in the figures. At low field (up to $\mathbf{E}_{ex} = 0.03$ a.u.) there is no significant chain formation, as confirmed using the snapshots (**Figure 6.22**), therefore the configurations remain isotropic and the field is not high enough to drive particle aggregation for this polarizability range. In the intermediate field range ($\mathbf{E_{ex}} = 0.03 \rightarrow 0.07$ a.u.) there is the characteristic maximum peak for the standard quenching runs as discussed in **Section 6.4.1** where the number of 'A' particle species present in chains rapidly increases in comparison to those generated by ramping the field over the same range. As discussed before the ramping runs have lower $\Delta p_A(k)$ in this region, principally due to the lack of reorganisation time given the field ramping process is quick over this time scale and particle positions are effectively 'frozen in'. In order to prove that the argument is kinetically (particle proximity) and not thermodynamically driven (due to energy differences) **Figure 6.21** (upper panel) shows the total energy minus the interaction with the external field, $U^{tot} - \boldsymbol{\mu} \cdot \mathbf{E}_{ex}$ as a function of applied field for the systems exhibited in **Figure 6.20**. **Figure 6.21** (lower panel) shows the polarization energy, again for the same systems. The energetics highlight, both for the quenching and ramp-generated configurations that any differences are relatively low (within the standard deviation error about the mean). As stated above, the sys-

tem (quenching runs) falls out of thermodynamic equilibrium (goes through a glass transition) on cooling. The energy differences quoted below correspond to temperatures of around $100K$ (i.e. much larger than the quench temperature of $T = 50K$) highlighting how the system has settled into local metastable energy minima. For $\{\alpha_1, \alpha_2\} = \{8, 12\}$ a.u. at $E_{ex} \sim 0.05$ a.u. the quenched configurations are marginally more stable (by $\Delta U \sim 0.18$kJmol^1 and for a comparison, 0.4kJmol^1 more stable in the $\{\alpha_1, \alpha_2\} = \{7, 13\}$ a.u. case). At high fields (away from the critical field at which the peak occurs) the energetic balance is reversed ($\{\alpha_1, \alpha_2\} = \{7, 13\}$ a.u. compared to $\{8, 12\}$ a.u.) with energy differences between ramped and quenched runs of $\Delta U \sim 0.47$kJmol^1 and 1.50kJmol^1 respectively. These energy differences are relatively small for these systems, for example, the dipole-dipole energy for an isolated particle pair with $\alpha = 10$ a.u. and $\mathbf{E_{ex}} = 0.05$ a.u. is of the order of 6kJmol^1 or the order of 15kJmol^{-1} for an infinite chain.

Given that $\Delta p_A(2)$ remains high (*green* curves in **Figure 6.20**) when reversing the field (from high to low) where $\Delta p_A(2)$(Ramp) exceeds $\Delta p_A(2)$(Quench), this demixing effect is reversed more slowly. 'A' particles tend to have already congregated around other 'A' particles starting from a lower field therefore at high field when all particle species are members of chains, particles are less mobile to effect the decrease in $\Delta p_A(2)$. In the quenching runs, at high field, the lower $\Delta p_A(2)$ configurations exist as a function of the time allowed for kinetic stability. This effect shows an additional method to increase tunability of the material properties. To summarize, there is increased gradual reorganisation of particle species to maximise the particles of higher polarizability in closer proximity to others of higher polarizability, in the ramping case. The important trend in **Figure 6.20(a)** and indeed in **Figure 6.20(b)** is the field ramping reversal (*green* curve).



(a) $\{\alpha_1, \alpha_2\} = \{7, 13\}$ *a.u.*.



(b) $\{\alpha_1, \alpha_2\} = \{8, 14\}$ *a.u.*.

Figure 6.20: Scaled coordination number difference functions, $\Delta p_A(2)$ as a function of $\mathbf{E}_{ex}\langle\alpha\rangle$ for two $\{\alpha_1, \alpha_2\}$ pairs ((a) - $\{7, 13\}$ and (b) - $\{8, 12\}$) with fixed $\langle\alpha\rangle = 10$ a.u.. This is a comparison between the field ramping case and the quenching case. The error bars are the true standard deviations about the sample mean.

When changing the direction of field ramping, $\Delta p_A(2)$ persists at a high value over a longer range given that the starting configuration at $\mathbf{E}_{ex} = 0.1$ a.u. contains a high proportion of AAA chains and the lower configurational reorganisation until at much smaller field (~ 0.4 a.u.). This persistent effect of large $\Delta p_A(2)$ is less effective at lower $\Delta\alpha$ given the closer similarity of 'A' and 'B' species.

Figure 6.22 shows molecular graphics snapshots showing the ramping effect for two $\{\alpha_1, \alpha_2\}$ systems and the time reversal of each. As shown chains are made from both species in their final configurations rather than preferentially from either 'A' or 'B'; see **Figure 6.3** for the comparison to the quenching runs.

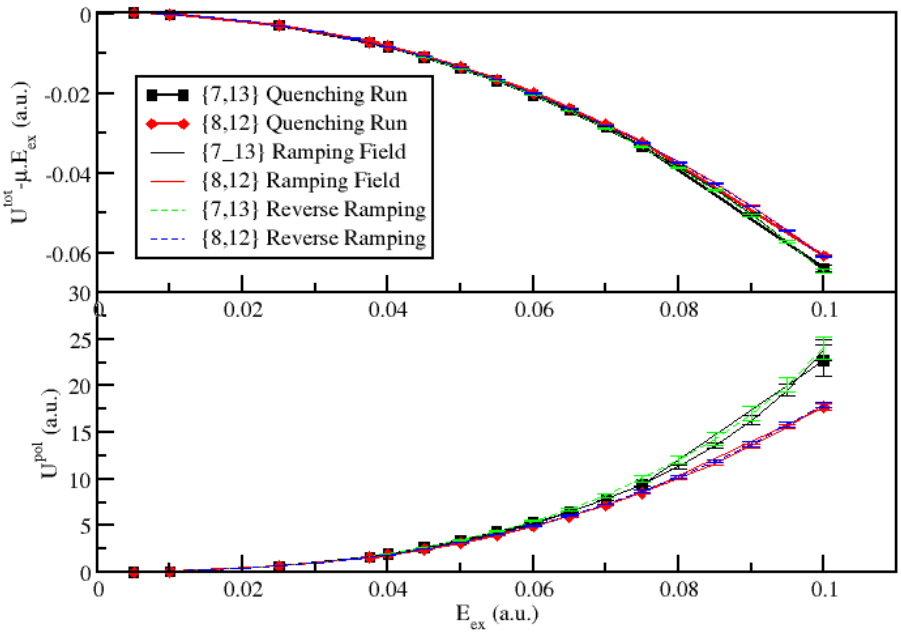
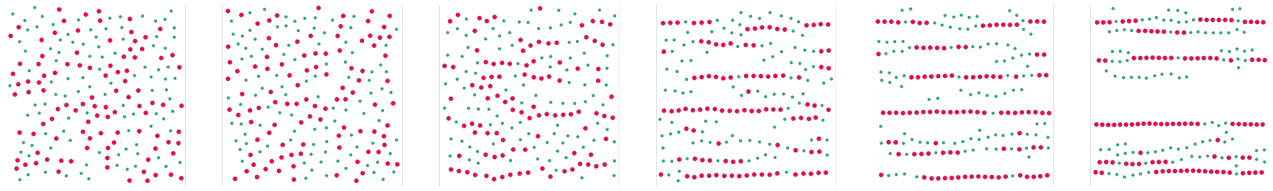
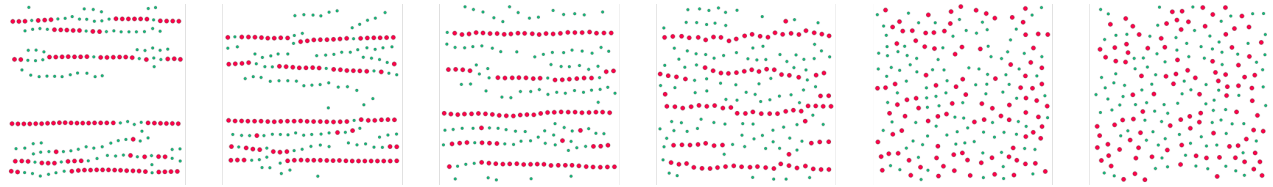


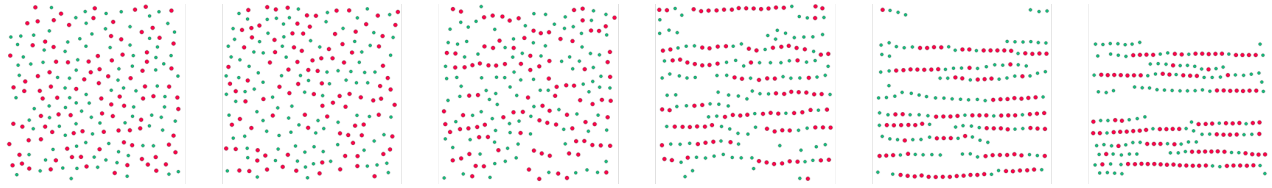
Figure 6.21: Upper: $U^{tot} - \boldsymbol{\mu} \cdot \mathbf{E}_{ex}$ as a function of the applied field. Lower U^{pol} also as a function of the applied field over the same range with $\{\alpha_1, \alpha_2\} = \{8, 12\}$ and $\{7, 13\}$ a.u..



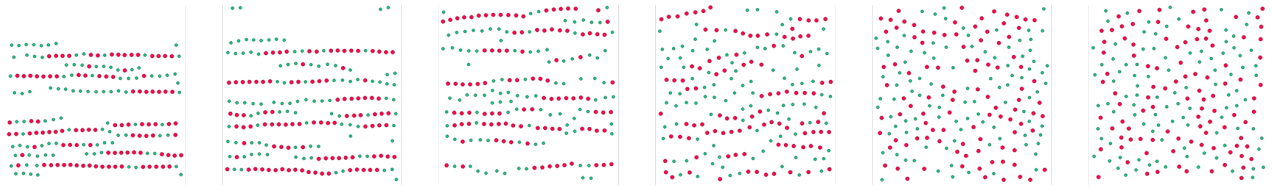
(a) {7,13} ramping field, $+t$.



(b) {7,13} reversed ramping field, $-t$.



(c) {8,12} ramping field, $+t$.



(d) {8,12} reversed ramping field, $-t$.

Figure 6.22: Molecular graphics 'snapshots' for a set of 6 configurations, ramping $\mathbf{E}_{ex}$ from $= 0.005 \rightarrow 0.1$ a.u. in steps of $= 0.005$ a.u. over the course of the run for two cases at fixed $\langle\alpha\rangle = 10$ a.u.. The direction of the applied field is along the x-axis and each set of images describes the progression of time and hence the ramping field from left to right is 0, 0.02, 0.04, 0.06, 0.08, 0.1 a.u. (for $+time$ and the reverse for $-time$). Each image has a set of polarizabilities $\{\alpha_1, \alpha_2\}$, the relatively low polarizability species is coloured *green* and the relatively high polarizability species is coloured *red*.

6.6 Radial Distribution Function and $S(k)$

Radial distribution functions were calculated for the quenching runs shown in the first few sections above. This is to investigate the average long range structure of the particles within the cells. First of all, without any field present, **Figure 6.23** shows the RDF calculation in the direction perpendicular and parallel to the x-axis (the method of calculation is outlined in **Section 2.8.2**). As is clearly observed, in the absence of an applied field, parallel and perpendicular RDFs are almost identical showing that the isotropic liquid is homogeneous containing no chains or mixed phases. This is true for all 'A' particles, all 'B' particles and the mixing of 'A' and 'B' particles, over the range of $\{\alpha_1, \alpha_2\}$ implying a random final configuration is observed.

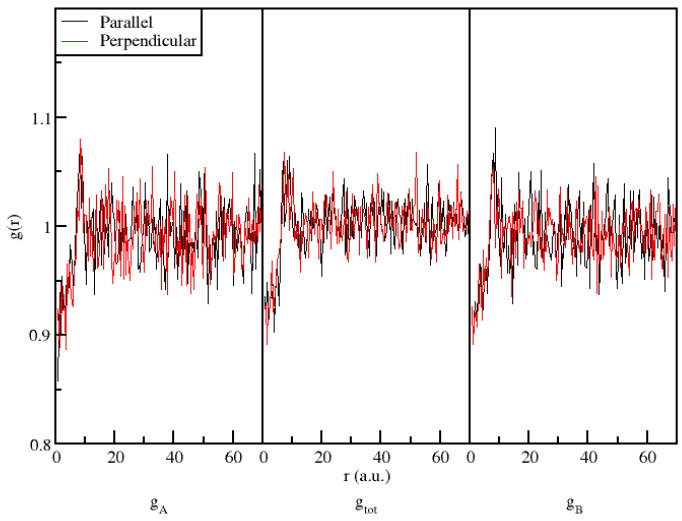


Figure 6.23: $g^{\parallel}$ (*black*) and $g^{\perp}$ (*red*) for A-A pairs, B-B pairs and total (all particle pairs) for the $\{\alpha_1, \alpha_2\} = \{7, 13\}$ a.u. set at zero field.

Figure 6.24 shows for the same simulations as in **Figure 6.23**, the parallel and perpendicular $S(k)$ calculation; for A-A, B-B and all particle pairs under the zero-

field regime. The average distribution of particles is liquid-like and there are no chain structures formed. The noise at high values of k can be rationalised as in **Section 2.8.3**).

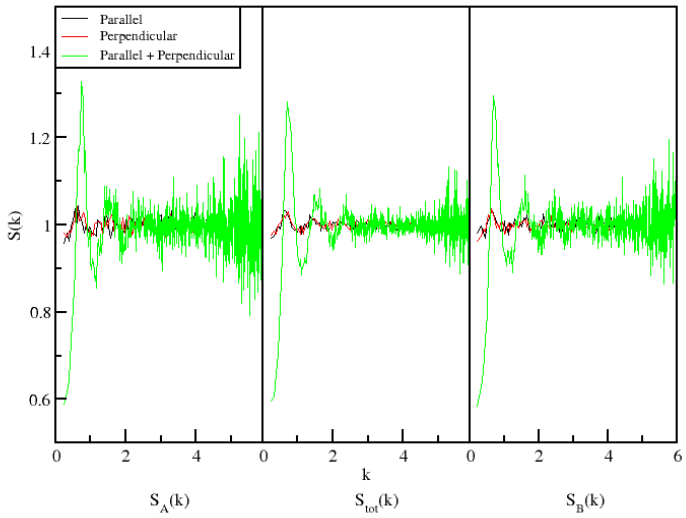


Figure 6.24: $S(k)$ calculations parallel and perpendicular to the cell dimensions for A-A pairs, B-B pairs and total (all particle pairs) for the $\{\alpha_1, \alpha_2\} = \{7, 13\}$ a.u. set at zero field.

Figures 6.25 to **6.30** confirm many of the points given in **Section 6.3**. Firstly **Figure 6.25** shows the RDF calculations, $g^{\parallel}$ and $g^{\perp}$ (with respect to the direction of the applied field, $\mathbf{E}_{ex}$) varying the value of the ratio $\Delta\alpha/\langle\alpha\rangle$ (for each set which is shown offset along the y-axis) for a fixed $\langle\alpha\rangle = 10$ a.u., therefore effectively varying $\Delta\alpha$. At low $\Delta\alpha/\langle\alpha\rangle = 0.2$, it can be seen from the similarity and frequency of the number of peaks in $g^{\parallel}(r)$ (**Figure 6.25(a)**) that the system has long range chain structure for $g_A(r)$ (only A particles considered in the sum), $g_B(r)$ (only B particles considered in the sum) and $g_{tot}(r)$ (all particles considered in the sum). The distance between peaks gives a value approximately the size of the particle diameter, σ de-

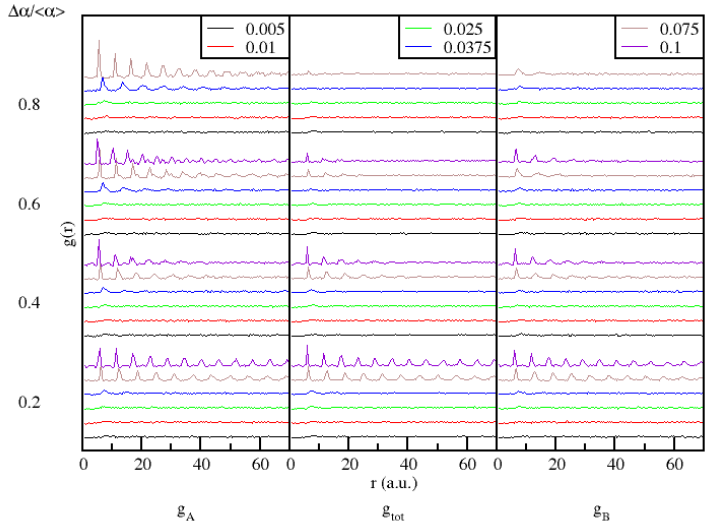
noting chain formation and long range ordering. Chains are comprised of 'A' and 'B' species, predominantly at high field given the large DID effect and is due to the lower difference in particle polarizabilities from the initial configurations such that the RDFs are comparable over each field value. For high $\Delta\alpha/\langle\alpha\rangle$ (= 0.8 in figure) chains are more likely to be comprised of de-mixed species, *i.e.* either 'A' or either 'B', therefore strong peaks are observed for the partial RDFs about all 'A' particles ($g_A(r)$), again especially at high field given the response from the higher polarizability particles. However the $g_B(r)$ RDFs (for both parallel and perpendicular cases) form less intense peaks as $\Delta\alpha/\langle\alpha\rangle$ increases (compared to $g_A(r)$) due to this increased polarizability difference. Hence at high $\Delta\alpha/\langle\alpha\rangle$ there are chains of 'A' species separated by liquid-like bands of 'B' species. For the RDF calculation perpendicular to the field in **Figure 6.25(b)**, greater long range chain-chain ordering is observed at high field and high $\Delta\alpha/\langle\alpha\rangle$ denoted by the peaks at 35 and 70 a.u. emerging in the $g_A^{\perp}(r)$ calculation. Otherwise the RDFs calculated here are similar over the remaining range (lower field and lower $\Delta\alpha/\langle\alpha\rangle$) implying a lesser extent of BBB chain structures especially at high $\Delta\alpha/\langle\alpha\rangle$ confirming the argument given previously. **Figure 6.26** shows for the same simulations, $S^{\parallel}(k)$ and $S^{\perp}(k)$ values confirming the analysis above which is included for completeness.

Secondly **Figures 6.27** and **6.28** show similar RDF calculations, both parallel and perpendicular to the direction of the applied field ($\mathbf{E}_{ex}$), varying the value of the ratio $\Delta\alpha/\langle\alpha\rangle$, however the key difference is that $\langle\mu\rangle$ is now fixed. As such, direct comparison can be made to the monodisperse **Figure 4.7** as shown previously which acts as the limit to the bidisperse case for low $\Delta\alpha/\langle\alpha\rangle$. By fixing the initial mean dipole and as the ratio $\Delta\alpha/\langle\alpha\rangle$ increases for the g_A case, a greater number of AAA chains are formed given the larger polarizability of half the particles present. Similarly this diminishes the BBB chain formation given the relative lower polarizability of

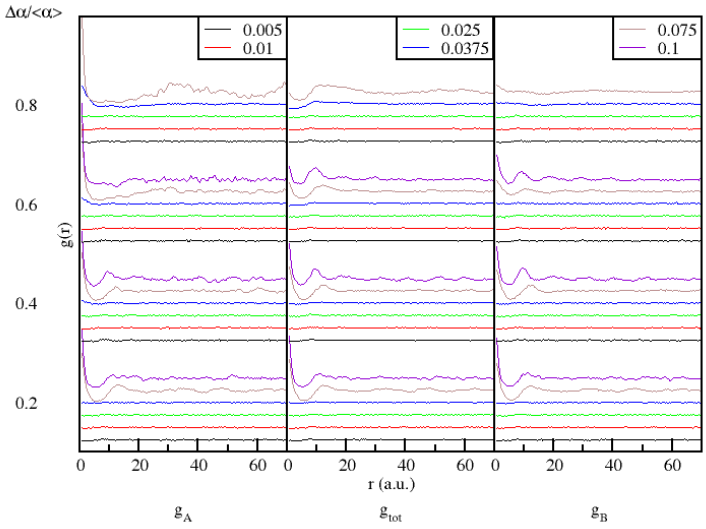
the other half of particles. This is the result as shown above with more clarity, highlighting the effect of the separation in $\Delta\alpha$ rather than merely the enveloping effect of the increasing field. **Figure 6.28** further highlights the effect of AAA chain formation by dividing r by the distance of the first peak. As such, average chain members can be counted, showing an obvious conclusion of large stable AAA chain-formation at high $\Delta\alpha/\langle\alpha\rangle$.

Finally **Figure 6.29** shows the additional RDF calculations along with **Figure 6.30** for the analogous $S(k)$ calculations (both parallel and perpendicular to the direction of the applied field) varying the value of the $\Delta\alpha$ for a fixed field ($\mathbf{E}_{ex} =$ 0.05 a.u.). The fine structure is clear in this case and mirrors the arguments above. At this fixed field magnitude, at large $\Delta\alpha$, the greater numbers of $g_A^{\parallel}$ peaks again showing ordering of particles along chains exclusively made of 'A' particles. $g_A^{\perp}$ at high $\Delta\alpha$ shows greater inter-chain ordering for 'A' species only, in contrast the $g_B^{\parallel}$ and $g_B^{\perp}$ figures are flat, implying no long range ordering and liguid-like nature. The corresponding structure factors show the effect of varying $\Delta\alpha/\langle\alpha\rangle$ with fixed $\langle\alpha\rangle =$ 10 *a.u.* as denoted by the legend. Long range ordering can be observed for $S_A^{\parallel}(k)$ at high $\Delta\alpha$ as shown for the RDFs above.

Varying $\langle\mu\rangle$ by fixing $\langle\alpha\rangle$

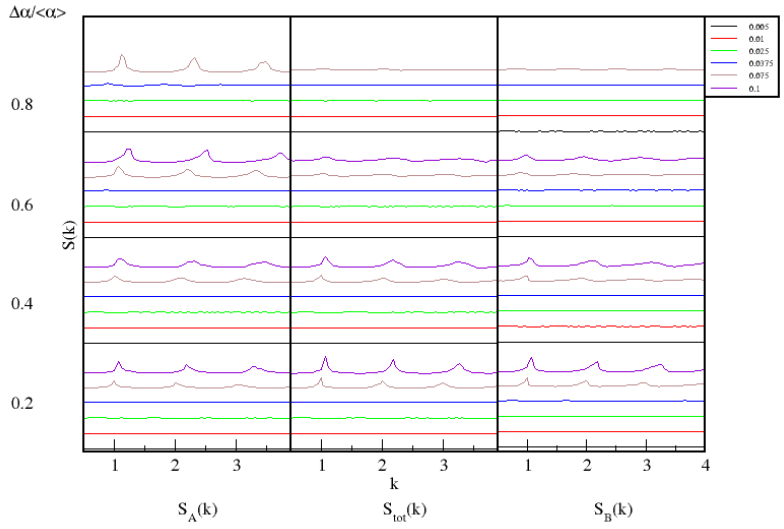


(a) $g^{\parallel}(r)$.

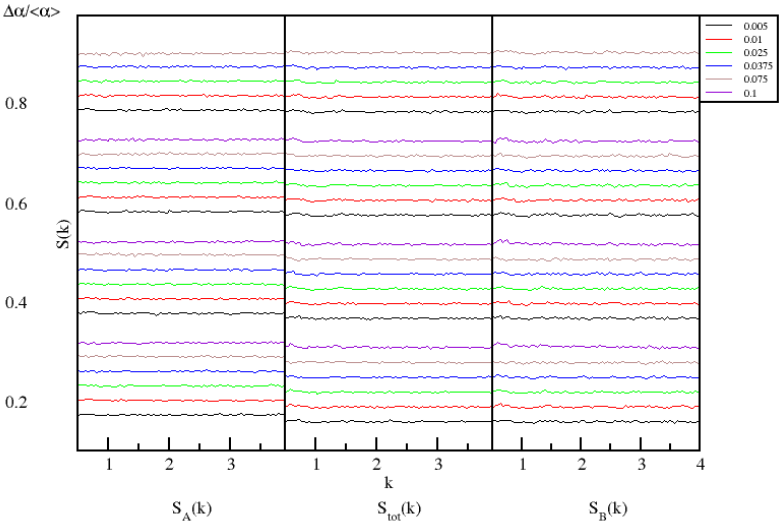


(b) $g^{\perp}(r)$.

Figure 6.25: $g^{\parallel}(r)$ (upper) and $g^{\perp}(r)$ (lower) calculations for a variety of $\mathbf{E}_{ex}$ (legend in a.u.) and $\Delta\alpha/\langle\alpha\rangle$ combinations (each set along the y-axis). Here the value of $\langle\mu\rangle$ is increased as $\mathbf{E}_{ex}$ increases.



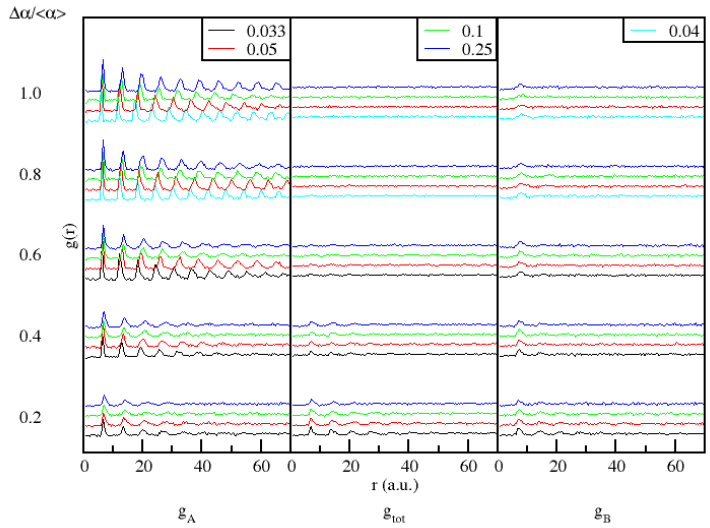
(a) $S^{\parallel}(k)$.



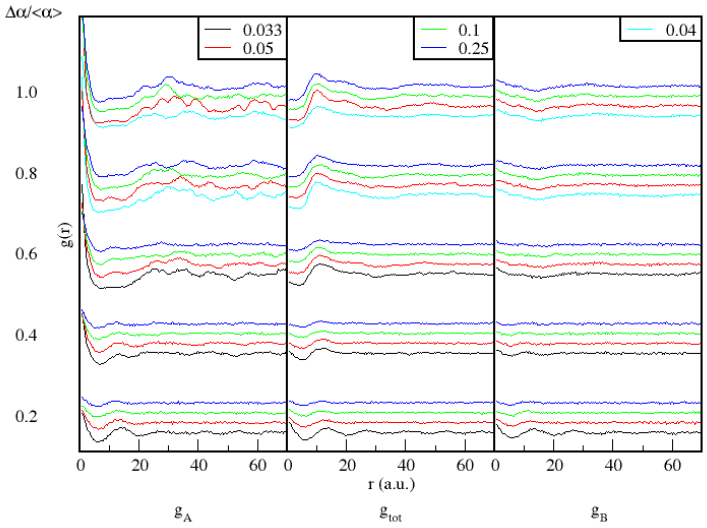
(b) $S^{\perp}(k)$.

Figure 6.26: $S^{\parallel}(k)$ (upper) and $S^{\perp}(k)$ (lower) calculations for a variety of $\mathbf{E}_{ex}$ (legend in a.u.) and $\Delta\alpha/\langle\alpha\rangle$ combinations. Here the value of $\langle\mu\rangle$ is increased as $\mathbf{E}_{ex}$ increases.

Fixing $\langle\mu\rangle$ by varying $\langle\alpha\rangle$



(a) $g^{\parallel}(r)$.



(b) $g^{\perp}(r)$.

Figure 6.27: $g^{\parallel}(r)$ (upper) and $g^{\perp}(r)$ calculations for a variety of $\mathbf{E}_{ex}$ and $\Delta\alpha/\langle\alpha\rangle$ combinations. Here the value of $\langle\mu\rangle = 0.5$ a.u. is fixed as $\mathbf{E}_{ex}$ increases.

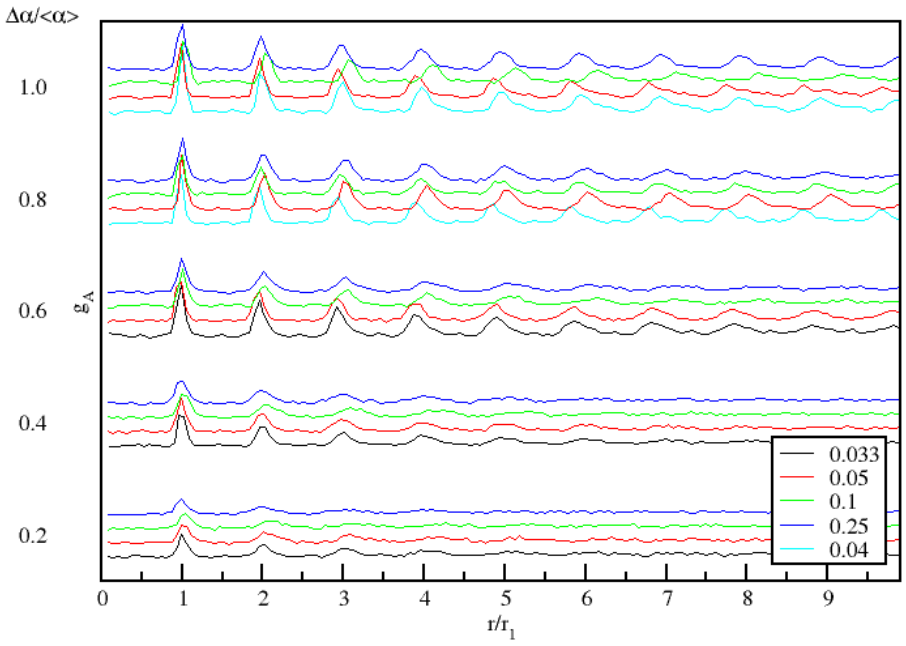
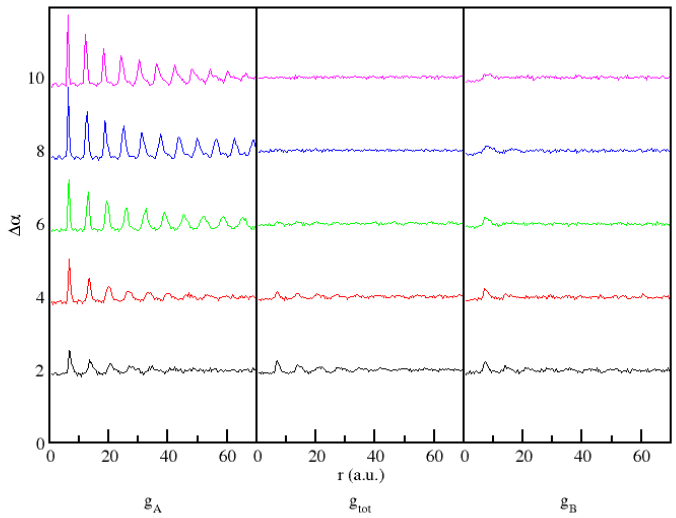
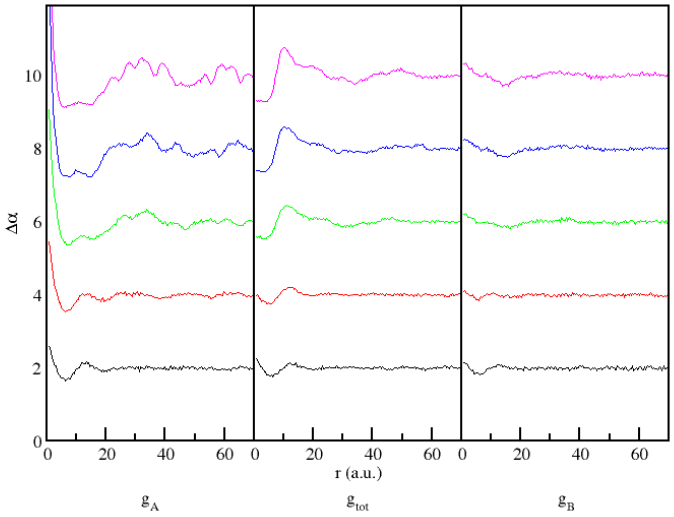


Figure 6.28: $g_A^{\parallel}(r)$ as a function of r/r_1 where r_1 is the distance of the 1st peak. The values in the legend are $\mathbf{E}_{ex}$ in a.u. and the ratio, $\Delta\alpha/\langle\alpha\rangle$ is also varied as shown along the y-axis. Scaling along the y-axis has been omitted for clarity, RDFs are shifted along the y-axis for illustration purposes only.

Varying $\Delta\alpha$

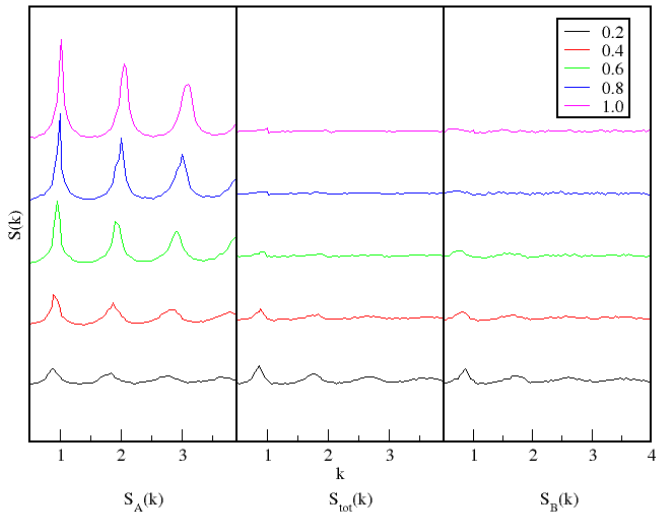


(a) $g^{\parallel}(r)$.

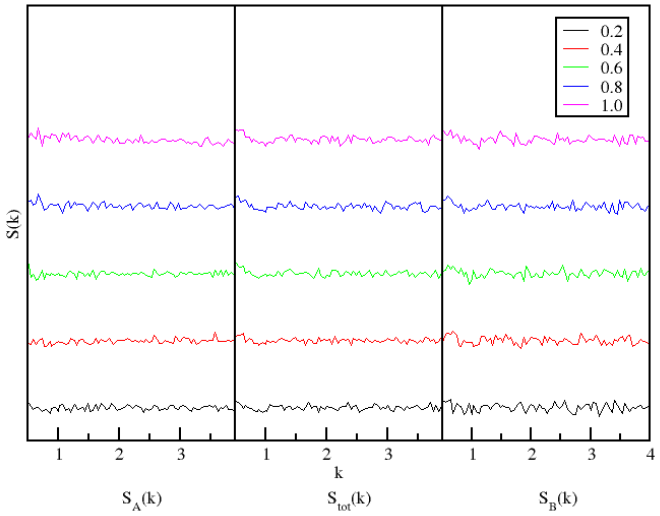


(b) $g^{\perp}(r)$.

Figure 6.29: Parallel and perpendicular RDF calculations for a variety of $\Delta\alpha$ combinations. Here the value of $\langle\mu\rangle$ is fixed at 10 a.u..



(a) $S^{\parallel}(k)$.



(b) $S^{\perp}(k)$.

Figure 6.30: $S^{\parallel}(k)$ (upper) and $S^{\perp}(k)$ (lower) calculations at fixed field strength, $\mathbf{E}_{ex} =$ 0.05 a.u. varying $\Delta\alpha$ $\Delta\alpha/\langle\alpha\rangle$ at fixed $\Delta\alpha$ as stated in the legend in a.u..

6.6.1 Partial RDF

Partial RDFs can be calculated in order to explore the average shell composition of the environments surrounding individual particles in the configurations. **Equation 2.8.3** shows the calculation whereby $g_1(r)$ describes the probability of finding the closest particle (relative to each particle) over a distance r, $g_2(r)$ the second closest particle and therefore $g_i(r)$ gives the probability of finding the i^{th} closest particle *etc.* In the figures below, $i = 1 \rightarrow 5$ are highlighted over the range of r sampled. These 'partial' RDFs can be further broken down based on the particles sampled in the system. Given that the theme of the analysis for bidisperse systems throughout this chapter has been to analyse each species ('A' and 'B'), this metric is no exception.

$g_{i,tot}(r)$ and $g_{tot}(r)$ are displayed in **Figures 6.31**, **6.32**, **6.33** and **6.34** (**(a)**, **(c)** and **(e)**) and $g_{i,x}(r)$ (**(b)**, **(d)** and **(f)**) - which is described below. $g_{tot}(r)$ is the full RDF calculated as a reference, $g_{i,tot}(r)$ is the partial RDF ($g_i(r)$) calculated over all particle species ('A' and 'B'). $g_{i,x}(r)$ (value of i given in legend) describes the RDF for 'A' species only ($g_{i,A}(r)$), 'B' species only ($g_{i,B}(r)$) and the sum ($g_{i,A}(r) + g_{i,B}(r)$) which does not include A-B or B-A pairs. Each set of figures is at different $\Delta\alpha/\langle\alpha\rangle$ ratios (see captions) each with fixed $\langle\alpha\rangle = 10$ a.u.. The external field (RDF is measured $\parallel$ to this) is increased from the top two figures in each set ($\mathbf{E}_{ex} = 0.025$ a.u.) to the bottom two figures in each set ($\mathbf{E}_{ex} = 0.075$ a.u.) to cover the range of fields.

General trends can be observed for each $\Delta\alpha/\langle\alpha\rangle$; for $g_{i,tot}(r)$ and $g_{tot}(r)$. At low field, $g_{tot}(r)$ shows less long range ordering over this range of r; as the field is increased the position of the first peak decreases implying more stable chains at shorter inter-particle distance. *E.g.* the first peak of the solid *black* curve from **Figure 6.31(a)** $\rightarrow$ **Figure 6.31(c)** $\rightarrow$ **Figure 6.31(e)** moves from $r \sim 9 \rightarrow 6.5 \rightarrow 5.5$ a.u.. At high field long range ordering is apparent with obvious peaks at each particle distance, the distance between which contracts at high field, again denoting more stable chains

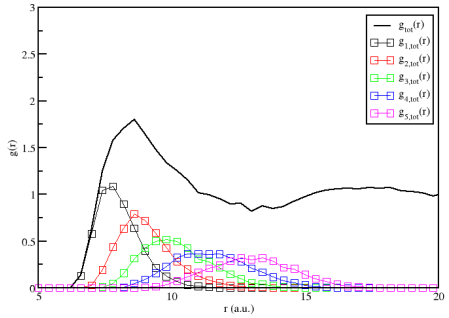
with shorter inter-particle distance. At low $\Delta\alpha/\langle\alpha\rangle$ there is less of a contraction between peaks at high field.

$g_{i,tot}(r)$ shows a broadening of the distributions and increase of mean r as i increases from $1 \rightarrow 5$ (*black* $\rightarrow$ *purple*). At low field, this effect is similar for each $\Delta\alpha/\langle\alpha\rangle$ which is indicative of no/little chain structure formation and the configurations are on average liquid-like with no long range ordering. The same properties can be observed for $g_{1,A}(r)$ and $g_{1,B}(r)$ which show their greatest similarity at low field and low $\Delta\alpha/\langle\alpha\rangle$. Only a slight difference is observed between peaks at high $\Delta\alpha/\langle\alpha\rangle$ with $g_{1,A}(r)$ marginally higher than $g_{1,B}(r)$. $g_{2,A}(r)$ is also marginally higher than $g_{2,B}(r)$ over the range of $\Delta\alpha$ at low field which implies that even with a small DID difference between species that 'A' particles are more likely to have long range ordering and stay in proximity to other 'A' particles at higher polarizability.

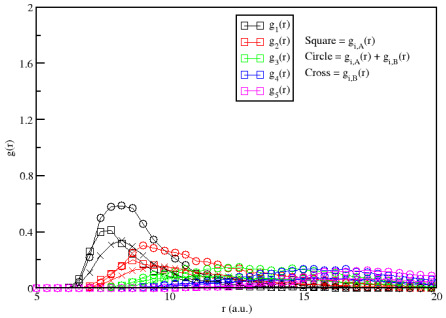
At intermediate field, chain-formation has occurred, highlighted by peaks at $g_{1,tot}(r)$, $g_{2,tot}(r)$ (first and second closest particles) for the first coordination shell surrounding a two-coordinate chain and $g_{3,tot}(r)$, $g_{4,tot}(r)$, $g_{5,tot}(r)$ for the second coordination shell. $g_{3,tot}(r)$ is a broad distribution at high $\Delta\alpha/\langle\alpha\rangle$ which remains constant over this field range highlighting that chains are formed separated by pockets of non-chain forming species. $g_{4,tot}(r)$ and $g_{5,tot}(r)$ subsequently flatten from high to low $\Delta\alpha/\langle\alpha\rangle$ given the reduced difference between the polarizabilities of particle species, where the more polarizable 'A' species is more likely to be a member of a chain structure. This can be proved by looking at $g_{i,A}(r)$ which has long range order (spikes in the distribution) over more than one coordination shell compared with $g_{i,B}(r)$ which is very broad at high $\Delta\alpha$ and forms peaks at low $\Delta\alpha$. This further highlights the extent of de-mixing in these systems. At high $\Delta\alpha$, chains are formed and composed entirely of 'A' species compared to low $\Delta\alpha$ where mixing occurs. This effect is shown by the greater heights of the peaks in $g_{i,A}(r)$ (square values) and

lower heights of the peaks in $g_{i,B}(r)$ (crosses) at high $\Delta\alpha$, compared to the similarity in the values of the peaks (and similar broadening of peaks) along with the total ($g_{i,A}(r) + g_{i,B}(r)$ (circles)) peaks becoming less sharp at low $\Delta\alpha$.

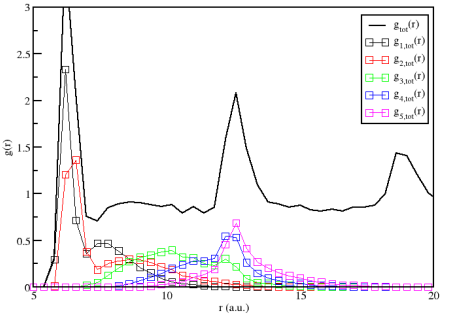
Finally at high field $g_{1,tot}(r)$ and $g_{2,tot}(r)$ narrows and increases in height from low to high $\Delta\alpha$. Peaks at the second coordination shell $g_{3,tot}(r)$, $g_{4,tot}(r)$ and $g_{5,tot}(r)$ become more defined with less $g_{3,tot}(r)$-$g_{2,tot}(r)$ overlap showing a clear de-mixing effect. At low $\Delta\alpha$ therefore species 'A' and 'B' are similar therefore $g_{i,tot}(r)$ resembles $g_{tot}(r)$. This is also evident in $g_{i,A}(r)$ and $g_{i,B}(r)$ at low $\Delta\alpha$, the peaks of which are present in both coordination shells over the range. At high $\Delta\alpha$ $g_{i,A}(r)$ and $g_{i,B}(r)$ show first peaks at separate r distances therefore indicating chains made of either 'A' species or 'B' species without mixing. This metric therefore is key in order to understand the extent of the mixing/de-mixing effect over this range of field and polarizability differences in a bidisperse system.



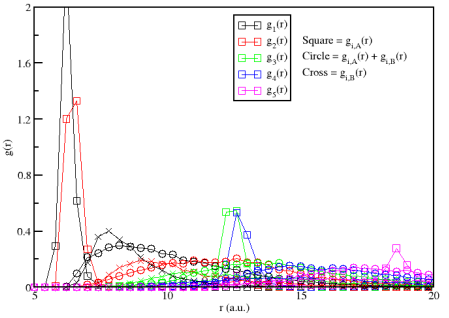
(a) $g_{i,tot}(r)$ for $\mathbf{E}_{ex} = 0.025$ a.u..



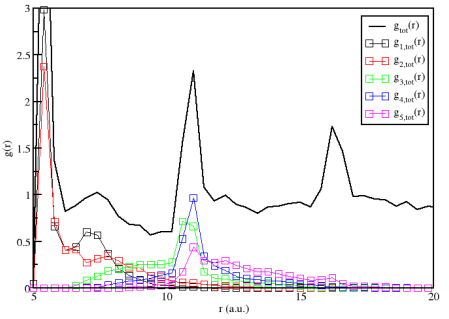
(b) $g_{i,x}(r)$ for $\mathbf{E}_{ex} = 0.025$ a.u..



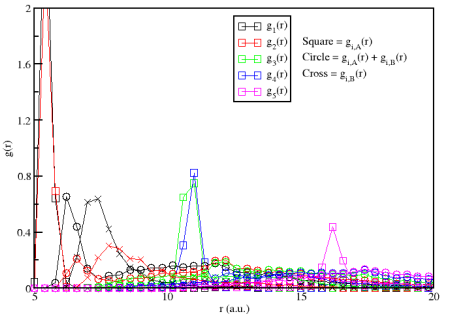
(c) $g_{i,tot}(r)$ for $\mathbf{E}_{ex} = 0.05$ a.u..



(d) $g_{i,x}(r)$ for $\mathbf{E}_{ex} = 0.05$ a.u..

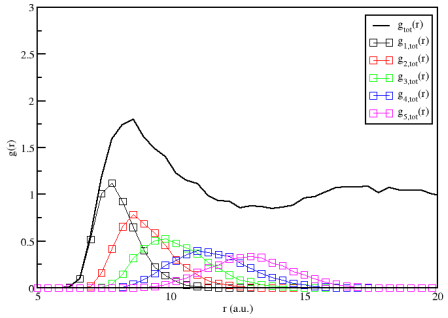


(e) $g_{i,tot}(r)$ for $\mathbf{E}_{ex} = 0.075$ a.u..

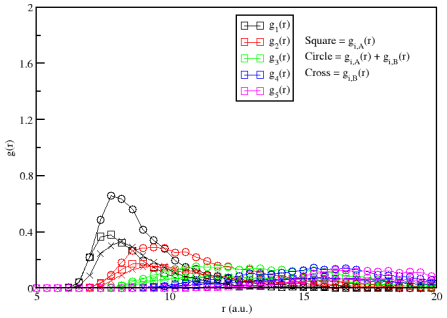


(f) $g_{i,x}(r)$ for $\mathbf{E}_{ex} = 0.075$ a.u..

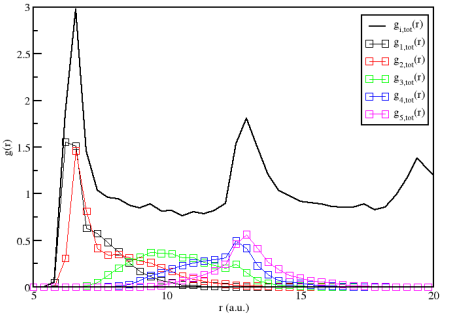
Figure 6.31: $g_{i,tot}(r)$ and $g_{tot}(r)$ including all particles in the calculation (**(a)**, **(c)** and **(e)**) and $g_{i,x}(r)$ (**(b)**, **(d)** and **(f)**) (value of i given in legend) for 'A' species only ($g_{i,A}(r)$), 'B' species only ($g_{i,B}(r)$) and the sum ($g_{i,A}(r) + g_{i,B}(r)$) at $\dfrac{\Delta\alpha}{\langle\alpha\rangle} = 0.8$ with $\langle\alpha\rangle = 10$ a.u.. The *black* solid line shows $g_{tot}(r)$ for the system without a coordination consideration.



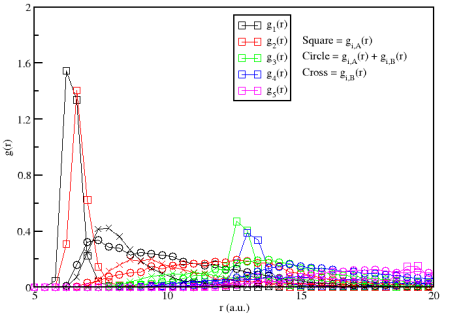
(a) $g_{i,tot}(r)$ for $\mathbf{E}_{ex} = 0.025$ a.u..



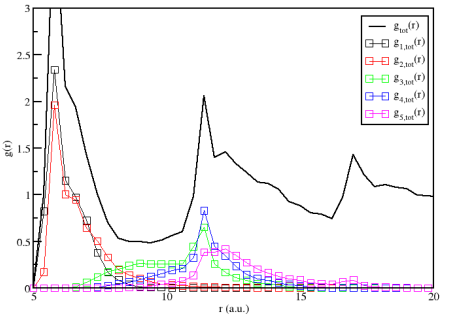
(b) $g_{i,x}(r)$ for $\mathbf{E}_{ex} = 0.025$ a.u..



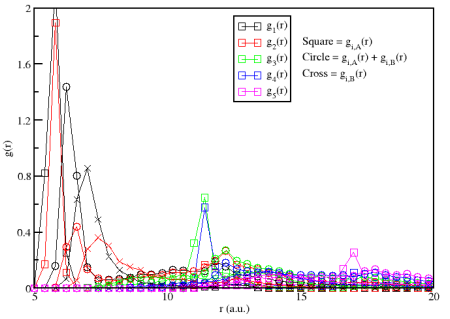
(c) $g_{i,tot}(r)$ for $\mathbf{E}_{ex} = 0.05$ a.u..



(d) $g_{i,x}(r)$ for $\mathbf{E}_{ex} = 0.05$ a.u..

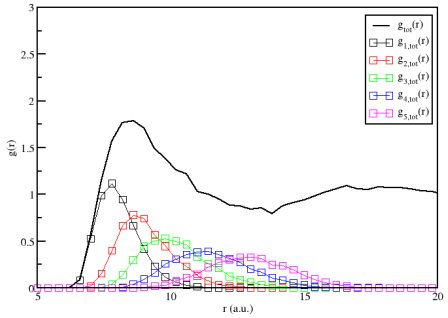


(e) $g_{i,tot}(r)$ for $\mathbf{E}_{ex} = 0.075$ a.u..

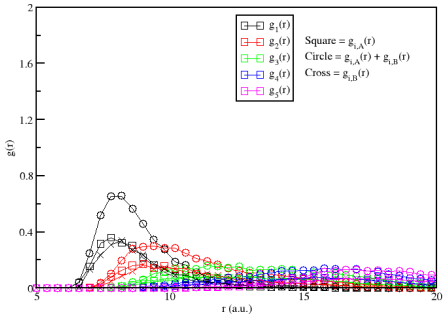


(f) $g_{i,x}(r)$ for $\mathbf{E}_{ex} = 0.075$ a.u..

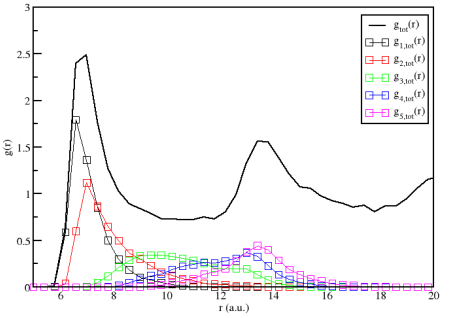
Figure 6.32: $g_{i,tot}(r)$ and $g_{tot}(r)$ including all particles in the calculation (**(a)**, **(c)** and **(e)**) and $g_{i,x}(r)$ (**(b)**, **(d)** and **(f)**) (value of i given in legend) for 'A' species only ($g_{i,A}(r)$), 'B' species only ($g_{i,B}(r)$) and the sum ($g_{i,A}(r) + g_{i,B}(r)$) at $\dfrac{\Delta\alpha}{\langle\alpha\rangle} = 0.6$ with $\langle\alpha\rangle = 10$ a.u.. The *black* solid line shows $g_{tot}(r)$ for the system without a coordination consideration.



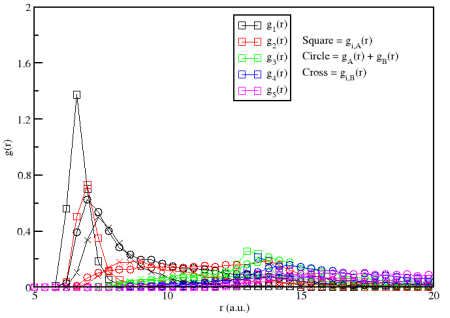
(a) $g_{i,tot}(r)$ for $\mathbf{E}_{ex} = 0.025$ a.u..



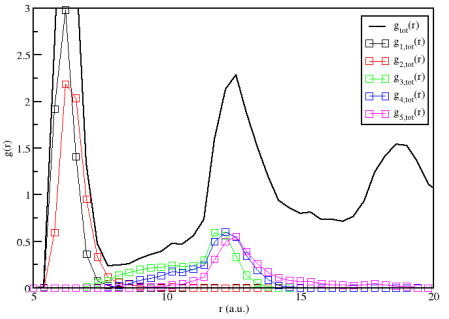
(b) $g_{i,x}(r)$ for $\mathbf{E}_{ex} = 0.025$ a.u..



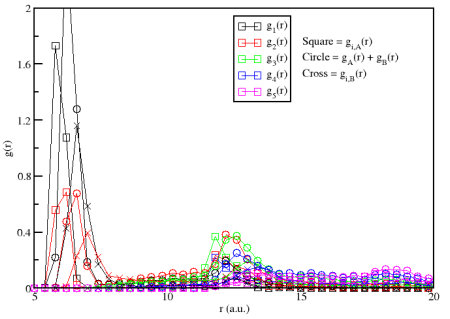
(c) $g_{i,tot}(r)$ for $\mathbf{E}_{ex} = 0.05$ a.u..



(d) $g_{i,x}(r)$ for $\mathbf{E}_{ex} = 0.05$ a.u..

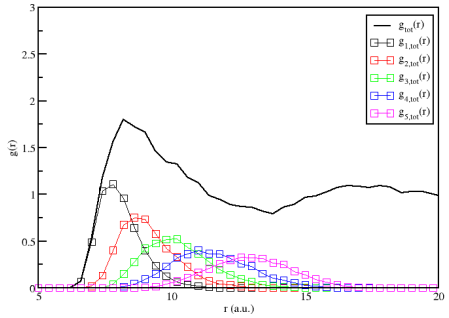


(e) $g_{i,tot}(r)$ for $\mathbf{E}_{ex} = 0.075$ a.u..

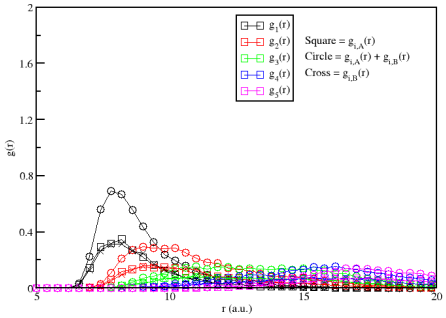


(f) $g_{i,x}(r)$ for $\mathbf{E}_{ex} = 0.075$ a.u..

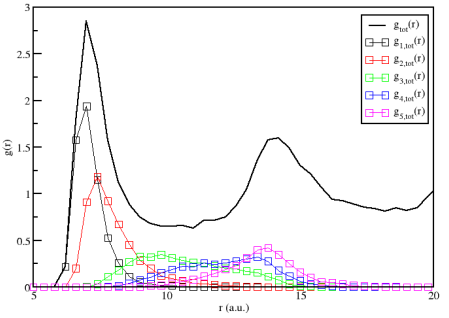
Figure 6.33: $g_{i,tot}(r)$ and $g_{tot}(r)$ including all particles in the calculation (**(a)**, **(c)** and **(e)**) and $g_{i,x}(r)$ (**(b)**, **(d)** and **(f)**) (value of i given in legend) for 'A' species only ($g_{i,A}(r)$), 'B' species only ($g_{i,B}(r)$) and the sum ($g_{i,A}(r) + g_{i,B}(r)$) at $\dfrac{\Delta\alpha}{\langle\alpha\rangle} = 0.4$ with $\langle\alpha\rangle = 10$ a.u.. The *black* solid line shows $g_{tot}(r)$ for the system without a coordination consideration.



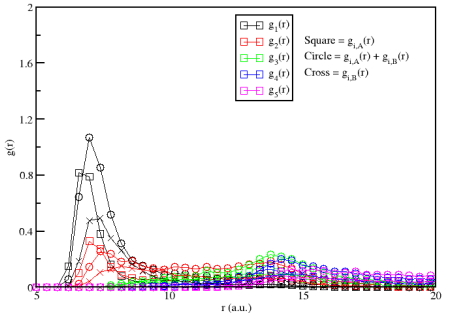
(a) $g_{i,tot}(r)$ for $\mathbf{E}_{ex} = 0.025$ a.u..



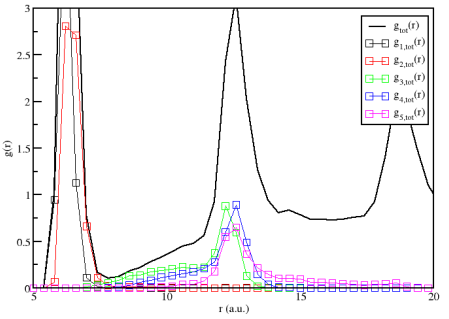
(b) $g_{i,x}(r)$ for $\mathbf{E}_{ex} = 0.025$ a.u..



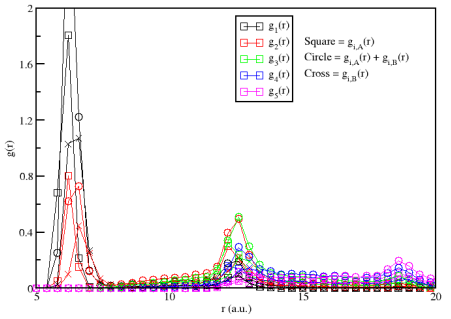
(c) $g_{i,tot}(r)$ for $\mathbf{E}_{ex} = 0.05$ a.u..



(d) $g_{i,x}(r)$ for $\mathbf{E}_{ex} = 0.05$ a.u..



(e) $g_{i,tot}(r)$ for $\mathbf{E}_{ex} = 0.075$ a.u..

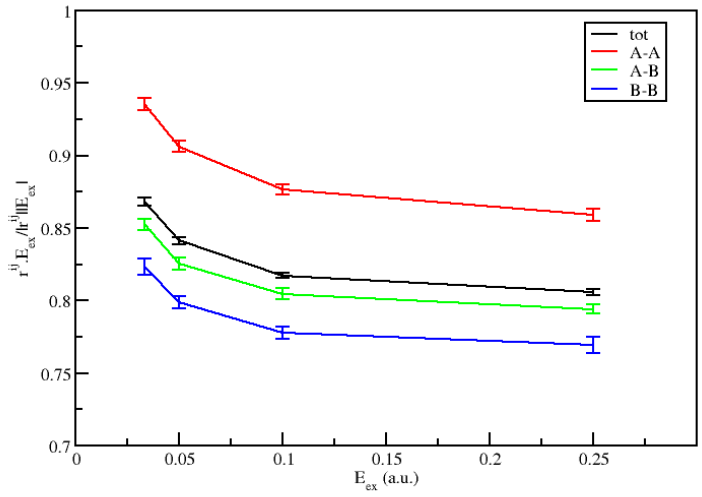


(f) $g_{i,x}(r)$ for $\mathbf{E}_{ex} = 0.075$ a.u..

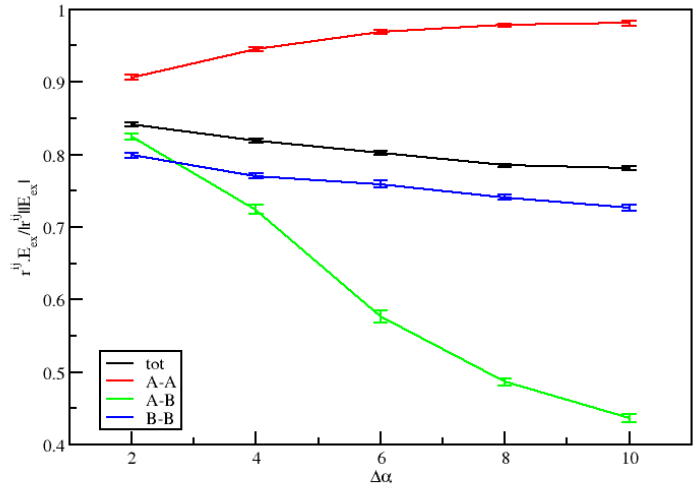
Figure 6.34: $g_{i,tot}(r)$ and $g_{tot}(r)$ including all particles in the calculation (**(a)**, **(c)** and **(e)**) and $g_{i,x}(r)$ (**(b)**, **(d)** and **(f)**) (value of i given in legend) for 'A' species only ($g_{i,A}(r)$), 'B' species only ($g_{i,B}(r)$) and the sum ($g_{i,A}(r) + g_{i,B}(r)$) at $\dfrac{\Delta\alpha}{\langle\alpha\rangle} = 0.2$ with $\langle\alpha\rangle = 10$ a.u.. The *black* solid line shows $g_{tot}(r)$ for the system without a coordination consideration.

6.7 Chain Alignment

As observed in **Section 4.3.4**, a metric to describe the average particle-pair alignment with the direction of the applied field, can be used. Again this is the dot product, $\mathbf{r}^{ij} \cdot \mathbf{E}_{ex} = |\mathbf{r}^{ij}||\mathbf{E}_{ex}| \cos\theta$. As previously outlined θ tends to zero or π for a system with idealized chain formation. **Figure 6.35(a)** (for a fixed $\Delta\alpha = 2$ a.u.) can be directly related to **Figure 4.8** (which is the limit of $\Delta\alpha = 0$ a.u.). Each $\mathbf{E}_{ex}$ is paired to a mean polarizability, $\langle\alpha\rangle$ such that $\langle\mu\rangle$ is fixed at 0.5 a.u.. For low $\mathbf{E}_{ex}$, high $\langle\alpha\rangle$ pair, the normalised dot product $\mathbf{r}^{ij} \cdot \mathbf{E}_{ex}$ (averaged over all pairs) is much closer to one than the high $\mathbf{E}_{ex}$, low $\langle\alpha\rangle$ pairing. Additionally, as in the monodisperse case, for A-A pairs only the values of the normalised dot product are much larger than observed in the B-B range, highlighting the preferential formation of AAA chains in the configurations, as a result of the larger dipole-induced-dipole effect leading to enhanced alignment with the external field. **Figure 6.35(b)** shows the effect of increasing $\Delta\alpha$ fixing the value of the applied field. AAA chains become more aligned and the value increases (*red* line) whereas fewer BAB pairs form (*green* line) and the average alignment decreases.



(a) A



(b) B

Figure 6.35: Upper: The dot product metric $\mathbf{r}^{ij} \cdot \mathbf{E}_{ex}$ (averaged over all pairs in question (tot), A-A pairs only, A-B pairs only or B-B pairs only) as a function of $\mathbf{E}_{ex}$. The ratio $\Delta\alpha/\langle\alpha\rangle$ is held constant at 0.2 a.u.. Lower: The dot product metric $\mathbf{r}^{ij} \cdot \mathbf{E}_{ex}$ as a function of $\Delta\alpha$. The field is held constant at $\mathbf{E}_{ex} = 0.05$ a.u.. The error bars are the true standard deviations about the sample mean.

6.8 Chapter Summary

This chapter has presented, in length, a number of useful metrics to introduce and account for the extent of mixing of species, in a bidisperse system, given that depending on the method of preparation the chain formation properties can be tuned. It is found that there is indeed a large departure from a monodisperse system which can be quantified using primarily dipole distribution analysis, whereby the role of the DID effect is key in directing chain structure formation in these systems. In addition to this, bidispersity in this model can be scaled by particle polarizability which is related to the behaviour of a standard two-state system. $\Delta\alpha$, $\langle\alpha\rangle$ and the ratio $\frac{\Delta\alpha}{\langle\alpha\rangle}$ are varied and an effective polarizability is calculated which allows scaling of these properties, principally by using the metric $\Delta p_A(k)$.

A number of key system variables such as applied field and effective polarizability have been shown to dictate chain-formation properties such that, the de-mixed separation of species can be shown to occur, even at low fields. These properties are explored by varying the method of field modulation (ramping compared with the method of quenching). The final chapter aims to depart from experimental influence and predict the behaviour of the monodisperse system under confinement, with interactions between particles and a potential wall.

Chapter 7

Self-Assembly Under Confinement

The ability to reproduce key experimental observations (as outlined in **Chapter 5**) allows us to utilise the model to consider systems under a host of different conditions. Systems under confinement, with a view to miniaturise technology, have become a point of interest in recent years especially in directing the extent of self-assembly in MR fluids. The extent of microstructure formation in these fluids can be topologically controlled using confining geometrically-simple microchannels [187]. Previous experimental work has also shown the effect of confinement in the layering of magnetic nanoparticles [188] and in the transition from 2D to 3D cell dimensions [12] using thin slits and a perpendicular field (see below). Furthermore it can be surmised that the properties of these systems will differ from the bulk monodisperse analogue, in terms of chain composition and orientation as discussed in previous chapters. Additionally by supressing network formation, free-standing magnetic bands can be produced, again using microfluidic channels [16]. It is therefore evident that the extent of confinement and structure of confining walls should be investigated in an effort to control self-assembly.

7.1 Confinement Using Discrete Particle Walls

Monodisperse particles are confined to a square cell by two bands of particles acting as a continuous wall, fixed along two sides of the cell. The walls are constructed by dividing the square cell length by a factor of 100 and placing a fixed, non-movable particle at each $1/100^{th}$ position along the 'top' and 'bottom' side of the cell x-axis. Long-range interactions between particles within the walls and the periodic images along the y-axis, (perpendicular to the cell confining walls) are reduced by extending the simulation box in the y-direction (by an additional 75%, an arbitrarily large value). Each pinned wall particle has a fixed particle diameter, $\sigma_{wall} = 5.4025$ a.u. and a Lennard-Jones potential well-depth ϵ^i_{wall}/k_B, which defines the extent of interaction between the system particles (fluid) and the wall particles. As such, values of ϵ^i_{wall}/k_B can be varied (which has the dispersive force included) allowing particle 'inclusions' to be modelled that interact with the system particles with different relative attractive force. The density of particles in the wall is such that it acts as a pseudo-continuous potential barrier. System particles are also described to have a single fixed polarizability α (monodisperse) as introduced in **Chapter 4** with particle pair interactions described with a repulsive, 'r^{-12}' potential. Simulations have been performed (50 system particles in each cell at $\rho^* = 0.1$), focusing on three cases:

1. With the continuous wall at fixed $\{\sigma_{wall} = 5.4025, \epsilon^i_{wall}/k_B = 57.9K\}$.

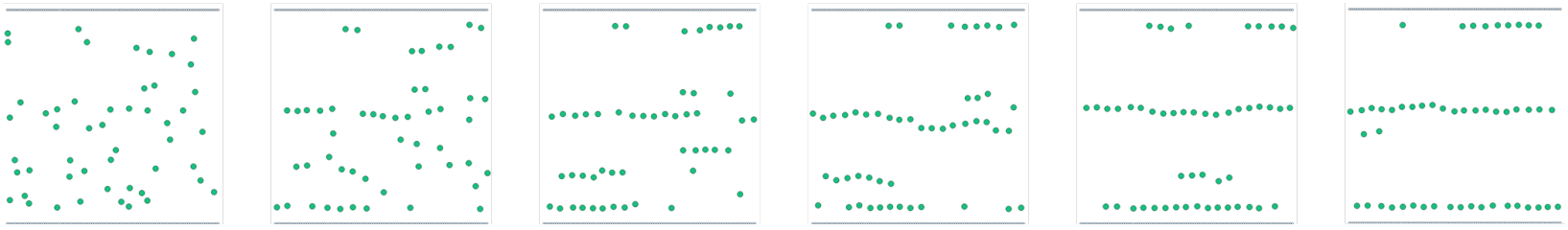
2. With the continuous wall particles ($\{\sigma_{wall} = 5.4025, \epsilon^i_{wall}/k_B = 57.9K\}$) containing a number of inclusions ($\{\sigma_{wall} = 5.4025, \epsilon^i_{inc}/k_B = 10\epsilon^i_{wall}/k_B\}$) at a much higher potential well-depth (ϵ^i_{inc}/k_B) placed centrally and symmetrically along the walls.

3. With the continuous wall particles ($\{\sigma_{wall} = 5.4025, \epsilon^i_{wall}/k_B = 57.9K\}$) containing a number of inclusions ($\{\sigma_{wall} = 5.4025, \epsilon^i_{inc}/k_B = 10\epsilon^i_{wall}/k_B\}$) where

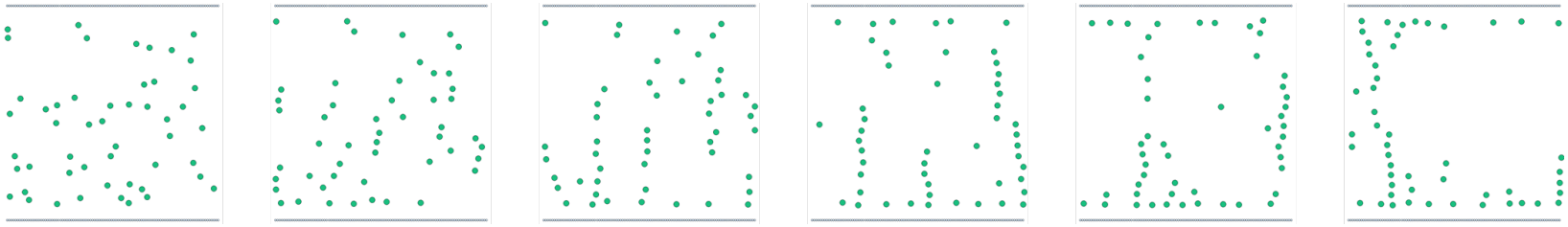
the inclusions are offset from each other, placed asymmetrically along the wall. The number and position of inclusions are therefore varied.

7.2 No Inclusions

Figure 7.1 shows the comparison between runs in a square cell with confining walls where the applied field direction is either parallel or perpendicular to the wall. The applied field strength and polarizability is fixed at $\{\alpha, \mathbf{E}_{ex}\} = \{10, 0.05\}$ a.u.. When the field is applied perpendicular to the wall, chains form preferentially along this vector. In addition there are a small number of system particles aggregating parallel to the the walls given the attractive interaction between fluid and wall particles governed by the LJ parameter, ϵ^{i}_{wall}/k_B, though this layer is a single particle thickness. When the field is applied parallel to the walls then particle aggregation occurs along each wall preferentially and in the centre of the cell away from the attractive force of the wall. **Figure 7.2** shows the chain length distributions, for the same runs with (lower window) or without (upper window) confining walls, where the applied field direction is either parallel ($\triangle$) or perpendicular ($\times$) to the x-axis. The theoretical values of P_n have also been included as a reference to ideal chain growth statistics. As is quite evident the chain length distributions are almost identical for each (parallel and perpendicular) P_n in the case with no wall, where chain growth is independent of the direction in which the field is applied. The mean chain length, μ_s therefore lies between a range of $\sim 1.5 \rightarrow 2.5$ particle units. However when introducing a particle wall with attractive potential interactions, the range of mean chain lengths expands to $\sim 1.5 \rightarrow 7$ units long, when the applied field is parallel with the wall. This is due to the attractive potential of the wall particles enhanced by the large DID effect present when particles aggregate to form chains. Particles in the system are trapped against the walls and form long chains at a single particle thickness.



(a) Parallel $\mathbf{E}_{ex}$.



(b) Perpendicular $\mathbf{E}_{ex}$.

Figure 7.1: Molecular graphics 'snapshots' of the configurations over time, from left to right, $t^* = 0$, 6.96, 13.91, 27.82, 55.65. $\{\alpha, \mathbf{E}_{ex}\} = \{10, 0.05\}$ a.u.. Wall particles have fixed $\{\sigma_{wall} = 5.4025 \text{ a.u.}, \epsilon^i_{wall}/k_B = 57.9K\}$ interaction parameters.

Conversely when the applied field is perpendicular to the wall, chain length distributions are similar to that with no wall, which can be observed in the upper graph window of **Figure 7.2**. The wall attracts the system particles such that the closest particles experience the greatest dispersive interaction. Given that the wall is effectively continuous and of even potential along its length, particles are pinned along the wall but not in a fixed position. Therefore chain formation is disjointed and less aggregation occurs along the wall than in the parallel field case, given that the field is applied perpendicular to the wall and chain formation occurs preferentially along that vector. Therefore given that there are competing interactions with the field and with the wall the chain growth is stunted compared with the constructive parallel field case with a potential wall. The following section acts to investigate variable inclusions in the potential wall and the effect on the chain growth.

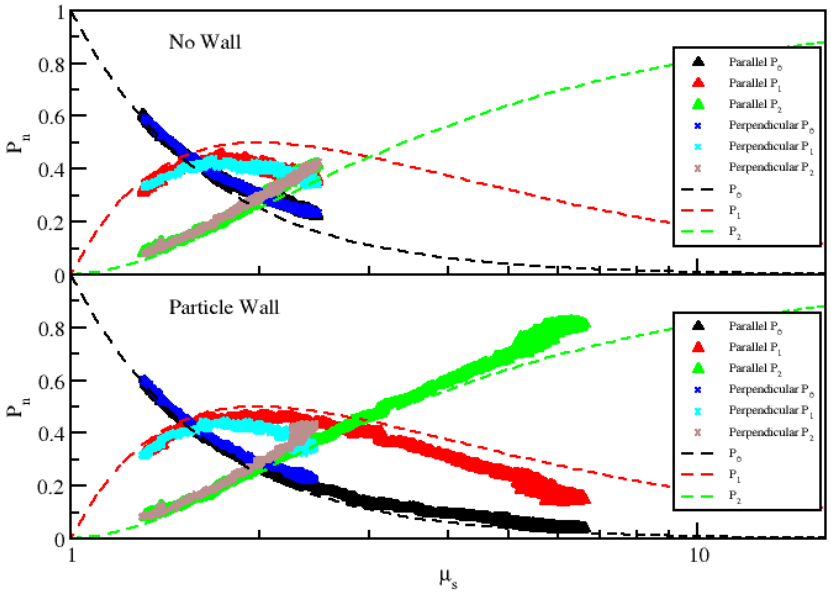


Figure 7.2: Chain length distributions with and without a pseudo-continuous potential wall. Particles in the confining are identical, no inclusions are present.

7.3 Symmetric Wall Inclusions

Figure 7.3 is a schematic view of the confining particle walls (*blue* particles) with particle inclusions, three in this diagram, placed in each wall (*red* particles), the number of which is varied. If the interaction between wall and system particles are described by LJ parameters, $\{\sigma_{wall} = 5.4025 \text{ a.u.}, \epsilon^i_{wall}/k_B = 57.9K\}$ then inclusions are described by $\{\sigma_{wall} = 5.4025 \text{ a.u.}, \epsilon^i_{inc}/k_B = 10\epsilon^i_{wall}/k_B\}$) at a much lower (more negative) attractive potential placed centrally and symmetrically along the walls and built outwards upon increasing their number.

If the two-dimensional cell is divided into a 10×10 grid then the frequency of particles inhabiting each sector can be totalled for analysis. **Figure 7.4** gives a graphical display of particle frequency along each grid line in the x-direction. It is important to note again that the particle walls are along the x-axes with the direction of the applied field perpendicular to this. The dashed *black* line denotes the initial configuration distribution (which is flat given the random distribution of particles), all other reported distributions denote the final configuration over a fixed run time for each simulation. The number of inclusions in each wall is increased from $1 \rightarrow 100$ (graph legend) where 100 is the maximum number of inclusions in each wall. All inclusions are placed along the central column and as the inclusions are increased from $0 \rightarrow 20$, the distribution narrows showing chain formation across the cell, from one patch to another, perpendicular to the walls. This is accompanied by reduced particle frequency in the grid sectors directly adjacent to the central band, highlighting the single stranded nature of chain formation due to a) the repulsive pair-potential and b) due to the low density. As the number of inclusions increases further ($\sim 20 \rightarrow 100$ particles in **Figure 7.4**) the distribution broadens again returning to a similar value in x over each grid sector at the limit. This is due to the increase in number of attractive particle inclusions which increases the width of the patches and

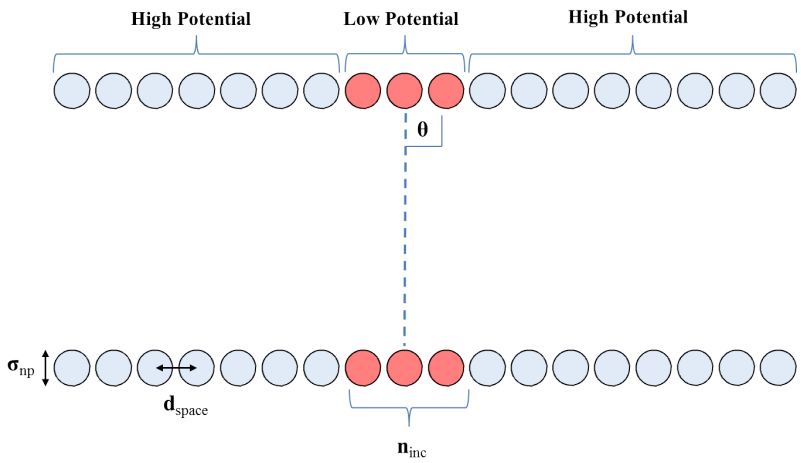


Figure 7.3: Schematic to show the build up of symmetric low (more negative) potential inclusions within the fixed walls. The angle $\theta = \pi/2$ denoting a symmetric inclusion placement.

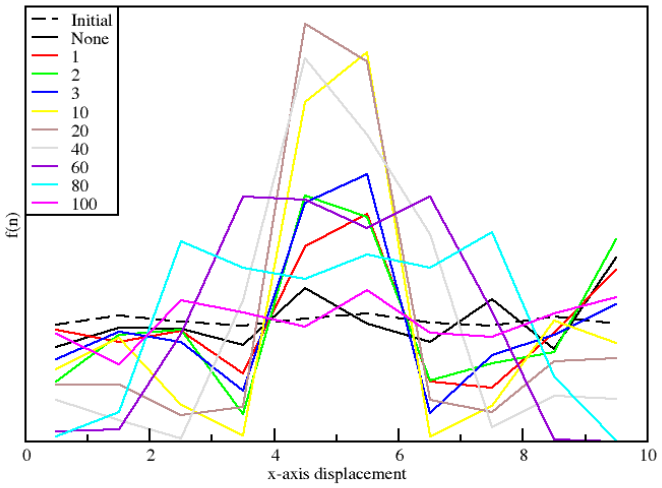
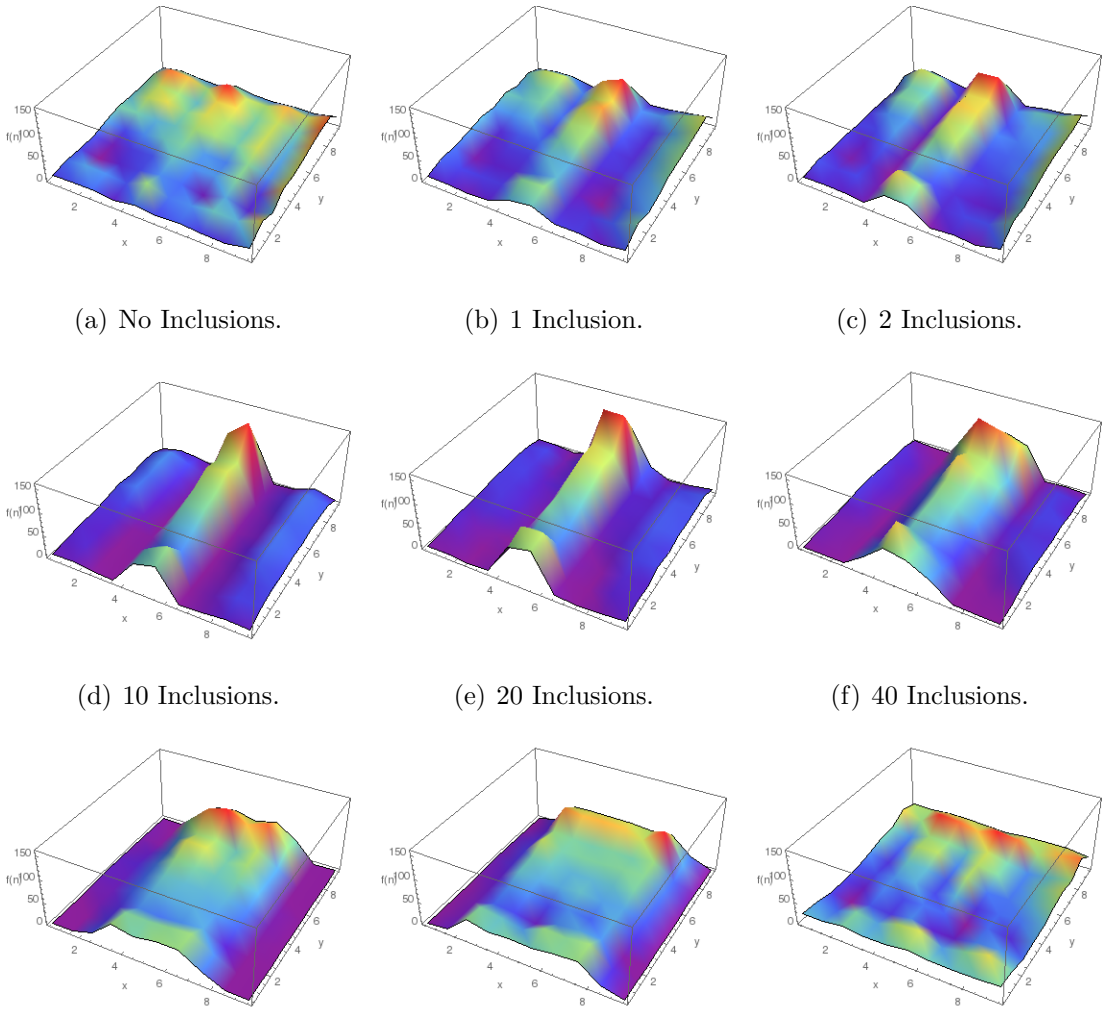


Figure 7.4: View along the x-axis as an average over the runs. The dashed line (initial) gives the starting configuration particle frequency per sector and subsequent distributions give that observed by increasing the inclusions in each wall. The simulation run is at $\{\alpha, \mathbf{E}_{ex}\} = \{5, 0.1\}$ a.u. with the external field $\perp$ to the x-axis. The legend denotes the number of inclusions.



(a) No Inclusions. (b) 1 Inclusion. (c) 2 Inclusions.

(d) 10 Inclusions. (e) 20 Inclusions. (f) 40 Inclusions.

(g) 60 Inclusions. (h) 80 Inclusions. (i) 100 Inclusions.

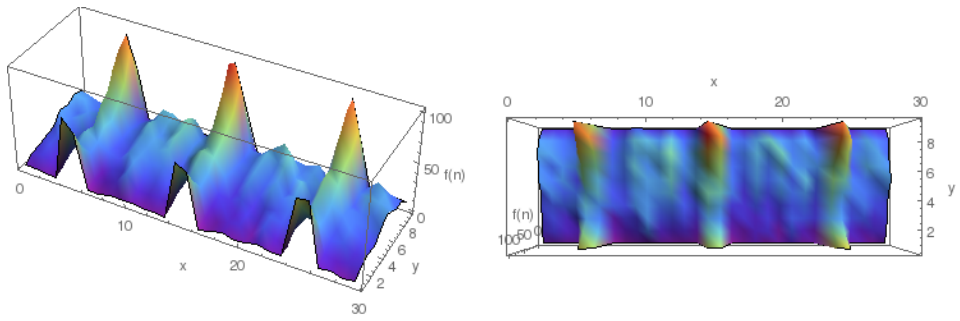
Figure 7.5: A 3-dimensional heat map denoting the average positions of particles in the cell and the evolution of frequency as the particle inclusions are increased in each wall. $\{\alpha, \mathbf{E}_{ex}\} = \{5, 0.1\}$ a.u..

prevents single-thickness particle chain aggregation perpendicular to the wall given the increased number of attractive sites (low potential) along the wall for the particles to aggregate around. **Figure 7.5** shows a 3-dimensional heat map of the average position of system particles when the field is applied perpendicular to the walls for a

varied number of low potential inclusions present. As is observed in **Figure 7.4** there is an optimum number of inclusions for this system that encourages single stranded chain growth (being $\sim$ 20 inclusions). This system is therefore highly tunable and depending on the difference in attractive dispersions forces, in the wall particles and in the inclusions then different structures can be favoured.

7.3.1 Elongated Cell

The square cell has been extended to three times the size, in the x-direction and additionally the number of particles inhabiting the cell has also increased three-fold. This acts to highlight the tune-ability of the simulation. By essentially replicating the $\{\alpha, \mathbf{E}_{ex}\} = \{10, 0.05\}$ a.u. case with 3 symmetrical wall inclusions in an elongated cell with three times the number of attractive points along the wall, we can highlight the ability of the simulation to control flow properties under confinement. Therefore **Figure 7.6** highlights that controllable, regular chain patterns can be produced, separated by a fixed distance.



(a) 3D perspective.

(b) Top-View.

Figure 7.6: A 3-dimensional plot showing the average position of particles in a cell elongated by three-times the size of those used in the previous cases. $\{\alpha, \mathbf{E}_{ex}\} = \{10, 0.05\}$ a.u. and there are 3 symmetric particle inclusions at grid sectors 5, 15 and 25 along each x-axis.

7.4 Offset Wall Inclusions

For the simulations in the following section there are blocks of inclusions placed into each 'upper' and 'lower' wall, again the interaction between wall and system particles are described by LJ parameters, $\{\sigma_{wall} = 5.4025 \text{ a.u.}, \epsilon^i_{wall}/k_B = 57.9K\}$ and inclusions are described by $\{\sigma_{wall} = 5.4025 \text{ a.u.}, \epsilon^i_{inc}/k_B = 10\epsilon^i_{wall}/k_B\}$. These inclusions are offset by a number of low potential particles from the 'upper' wall to the 'lower' wall, as highlighted in **Figure 7.7** as $\mathrm{n_{off}}$.

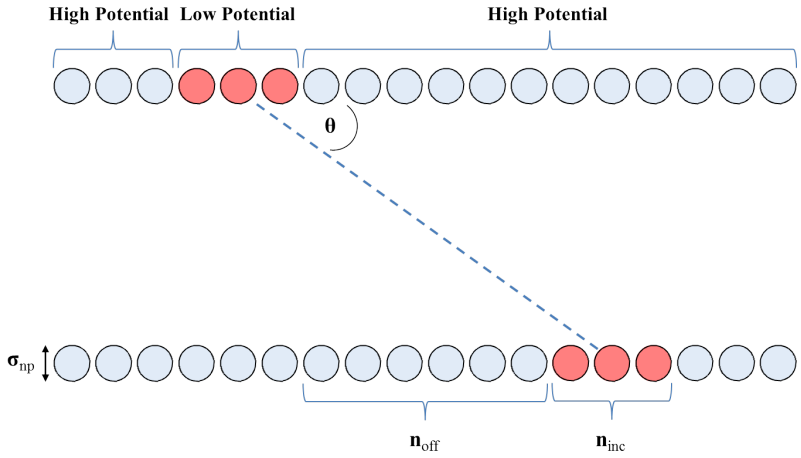


Figure 7.7: Schematic to show the build up of asymmetric low (more negative) potential inclusions, within the fixed walls. The angle θ shows the displacement between offset bands in the 'upper' wall relative to the 'lower' wall.

Reduced units are used such that the difference in x between the upper band of lower potential particle wall inclusions and the lower band can be described by γ_{off}.

$$\gamma_{\mathrm{off}} = \frac{d_{\mathrm{space}}(\mathrm{n_{off}} + \mathrm{n_{inc}})}{\sigma_{\mathrm{np}}} \tag{7.4.1}$$

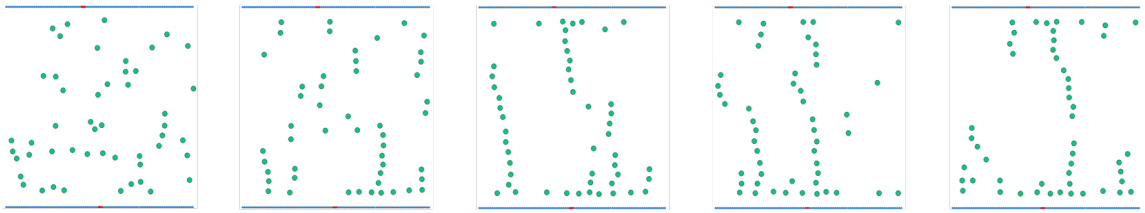
where d_{space} is the distance between wall particle centres, $\mathrm{n_{off}}$ is the number of particles between the upper and the lower wall inclusions and

$$\mathrm{n_{inc}} = \frac{\mathrm{n_{upper}} + \mathrm{n_{lower}}}{2} \tag{7.4.2}$$

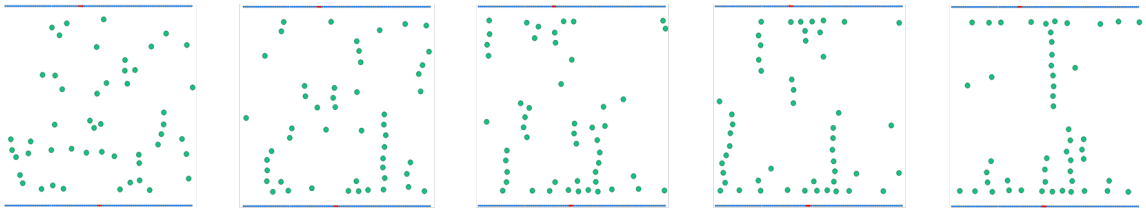
where n_{upper} is the number of inclusions in the upper wall and n_{lower} is the number of inclusions in the lower wall such that the average is taken for unit description.

7.4.1 Varying $\{\alpha, \mathbf{E}_{ex}\}$ at Constant μ

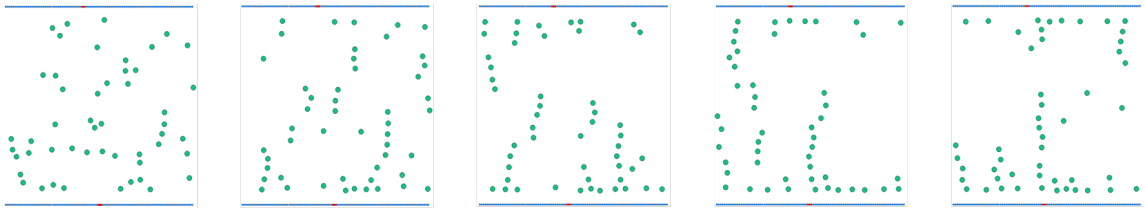
The effect of offsetting the wall inclusions changes the stability of the chains perpendicular to the patchy walls. All cell images below (**Figure 7.8**), show examples of runs with $n_{inc} = 3$ wall inclusions offset by $n_{off} = 6$, at different field strength and polarizability pairs such that $\gamma_{off} = 2.40$. The *red* coloured particles are the inclusions, the *light-blue* are fixed wall particles and the *green* particles are the 50 simulation particles confined to the cell. Additionally the average position of the particles over all configurations can be visualised suitably in a 3D frequency diagram (**Figures 7.9**, **7.10**, **7.11**). Each cell is mapped onto a 10×10 grid split according to the cell dimensions and from this, a simple sum of all particles within each sector can be calculated, $f(n)$. Similarly the dipole magnitude can be calculated in each sector allowing the production of an analogous 3D dipole plot (**Figures 7.9(c)**, **7.9(d)**, **7.10(c)**, **7.10(d)**, **7.11(c)**, **7.11(d)**). $\mu \cdot f(n)$ is shown (**Figures 7.9(e)**, **7.9(f)**, **7.10(e)**, **7.10(f)**, **7.11(e)**, **7.11(f)**) which highlights the effect of the dipoles at certain sectors within the grid. The colour map gives a relative range of values in the z-direction, from *purple* (lowest) to *red* (highest). As can be observed, by introducing particle offsets with higher ϵ^{i}_{wall}/k_B, the chain formed perpendicular to the wall buckles producing a kink in the chain. This is particularly observed in the low field, high α case where the DID effect is much stronger and chain stability is more favourable than simple aggregation around the inclusions. As the wall inclusions are offset here, the 'kink' in the central chain (as shown in high-field, low-α simulations) is removed when increasing the field strength, reducing the average particle polarizability and thus reducing the overall contribution of the DID effect.



(a) Parallel $\mathbf{E}_{ex}$.



(b) Perpendicular $\mathbf{E}_{ex}$.



(c) Parallel $\mathbf{E}_{ex}$.

Figure 7.8: $\{\alpha, \mathbf{E}_{ex}\}$ = **(a)**$\{10, 0.05\}$ a.u., **(b)**$\{5, 0.1\}$ a.u. and **(c)**$\{2, 0.25\}$ a.u.. Snapshots of the configurations over time, from left to right, $t^* = 0$, 6.96, 13.91, 27.82, 55.65.

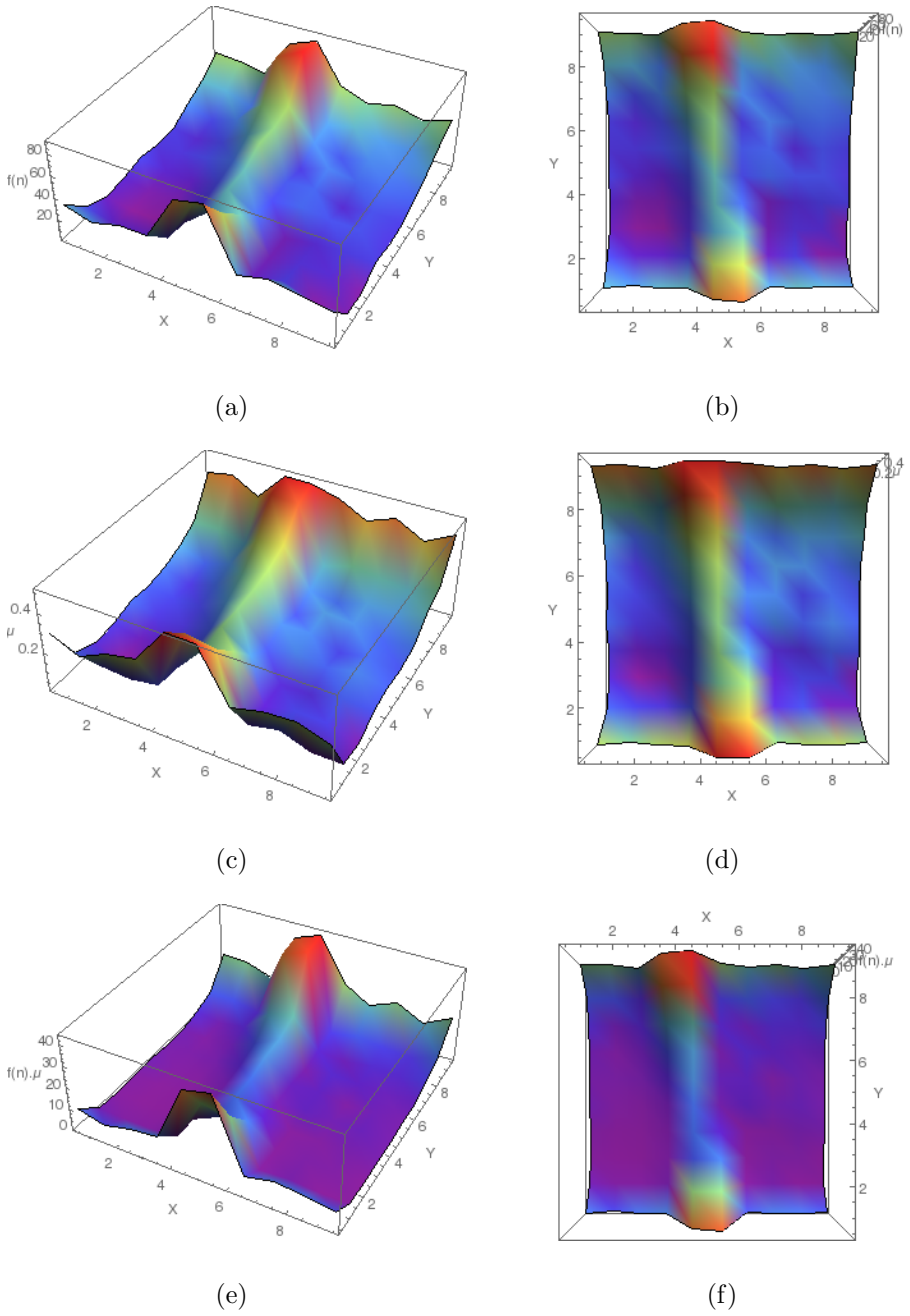
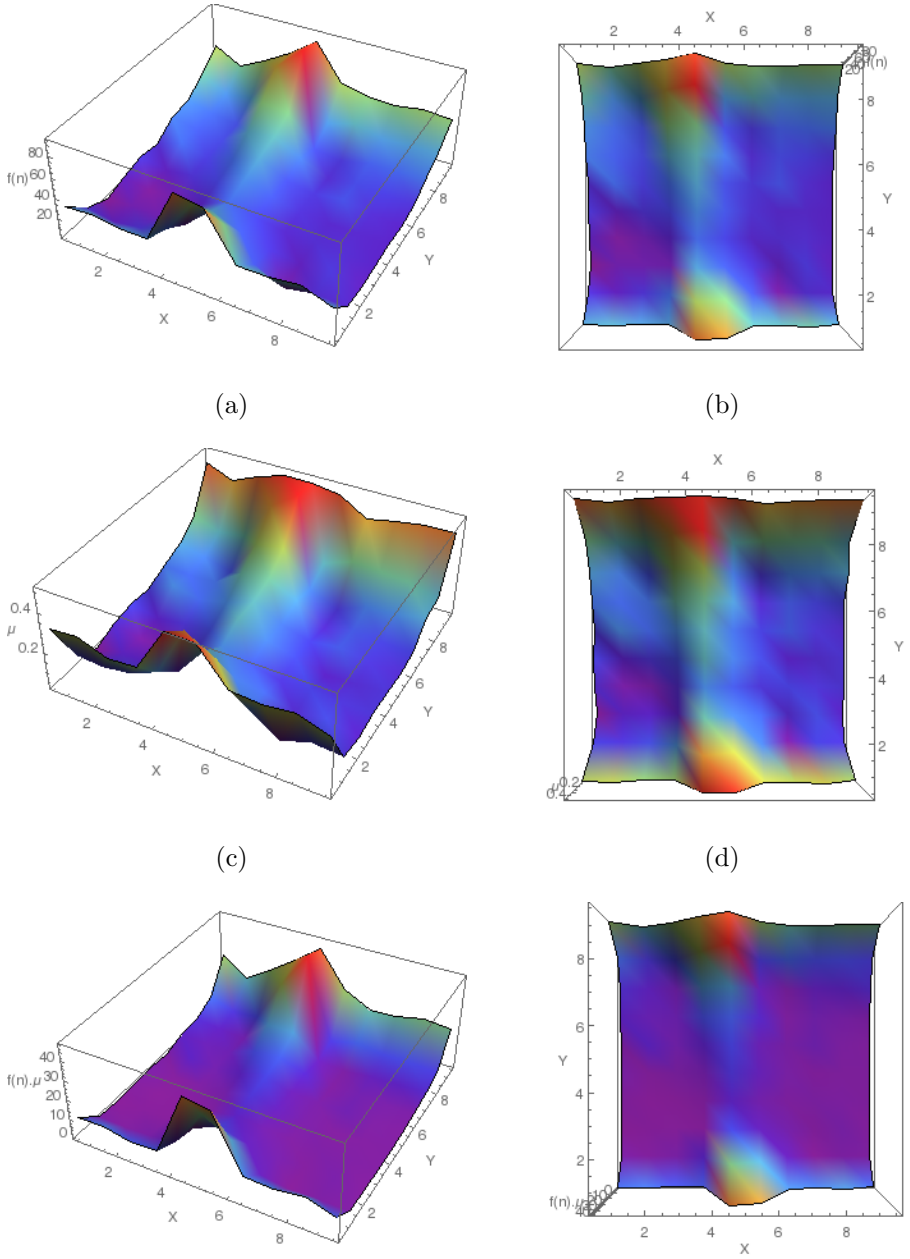


Figure 7.9: A 3D frequency heat map plot (**(a)** and **(b)**), a 3D average dipole plot (**(c)** and **(d)**) and the product $\mu \cdot f(n)$ (**(e)** and **(f)**) for $\{\alpha, \mathbf{E}_{ex}\} = \{10, 0.05\}$ a.u. with 3 inclusions offset by 6 particles.



(a) (b) (c) (d) (e) (f)

Figure 7.10: A 3D frequency heat map plot (**(a)** and **(b)**), a 3D average dipole plot (**(c)** and **(d)**) and the product $\mu \cdot f(n)$ (**(e)** and **(f)**) for $\{\alpha, \mathbf{E}_{ex}\} = \{5, 0.1\}$ a.u. with 3 inclusions offset by 6 particles.

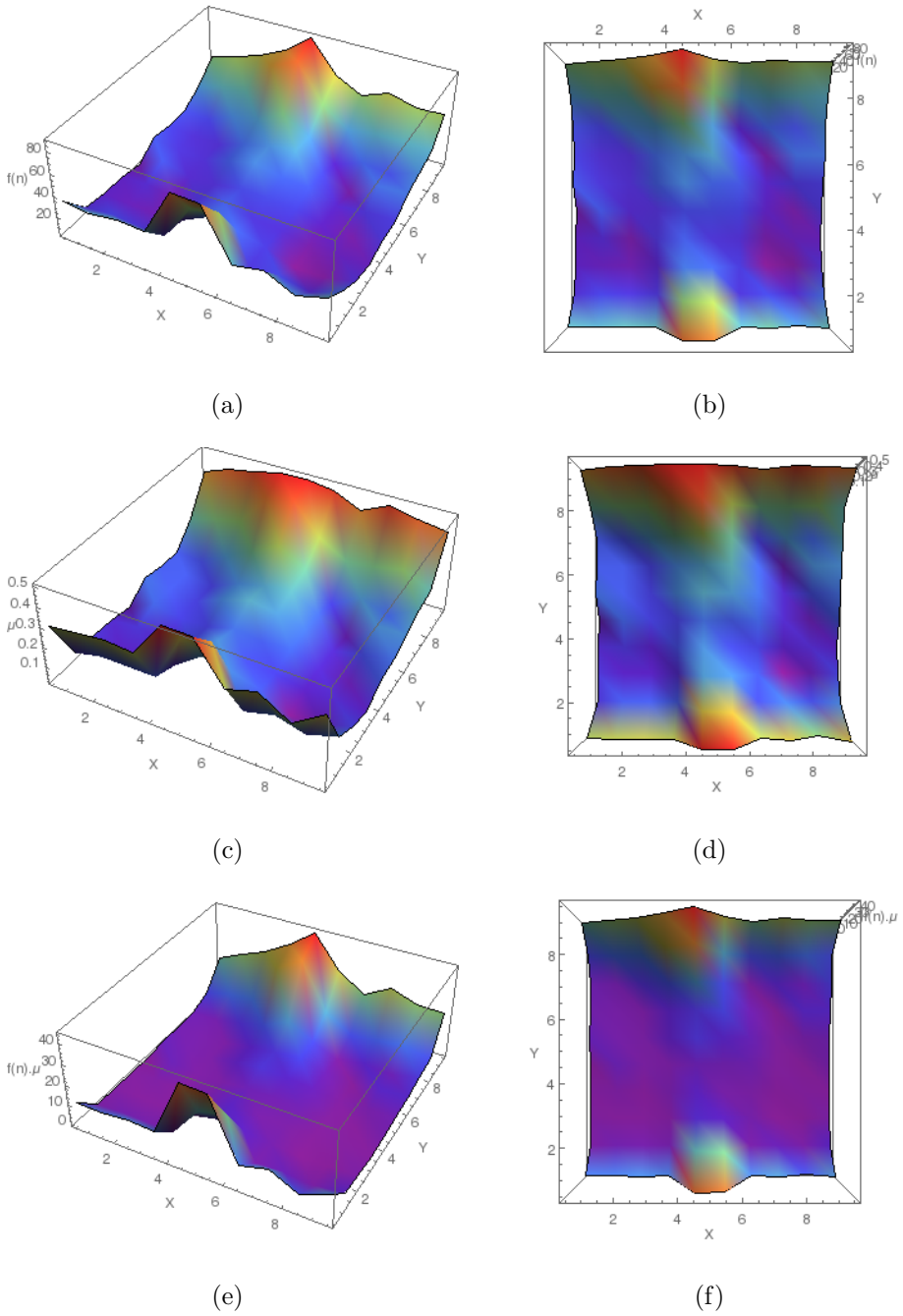


Figure 7.11: A 3D frequency heat map plot (**(a)** and **(b)**), a 3D average dipole plot (**(c)** and **(d)**) and the product $\mu \cdot f(n)$ (**(e)** and **(f)**) for $\{\alpha, \mathbf{E}_{ex}\} = \{2, 0.25\}$ a.u. with 3 inclusions offset by 6 particles.

7.4.2 Varying γ_{off}

The effect of varying the offset separation, γ_{off}, is shown in (**Figure 7.12**). By increasing the difference between bands of offsets, chains form due to the inclusion of high ϵ^i_{wall}/k_B wall particles, the position of which directs the construction and length of the chains, for example a single long chain from one wall to the adjacent wall or smaller chains appended to the patches present in the walls without connecting the walls. This can be observed along the x-axis as the distance between bands of low potential inclusions increases, the distributions migrate from a single-peak to a bimodal distribution of smaller peak height. This indicates that the chains are unstable at high separation and tend to smaller protrusive 'dangling' chains. **Figure 7.13** gives the 3D heat map plots showing the decrease in stability of a single stranded chain as γ_{off} increases (denoted by the kink in the chain) up to the limit where two chains are formed preferentially.

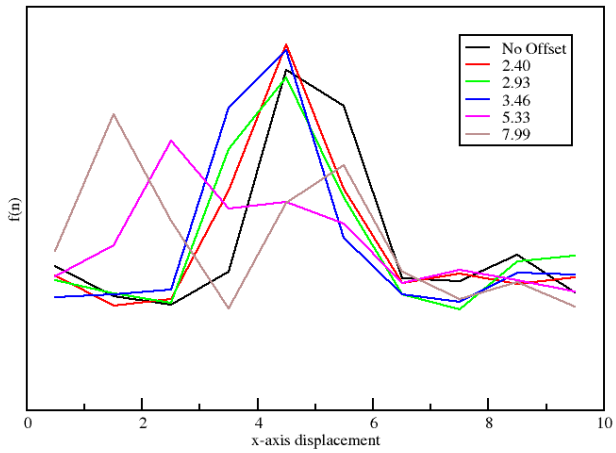
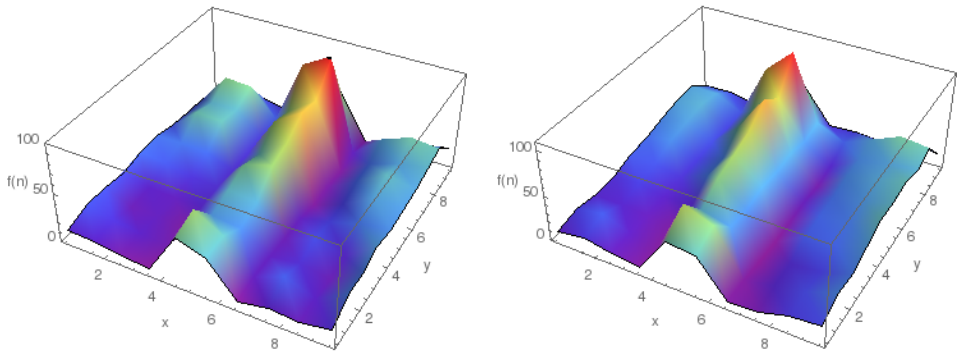
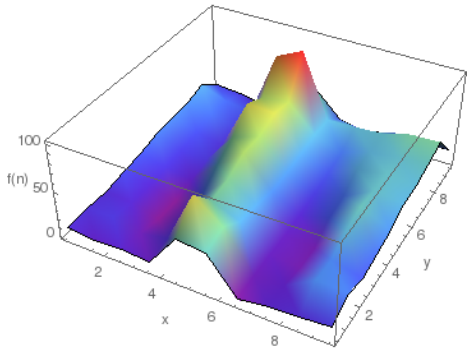


Figure 7.12: View along the x axis as an average over the runs. The *black* line gives the particle frequency for the configurations with no offset and subsequent distributions denote the value of γ_{off} as seen in the legend. The simulation run is at $\{\alpha, \mathbf{E}_{ex}\} = \{5, 0.1\}$ a.u. with the external field $\perp$ to the x-axis.

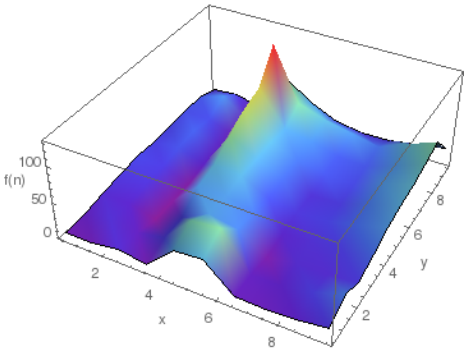


(a) $\gamma_{\text{off}} = 0$

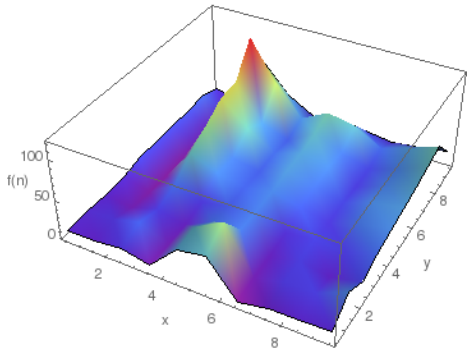
(b) $\gamma_{\text{off}} = 2.40$



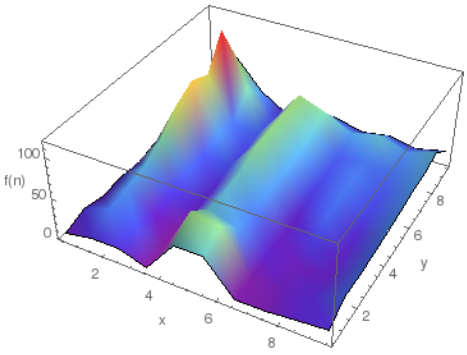
(c) $\gamma_{\text{off}} = 2.93$



(d) $\gamma_{\text{off}} = 3.46$



(e) $\gamma_{\text{off}} = 5.33$



(f) $\gamma_{\text{off}} = 7.99$

Figure 7.13: A 3D frequency heat map plot (**(a)** and **(b)**) for $\{\alpha, \mathbf{E}_{ex}\} = \{5, 0.1\}$ a.u. with 3 inclusions offset as described by γ_{off} values.

7.4.3 Varying Field Direction

If the direction of the electric field is altered the growth of chain structures becomes more varied. **Figure 7.14** shows the chain length probabilities for a system with three high potential particles in each wall where $\gamma_{\text{off}} = 2.40$ and the applied field is parallel to the inclusion displacement vector ($\theta = 0.471\pi$) or away from the displacement vector ($\theta = 0.529\pi$). The P_0 distribution for each case is similar, as expected, where the probability of finding a lone-particle is less variable over the range observed. However the P_1 and P_2 distribution curves show, albeit subtly, the DID effect in this system and how single-thickness chains along the central band, pinned with high potential inclusion are strengthened with the induced field parallel to this vector. When the applied field is along the inclusion displacement vector ($\theta = 0.471\pi$, *brown* points), P_2 is greater at the high mean chain length end of the distribution than the converse ($\theta = 0.529\pi$, *green* points), when the induced field direction is the same angle away from the inclusion displacement vector. **Figure 7.15** further highlights this point whereby the frequency of particles between sectors 3 and 4 (the direction in which the high potential inclusions are displaced) increases when the direction of the field is along the inclusion displacement vector.

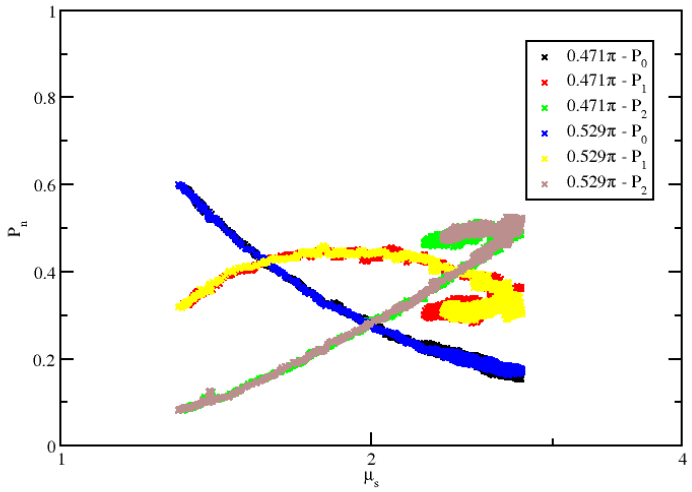


Figure 7.14: Chain length distributions for the confined, patchy wall system with 3 high potential inclusions in each wall, $\gamma_{\text{off}} = 2.40$. The legend gives the angle (describing the vector) of the applied field and the probability of finding a particle of coordination number n in a chain of mean length, μ_s.

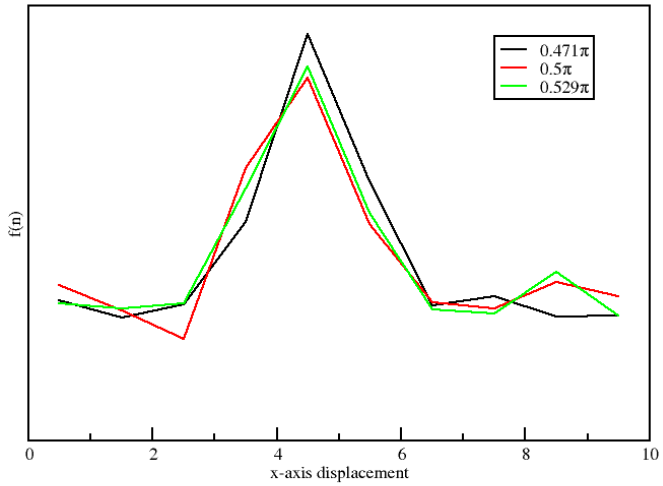


Figure 7.15: Particle frequency distributions along the x-axis for the system $\{\alpha, \mathbf{E}_{ex}\} = \{10, 0.05\}$ a.u. with 3 high potential inclusions in each wall, $\gamma_{\text{off}} = 2.40$. The field direction is varied, either in the direction of the inclusion displacement vector or away from it. The legend gives the vector of the applied field (described by θ).

7.5 Chapter Summary

This more speculative chapter has offered a future direction to experimental work in the area of MR confinement and flow control. Using these simple yet tractable models provides an excellent representation of the system and can justify particle aggregation in a host of systems. Three different confinement scenarios were investigated, 1) with confining pseudo-continuous potential walls without 'inclusions'; 2) confining particle walls with 'inclusions' at high attractive interaction potential, placed symmetrically on either side of the 2D cell and 3) confining particle walls with 'inclusions' at high attractive interaction potential placed asymmetrically on either side of the 2D cell with a defined offset between bands of inclusions. Chain formation can therefore be controlled in a variety of different manners and therefore the extent of chain formation in this system is entirely tunable.

Chapter 8

Conclusions

The work in this thesis is by no means a complete, self-contained review of MD simulation techniques using tractable pair-potentials, in the effort to predict particle aggregation and chain growth over the entire range of parameter space. This work does however highlight that the choice of pair-potential (r^{-12}) coupled with an induced dipole term (an improvement over the system with permanent dipole moments) can be shown to replicate compound growth processes as observed in experimental work, particularly at the low-mid density region of system particles. Overall it has shown that the system appears to 'self assemble' as a function of the distribution of the low and high dipole moments. The effect is more pronounced at high α, a direct result of the strength of the DID term (which acts to weight $\boldsymbol{\mu}^{(i)}$ strongly due to the large internal field contribution). The study of induced, rather than permanent, dipole moments adds a further degree of freedom in that the dipoles may be induced both by the applied (external) electric field and by the internal field resulting from the presence of other dipoles in the system (dipole-induced-dipoles).

Consequently, the simple simulation model used throughout this thesis has been fully justified in describing the growth aggregation process of monodisperse, superparamagnetic particles at low density. Comparison to analogous experimental work

has allowed an excellent prediction for the mean chain length distributions which are proportional to the change in mean coordination number over time. The distribution of dipole moments can be controlled by selecting particle polarizabilities where both systems, one with a set of fixed particle polarizabilities (monodisperse) and one with two sets of fixed particle polarizabilities (bidisperse) have been investigated. In the bidisperse case, for configurations generated from isotropic configurations at fixed field (quenching) there exists a range of applied field strengths which maximise the fraction of the more polarizable species within the formed chains. The difference in polarizability between particle species alters the extent of mixing/de-mixing (*i.e.* whether chains are comprised of only high (or only low) polarizabilty species or if the chain is made from both species equally, over a range of field strengths. These properties can be scaled as shown in this thesis given that there is comparable behaviour to a two state liquid system.

Finally, the results above show how easily the system can be tuned, in order to produce a wide range of chain and network structures. The model used is extremely tractable and it has been successfully related to analogous experimental work. Therefore the simulation model acts as a predictive tool for future work, as highlighted in the final chapter on confinement. The symbiosis between experiment, computation and theory that allowed this thesis to develop successfully, is the key for all future approaches in the understanding of MR fluid structure behaviour.

Appendix A

Multipole Interaction Tensors

A.1 Tensor Expressions

Tensors are an n-dimensional generalization of a scalar ($n = 1$) or vector ($n > 1$) and useful in this work to provide a condensed expression for the interaction terms: charge-charge (T^{ij}), charge-dipole (T^{ij}_{α}), dipole-dipole ($T^{ij}_{\alpha\beta}$), dipole-quadrupole ($T^{ij}_{\alpha\beta\gamma}$) and quadrupole-quadrupole interactions ($T^{ij}_{\alpha\beta\gamma\delta}$) [120].

$$T^{ij}_{\alpha\beta\gamma\delta...} = \nabla_{\alpha}\nabla_{\beta}\nabla_{\gamma}\nabla_{\delta}...\Big(\frac{1}{\mathbf{r}^{ij}}\Big) \tag{A.1.1}$$

Such that Greek indices denote coordinate axis $\{x, y, z\}$ and

$$\mathbf{r}^{ij} = \left[(r^{ij}_{x})^2 + (r^{ij}_{y})^2 + (r^{ij}_{z})^2\right]^{\frac{1}{2}}, \tag{A.1.2}$$

the distance between particle i and j.

A.1.1 Derivation of Interaction Tensors

$$T^{ij} = \frac{1}{\mathbf{r}^{ij}} \tag{A.1.3}$$

$$T^{ij}_{\alpha} = \nabla_\alpha \left(\frac{1}{\mathbf{r}^{ij}} \right) \tag{A.1.4}$$

$$= \nabla_\alpha []^2)^{\frac{-1}{2}}$$

$$= \frac{\partial}{\partial r^{ij}_\alpha} \left[(r^{ij}_x)^2 + (r^{ij}_y)^2 + (r^{ij}_z)^2 \right]^{\frac{-1}{2}}$$

$$= -r^{ij}_\alpha \left[(r^{ij}_x)^2 + (r^{ij}_y)^2 + (r^{ij}_z)^2 \right]^{\frac{-3}{2}}$$

$$= \frac{-r^{ij}_\alpha}{(\mathbf{r}^{ij})^3}$$

$$T^{ij}_{\alpha\beta} = \nabla_\alpha \nabla_\beta \frac{1}{\mathbf{r}^{ij}} \tag{A.1.5}$$

$$= \nabla_\alpha \left[\frac{-r^{ij}_\beta}{(\mathbf{r}^{ij})^3} \right]$$

$$= \frac{\partial}{\partial r^{ij}_\alpha} \left\{ -r^{ij}_\beta \left[(r^{ij}_x)^2 + (r^{ij}_y)^2 + (r^{ij}_z)^2 \right]^{\frac{-3}{2}} \right\}$$

$$= 3 r^{ij}_\alpha r^{ij}_\beta \left[(r^{ij}_x)^2 + (r^{ij}_y)^2 + (r^{ij}_z)^2 \right]^{\frac{-5}{2}} - \frac{\partial r^{ij}_\beta}{\partial r^{ij}_\alpha} \left[(r^{ij}_x)^2 + (r^{ij}_y)^2 + (r^{ij}_z)^2 \right]^{\frac{-3}{2}}$$

$$= 3 \frac{r^{ij}_\alpha r^{ij}_\beta}{(\mathbf{r}^{ij})^5} - \frac{\delta_{\alpha\beta}}{(\mathbf{r}^{ij})^3}$$

$$T^{ij}_{\alpha\beta\gamma} = \nabla_\alpha \nabla_\beta \nabla_\gamma \frac{1}{\mathbf{r}^{ij}} \tag{A.1.6}$$

$$= \nabla_\alpha \left[3 \frac{r^{ij}_\beta r^{ij}_\gamma}{(\mathbf{r}^{ij})^5} - \frac{\delta_{\beta\gamma}}{(\mathbf{r}^{ij})^3} \right]$$

$$= \frac{\partial}{\partial r^{ij}_\alpha} \left\{ 3 r^{ij}_\beta r^{ij}_\gamma \left[(r^{ij}_x)^2 + (r^{ij}_y)^2 + (r^{ij}_z)^2 \right]^{\frac{-5}{2}} \right.$$

$$\left. - \delta_{\beta\gamma} \left[(r^{ij}_x)^2 + (r^{ij}_y)^2 + (r^{ij}_z)^2 \right]^{\frac{-3}{2}} \right\}$$

$$= -15 r^{ij}_\alpha r^{ij}_\beta r^{ij}_\gamma \left[(r^{ij}_x)^2 + (r^{ij}_y)^2 + (r^{ij}_z)^2 \right]^{\frac{-7}{2}}$$

$$+ 3 \frac{\partial r^{ij}_\beta}{\partial r^{ij}_\alpha} r^{ij}_\gamma \left[(r^{ij}_x)^2 + (r^{ij}_y)^2 + (r^{ij}_z)^2 \right]^{\frac{-5}{2}}$$

$$+ 3 \frac{\partial r^{ij}_\gamma}{\partial r^{ij}_\alpha} r^{ij}_\beta \left[(r^{ij}_x)^2 + (r^{ij}_y)^2 + (r^{ij}_z)^2 \right]^{\frac{-5}{2}}$$

$$+ 3 \delta_{\beta\gamma} r^{ij}_\alpha \left[(r^{ij}_x)^2 + (r^{ij}_y)^2 + (r^{ij}_z)^2 \right]^{\frac{-5}{2}}$$

$$= -3\left[5\frac{r_\alpha^{ij}r_\beta^{ij}r_\gamma^{ij}}{(\mathbf{r}^{ij})^7} - \frac{(\delta_{\alpha\beta}r_\gamma^{ij} + \delta_{\alpha\gamma}r_\beta^{ij} + \delta_{\beta\gamma}r_\alpha^{ij})}{(\mathbf{r}^{ij})^5}\right]$$

$$\begin{aligned}
T_{\alpha\beta\gamma\delta}^{ij} &= \nabla_\alpha\nabla_\beta\nabla_\gamma\nabla_\delta\frac{1}{\mathbf{r}^{ij}} \qquad \text{(A.1.7)}\\
&= \nabla_\alpha\left\{-3\left[5\frac{r_\beta^{ij}r_\gamma^{ij}r_\delta^{ij}}{(\mathbf{r}^{ij})^7} - \frac{(\delta_{\beta\delta}r_\gamma^{ij} + \delta_{\gamma\delta}r_\beta^{ij} + \delta_{\beta\gamma}r_\delta^{ij})}{(\mathbf{r}^{ij})^5}\right]\right\}\\
&= -3\frac{\partial}{\partial r_\alpha^{ij}}\Big\{5r_\beta^{ij}r_\gamma^{ij}r_\delta^{ij}\left[(r_x^{ij})^2 + (r_y^{ij})^2 + (r_z^{ij})^2\right]^{\frac{-7}{2}}\\
&\qquad -(\delta_{\beta\delta}r_\gamma^{ij} + \delta_{\gamma\delta}r_\beta^{ij} + \delta_{\beta\gamma}r_\delta^{ij})\left[(r_x^{ij})^2 + (r_y^{ij})^2 + (r_z^{ij})^2\right]^{\frac{-5}{2}}\Big\}\\
&= 15\Big\{7r_\alpha^{ij}r_\beta^{ij}r_\gamma^{ij}r_\delta^{ij}\left[(r_x^{ij})^2 + (r_y^{ij})^2 + (r_z^{ij})^2\right]^{\frac{-9}{2}}\\
&\qquad - \frac{\partial r_\beta^{ij}}{\partial r_\alpha^{ij}}r_\gamma^{ij}r_\delta^{ij}\left[(r_x^{ij})^2 + (r_y^{ij})^2 + (r_z^{ij})^2\right]^{\frac{-7}{2}}\\
&\qquad - \frac{\partial r_\gamma^{ij}}{\partial r_\alpha^{ij}}r_\beta^{ij}r_\delta^{ij}\left[(r_x^{ij})^2 + (r_y^{ij})^2 + (r_z^{ij})^2\right]^{\frac{-7}{2}}\\
&\qquad - \frac{\partial r_\delta^{ij}}{\partial r_\alpha^{ij}}r_\beta^{ij}r_\gamma^{ij}\left[(r_x^{ij})^2 + (r_y^{ij})^2 + (r_z^{ij})^2\right]^{\frac{-7}{2}}\Big\}\\
&\qquad + 3\Big\{-5(\delta_{\beta\delta}r_\alpha^{ij}r_\gamma^{ij} + \delta_{\gamma\delta}r_\alpha^{ij}r_\beta^{ij}\\
&\qquad + \delta_{\beta\gamma}r_\alpha^{ij}r_\delta^{ij})\left[(r_x^{ij})^2 + (r_y^{ij})^2 + (r_z^{ij})^2\right]^{\frac{-7}{2}}\\
&\qquad + (\delta_{\beta\delta}\delta_{\alpha\gamma} + \delta_{\gamma\delta}\delta_{\alpha\beta} + \delta_{\beta\gamma}\delta_{\alpha\delta})\left[(r_x^{ij})^2 + (r_y^{ij})^2 + (r_z^{ij})^2\right]^{\frac{-5}{2}}\Big\}\\
&= \frac{105}{(\mathbf{r}^{ij})^9}\left(r_\alpha^{ij}r_\beta^{ij}r_\gamma^{ij}r_\delta^{ij}\right) + \frac{3}{(\mathbf{r}^{ij})^5}(\delta_{\beta\delta}\delta_{\alpha\gamma} + \delta_{\gamma\delta}\delta_{\alpha\beta} + \delta_{\beta\gamma}\delta_{\alpha\delta})\\
&\qquad - \frac{15}{(\mathbf{r}^{ij})^7}\left(\delta_{\beta\delta}r_\alpha^{ij}r_\gamma^{ij} + \delta_{\gamma\delta}r_\alpha^{ij}r_\beta^{ij} + \delta_{\beta\gamma}r_\alpha^{ij}r_\delta^{ij}\right.\\
&\qquad\qquad \left.+\delta_{\alpha\beta}r_\gamma^{ij}r_\delta^{ij} + \delta_{\alpha\gamma}r_\beta^{ij}r_\delta^{ij} + \delta_{\alpha\delta}r_\beta^{ij}r_\gamma^{ij}\right).
\end{aligned}$$

As explored by Buckingham [119] describing the interaction between two molecules, separated by a large enough distance such that electron exchange can be neglected. An interaction Hamiltonian (given as the perturbation of the sum of Hamiltonians that describe the free molecules) can be set up. This Hamiltonian is written as a multipole series containing the field and field-gradient operators along with charge,

dipole and quadrupole moment operators, employing the use of tensor notation as has been used in this work with influence from Wilson's model [120].

A.2 Einstein Summation Convention

In order to circumvent the need to write out explicit indices for summation formulae, in tensor notation we use the Einstein summation convention whereby a summation is assumed over indices that appear twice in a vector product [189].

$$\sum_{i}^{n} A_{\alpha\beta} B_{\beta} = A_{\alpha\beta} B_{\beta} \tag{A.2.1}$$

where β is the dummy index and α is the running index.

Appendix B

Further Simulation Methods

B.1 Energy Conservation

The total energy of an isolated mechanical system is conserved as shown:

$$\begin{aligned}\frac{dE}{dt} &= \frac{d}{dt}\left[\sum_i^N \frac{1}{2} m^i (\dot{\mathbf{r}}^i)^2 + \mathscr{U}(\mathbf{r}^N)\right] = \sum_i^N m^i \dot{\mathbf{r}}^i \cdot \ddot{\mathbf{r}}^i + \sum_i^N \frac{\partial \mathscr{U}}{\partial \mathbf{r}^i} \cdot \dot{\mathbf{r}}^i \\ &= \sum_i^N \dot{\mathbf{r}}^i \cdot \mathbf{f}^i - \sum_i^N \dot{\mathbf{f}}^i \cdot \mathbf{r}^i = 0.\end{aligned} \tag{B.1.1}$$

B.2 Velocity Verlet Integration Algorithm

Using a truncated Taylor expansion about time t, then the particle positions, $\mathbf{r}^i$ at time $t + \delta t$ are:

$$\mathbf{r}^i(t + \delta t) = \mathbf{r}^i(t) + \dot{\mathbf{r}}^i(t)\delta t + \frac{\ddot{\mathbf{r}}^i(t)}{2}\delta t^2 + \mathcal{O}(\delta t^3). \tag{B.2.1}$$

Thus with the substitution of $\dot{\mathbf{r}}^i = \mathbf{v}^i$ and $m^i \ddot{\mathbf{r}} = \mathbf{f}^i$, **Equation B.2.1** becomes

$$\mathbf{r}^i(t + \delta t) = \mathbf{r}^i(t) + \mathbf{v}^i(t)\delta t + \frac{\mathbf{f}^i(t)}{2m^i}\delta t^2 + \mathcal{O}(\delta t^3). \tag{B.2.2}$$

The analogous Taylor expansion of $\mathbf{v}^i(t+\delta t)$ is

$$\mathbf{v}^i(t+\delta t) = \mathbf{v}^i(t) + \dot{\mathbf{v}}^i(t)\delta t + \frac{\ddot{\mathbf{v}}^i(t)}{2}\delta t^2 + \mathcal{O}(\delta t^3) \tag{B.2.3}$$

and for $\dot{\mathbf{v}}^i(t)$

$$\dot{\mathbf{v}}^i(t+\delta t) = \dot{\mathbf{v}}^i(t) + \ddot{\mathbf{v}}^i(t)\delta t + \mathcal{O}(\delta t^2), \tag{B.2.4}$$

which can be rearranged to the form

$$\ddot{\mathbf{v}}^i(t)\delta t = \dot{\mathbf{v}}^i(t+\delta t) - \dot{\mathbf{v}}^i(t) + \mathcal{O}(\delta t^2). \tag{B.2.5}$$

Further substitution of $\dot{\mathbf{v}} = \mathbf{f}^i/m^i$ and $\ddot{\mathbf{v}}^i(t)$ (**Equation B.2.5**) into **Equation B.2.3** yields

$$\begin{aligned} \mathbf{v}^i(t+\delta t) &= \mathbf{v}^i(t) + \frac{\mathbf{f}^i(t)}{m^i}\delta t + \frac{1}{2}\left(\dot{\mathbf{v}}^i(t+\delta t) - \dot{\mathbf{v}}^i(t)\right)\delta t + \mathcal{O}(\delta t^3) & \text{(B.2.6)} \\ &= \mathbf{v}^i(t) + \frac{1}{2m^i}\left(\mathbf{f}^i(t+\delta t) + \mathbf{f}^i(t)\right)\delta t + \mathcal{O}(\delta t^3). & \text{(B.2.7)} \end{aligned}$$

Therefore **Equations B.2.2** and **B.2.6** give the self-starting positions and velocities for the velocity Verlet algorithm.

B.3 Verlet Integration Algorithm

A derivation of the verlet integration scheme can be obtained by starting with a Taylor expansion of the particle positions $\mathbf{r}^i$ at time $t+\delta t$ such that

$$\mathbf{r}^i(t+\delta t) = \mathbf{r}^i(t) + \dot{\mathbf{r}}^i(t)\delta t + \frac{1}{2}\ddot{\mathbf{r}}^i(t)\delta t^2 + \mathcal{O}(t^3). \tag{B.3.1}$$

Thus with the substitution of $\dot{\mathbf{r}}^i = \mathbf{v}^i$ and $m^i\ddot{\mathbf{r}} = \mathbf{f}^i$, **Equation B.3.1** becomes

$$\mathbf{r}^i(t+\delta t) = \mathbf{r}^i(t) + \mathbf{v}^i(t)\delta t + \frac{\mathbf{f}^i(t)}{m^i}\delta t^2 + \mathcal{O}(t^3). \tag{B.3.2}$$

Additionally,

$$\mathbf{r}^i(t-\delta t) = \mathbf{r}^i(t) - \mathbf{v}^i(t)\delta t + \frac{\mathbf{f}^i(t)}{m_i}\delta t^2 + \mathcal{O}(t^3). \tag{B.3.3}$$

Therefore the addition of **Equations B.3.2** and **B.3.3** gives the desired result:

$$\mathbf{r}^i(t+\delta t) = 2\mathbf{r}^i(t) - \mathbf{r}^i(t-\delta t) + \frac{\mathbf{f}^i(t)}{m^i}\delta t^2 + \mathcal{O}(t^3), \tag{B.3.4}$$

which describes the position of the particle at time $(t+\delta t)$ in terms of the position of the previous step and the force acting on particle i. The velocity at time t can also be obtained where

$$\mathbf{v}^i(t) = \frac{1}{2\delta t}[\mathbf{r}^i(t+\delta t) - \mathbf{r}^i(t-\delta t)] + \mathcal{O}(t^3). \tag{B.3.5}$$

A leapfrog algorithm [114] can be used to obtain more accurate velocities without introducing an error to order of δt^2 that is produced by solving **Equation B.3.4** for the velocities given in **Equation B.3.5**. Thus after some algebraic manipulation:

$$\mathbf{r}^i(t+\delta t) = \mathbf{r}^i(t) + \mathbf{v}^i(t+\frac{1}{2}\delta t)\delta t \tag{B.3.6}$$

$$\mathbf{v}^i(t+\frac{1}{2}\delta t) = \mathbf{v}^i(t-\frac{1}{2}\delta t) + \frac{\mathbf{f}^i(t)}{m^i}\delta t \tag{B.3.7}$$

Therefore new velocities are calculated at a half-time step after the positions are calculated. However as is evident this algorithm requires knowledge of the positions at time $(t-\delta t)$ and is thus awkward computationally.

B.4 Steepest Descent Minimisation

Another method for energy minimisation is the first order steepest descent (or gradient descent) approach. System configurations can be relaxed by minimising the energy by systematically removing any kinetic energy from the particle ensemble in order to stymie the system from mounting any activation barriers. The process of

using a steepest descent algorithm is set out by Leach [142]. The gradient of the energy function is used to iteratively determine the next set of coordinates in the system. This minimisation technique encourages a system with initial coordinates $\mathbf{x}_0$, close to a given global minimum, to converge to local minima instead. The new set of coordinates as determined at each step in the steepest descent are

$$\mathbf{x}_{n+1} = \mathbf{x}_n + \lambda_n \mathbf{s}_n, \tag{B.4.1}$$

where $\mathbf{s}_n$ is a $3N$ dimensional unit vector related to the gradient of the energy at $\mathbf{x}_n$ and λ_n is essentially the step size of the n^{th} move that depends on the nature of the energy surface. The value of λ_n increases greatly at each step when the function describing the energy of the system ($f(\mathbf{x}_n)$) decreases in value (and *vice versa*). Therefore, when the value of $f(\mathbf{x}_n)$ starts to increase, after previously decreasing in value, then the potential function has crossed to the opposite side of the potential well; thus when a local minimum is surmounted, the magnitude of λ_n is reduced. This process continues until the local minimum is found.

Appendix C

Analytical Techniques

C.1 Chain Length Distribution Derivations

The mathematical basis of the discrete probability distribution for chain lengths in a compound growth process is as follows: The probability of a particle i being part of a cluster of size s (with mean cluster size, μ_s) is

$$P(i;s) = \frac{s\,P(s)}{\sum_{s=1}^{\infty} s\,P(s)} = \frac{s}{\mu_s^2}\left(1 - \frac{1}{\mu_s}\right)^{s-1} \tag{C.1.1}$$

The probability that a particle, i has a coordination number n is conditional on s, the size of the chain containing particle i and is written as $P(n|i;s)$. The product of these probabilities, $P(n \cap i;s) = P(n|i;s)P(i;s)$, is the probability of randomly selecting a particle that is in a cluster of size s and has a coordination number n. Subsequently it follows that the probability of a particle selected at random, that has coordination n is given by the sum over all cluster sizes of this probability, therefore

$$P_n = \sum_{s=1}^{\infty} P(n \cap i;s) = \sum_{s=1}^{\infty} P(n|i;s)P(i;s). \tag{C.1.2}$$

Furthermore, $P(n|i;s)$ is described in terms of cluster size and for this system, only linear chains are considered with possible coordination numbers, $n = 0$, 1 or 2. Thus

$P(n=0|i;s)=1$, $P(n=1|i;s)=2/s$ and $P(n=2|i;s)=(s-2)/s$ by definition for linear chains. The probability as a function of chain length ,for $n=0$ is therefore given by

$$\begin{aligned} P_0 &= P(i;s=1)=\frac{1.\left(1-\frac{1}{\mu_s}\right)^o}{\mu_s^2} \\ &= \frac{1}{\mu_s^2} \end{aligned} \tag{C.1.3}$$

which is the result displayed in **Equation 5.5.7**. Similarly for one-coordinate particles **Equation C.1.1** becomes

$$\begin{aligned} P_1 &= \sum_{s=2}^{\infty}\frac{2P(i;s)}{s} \\ &= \frac{2}{\mu_s^2}\left\{\frac{2\left(1-\frac{1}{\mu_s}\right)}{2}+\frac{3\left(1-\frac{1}{\mu_s}\right)^2}{3}+...\right\} \\ &\equiv \frac{2}{\mu_s^2}(x+x^2+...)=\frac{2x}{\mu_s^2}(1+x+...)=\frac{2x}{\mu_s^2}\frac{1}{1-x} \\ &\equiv \frac{2(\mu_s-1)}{\mu^3}\mu_s \\ &= \frac{2(\mu_s-1)}{\mu_s^2}, \end{aligned} \tag{C.1.4}$$

which is the result displayed in **Equation 5.5.8**, where $x=1-\frac{1}{\mu_s}$ using the standard geometric series

$$\sum_{k=0}^{\infty}ar^k=\frac{a}{1-r}. \tag{C.1.5}$$

Finally, for two-coordinate particles the probability can be written as

$$\begin{aligned} P_2 &= \sum_{s=2}^{\infty}\frac{(s-2)P(i;s)}{s} \\ &= \sum_{s=2}^{\infty}P(i;s)-\sum_{s=2}^{\infty}\frac{2P(i;s)}{s} \\ &= 1-\frac{1}{\mu_s^2}-\frac{2(\mu_s-1)}{\mu_s^2} \\ &= \frac{(\mu_s-1)^2}{\mu_s^2} \end{aligned} \tag{C.1.6}$$

which is the result displayed in **Equation 5.5.9**. Consequently by using the equations above, the mean coordination number can be described as:

$$\begin{aligned}
\mu_n &= P_n(n=1) + 2P_n(n=2), \\
&= \frac{2(\mu_s - 1)}{\mu_s^2} + \frac{2(\mu_s - 1)^2}{\mu_s^2} \\
&= \frac{2\mu_s - 2 + 2(\mu_s^2 - 2\mu_s + 1)}{\mu_s^2} \\
&= \frac{2\mu_s^2 - 2\mu_s}{\mu_s^2} = 2 - \frac{2}{\mu_s},
\end{aligned} \tag{C.1.7}$$

which is the result given in **Equation 5.5.10**.

C.2 Continuous Analogue of Chain Length Distributions

For completeness, the analogous continuous distribution of that derived in **Appendix C.1** is as follows: For spherical particles, where chains are formed only in one-dimension, the probability, $P(s)$, that a chain of length s exists in a simulation cell (with mean chain length, $\bar{s}$) can be described with a shifted Poisson distribution,

$$P(s) = \frac{\mathrm{e}^{1-\bar{s}}(\bar{s}-1)^{s-1}}{(s-1)!}. \tag{C.2.1}$$

The probability that a particle, i selected in a chain with zero-coordination ($s = 1$) then becomes

$$P_0 = P(i; s=1) = \mathrm{e}^{1-\bar{s}}. \tag{C.2.2}$$

For one-coordinate particles,

$$\begin{aligned} P_1 &= \sum_{s=2}^{\infty} \frac{2P(i;s)}{s} \\ &= 2\left\{ \frac{\mathrm{e}^{1-\bar{s}}(\bar{s}-1)^1}{2.1!} + \frac{\mathrm{e}^{1-\bar{s}}(\bar{s}-1)^2}{3.2!} + ... \right\} \\ &= 2\mathrm{e}^{1-\bar{s}} \left\{ \frac{x}{2!} + \frac{x^2}{3!} + ... \right\}, \\ &= \frac{2\mathrm{e}^{1-\bar{s}}}{x} \left\{ \frac{x^2}{2!} + \frac{x^3}{3!} + ... \right\}, \end{aligned} \tag{C.2.3}$$

where $x = \bar{s} - 1$ and the terms expressed as "2.1!" arise from the respective factors of s and $(s-1)!$ in the denominator. The term in the last set of brackets can be written as a Taylor expansion,

$$\mathrm{e}^x - 1 - x = \frac{x^2}{2!} + \frac{x^3}{3!} + ... \tag{C.2.4}$$

As a result,

$$\begin{aligned} P_1 &= \frac{2\mathrm{e}^{1-\bar{s}}}{\bar{s}-1} \left[\mathrm{e}^{s-1} - 1 - (\bar{s}-1) \right], \\ &= \frac{2\mathrm{e}^{1-\bar{s}}(\mathrm{e}^{\bar{s}-1} - \bar{s})}{\bar{s}-1}, \\ &= \frac{2(1-\bar{s}\mathrm{e}^{1-\bar{s}})}{\bar{s}-1}. \end{aligned} \tag{C.2.5}$$

Finally for two-coordinate particles,

$$\begin{aligned} P_2 &= \sum_{i;s=2}^{\infty} \frac{s-2}{s} P(s), \\ &= \sum_{s=2}^{\infty} P(i;s) - \sum_{s=2}^{\infty} \frac{2P(i;s)}{s}. \end{aligned} \tag{C.2.6}$$

The first term can be written as

$$\begin{aligned}\sum_{i;s=2}^{\infty} P(s) &= \mathrm{e}^{1-\bar{s}}\left\{\frac{(\bar{s}-1)^1}{1!}+\frac{(\bar{s}-1)^2}{2!}+...\right\},\\ &\equiv \mathrm{e}^{1-\bar{s}}\left\{x+\frac{x^2}{2!}+...\right\},\\ &= \mathrm{e}^{1-\bar{s}}(\mathrm{e}^{x}-1),\\ &\equiv \mathrm{e}^{1-\bar{s}}(\mathrm{e}^{\bar{s}-1}-1),\\ &= 1-\mathrm{e}^{1-\bar{s}}. \end{aligned} \tag{C.2.7}$$

The second term is given by **Equation C.2.5**. As a result,

$$\begin{aligned}P_2 &= 1-\mathrm{e}^{1-\bar{s}}-\frac{2(1-\bar{s}\mathrm{e}^{1-\bar{s}})}{\bar{s}-1},\\ &= \frac{\bar{s}-1-(\bar{s}-1)\mathrm{e}^{1-\bar{s}}-2+2\bar{s}\mathrm{e}^{1-\bar{s}}}{\bar{s}-1},\\ &= \frac{\bar{s}+(\bar{s}+1)\mathrm{e}^{1-\bar{s}}-3}{\bar{s}-1}. \end{aligned} \tag{C.2.8}$$

The mean coordination number, $\bar{c}$, is given by

$$\bar{c} = P_1 + 2P_2, \tag{C.2.9}$$

as $P_0 + P_1 + P_2 = 1$, therefore,

$$\begin{aligned}\bar{c} &= \frac{2(1-\bar{s}\mathrm{e}^{1-\bar{s}})}{\bar{s}-1}+\frac{2\bar{s}+2(\bar{s}+1)\mathrm{e}^{1-\bar{s}}-6}{\bar{s}-1},\\ &= \frac{2(\bar{s}+\mathrm{e}^{1-\bar{s}}-2)}{\bar{s}-1}. \end{aligned} \tag{C.2.10}$$

C.3 Reduced Units

Reduced units are used which vary, depending on the form of the short range potential and act to scale the nano-particle problem (observed in experiment) to the atomic analogue. An example being $\rho^* = N\sigma^2/A$, the reduced density for a two-dimensional soft-sphere system. Here N gives the number of particles in the simulation cell, σ the particle diameter and A is the area of the cell in two dimensions. Not only does the use of these units allow for a more sensible scaling system but they also contextualise the problem for a quicker comparison with similar computational or experimental work (*e.g.* [3, 16, 17, 58, 188, 190–196]).

Other reduced units of interest, but not necessarily used in this thesis, are; temperature (T^*), dipole moment (μ^*), field strength (H^*), time (t^*) and the dipole-dipole coupling parameter (λ):

$$T^* = \frac{k_B T}{\epsilon} \tag{C.3.1}$$

$$\mu^* = \frac{\mu}{\sqrt{\epsilon\sigma^2}} \tag{C.3.2}$$

$$H^* = \frac{H\mu}{k_B T} \tag{C.3.3}$$

$$t^* = t\left(\frac{\epsilon}{m\sigma^2}\right)^{1/2} \tag{C.3.4}$$

$$\lambda = \frac{\mu^2}{k_B T \sigma^2}. \tag{C.3.5}$$

Appendix D

Dipoles in Chains

The derivations in this section complement the dipole distribution work in **Sections 4.2** and **6.1** for monodisperse and bidisperse chains respectively.

D.1 Two Dipoles

Consider two dipoles, $\boldsymbol{\mu}_{ex}$, separated by a distance r, induced by an external field, $\mathbf{E}_{ex}$, which is applied along the vector joining the two dipoles. The field at one site as a result of the other dipole is

$$\mathbf{E}_{(2 \text{ particles})} = \frac{2\boldsymbol{\mu}_{ex}}{r^3}. \tag{D.1.1}$$

As a result, the first-order DID correction to the dipole is given by

$$\mu_{DID}^{(1)} = \frac{2\alpha\boldsymbol{\mu}_{ex}}{r^3}, \tag{D.1.2}$$

where α is the particle polarizability. The total dipole is now

$$\mu^{(1)} = \boldsymbol{\mu}_{ex} + \mu_{DID}^{(1)}. \tag{D.1.3}$$

As a result,

$$\mu_{DID}^{(2)} = \frac{2\alpha\mu^{(1)}}{r^3}, \tag{D.1.4}$$

and so

$$\mu^{(2)} = \boldsymbol{\mu}_{ex} + \mu^{(2)}_{DID}, \tag{D.1.5}$$

etc. until the induced dipole converges at the limit $\mu^{(\infty)}_{DID}$.

D.2 A Chain of Dipoles

For a chain of dipoles all separated by r, the field is given by

$$\begin{aligned}
\mathbf{E}_{chain} &= \frac{4\alpha\mathbf{E}_{ex}}{r^3} + \frac{4\alpha\mathbf{E}_{ex}}{(2r)^3} + ... \\
&= \frac{4\alpha\mathbf{E}_{ex}}{r^3}\left\{1 + \frac{1}{8} + \frac{1}{27} + ...\right\}, \\
&= \frac{4\alpha\mathbf{E}_{ex}}{r^3}\sum_{n=1}^{\infty} n^{-3}, \\
&= \frac{4\alpha\mathbf{E}_{ex}}{r^3}\zeta(3),
\end{aligned} \tag{D.2.1}$$

where the '4' arises from the chains of dipoles percolating away in two directions from a given site and $\zeta(3)$ is a Riemann zeta function (also known as Apéry's constant) having a value of $\zeta(3) \simeq 1.2021$.

D.3 The Distribution of Dipoles along a Chain

The first-order field of a single-coordinate particle on the end of an infinite chain is given by

$$\epsilon_1 = \frac{2\alpha\mathbf{E}_{ex}}{r^3}\zeta(3). \tag{D.3.1}$$

The field on the next particle along the chain is then described by

$$\epsilon_2 = \epsilon_1 + \frac{2\alpha\mathbf{E}_{ex}}{r^3}, \tag{D.3.2}$$

therefore for the next particle along

$$\epsilon_3 = \epsilon_2 + \frac{2\alpha\mathbf{E}_{ex}}{(2r)^3}, \tag{D.3.3}$$

and in general

$$\epsilon_n = \epsilon_{n-1} + \frac{2\alpha \mathbf{E}_{ex}}{[(n-1)r]^3}. \tag{D.3.4}$$

The dipoles reach their saturated infinite chain value relatively rapidly, as the chain length increases. As a result, the dipole distributions differentiate very clearly between the zero-, one- and two-coordinate sites.

D.4 The Monodisperse Model

For monodisperse calculations $\boldsymbol{\mu}_{ex}$ is fixed at $\boldsymbol{\mu}_{ex} = \alpha \cdot \mathbf{E}_{ex} = 0.5$ a.u.. Particles in the system are be assumed to occupy long chains such that

$$\mu^{(1)} = \boldsymbol{\mu}_{ex} + \frac{4\alpha^2 \mathbf{E}_{ex}\zeta(3)}{r^3}, \tag{D.4.1}$$

and since $\boldsymbol{\mu}_{ex}$ is fixed, the above equation can be rearranged as

$$\mu^{(1)} = \boldsymbol{\mu}_{ex} + \frac{4\boldsymbol{\mu}_{ex}^2\zeta(3)}{r^3}\frac{1}{\mathbf{E}_{ex}}. \tag{D.4.2}$$

Therefore it follows that

$$\begin{aligned} \Delta\mu &= \mu^{(1)} - \boldsymbol{\mu}_{ex} = \frac{4\boldsymbol{\mu}_{ex}^2\zeta(3)}{r^3}\frac{1}{\mathbf{E}_{ex}}, \\ &\propto \frac{1}{\mathbf{E}_{ex}}. \end{aligned} \tag{D.4.3}$$

Appendix E

Table of Bidisperse Runs

Parameter sets investigated in **Chapter 6** are listed in the table below.

Row #	$\mathbf{E}_{ex}$ (a.u.)	α_1 (a.u.)	α_2 (a.u.)	$\langle\alpha\rangle$ (a.u.)	$\Delta\alpha$ (a.u.)	$\frac{\Delta\alpha}{\langle\alpha\rangle}$	$\langle\alpha\rangle \cdot \mathbf{E}_{ex}$ (a.u.)
1	0.25	1.0	3.0	2.0	2.0	1.0	0.5
2	0.25	1.2	2.8	2.0	1.6	0.8	0.5
3	0.25	1.4	2.6	2.0	1.2	0.6	0.5
4	0.25	1.6	2.4	2.0	0.8	0.4	0.5
5	0.25	1.8	2.2	2.0	0.4	0.2	0.5
6	0.17	3.0	7.0	5.0	4.0	0.8	0.85
7	0.17	3.5	6.5	5.0	3.0	0.6	0.85
8	0.17	4.0	6.0	5.0	2.0	0.4	0.85
9	0.17	4.5	5.5	5.0	1.0	0.2	0.85
10	0.155	3.0	7.0	5.0	4.0	0.8	0.775
11	0.155	3.5	6.5	5.0	3.0	0.6	0.775
12	0.155	4.0	6.0	5.0	2.0	0.4	0.775
13	0.155	4.5	5.5	5.0	1.0	0.2	0.775

Row #	$\mathbf{E}_{ex}$ (a.u.)	α_1 (a.u.)	α_2 (a.u.)	$\langle\alpha\rangle$ (a.u.)	$\Delta\alpha$ (a.u.)	$\frac{\Delta\alpha}{\langle\alpha\rangle}$	$\langle\alpha\rangle \cdot \mathbf{E}_{ex}$ (a.u.)
14	0.14	3.0	7.0	5.0	4.0	0.8	0.7
15	0.14	3.5	6.5	5.0	3.0	0.6	0.7
16	0.14	4.0	6.0	5.0	2.0	0.4	0.7
17	0.14	4.5	5.5	5.0	1.0	0.2	0.7
18	0.125	3.0	7.0	5.0	4.0	0.8	0.625
19	0.125	3.5	6.5	5.0	3.0	0.6	0.625
20	0.125	4.0	6.0	5.0	2.0	0.4	0.625
21	0.125	4.5	5.5	5.0	1.0	0.2	0.625
22	0.11	3.0	7.0	5.0	4.0	0.8	0.55
23	0.11	3.5	6.5	5.0	3.0	0.6	0.55
24	0.11	4.0	6.0	5.0	2.0	0.4	0.55
25	0.11	4.5	5.5	5.0	1.0	0.2	0.55
26	0.10	2.5	7.5	5.0	5.0	1.0	0.5
27	0.10	3.0	7.0	5.0	4.0	0.8	0.5
28	0.10	3.5	6.5	5.0	3.0	0.6	0.5
29	0.10	4.0	6.0	5.0	2.0	0.4	0.5
30	0.10	4.5	5.5	5.0	1.0	0.2	0.5
N/W	0.10	6.0	14.0	10.0	8.0	0.8	1.0
31	0.10	7.0	13.0	10.0	6.0	0.6	1.0
32	0.10	8.0	12.0	10.0	4.0	0.4	1.0
33	0.10	9.0	11.0	10.0	2.0	0.2	1.0
N/W	0.10	13.0	17.0	15.0	4.0	0.2666	1.5
N/W	0.10	14.0	16.0	15.0	2.0	0.1333	1.5

Row #	$\mathbf{E}_{ex}$ (a.u.)	α_1 (a.u.)	α_2 (a.u.)	$\langle\alpha\rangle$ (a.u.)	$\Delta\alpha$ (a.u.)	$\frac{\Delta\alpha}{\langle\alpha\rangle}$	$\langle\alpha\rangle \cdot \mathbf{E}_{ex}$ (a.u.)
34	0.095	3.0	7.0	5.0	4.0	0.8	0.475
35	0.095	3.5	6.5	5.0	3.0	0.6	0.475
36	0.095	4.0	6.0	5.0	2.0	0.4	0.475
37	0.095	4.5	5.5	5.0	1.0	0.2	0.475
38	0.08	3.0	7.0	5.0	4.0	0.8	0.4
39	0.08	3.5	6.5	5.0	3.0	0.6	0.4
40	0.08	4.0	6.0	5.0	2.0	0.4	0.4
41	0.08	4.5	5.5	5.0	1.0	0.2	0.4
42	0.075	3.0	7.0	5.0	4.0	0.8	0.375
43	0.075	4.0	6.0	5.0	2.0	0.4	0.375
44	0.075	6.0	14.0	10.0	8.0	0.8	0.75
45	0.075	7.0	13.0	10.0	6.0	0.6	0.75
46	0.075	8.0	12.0	10.0	4.0	0.4	0.75
47	0.075	9.0	11.0	10.0	2.0	0.2	0.75
N/W	0.075	13.0	17.0	15.0	4.0	0.2666	1.125
N/W	0.075	14.0	16.0	15.0	2.0	0.1333	1.125
48	0.07	3.0	7.0	5.0	4.0	0.8	0.35
49	0.07	4.0	6.0	5.0	2.0	0.4	0.35
50	0.07	6.0	14.0	10.0	8.0	0.8	0.7
51	0.07	7.0	13.0	10.0	6.0	0.6	0.7
52	0.07	8.0	12.0	10.0	4.0	0.4	0.7
53	0.07	9.0	11.0	10.0	2.0	0.2	0.7

Row #	$\mathbf{E}_{ex}$ (a.u.)	α_1 (a.u.)	α_2 (a.u.)	$\langle\alpha\rangle$ (a.u.)	$\Delta\alpha$ (a.u.)	$\frac{\Delta\alpha}{\langle\alpha\rangle}$	$\langle\alpha\rangle \cdot \mathbf{E}_{ex}$ (a.u.)
54	0.065	3.0	7.0	5.0	4.0	0.8	0.325
55	0.065	3.5	6.5	5.0	3.0	0.6	0.325
56	0.065	4.0	6.0	5.0	2.0	0.4	0.325
57	0.065	4.5	5.5	5.0	1.0	0.2	0.325
58	0.065	6.0	14.0	10.0	8.0	0.8	0.65
59	0.065	7.0	13.0	10.0	6.0	0.6	0.65
60	0.065	8.0	12.0	10.0	4.0	0.4	0.65
61	0.065	9.0	11.0	10.0	2.0	0.2	0.65
62	0.06	3.0	7.0	5.0	4.0	0.8	0.3
63	0.06	4.0	6.0	5.0	2.0	0.4	0.3
64	0.06	6.0	14.0	10.0	8.0	0.8	0.6
65	0.06	7.0	13.0	10.0	6.0	0.6	0.6
66	0.06	8.0	12.0	10.0	4.0	0.4	0.6
67	0.06	9.0	11.0	10.0	2.0	0.2	0.6
68	0.055	3.0	7.0	5.0	4.0	0.8	0.275
69	0.055	3.5	6.5	5.0	3.0	0.6	0.275
70	0.055	4.0	6.0	5.0	2.0	0.4	0.275
71	0.055	4.5	5.5	5.0	1.0	0.2	0.275
72	0.055	6.0	14.0	10.0	8.0	0.8	0.55
73	0.055	7.0	13.0	10.0	6.0	0.6	0.55
74	0.055	8.0	12.0	10.0	4.0	0.4	0.55
75	0.055	9.0	11.0	10.0	2.0	0.2	0.55

Row #	$\mathbf{E}_{ex}$ (a.u.)	α_1 (a.u.)	α_2 (a.u.)	$\langle\alpha\rangle$ (a.u.)	$\Delta\alpha$ (a.u.)	$\frac{\Delta\alpha}{\langle\alpha\rangle}$	$\langle\alpha\rangle \cdot \mathbf{E}_{ex}$ (a.u.)
76	0.05	3.0	7.0	5.0	4.0	0.8	0.25
77	0.05	3.5	6.5	5.0	3.0	0.6	0.25
78	0.05	4.0	6.0	5.0	2.0	0.4	0.25
79	0.05	4.5	5.5	5.0	1.0	0.2	0.25
80	0.05	5.0	15.0	10.0	10.0	1.0	0.5
81	0.05	6.0	14.0	10.0	8.0	0.8	0.5
82	0.05	7.0	13.0	10.0	6.0	0.6	0.5
83	0.05	8.0	12.0	10.0	4.0	0.4	0.5
84	0.05	9.0	11.0	10.0	2.0	0.2	0.5
85	0.045	3.0	7.0	5.0	4.0	0.8	0.225
86	0.045	4.0	6.0	5.0	2.0	0.4	0.225
87	0.045	6.0	14.0	10.0	8.0	0.8	0.45
88	0.045	7.0	13.0	10.0	6.0	0.6	0.45
89	0.045	8.0	12.0	10.0	4.0	0.4	0.45
90	0.045	9.0	11.0	10.0	2.0	0.2	0.45
91	0.04	3.0	7.0	5.0	4.0	0.8	0.2
92	0.04	3.5	6.5	5.0	3.0	0.6	0.2
93	0.04	4.0	6.0	5.0	2.0	0.4	0.2
94	0.04	4.5	5.5	5.0	1.0	0.2	0.2
95	0.04	6.0	14.0	10.0	8.0	0.8	0.4
96	0.04	7.0	13.0	10.0	6.0	0.6	0.4
97	0.04	8.0	12.0	10.0	4.0	0.4	0.4
98	0.04	9.0	11.0	10.0	2.0	0.2	0.4
99	0.04	6.25	18.75	12.5	12.5	1.0	0.5

Row #	$\mathbf{E}_{ex}$ (a.u.)	α_1 (a.u.)	α_2 (a.u.)	$\langle\alpha\rangle$ (a.u.)	$\Delta\alpha$ (a.u.)	$\frac{\Delta\alpha}{\langle\alpha\rangle}$	$\langle\alpha\rangle \cdot \mathbf{E}_{ex}$ (a.u.)
100	0.04	7.5	17.5	12.5	10.0	0.8	0.5
101	0.04	8.5	16.5	12.5	8.0	0.64	0.5
102	0.04	9.5	15.5	12.5	6.0	0.48	0.5
103	0.04	10.5	14.5	12.5	4.0	0.32	0.5
104	0.04	11.5	13.5	12.5	2.0	0.16	0.5
105	0.0375	3.0	7.0	5.0	4.0	0.8	0.1875
106	0.0375	4.0	6.0	5.0	2.0	0.4	0.1875
107	0.0375	6.0	14.0	10.0	8.0	0.8	0.375
108	0.0375	7.0	13.0	10.0	6.0	0.6	0.375
109	0.0375	8.0	12.0	10.0	4.0	0.4	0.375
110	0.0375	9.0	11.0	10.0	2.0	0.2	0.375
111	0.0375	11.0	19.0	15.0	8.0	0.5333	0.5625
112	0.0375	13.0	17.0	15.0	4.0	0.2666	0.5625
113	0.0375	14.0	16.0	15.0	2.0	0.1333	0.5625
114	0.035	3.0	7.0	5.0	4.0	0.8	0.175
115	0.035	3.5	6.5	5.0	3.0	0.6	0.175
116	0.035	4.0	6.0	5.0	2.0	0.4	0.175
117	0.035	4.5	5.5	5.0	1.0	0.2	0.175
118	0.0333	10.5	19.5	15.0	9.0	0.6	0.5
119	0.0333	12.0	18.0	15.0	6.0	0.4	0.5
120	0.0333	13.5	16.5	15.0	3.0	0.2	0.5

Row #	$\mathbf{E}_{ex}$ (a.u.)	α_1 (a.u.)	α_2 (a.u.)	$\langle\alpha\rangle$ (a.u.)	$\Delta\alpha$ (a.u.)	$\frac{\Delta\alpha}{\langle\alpha\rangle}$	$\langle\alpha\rangle \cdot \mathbf{E}_{ex}$ (a.u.)
121	0.025	3.0	7.0	5.0	4.0	0.8	0.125
122	0.025	3.5	6.5	5.0	3.0	0.6	0.125
123	0.025	4.0	6.0	5.0	2.0	0.4	0.125
124	0.025	4.5	5.5	5.0	1.0	0.2	0.125
125	0.025	6.0	14.0	10.0	8.0	0.8	0.25
126	0.025	7.0	13.0	10.0	6.0	0.6	0.25
127	0.025	8.0	12.0	10.0	4.0	0.4	0.25
128	0.025	9.0	11.0	10.0	2.0	0.2	0.25
129	0.025	11.0	19.0	15.0	8.0	0.5333	0.375
130	0.025	13.0	17.0	15.0	4.0	0.2666	0.375
131	0.025	14.0	16.0	15.0	2.0	0.1333	0.375
132	0.02	3.0	7.0	5.0	4.0	0.8	0.1
133	0.02	3.5	6.5	5.0	3.0	0.6	0.1
134	0.02	4.0	6.0	5.0	2.0	0.4	0.1
135	0.02	4.5	5.5	5.0	1.0	0.2	0.1
136	0.01	3.0	7.0	5.0	4.0	0.8	0.05
137	0.01	3.5	6.5	5.0	3.0	0.6	0.05
138	0.01	4.0	6.0	5.0	2.0	0.4	0.05
139	0.01	4.5	5.5	5.0	1.0	0.2	0.05
140	0.01	6.0	14.0	10.0	8.0	0.8	0.1
141	0.01	7.0	13.0	10.0	6.0	0.6	0.1

Row #	$\mathbf{E}_{ex}$ (a.u.)	α_1 (a.u.)	α_2 (a.u.)	$\langle\alpha\rangle$ (a.u.)	$\Delta\alpha$ (a.u.)	$\frac{\Delta\alpha}{\langle\alpha\rangle}$	$\langle\alpha\rangle \cdot \mathbf{E}_{ex}$ (a.u.)
142	0.01	8.0	12.0	10.0	4.0	0.4	0.1
143	0.01	9.0	11.0	10.0	2.0	0.2	0.1
144	0.01	11.0	19.0	15.0	8.0	0.5333	0.15
145	0.01	13.0	17.0	15.0	4.0	0.2666	0.15
146	0.01	14.0	16.0	15.0	2.0	0.1333	0.15
147	0.005	3.0	7.0	5.0	4.0	0.8	0.025
148	0.005	3.5	6.5	5.0	3.0	0.6	0.025
149	0.005	4.0	6.0	5.0	2.0	0.4	0.025
150	0.005	4.5	5.5	5.0	1.0	0.2	0.025
151	0.005	6.0	14.0	10.0	8.0	0.8	0.05
152	0.005	7.0	13.0	10.0	6.0	0.6	0.05
153	0.005	8.0	12.0	10.0	4.0	0.4	0.05
154	0.005	9.0	11.0	10.0	2.0	0.2	0.05
155	0.005	11.0	19.0	15.0	8.0	0.5333	0.075
156	0.005	13.0	17.0	15.0	4.0	0.2666	0.075
157	0.005	14.0	16.0	15.0	2.0	0.1333	0.075
158	0	10.0	10.0	10.0	0	1.0	0

Table E.1: N/W denotes a run with field strength and polarizability which does not compute, likely due to the polarization catastrophe.

Bibliography

[1] S. H. L. Klapp. Dipolar fluids under external perturbations. *Journal of Physics: Condensed Matter*, 17(15):R525–R550, 2005.

[2] B. Huke and M. Lücke. Magnetic properties of colloidal suspensions of interacting magnetic particles. *Reports on Progress in Physics*, 67(10):1731–1768, 2004.

[3] C. Holm and J. Weis. The structure of ferrofluids: A status report. *Current Opinion in Colloid & Interface Science*, 10(3-4):133–140, 2005.

[4] B. J. Alder and E. L. Pollock. Simulation of polar and polarizable fluids. *Annual Review of Physical Chemistry*, 32(1):311–329, 1981.

[5] A. F. Bakuzis, Luis C. Branquinho, L. Luiz e Castro, M. T. de Amaral e Eloi, and R. Miotto. Chain formation and aging process in biocompatible polydisperse ferrofluids: Experimental investigation and Monte Carlo simulations. *Advances in Colloid and Interface Science*, 191–192:1–21, 2013.

[6] J. de Vicente, D. J. Klingenberg, and R. Hidalgo-Alvarez. Magnetorheological fluids: a review. *Soft Matter*, 7(8):3701–3710, 2011.

[7] H. Löwen. Colloidal dispersions in external fields: recent developments. *Journal of Physics: Condensed Matter*, 20(40):404201, 2008.

[8] A. T. Skjeltorp. Ordering phenomena of particles dispersed in magnetic fluids (invited). *Journal of Applied Physics*, 57(8):3285–3290, 1985.

[9] G. Yang, B. F. Spencer, J. D. Carlson, and M. K. Sain. Large-scale MR fluid dampers: modeling and dynamic performance considerations. *Engineering Structures*, 24(3):309–323, 2002.

[10] D. J. Klingenberg. Magnetorheology: Applications and challenges. *AIChE Journal*, 47(2):246–249, 2001.

[11] M. Fermigier and A. P. Gast. Structure evolution in a paramagnetic latex suspension. *Journal of Colloid and Interface Science*, 154(2):522–539, 1992.

[12] R. Haghgooie and P. S. Doyle. Transition from two-dimensional to three-dimensional behavior in the self-assembly of magnetorheological fluids confined in thin slits. *Physical Review E - Statistical, Nonlinear and Soft Matter Physics*, 75(6):061406, 2007.

[13] M. Klokkenburg, B. H. Erné, J. D. Meeldijk, A. Wiedenmann, A. V. Petukhov, R. P. A. Dullens, and A. P. Philipse. In situ imaging of field-induced hexagonal columns in magnetite ferrofluids. *Physical Review Letters*, 97(18):185702, 2006.

[14] K. Butter, P. H. Bomans, P. M. Frederik, G. J. Vroege, and A. P. Philipse. Direct observation of dipolar chains in ferrofluids in zero field using cryogenic electron microscopy. *Journal of Physics: Condensed Matter*, 15(15):S1451–S1470, 2003.

[15] M. Klokkenburg, R. P. A. Dullens, W. K. Kegel, B. H. Erné, and A. P. Philipse. Quantitative real-space analysis of self-assembled structures of magnetic dipolar colloids. *Physical Review Letters*, 96(3):037203, 2006.

[16] J. J. Weis. Low density quasi-two-dimensional dipolar hard spheres in an external field. *Molecular Physics*, 103(1):7–10, 2005.

[17] P. Camp. Structure and phase behavior of a two-dimensional system with core-softened and long-range repulsive interactions. *Physical Review E*, 68(6):061506, 2003.

[18] C. R. Acad. Sci. Paris. La variation du ferromagnetisme du temperature. *Comptes Rendus*, 143:1136–1149, 1906.

[19] R. E. Rosensweig. *Ferrohydrodynamics*. Dover Publications, Inc. (originally published by Cambridge University press 1985), 2013.

[20] J. Frenkel. *Kinetic Theory of Liquids*. Dover, 1955.

[21] L. Néel. Effect of thermal fluctuations on the magnetization of small particles. *C. R. Acad. Sci. Paris*, 228:664, 1949.

[22] J. Černák, G. Helgesen, and A. T. Skjeltorp. Aggregation dynamics of nonmagnetic particles in a ferrofluid. *Physical Review E*, 70(3):031504, 2004.

[23] G. Helgesen, A. T. Skjeltorp, P. M. Mors, R. Botet, and R. Jullien. Aggregation of magnetic microspheres: Experiments and simulations. *Physical Review Letters*, 61(15):1736–1739, 1988.

[24] J. H. E. Promislow, A. P. Gast, and M. Fermigier. Aggregation kinetics of paramagnetic colloidal particles. *The Journal of Chemical Physics*, 102(13):5492–5498, 1995.

[25] P. Domínguez-García, Sonia Melle, J. M. Pastor, and M. A. Rubio. Scaling in the aggregation dynamics of a magnetorheological fluid. *Physical Review E*, 76(5):051403, 2007.

[26] P. Domínguez-García, J. M. Pastor, and M. A. Rubio. Aggregation and disaggregation dynamics of sedimented and charged superparamagnetic micro-particles in water suspension. *The European Physical Journal E*, 34(4):36, 2011.

[27] J. Černák and G. Helgesen. Aggregation of magnetic holes in a rotating magnetic field. *Physical Review E - Statistical, Nonlinear and Soft Matter Physics*, 78(6):1–6, 2008.

[28] R. M. Erb, M. D. Krebs, E. Alsberg, B. Samanta, V. M. Rotello, and B. B. Yellen. Beyond diffusion-limited aggregation kinetics in microparticle suspensions. *Physical Review E*, 80(05):051402, 2009.

[29] G. Pál, F. Kun, I. Varga, D. Sohler, and G. Sun. Attraction-driven aggregation of dipolar particles in an external magnetic field. *Physical Review E*, 83(6):061504, 2011.

[30] F. Martínez-Pedrero, A. El-Harrak, J. C. Fernández-Toledano, M. Tirado-Miranda, J. Baudry, A. Schmitt, J. Bibette, and J. Callejas-Fernández. Kinetic study of coupled field-induced aggregation and sedimentation processes arising in magnetic fluids. *Physical Review E*, 78(1):011403, 2008.

[31] R. E. Moctezuma, F. Donado, and J. L. Arauz-Lara. Lateral aggregation induced by magnetic perturbations in a magnetorheological fluid based on non-Brownian particles. *Physical Review E*, 88(3):032305, 2013.

[32] T. Ukai, H. Morimoto, and T. Maekawa. Cluster-cluster aggregations of superparamagnetic particles in a rotational magnetic field. *Physical Review E*, 83(6):061406, 2011.

[33] S. Melle, O. G. Calderón, M. A. Rubio, and G. G. Fuller. Microstructure evolution in magnetorheological suspensions governed by Mason number. *Physical Review E*, 68(4):041503, 2003.

[34] D. Sohn. Kinetic studies of magnetic latex particles' self-assembly under applied magnetic field. *Journal of Magnetism and Magnetic Materials*, 173(3):305–313, 1997.

[35] F. Martinez Pedrero, M. Tirado Miranda, A. Schmitt, and J. Callejas Fernandez. Forming chainlike filaments of magnetic colloids: The role of the relative strength of isotropic and anisotropic particle interactions. *The Journal of Chemical Physics*, 125(8):084706, 2006.

[36] R. Rosman, J. J. M. Janssen, and M. Th. Rekveldt. Interparticle correlations in Fe_3O_4 ferrofluids, studied by the small angle neutron scattering technique. *Journal of Magnetism and Magnetic Materials*, 85(1):97–99, 1990.

[37] G. Mériguet, E. Dubois, M. Jardat, et al. Understanding the structure and the dynamics of magnetic fluids: coupling of experiment and simulation. *Journal of Physics: Condensed Matter*, 18(38):S2685–S2696, 2006.

[38] P. C. Jordan. Association phenomena in a ferromagnetic colloid. *Molecular Physics*, 25(4):961–973, 1973.

[39] S. Melle, M. A. Rubio, and G. G. Fuller. Time scaling regimes in aggregation of magnetic dipolar particles: Scattering dichroism results. *Physical Review Letters*, 87(11):115501, 2001.

[40] J. E. Martin and J. Odinek. Light scattering studies of the electrorheological transition. *Journal of Non-Crystalline Solids*, 172-174, Part 2:1135–1141, 1994.

[41] J. E. Martin, J. Odinek, and T. C. Halsey. Evolution of structure in a quiescent electrorheological fluid. *Physical Review Letters*, 69(10):1524–1527, 1992.

[42] J. M. Laskar, J. Philip, and B. Raj. Experimental investigation of magnetic-field-induced aggregation kinetics in nonaqueous ferrofluids. *Physical Review E*, 82(2):021402, 2010.

[43] J. J. M. Janssen, J. J. M. Baltussen, A. P. van Gelder, et al. Kinetics of magnetic flocculation. I. Flocculation of colloidal particles. *Journal of Physics D: Applied Physics*, 23(11):1447–1454, 1990.

[44] M. Hagenbüchle and J. Liu. Chain formation and chain dynamics in a dilute magnetorheological fluid. *Applied Optics*, 36(30):7664–7671, 1997.

[45] C. P. Reynolds, D. Robinson, D. G. A. L. Aarts, M. Wilson, W. W. Sampson, and R. P. A. Dullens. Coordination number statistics of cluster formation. *Forthcoming*, 2016.

[46] P. G. Gennes and P. A. Pincus. Pair correlations in a ferromagnetic colloid. *Physik der Kondensierten Materie*, 11(3):189–198, 1970.

[47] P. C. Jordan. Field dependent chain formation by ferromagnetic colloids. *Molecular Physics*, 38(3):769–780, 1979.

[48] J. P. Hansen and I. R. McDonald. *Theory of simple liquids: with applications to soft matter*. Academic Press, 1986.

[49] N. H. March and M. P. Tosi. *Coulomb liquids*. Academic Press, London; Orlando, 1984.

[50] M. E. van Leeuwen and B. Smit. What makes a polar liquid a liquid? *Physical Review Letters*, 71(24):3991–3994, 1993.

[51] T. Tlusty and S. A. Safran. Defect-induced phase separation in dipolar fluids. *Science*, 290(5495):1328–1331, 2000.

[52] D. Wei and G. N. Patey. Orientational order in simple dipolar liquids: Computer simulation of a ferroelectric nematic phase. *Physical Review Letters*, 68(13):2043–2045, 1992.

[53] D. Levesque and J. J. Weis. Orientational and structural order in strongly interacting dipolar hard spheres. *Physical Review E*, 49(6):5131–5140, 1994.

[54] J. J. Weis and D. Levesque. Ferroelectric phases of dipolar hard spheres. *Physical Review E*, 48(5):3728–3740, 1993.

[55] J. J. Weis and D. Levesque. Chain formation in low density dipolar hard spheres: A Monte Carlo study. *Physical Review Letters*, 71(17):2729–2732, 1993.

[56] D. Wei and G. N. Patey. Ferroelectric liquid-crystal and solid phases formed by strongly interacting dipolar soft spheres. *Physical Review A*, 46(12):7783–7792, 1992.

[57] J. J. Weis, D. Levesque, and G. J. Zarragoicoechea. Orientational order in simple dipolar liquid-crystal models. *Physical Review Letters*, 69(6):913–916, 1992.

[58] H. Schmidle and S. H. L. Klapp. Phase transitions of two-dimensional dipolar fluids in external fields. *The Journal of Chemical Physics*, 134(11):114903, 2011.

[59] E. A. Elfimova, A. O. Ivanov, and P. J. Camp. Theory and simulation of anisotropic pair correlations in ferrofluids in magnetic fields. *The Journal of Chemical Physics*, 136(19):194502, 2012.

[60] E. A. Elfimova, A. O. Ivanov, and P. J. Camp. Thermodynamics of dipolar hard spheres with low-to-intermediate coupling constants. *Physical Review E*, 86(2):021126, 2012.

[61] J. J. Weis and D. Levesque. Orientational order in high density dipolar hard sphere fluids. *The Journal of Chemical Physics*, 125(3):034504, 2006.

[62] G. Ganzenmüller, G. N. Patey, and P. J. Camp. Vapourliquid phase transition of dipolar particles. *Molecular Physics*, 107(4-6):403–413, 2009.

[63] X. S. Chen, M. Kasch, and F. Forstmann. Demixing phase transition in a mixture of hard-sphere dipoles and neutral hard spheres. *Physical Review Letters*, 67(19):2674–2677, 1991.

[64] X. S. Chen and F. Forstmann. The phase instability of molecular fluid mixtures: dipolar and neutral hard spheres. *Molecular Physics*, 76(5):1203–1211, 1992.

[65] A. F. Pshenichnikov and V. V. Mekhonoshin. Cluster structure and the first-order phase transition in dipolar systems - Monte Carlo simulation. *The European Physical Journal E*, 6(5):399–407, 2001.

[66] N. G. Almarza, E. Lomba, C. Martin, and A. Gallardo. Demixing in binary mixtures of apolar and dipolar hard spheres. *The Journal of Chemical Physics*, 129(23):234504, 2008.

[67] A. Goyal, C. K. Hall, and O. D. Velev. Self-assembly in binary mixtures of dipolar colloids: molecular dynamics simulations. *The Journal of Chemical Physics*, 133(6):064511, 2010.

[68] P. H. Lee and B. M. Ladanyi. Structural and dielectric properties of dipolar hard sphere mixtures: Reference hypernetted chain and pertubation theory results. *The Journal of Chemical Physics*, 91(11):7063–7074, 1989.

[69] S. W. de Leeuw, B. Smit, and C. P. Williams. Molecular dynamics studies of polar/nonpolar fluid mixtures. I. Mixtures of Lennard-Jones and Stockmayer fluids. *The Journal of Chemical Physics*, 93(4):2704–2714, 1990.

[70] G. C. A. M. Mooij, S. W. de Leeuw, C. P. Williams, and B. Smit. Free energy computations of mixtures of Stockmayer and polarizable Lennard-Jones fluids. *Molecular Physics*, 71:909–911, 1990.

[71] G. C. A. M. Mooij, S. W. de Leeuw, B. Smit, and C. P. Williams. Molecular dynamics studies of polar/nonpolar fluid mixtures. II. Mixtures of Stockmayer and polarizable Lennard-Jones fluids. *The Journal of Chemical Physics*, 97(7):5113–5120, 1992.

[72] A. Müller, J. Winkelmann, and J. Fischer. Simulation studies on mixtures of dipolar and nonpolar linear molecules: I. Liquid/liquid phase separation. *Fluid Phase Equilibria*, 99:35–47, 1994.

[73] C. Kriebel, A. Müller, J. Winkelmann, and J. Fischer. A hybrid equation of state for Stockmayer pure fluids and mixtures. *Fluid Phase Equilibria*, 119(1):67–80, 1996.

[74] A. Müller, J. Winkelmann, T. Boublík, and J. Fischer. Mixtures of dipolar with nonpolar linear molecules. *Molecular Physics*, 78(1):121–135, 1993.

[75] G. M. Range and S. H. L. Klapp. Density functional study of the phase behavior of asymmetric binary dipolar mixtures. *Physical Review E*, 69(4):041201, 2004.

[76] M. J. Blair and G. N. Patey. Gas-liquid coexistence and demixing in systems with highly directional pair potentials. *Physical Review E*, 57(5):5682–5686, 1998.

[77] E. L. Pollock, B. J. Alder, and G. N. Patey. Static dielectric properties of polarizable Stockmayer fluids. *Physica A: Statistical Mechanics and its Applications*, 108(1):14–26, 1981.

[78] J. M. Caillol, D. Levesque, J. J. Weis, P. G. Kusalik, and G. N. Patey. Computer simulation and theoretical results for a polar-polarizable fluid. *Molecular Physics*, 55(1):65–76, 1985.

[79] S. Dobra, I. Szalai, and S. Varga. Ordering transition and demixing of a binary mixture of thick and thin rodlike molecules in the presence of an external field. *The Journal of Chemical Physics*, 125(7):074907, 2006.

[80] C. Brunet, J. G. Malherbe, and S. Amokrane. Binary mixture adsorbed in a slit pore: Field-induced population inversion near the bulk instability. *Physical Review E*, 82(2):021504, 2010.

[81] A. Bradbury, S. Menear, and R. W. Chantrell. A Monte Carlo calculation of the magnetic properties of a ferrofluid containing interacting polydispersed particles. *Journal of Magnetism and Magnetic Materials*, 54-57:745–746, 1986.

[82] B. J. Costa Cabral. Structure of polydisperse dipolar hard-sphere fluids. *The Journal of Chemical Physics*, 112(9):4351–4356, 2000.

[83] T. Kruse, A. Spanoudaki, and R. Pelster. Monte Carlo simulations of polydisperse ferrofluids: Cluster formation and field-dependent microstructure. *Physical Review B*, 68(5):054208, 2003.

[84] A. O. Ivanov and S. S. Kantorovich. Structure of Chain Aggregates in Ferrocolloids. *Colloid Journal*, 65(2):166–176, 2003.

[85] A. O. Ivanov and S. S. Kantorovich. Chain aggregate structure and magnetic birefringence in polydisperse ferrofluids. *Physical review E - Statistical, Nonlinear and Soft Matter Physics*, 70(2):021401, 2004.

[86] Z. Wang and C. Holm. Structure and magnetic properties of polydisperse ferrofluids: a molecular dynamics study. *Physical review E - Statistical, Nonlinear and Soft Matter Physics*, 68(4):041401, 2003.

[87] A. O. Ivanov. Phase separation in bidisperse ferrocolloids. *Journal of Magnetism and Magnetic Materials*, 154(1):66–70, 1996.

[88] W. Poon. Physics. Colloids as big atoms. *Science (New York, N.Y.)*, 304(5672):830–831, 2004.

[89] J. Philibert. One and a half century of diffusion: Fick, Einstein, before and beyond. *Diffusion Fundamentals*, 4(6):1–19, 2006.

[90] A. Einstein. Zur Theorie der Brownschen Bewegung. *Annalen der Physik*, 324(2):371–381, 1906.

[91] J. Inczedy, T. Lengyel, and A. M. Ure. *Compendium on analytical nomenclature.* Blackwell Science, 1998.

[92] E. R. Weeks. *Soft jammed materials.* 2007.

[93] O. Stern. Zur theorie der elektrolytischen doppelschicht. *Berichte der Bunsengesellschaft für Physikalische Chemie*, 30(2122):508–516, 1924.

[94] K. Dmitri. *Stabilization of Colloids, www.substech.com, http://www.substech.com/dokuwiki/doku.php?id=stabilization_of_colloids, date accessed: January 09 2017.*

[95] J.C. Crocker and D. G. Grier. Microscopic measurement of the pair interaction potential of charge-stabilized colloid. *Physical Review Letters*, 73(2):352–355, 1994.

[96] B. Derjaguin and L. Landau. Theory of the stability of strongly charged lyophobic sols and of the adhesion of strongly charged particles in solutions of electrolytes. *Actaphysicochim*, 14(6):633–662, 1941.

[97] E. J. W. Verwey and J. Th. G. Overbeek. *Theory of the Stability of Lyophobic Colloids*. Courier Corporation, 1999.

[98] J. A. Weiss, A. E. Larsen, and D. G. Grier. Interactions, dynamics, and elasticity in charge-stabilized colloidal crystals. *The Journal of Chemical Physics*, 109(19):8659–8666, 1998.

[99] S. Wiederseiner, N. Andreini, G. Epely-Chauvin, and C. Ancey. Refractive-index and density matching in concentrated particle suspensions: a review. *Experiments in Fluids*, 50(5):1183–1206, 2010.

[100] M. Wilson. Computational study of the formation of inorganic nanotubes. In Elena Bichoutskaia, editor, *Computational Nanoscience*, chapter 10, pages 307–333. RSC Publishing, 2011.

[101] C. Bishop. *The construction, development and application of potential simulation models to the filling of carbon nanotubes by molten salts*. Phd thesis, *University College London*, 2009.

[102] R. Car and M. Parrinello. Unified Approach for Molecular Dynamics and Density-Functional Theory. *Physical Review Letters*, 55(22):2471–2474, 1985.

[103] M. Wilson and P. A. Madden. Polarization effects in ionic systems from first principles. *Journal of Physics: Condensed Matter*, 5(17):2687–2706, 1993.

[104] D. R. Robinson and M. Wilson. The liquid–amorphous transition and the high pressure phase diagram of carbon. *Journal of Physics: Condensed Matter*, 25(15):155101, 2013.

[105] M. Sprik. Hydrogen-bonding and the static dielectric-constant in liquid water. *The Journal of Chemical Physics*, 95(9):6762–6769, 1990.

[106] D. K. Remler and P. A. Madden. Molecular dynamics without effective potentials via the Car-Parrinello approach. *Molecular Physics*, 70(6):921–966, 1990.

[107] J. Tersoff. New empirical approach for the structure and energy of covalent systems. *Physical Review B*, 37(12):6991–7000, 1988.

[108] M. Huggins and J. Mayer. Interatomic distances in crystals of the alkali halides. *Chemical Physics*, 1:643–646, 1933.

[109] S. Erkoc. Empirical many-body potential energy functions used in computer simulations of condensed matter properties. *Physics Reports*, 278(2):79–105, 1997.

[110] J. Tersoff. Empirical interatomic potential for carbon, with applications to amorphous carbon. *Physical Review Letters*, 61(25):2879–2882, 1988.

[111] F. H. Stillinger and T. A. Weber. Computer simulation of local order in condensed phases of silicon. *Physical Review B*, 31(8):5262–5271, 1985.

[112] D. Frenkel and B. Smit. *Understanding molecular simulation: From algorithms to applications*. Academic Press, 2nd edition, 2002.

[113] D. R. Robinson. *The control of complex network topologies in amorphous carbon in two- and three-dimensions*. Part ii thesis, *University of Oxford*, 2012.

[114] M. P. Allen and D. J. Tildesley. *Computer simulation of liquids*. Oxford Science Publications, 1989.

[115] H. Goldstein. *Classical mechanics*. Addison-Wesley Pub. Co., 2nd edition, 1980.

[116] M. Born and J. R. Oppenheimer. No Title. *Annals of Physics*, 84:457, 1927.

[117] L. Verlet. Computer "experiments" on classical fluids. I. Thermodynamical properties of Lennard-Jones molecules. *Physical Review*, 159(1):98–103, 1967.

[118] W. C. Swope, H. C. Andersen, P. H. Berens, and K. R. Wilson. A computer simulation method for the calculation of equilibrium constants for the formation of physical clusters of molecules: Application to small water clusters. *The Journal of Chemical Physics*, 76(1):637–649, 1982.

[119] A. D. Buckingham. *Advances in Chemical Physics*, volume 12. John Wiley & Sons, Inc., Hoboken, NJ, USA, 1967.

[120] M. Wilson. *Many-body effects in ionic systems.* PhD thesis, *University of Oxford*, 1994.

[121] M. Sprik and M. L. Klein. A polarizable model for water using distributed charge sites. *The Journal of Chemical Physics*, 89(12):7556–7560, 1988.

[122] M. Wilson, P. A. Madden, and B. J. Costa-Cabral. Quadrupole polarization in simulations of ionic systems: Application to AgCl. *The Journal of Physical Chemistry*, 100(4):1227–1237, 1996.

[123] M. J. L. Sangster and M. Dixon. Interionic potentials in alkali halides and their use in simulations of the molten salts. *Advances in Physics*, 25(3):247–342, 1976.

[124] C. J. F. Böttcher. *Theory of Electric Polarization.* Elsevier, 1973.

[125] G. Pastore, E. Smargiassi, and F. Buda. Theory of ab initio molecular-dynamics calculations. *Physical Review A*, 44(10):6334–6347, 1991.

[126] E. S. Fois, J. I. Penman, and P. A. Madden. Control of the adiabatic electronic state in ab initio molecular dynamics. *The Journal of Chemical Physics*, 98(8):6361–6368, 1993.

[127] M. N. Rosenbluth and A. W. Rosenbluth. Further results on Monte Carlo equations of state. *The Journal of Chemical Physics*, 22(5):881–884, 1954.

[128] W. W. Wood and J. D. Jacobson. Preliminary results from a recalculation of the Monte Carlo equation of state of hard spheres. *The Journal of Chemical Physics*, 27(5):1207–1208, 1957.

[129] B. J. Alder and T. E. Wainwright. Phase transition for a hard sphere system. *The Journal of Chemical Physics*, 27(5):1208–1209, 1957.

[130] J. E. Jones. On the determination of molecular fields. I. From the variation of the viscosity of a gas with temperature. *Proceedings of the Royal Society A: Mathematical, Physical and Engineering Sciences*, 106(738):441–462, 1924.

[131] J. E. Jones. On the determination of molecular fields. II. From the equation of state of a gas. *Proceedings of the Royal Society A: Mathematical, Physical and Engineering Sciences*, 106(738):463–477, 1924.

[132] W. H. Stockmayer. Second virial coefficients of polar gases. *The Journal of Chemical Physics*, 9(5):398–402, 1941.

[133] M. Parrinello. Polymorphic transitions in single crystals: A new molecular dynamics method. *Journal of Applied Physics*, 52(12):7182–7190, 1981.

[134] W. G. Hoover. Canonical dynamics: Equilibrium phase-space distributions. *Physical Review A*, 31(3):1695–1697, 1985.

[135] S. Nosé. A Molecular-Dynamics method for simulations in the canonical ensemble. *Molecular Physics*, 52(2):255–268, 1984.

[136] S. Nosé. A unified formulation of the constant temperature molecular dynamics methods. *The Journal of Chemical Physics*, 81(1):511–519, 1984.

[137] P. P. Ewald. Die Berechnung optischer und elektrostatischer Gitterpotentiale. *Annalen der Physik*, 369(3):253–287, 1921.

[138] M. Mohebi, N. Jamasbi, and J. Liu. Simulation of the formation of nonequilibrium structures in magnetorheological fluids subject to an external magnetic field. *Physical Review E*, 54(5):5407–5413, 1996.

[139] Z. Wang, C. Holm, and H. W. Müller. Molecular dynamics study on the equilibrium magnetization properties and structure of ferrofluids. *Physical Review E - Statistical, Nonlinear and Soft Matter Physics*, 66(2):021405, 2002.

[140] A. O. Ivanov, Z. Wang, and C. Holm. Applying the chain formation model to magnetic properties of aggregated ferrofluids. *Physical review. E, Statistical, nonlinear, and soft matter physics*, 69(3):031206, 2004.

[141] Z. Wang and C. Holm. Estimate of the cutoff errors in the Ewald summation for dipolar systems. *The Journal of Chemical Physics*, 115(14):6351–6359, 2001.

[142] A. Leach. *Molecular modelling: Principles and applications*. Pearson Education, 2001.

[143] N. J. K. Withey. *Computer simulations of dipolar fluids using Ewald summations*. PhD thesis, *University of Reading*, 2012.

[144] S. W. de Leeuw, J. W. Perram, and E. R. Smith. Simulation of electrostatic systems in periodic boundary conditions. I. Lattice sums and dielectric constants. *Proceedings of the Royal Society A: Mathematical, Physical and Engineering Sciences*, 373(1752):27–56, 1980.

[145] T. R. Gingrich and M. Wilson. On the Ewald summation of Gaussian charges for the simulation of metallic surfaces. *Chemical Physics Letters*, 500(1-3):178–183, 2010.

[146] S. K Reed, O. J Lanning, and P. A Madden. Electrochemical interface between an ionic liquid and a model metallic electrode. *The Journal of Chemical Physics*, 126(8):084704, 2007.

[147] S. W. De Leeuw and J. W. Perram. Electrostatic lattice sums for semi-infinite lattices. *Molecular Physics*, 37(4):1313–1322, 1979.

[148] J. Miller. *Computer simulation of the filling of carbon nanotubes by molten salts.* Masters thesis, *University of Oxford*, 2009.

[149] N. E. Ahmed. *Computer simulation of dipole-dipole interactions towards understanding nanostructure formation.* PhD thesis, *University College London*, 2010.

[150] I. Saika-Voivod, F. Sciortino, and P. H. Poole. Fragile-to-strong crossover and polyamorphism in liquid silica: changes in liquid structure. *Philosophical Magazine*, 84(13-16):1437–1445, 2004.

[151] J. P. Hansen and I. R. McDonald. *Theory of simple liquids.* Academic Press, 3rd edition, 2006.

[152] M. Hemmati, M. Wilson, and P. A. Madden. Structure of liquid Al_2O_3 from a computer simulation model. *The Journal of Physical Chemistry B*, 103(20):4023–4028, 1999.

[153] M. C. Wilding, M. Wilson, C. J. Benmore, J. K. R. Weber, and P. F. McMillan. Structural changes in supercooled Al_2O_3-Y_2O_3 liquids. *Physical chemistry chemical physics : PCCP*, 15(22):8589–8605, 2013.

[154] L. Guttman. Ring structure of the crystalline and amorphous forms of silicon dioxide. *Journal of Non-Crystalline Solids*, 116(2-3):145–147, 1990.

[155] S. V. King. Ring configurations in a random network model of vitreous silica. *Nature*, 213(5081):1112–1113, 1967.

[156] K. Goetzke and H. J. Klein. Properties and efficient algorithmic determination of different classes of rings in finite and infinite polyhedral networks. *Journal of Non-Crystalline Solids*, 127(2):215–220, 1991.

[157] S. Le Roux and V. Petkov. ISAACS interactive structure analysis of amorphous and crystalline systems. *Journal of Applied Crystallography*, 43(1):181–185, 2010.

[158] G. Bossis, O. Volkova, S. Lacis, and A. Meunier. *Ferrofluids*, volume 594 of *Lecture Notes in Physics*. Springer Berlin Heidelberg, Berlin, Heidelberg, 2002.

[159] M. Wilson and P. A. Madden. α and β relaxation processes in $ZnCl_2$ - a computer simulation study. *Journal of Physics: Condensed Matter*, 11(10A):A237–A246, 1999.

[160] Wolfram Research Inc. Mathematica, 2014.

[161] C. P. Reynolds. *Field induced assembly of superparamagnetic colloidal particles*. PhD thesis, *University of Oxford*, 2016.

[162] P. H. Hess and P. H. Parker. Polymers for stabilization of colloidal cobalt particles. *Journal of Applied Polymer Science*, 10(12):1915–1927, 1966.

[163] M. Juniper. *Self-assembly of super-paramagnetic colloidal particles under an external magnetic field in bulk and confined systems*. PhD thesis, *University of Oxford*, 2010.

[164] C. P. Reynolds, K. E. Klop, F. A. Lavergne, S. M. Morrow, D. G. A. L. Aarts, and R. P. A. Dullens. Deterministic aggregation kinetics of superparamagnetic colloidal particles. *The Journal of Chemical Physics*, 143(21):214903, 2015.

[165] N. Arkus, V. N. Manoharan, and M. P. Brenner. Minimal energy clusters of hard spheres with short range attractions. *Physical Review Letters*, 103(11):118303, 2009.

[166] G. Meng, N. Arkus, M. P. Brenner, V. N. Manoharan, et al. The free-energy landscape of clusters of attractive hard spheres. *Science (New York, N.Y.)*, 327(5965):560–563, 2010.

[167] A. I. Campbell, V. J. Anderson, J. S. van Duijneveldt, and P. Bartlett. Dynamical arrest in attractive colloids: the effect of long-range repulsion. *Physical Review Letters*, 94(20):208301, 2005.

[168] M. M. Van Schooneveld, V. W. A. De Villeneuve, R. P. A. Dullens, D. G. A. L. Aarts, M. E. Leunissen, and W. K. Kegel. Structure, stability, and formation pathways of colloidal gels in systems with short-range attraction and long-range repulsion. *Journal of Physical Chemistry B*, 113(14):4560–4564, 2009.

[169] B. Ruzicka, E. Zaccarelli, L. Zulian, R. Angelini, M. Sztucki, A. Moussaïd, T. Narayanan, and F. Sciortino. Observation of empty liquids and equilibrium gels in a colloidal clay. *Nature materials*, 10(1):56–60, 2011.

[170] O. Markova, J. Alberts, E. Munro, and P. F. Lenne. Clustering of low-valence particles: structure and kinetics. *Physical Review E - Statistical, Nonlinear and Soft Matter Physics*, 90(2):022301, 2014.

[171] P. F. Damasceno, M. Engel, S. C. Glotzer, L. Pauling, et al. Predictive self-assembly of polyhedra into complex structures. *Science (New York, N.Y.)*, 337(6093):453–457, 2012.

[172] J. M. Lehn. *Supramolecular Chemistry*. Wiley-VCH Verlag GmbH & Co. KGaA, Weinheim, FRG, 1995.

[173] S. C. Glotzer and M. J. Solomon. Anisotropy of building blocks and their assembly into complex structures. *Nature Materials*, 6(7):557–562, 2007.

[174] Y. Wang, Y. Wang, D. R. Breed, V. N. Manoharan, L. Feng, A. D. Hollingsworth, M. Weck, and D. J. Pine. Colloids with valence and specific directional bonding. *Nature*, 491(7422):51–55, 2012.

[175] J. R. Wolters, G. Avvisati, F. Hagemans, T. Vissers, D. J. Kraft, M. Dijkstra, and

W. K. Kegel. Self-assembly of "Mickey Mouse" shaped colloids into tube-like structures: experiments and simulations. *Soft Matter*, 11(6):1067–1077, 2015.

[176] M. Sabapathy, S. D. Christdoss Pushpam, M. G. Basavaraj, and E. Mani. Synthesis of single and multipatch particles by dip-coating method and self-assembly thereof. *Langmuir : the ACS journal of surfaces and colloids*, 31(4):1255–1261, 2015.

[177] D. J. Kraft, J. Groenewold, W. K. Kegel, S. C. Glotzer, M. J. Solomon, et al. Colloidal molecules with well-controlled bond angles. *Soft Matter*, 5(20):3823–3826, 2009.

[178] D. Kraft, R. Ni, F. Smallenburg, M. Hermes, K. Yoon, D. Weitz, A. Blaaderen, J. Groenewold., M. Dijkstra, and W. Kegel. Surface roughness directed self-assembly of patchy particles into colloidal micelles. *Proceedings of the National Academy of Sciences of the United States of America*, 109(27):10787–10792, 2012.

[179] S. Sacanna, M. Korpics, K. Rodriguez, L. Colón-Meléndez, S. H. Kim, D. J. Pine, and G. R. Yi. Shaping colloids for self-assembly. *Nature Communications*, 4:1688, 2013.

[180] Q. Chen, S. C. Bae, and S. Granick. Directed self-assembly of a colloidal kagome lattice. *Nature*, 469(7330):381–384, 2011.

[181] A. Papoulis and S. U. Pillai. *Probability, random variables and stochastic processes*. McGraw Hill, 4th edition, 2002.

[182] M Von Smoluchowski. Versuch einer mathematischen Theorie der Koagulationskinetik. *Phys Chem*, 92(1912):156, 1917.

[183] T. Rudas. *Handbook of probability : theory and applications*. Sage Publications, 2008.

[184] E. M. Furst and A. P. Gast. Micromechanics of dipolar chains using optical tweezers. *Physical Review Letters*, 82(20):4130–4133, 1999.

[185] E. Rapoport. Model for melting-curve maxima at high pressure. *The Journal of Chemical Physics*, 46(8):2891–2895, 1967.

[186] E. Guggenheim. Modern thermodynamics by The Methods of Willard gibbs London: Methuen & Co., 1933. 10s. 6d. *Journal of the Society of Chemical Industry*, 53(18):379–379, 1934.

[187] R. Haghgooie, P. S. Doyle, K. Channon, C. E. MacPhee, et al. Directed self-assembly of field-responsive fluids in confined geometries. *Soft Matter*, 5(6):1192–1197, 2009.

[188] J. Jordanovic and S. H. L. Klapp. Structure of ferrofluid nanofilms in homogeneous magnetic fields. *Physical Review E - Statistical, Nonlinear and Soft Matter Physics*, 79(2):021405, 2009.

[189] K. Peeters and K. Dullemond. Introduction to tensor calculus. Technical report, *University of Heidelberg*, 1991.

[190] J. Jordanovic and S. H. L. Klapp. Field-induced layer formation in dipolar nanofilms. *Physical Review Letters*, 101(3):038302, 2008.

[191] V. V. Murashov, P. J. Camp, and G. N. Patey. Dielectric relaxation of chained ferrofluids. *The Journal of Chemical Physics*, 116(15):6731–6737, 2002.

[192] P. D. Duncan and P. J. Camp. Structure and dynamics in a monolayer of dipolar spheres. *The Journal of Chemical Physics*, 121(22):11322–11331, 2004.

[193] P. J. Camp. Dynamics in a two-dimensional core-softened fluid. *Physical Review E*, 71(3):031507, 2005.

[194] P. Duncan and P. J. Camp. Aggregation kinetics and the nature of phase separation in two-dimensional dipolar fluids. *Physical Review Letters*, 97(10):107202, 2006.

[195] J. Richardi and J. J. Weis. Low density mesostructures of confined dipolar particles in an external field. *The Journal of Chemical Physics*, 135(12):124502, 2011.

[196] E. Furst and A. Gast. Dynamics and lateral interactions of dipolar chains. *Physical Review E*, 62(5):6916–6925, 2000.